UNIVERSITY OF STRATHCLYDE

FACULTY OF ENGINEERING
DEPARTMENT OF BIOMEDICAL ENGINEERING

# APPLICATION OF ADVANCED MATERIAL ANALYSES FOR THE INVESTIGATION OF THE ROLE OF NANO-MECHANICAL PROPERTIES IN CELL - SCAFFOLD INTERACTIONS
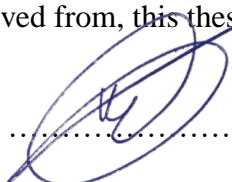
by

MILOVAN JOE CARDONA

A thesis presented in fulfilment for the requirements of the

degree of Doctor of Philosophy

2016

# Declaration of Authenticity

This thesis is the result of the author's original research. It has been composed by the author and has not been previously submitted for examination which has led to the award of a degree.

The copyright of this thesis belongs to the author under the terms of the United Kingdom Copyright Acts as qualified by University of Strathclyde Regulation 3.50. Due acknowledgement must always be made of the use of any material contained in, or derived from, this thesis.

Signed:    …………………………                                Date: .20./ ..6../ 2016

# Abstract

The fate of cells seeded onto a scaffold is determined by a number of factors including chemical, topographical and mechanical stimuli. The combination of these factors regulates a number of cellular functions and ultimately determines the performance of the engineered tissue. In recent years, focus has shifted from investigating bulk scaffold properties to nano-scale properties that are more relevant on the cellular scale. This trend has been partially fuelled by a significant increase in the availability of nano-scale analysis techniques and a general development in scientific investigations on such scales. Standard Euler's principles do not apply on the nano-scale, and a number of previous publications have examined and modelled various strain dependent nano-mechanical properties. Size effect theories predict that the effective modulus of elasticity increases as the length scale of measurement decreases. These changes occur at the length scales of the order of the cell and their effects on cellular mechanotransduction have not yet been investigated. This body of work attempts to lay the foundations and develop techniques that can eventually be used to investigate the influence of nano-mechanical properties on cell mechanotransduction in fibrous scaffolds.

Medical grade polyurethanes (*Biomer Technology Limited, Runcorn, UK*) were chosen for this study because of their wide range of mechanical properties while maintaining similar chemistry. Solvent-cast films fabricated from various grades of these materials were first characterised on both the nano- and macro- scale in order to inform the fabrication of three-dimensional electrospun fibrous scaffolds. Such scaffolds were then fabricated with a variety of nano-mechanical properties by altering fibre diameter distributions. Dual spinning was also used in order to fabricate a scaffold with mixed nano-mechanical properties.

The stability of such polymers when stored under physiological conditions over a period of 90 days was then investigated. Thereafter, samples were prepared for use in an initial assessment of cell attachment in order to investigate the extent to which three different cell types were able to adhere and proliferate on both scaffold forms

fabricated from two grades of polyurethane with distinct macro- and nano-mechanical properties. The implications that such changes in nano-mechanical properties could have on cell mechanotransduction are discussed. Further experiments are suggested in order to develop a better understanding of these interactions.

# Acknowledgments

First and foremost, I would like to thank my supervisor Dr. Richard A. Black, who was responsible for the successful progress and completion of my work. His suggestions, knowledge and expertise in the subject were greatly appreciated. I would also like to express my deep gratitude for his patience and continuous guidance throughout the entire process.

I am grateful for the University of Strathclyde Scholarship which allowed me to pursue the research and the Advanced Materials Research Laboratory for making equipment available. I would also like to thank Biomer Technology Ltd. and especially Simon Dixon for his support and for making polymers available. My sincere thanks go to Katie Henderson and Brian Cartlidge for their expertise and technical assistance. Their availability and assistance was instrumental at the several stages of this project.

I would like to thank all my friends and colleagues with special thanks to Anna Galluzzo, Davide Erbogasto and Thomas Harrison for their company, support and suggestions which were essential for the completion of this thesis. Finally, I am as ever thankful to my family. I would like to give my sincere gratitude to my parents for their unyielding love and continuous support. I would also like to give special thanks to my sister for her patience, continuous support and advice throughout my thesis. I am sure that this work would not have been possible without all their help.

# Table of Contents

# List of Figures

# List of Tables

# List of Abbreviations

| | |
|---|---|
| AB | AlamarBlue |
| AFM | Atomic force microscope |
| DMAC | Dimethylacetamide |
| DMEM | Dulbecco's modified eagle's medium |
| DMF | Dimethylformamide |
| D-PBS | Dulbecco's phosphate-buffered saline |
| DSC | Differential scanning calorimetry |
| ECM | Extracellular matrix |
| FAK | Focal adhesion kinase |
| FTIR | Fourier transform infrared spectroscopy |
| GNDs | Geometrically necessary dislocations |
| HS | Hard segment |
| HUVEC | Human umbilical vein endothelial cells |
| LFM | Lateral force microscopy |
| PAAm | Poly (acrylamide) |
| PBS | Phosphate buffered saline |
| PCL | Polycaprolactone |
| PDMS | Poly (dimethyl siloxane) |
| PEG | Poly (ethylene glycol) |
| PEO | Poly (ethylene oxide) |
| PLA | Poly (lactic acid) |
| PPAEC | Porcine pulmonary artery endothelial cells |
| PTFE | Polytetrafluoroethylene |
| PVA | Poly(vinyl acetate) |
| RGD | Arginyl-glycyl-aspartic |
| RPM | Revs per minute |
| SEM | Scanning electron microscope |
| SS | Soft segment |
| TCP | Tissue culture plastic |
| THF | Tetrahydrofuran |
| TPU | Thermoplastic polyurethane |
| TTC | Tip to collector |
| UHMWPE | Ultra-high molecular weight polyethylene |
| XPS | X-ray photoelectron spectroscopy |

# Chapter 1

# Introduction

## 1.1. Overview of Research

Over the past few decades, tissue engineering has developed into a major discipline in the field of regenerative medicine, and presents potential solutions to problems associated with current therapies in the treatment of tissue defects caused by diseases, age related conditions and trauma. The basic principles of tissue engineering are illustrated in *Figure 1.1*. Healthy cells are first isolated from a biopsy obtained from a target organ and then expanded in culture to acquire an extensive supply of healthy cells. Simultaneously, a scaffold that mimics the original extracellular structure of the target organ is fabricated using one of a wide range of manufacturing techniques. Scaffolds are constructed using a biocompatible material and must not only provide the bulk mechanical properties required for the tissue to carry out its function but must also provide adequate stimuli to cells for successful growth and proliferation [1]. Cells are then seeded onto the scaffold and cultured in a bioreactor where appropriate chemical and mechanical stimuli are applied in order to promote cell organisation and further proliferation. This artificial tissue can then be implanted into the patient to help recover the function of the original organ.

There are a large number of potential applications for tissue engineering products with a significant number of studies focusing on the numerous variables involved in the production of a successful engineered tissue. Wound care is one of the leading sectors in which artificial tissues are used. By mimicking the extracellular matrix, fibrous scaffolds facilitate tissue morphogenesis and the healing process of damaged tissue [2]. Around 16,000 patients are admitted to NHS hospitals each year requiring medical treatment on burn wounds [3]. Fibrous scaffolds have been shown to provide an alternative to autografting and traditional wound dressings for patients with larger

burn areas [4]. The number of patients that can take advantage of these technologies can be further expanded by considering patients with chronic wounds such as diabetic ulcers, pressure ulcers and venous ulcers [5].
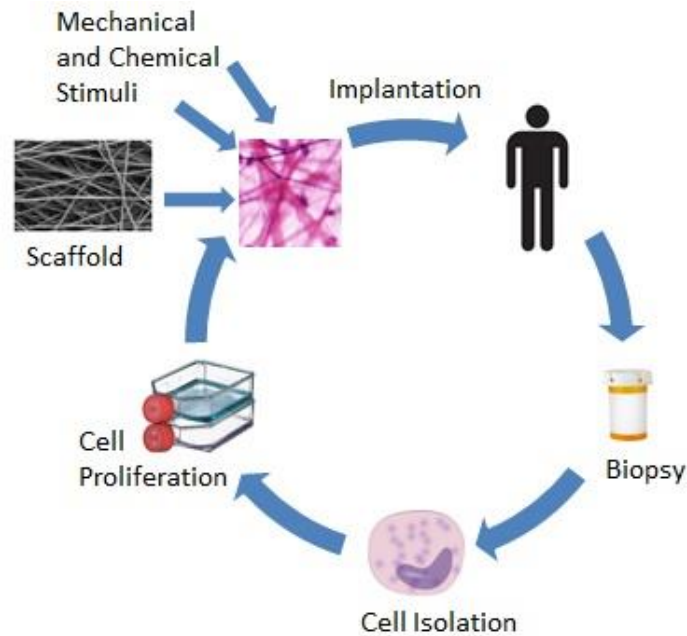


Figure 1.1 – Schematic illustration of the tissue engineering approach

A natural development from wound care was in the use of artificial tissue as drug-delivery systems. Fibrous scaffolds can be modified to alter drug delivery profiles by varying factors such as mesh porosity and drug binding mechanisms to ensure optimal results [6]. Drug-loaded fibrous meshes are also used as site-specific drug delivery systems where drugs are placed directly into, or adjacent to, the target area. These have numerous advantages over drugs that are carried through the blood system as they only target affected areas and therefore reduce side-effects that can be severe [7].

Tissue engineering has also found its place in the regeneration of articular cartilage with joint pain, usually resulting from the degradation of the joint cartilage, which is one of the major causes of disability in the middle-aged and older demographic. Since cartilage does not usually repair itself, tissue engineering solutions are being

used in an attempt to recover its functions in damaged tissue [8, 9]. Similarly, self-regeneration in the nervous system is very limited and usually has a larger burden on the patient's quality of life. Autologous nerve grafting is the current gold standard and has a number of inherent disadvantages including the limited supply of donor nerves, the need for multiple surgeries, and mismatch between the donor nerve and the recipient site. In an attempt to supplement or even substitute current techniques, research into tissue engineered nerve grafts has increased significantly in recent years [10].

It is evident that cellular function is particularly important in the production of successful engineered tissues. However, without the appropriate stimuli, these cannot proliferate or survive. Such stimuli originate from multiple sources and literature has pointed out that a combination of chemical and mechanical cues are key for the viability of cells cultured on such scaffolds.

## 1.2. Thesis Outline

In fibrous tissues, cells interact with individual fibres on the nano-micro scale rather than with the scaffold as a whole. Size effects have been demonstrated to possess a significant influence on the scale at which cells mechanosense. In fibrous scaffolds, the nano-mechanical properties of individual fibres are not only dependant on the material used but also on the mode of loading as well as the fibre diameter. It is therefore important to explore these nano-mechanical properties as changes on this scale might result in changes in cell motility, viability and differentiation. The remaining chapters of this thesis are organised as follows:

**Chapter 2** encompasses a literature review on the manufacture of artificial cell substrates and the influence of size effects at different scales. It also introduces cell‑scaffold interactions and the influence of different surface cues on cell behaviour.

**Chapter 3** outlines the experimental theory and techniques used. It also describes the exact methodologies described in this thesis.

**Chapter 4** reports on the investigation of mechanical, topographical and thermal properties in specific medical grade polyurethanes of similar composition but different stiffness, both in solvent-cast films as well as in fibrous scaffolds. Analysis is performed on both the macro and nano-scale in order to obtain a better understanding of the scale on which cells interact within the scaffold.

**Chapter 5** reports on the manufacture and the investigation of electrospun mats with different nano-mechanical properties from a range of polyurethane grades.

**Chapter 6** reports on an investigation into whether exposure to a physiological environment could alter the surface properties of the polyurethanes over an extended period of time.

**Chapter 7** reports on an initial assessment of cell attachment and whether or not it is possible to culture cells on this polyurethane range in both solvent-cast and electrospun forms.

**Chapter 8** concludes with a general discussion of the findings of this research and discusses possible future research and experiments in this field.

# Chapter 2
# Literature Review

## 2.1. Scaffolds in Tissue Engineering

Scaffolds represent a major component in tissue engineering as they have to provide structural support for cell attachment and subsequent tissue development. The vast majority of cell types found in human tissues have to adhere to a solid matrix called the extracellular matrix (ECM) and each cell type typically attaches preferentially to a tissue-specific ECM with multiple components. Even though the complexities of native ECM are difficult to replicate, the main aim in tissue engineering is to synthesise artificial scaffolds that can host cells and encourage cell proliferation while maintaining the overall architecture required for tissue regeneration.

The closest replications of ECM use tissue engineering are sometimes obtained by decellularising allogeneic or xenogeneic tissues as shown by Weber *et al.* and Badylak *et al.* respectively [11, 12]. This process involves specialised techniques that completely remove the cellular component of a tissue while preserving the ECM components in order to minimise the immune response when the tissue is implanted into the patient. These decellularisation techniques typically vary depending on the tissue being processed but usually involve a combination of physical, chemical and enzymatic methods to completely remove each component of the cellular structure. Since aggressive detergents are sometimes used, the process parameters have to be optimised to minimise the influence on the mechanical, topographical and biochemical properties of the ECM [13, 14]. These decellariased ECM are then seeded with cells, cultured in a bioreactor and implanted in the patient. This technique has been proven to be successful with a number of tissues including tendons [15], heart valves [16], blood vessels [17] and nerves [18]. The possibility of

incomplete decellularisation is the main risk of this technique as this could elicit a potentially life-threatening immune response upon implantation [19].

Another technique used in the formation of ECM for tissue engineering is by the production of cell sheets in which cells are encouraged to manufacture their own ECM. In a technique enhanced by Okano *et al.*, cells were cultured to confluency on a specialised surface and then detached in a complete sheet by altering the hydrophobicity of the substrate [20, 21]. This was then repeated a number of times to create a matrix with multiple layers of cells. This process is mainly used in cell-rich tissues as confluency has to be reached before the sheet can be harvested. ECM-rich tissues used for load-bearing such as bone and cartilage are unlikely to be created using this technique as the amount of ECM produced is very limited. Literature shows that cell sheets with self-secreted ECM have demonstrated potential in tissues such as corneas and in the myocardium but the clinical challenges of producing a tissue from cell layers of about 30 µm thick is proving to be one of the main disadvantages of this technique [22, 23].

Cell encapsulation is another form of tissue engineering in which living cells are entrapped within a semi-permeable mass [24, 25]. The materials usually used in this application are hydrogels made from a number of both natural and synthetic materials such as sodium alginate and poly(ethylene glycol) (PEG). These materials have to be permeable to nutrients and cell secreted therapeutic biomolecules while being impermeable to antibodies or cellular antigens that might harm the encapsulated cells [26]. This technique has been reported to be highly successful in the treatment of diabetes by the encapsulation of xenogeneic pancreatic cells in a hydrogel to secrete insulin in patients without triggering an immune response. Even though this technique is very versatile, hydrogels usually have poor mechanical properties meaning they are rarely used in tissues with load bearing functions [24].

The fabrication of scaffolds using industrial manufacturing techniques has always been the focus of the majority of research in this field leading to significant developments in novel biomaterials and fabrication techniques. Scaffolds can be

manufactured from a variety of bio-compatible materials and these processes are not limited to natural materials such as proteins and polysaccharides. Synthetic materials such as synthetic polymers as well as metals and ceramics can be used to tailor the mechanical, chemical and topographical properties of the manufactured substrates. These scaffolds can then be further processed to modify the surface and bulk mechanical properties to improve their biocompatibility and cell affinity [27].

Numerous processing techniques have been developed and adapted for the manufacture of cell substrates. The most basic techniques involve processes that manufacture three-dimensional structures using porogens in biomaterials. These include solvent-casting, freeze drying, phase separation and particulate leaching [28]. Rapid prototyping is another widely used class of manufacturing processes and has seen a large increase in interest in recent years with hierarchical porous structures being manufactured by the various free-form fabrication techniques [29]. Amongst other variables, Valerie and Sangeeta used cell-laden pastes which are sometimes used to manufacture scaffolds that have already been seeded with the right cell density and phenotype [30, 31]. A third category utilises woven or non-woven fibrous structures that imitate the fibrous components found in native ECM. The large surface area to volume ratio that these scaffolds present makes them ideal for three-dimensional cell culture [32, 33]. These approaches carry a number of limitations. Cell seeding after the substrate is manufactured is usually very time consuming and can lead to heterogeneities of cell densities across the scaffold. Rose *et al*. emphasise that this is highly dependent on the porosity of the substrate as the ability of cells to penetrate the scaffold can be limited [34]. Although the ability of using synthetic materials is advantageous in the manufacture of scaffolds with tailored chemical and mechanical properties, improving cell affinity to the required specifications usually necessitates a substantial amount of time and research. Even though these limitations play a considerable role in the selection of scaffold manufacture technique used, the use of artificially fabricated scaffolds still remain the most varied and versatile cell substrate manufacturing techniques in tissue engineering.

## 2.1.1. The role of polymers in tissue engineering

Polymers are considered to be the largest and most promising class of biomaterials owing to their wide range of mechanical and chemical properties [35]. A vast range of chemically different polymers can be easily synthesised and formed into a wide variety of shapes and forms, as well as being economically feasible to mass-produce. A wide variety of polymers has also been successfully produced and tested rigorously to ensure their biostability and biocompatibility [36]. This combination has led to copious research being conducted on the various aspects of polymeric biomaterials.

A considerable number of polymers have also been used for tissue engineering in the formation of cell scaffolds. These include degradable and non-degradable polymers which can originate from a natural source or be completely synthetic [37, 38]. Degradable polymers allow cells to build their own extracellular matrix and slowly degrade to leave behind an organ made entirely of natural materials. Non-degradable polymers influence tissue turnover while having the advantage that their chemical and mechanical properties remain, to a certain extent, unaffected by time [39].

Biocompatible polyurethanes have a proven track record in the manufacture of medical implants as they show excellent biocompatibility and tuneable mechanical properties [40]. They have been used in medical devices such as cardiac pacemakers, vascular grafts and in the production of artificial scaffolds [41]. A study by Carlberg *et al.* [42] investigated the proliferation and differentiation of human embryonic stem cells on polyurethane scaffolds. They confirm that polyurethane is a suitable material for the manufacture of cell scaffolds, displaying favourable interaction between the cells and the substrate. They also indicate that the physical cues provided by their scaffolds directed stem cells towards a neuronal cell fate. Another study by Grenier *et al.* [43] investigated the interactions between polyurethane scaffolds and coronary artery smooth muscle cells. They, amongst others, also concluded that polyurethane is a suitable substrate material for scaffold manufacture [44].

## 2.1.2. Manufacture of fibrous cell scaffolds

Various techniques have been developed to manufacture nano-fibrous scaffolds. For the purpose of this study, only techniques used in polymer processing will be described. These include: drawing, template synthesis, self-assembly and electrospinning.

In *drawing*, a micro-manipulator is used to bring a pipette into contact with a polymer solution droplet. The micropipette is then slowly withdrawn from the droplet at a fixed speed resulting in the production of a nanofibre. The equipment required is minimal, but the process is not continuous, producing fibres no more than millimetres long [45, 46].

In *template synthesis*, a metal oxide membrane with pores of a set diameter is used as an extrusion dye to create nanofibres from a polymer solution under the application of pressure. The fibre diameter produced depends on pore diameter of the membrane and can easily be varied by using a different membrane. The main disadvantage of this process is that it cannot be scaled up and usually only produces fibres of around 10 microns in length [47].

*Self-assembly* of nanofibres is a process in which molecules are used as basic building blocks for nanoscale fibres. Molecules are arranged such that bonds are formed concentrically resulting in an individual nanofibre with diameters ranging from 7 nm to 100 nm. Even though this technique was used on a wide range of polymers, the process involved is complex and the nanofibres produced are no longer than several microns [46, 48, 49].

*Electrospinning* is a technique in which a high voltage potential is used to draw out a nanofibre from a polymer solution droplet. The first documented technique that manufactured nanofibres from a polymer solution dates back to 1902 in a patent filed by *Cooley* and *Morton.* This patent describes a method that deposits a viscous polymer solution onto a positively charged electrode when it is held close to an

electrode of opposite charge. The principal ideas set by these century-old patents are still being used in today's electrospinning processes [46]. A substantial number of patents that build up on the original idea of electrospinning were later filed by various individuals, each contributing to laying down an enhanced overall technique for the electrospinning process. In the past two decades, with recent advancements in the understanding of fluid dynamics and electrostatics as well as the availability of newer technologies such as electron microscopy, this technique was rediscovered, refined and expanded into numerous new applications [50]. Various parameters, such as the polymer solution properties, the voltages applied and the distance between the polymer solution and the collector can be manipulated to obtain different fibre diameters and morphologies [51]. Fibrous mats have been successfully produced from a wide range of polymers and diameters ranging from 3 nm to 2 μm have been reported. Electrospinning is also very cost-effective and the process can, to a certain extent, be scaled up if needed. The major drawback of this technique is polymer jet instability that causes intermittent electrospinning. However, continuous fibres up to several metres in length can still be produced making electrospinning the most attractive manufacturing technique for the purpose of tissue engineering [46, 52].

## 2.2. Mechanical Analysis of Fibrous Scaffolds

Fibrous scaffolds are required to retain their structural integrity and maintain the desired shape before new tissue is completely regenerated. Bulk mechanical characterisation is therefore beneficial for understanding how an implant will act under external loading. With cell size being on the scale of a few tens of micro-meters, individual cells cultured on electrospun scaffolds only interact with individual fibres rather than the electrospun mesh as a whole [53]. It is therefore also important to understand the nano-mechanical properties of electrospun scaffolds as these may possibly vary from the bulk [54]. This section will focus on some of the techniques available to measure the mechanical properties of fibrous scaffolds and those of individual fibres.

## 2.2.1. Mechanical properties of fibrous scaffolds

The techniques used to measure the mechanical properties of fibrous scaffolds have mostly been adapted from the textile industry. The most widely used and straight-forward technique involves cutting specimens of randomly-aligned fibres into rectangular or typical dumbbell-shaped test samples and tested using a tensile test machine to obtain the tensile properties. This technique is reported in various publications in the testing of fibrous cell scaffolds manufactured from both artificial and natural materials [55 – 57]. A number of authors have also attempted to investigate the influence of alignment and pore size in such substrates as well as model such substrates *in silico* [58 – 61]. This method of analysis however only investigates bulk mechanical properties of the scaffold which, even though have an essential role in the success of the implant, are not representative of mechanical properties that individual cells respond to.

## 2.2.2. Single fibre characterisation

Despite its various challenges, characterisation of individual fibres is critical as invariably, the mechanical properties of a fibrous scaffold are governed by the mechanical properties of the individual nanofibres. Cells also interact with single fibres rather than the mesh as a whole while tensile forces applied by the cells on the scaffold during motion are on the nano-newton scale. It is therefore important to characterise scaffolds on the nano-scale for a better understanding of the forces encountered by cells. The main challenges associated with characterisation of fibres include manipulation, suitable modes of observation, sourcing accurate force transducers and the preparation of samples with single nanofibre strands [50, 62, 63]. Atomic force microscopy (AFM) is a technique that uses cantilevers with a wide range of spring constants (0.01 N/m to 100 N/m) which in turn have tips with radii of tens to a few hundred nanometres [64]. This technique has therefore been widely used for nano-mechanical testing as it allows for manipulation, imaging and loading on the nano-scale. A number of different methods have also been developed that use AFM cantilevers that investigate different modes of loading. Three-point bending as illustrated in *Figure 2.1(a),* is the most widely used technique and involves applying

a force at the midpoint of a suspended fibre [65]. Tensile testing is also been performed using a functionalised tip as illustrated in *Figure 2.1(b)* [66]. Lateral force microscopy monitors torsional movement of the AFM tip and has also been used to determine the elastic modulus on the nano-scale as shown in *Figure 2.1(c)* [67]. Nano-indentation is another technique that can be used to investigate the compressive modulus on the nanoscale and is widely used as sample preparation is considered to be more straightforward when compared to other techniques.
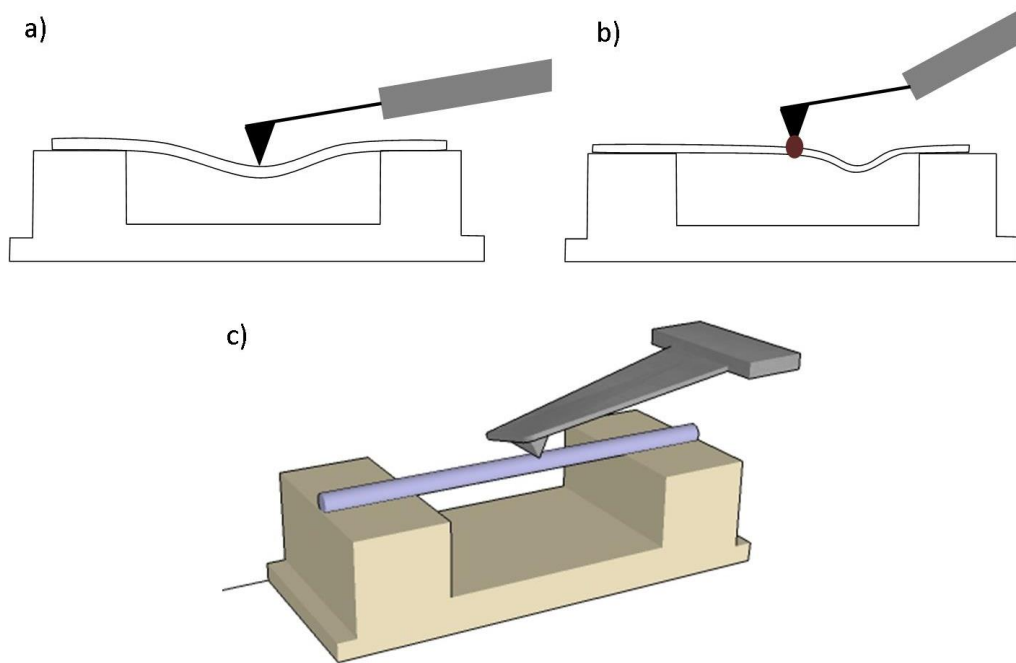


Figure 2.1 - Fibre loading using AFM:. a) three-point bending, b) tensile testing, c) lateral bending

## 2.2.3. Size effects

A large body of literature has demonstrated size effects whereby a change in the size of the object being tested produces a change in the mechanical response. This has been observed in nano-indentation where shallower indents demonstrate an increased hardness, torsion loaded wires displaying greater strengths when the radii are reduced and in bending of fibres where smaller radii demonstrated an increased modulus [68]. Conventional plasticity theories do not take into consideration these size effects and only work when the length scale associated with the deformation is small when compared to the size of the object being investigated [68]. Fleck *et al.* [69] explain that this elevated stiffness only arises when a large strain gradient is present. These strain gradients appear either because of the geometry of loading or because of heterogeneities within the material itself [70].

In a beam, strain is zero along the axis of twist or bending i.e. the neutral axis, but a finite value at the surface as shown in *Figure 2.2*. For a given strain, as the radius of the beam decreases, the gradient of strain from the axis to the surface increases. This increase in strain gradient due to geometry of loading can also be seen in nano-indentation. Here, the maximum strain is observed just below indenter tip and is zero far away from it. As indents become shallower, this distance is decreased thus increasing the strain gradient [69]. Heterogeneities within the material structure such as hard, non-deforming particles within a soft lattice generate strain gradients between particles. This is similar to polycrystalline materials that have a mismatch in the slip at grain boundaries causing a localised increase in strain gradient [69].

When objects deform, dislocations are generated, translated and stored. Storage of dislocations will in turn cause the material to work-harden. These dislocations become stored by two mechanisms: by a random trapping process (also called statistically-stored dislocations) or appear as they are required to permit deformation in different parts of the crystal. The latter are known as "geometrically-necessary dislocations" (GNDs) and are caused primarily by gradients in strain [71]. GNDs were first introduced by *Nye* in 1953 [72] and further investigated in a number of

publications by *Kroner* [73] and *Ashby* [71]. They have since been regarded as the physical basis for theories regarding strain gradient dependent material behaviour. These theories have been mostly concerned with defining mathematical relationships between the properties of strain gradients and the resulting mechanical behaviour in an attempt to develop continuum theories that are valid on these scales [74].
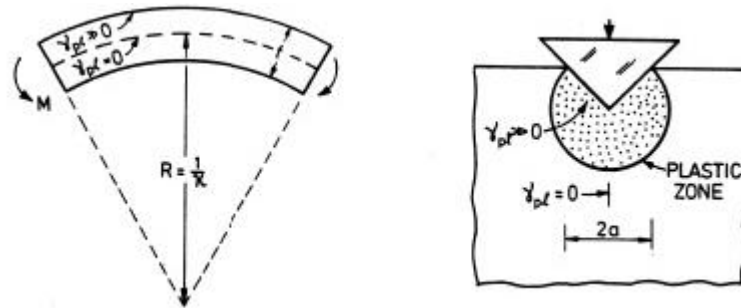


Figure 2.2 - Illustration of large strain gradients observed during bending and indentation. Reproduced from Fleck *et al.* [70].

The consensus between these publications is that on the micro- and nano-scales, conventional plasticity theories do not suffice as they lack an intrinsic length scale and therefore cannot predict the size effects described above. An increase in the stiffness of beams when loaded radially or in torsion is observed when beam radii are reduced. This phenomenon is, however, not observed when beams are loaded axially as strain gradients are not created in this mode of loading. Indentation is also well described with GNDs being created at the indentation location as material originally occupying the deformed region has to be pushed into the substrate material and stored as geometrically necessary dislocations. These defects are more predominant when the characteristic length of deformation is reduced sufficiently to create a large strain gradient.

While the concepts of strain gradient plasticity and geometrically necessary dislocations have been successful in providing a physical explanation for size effects observed during plastic deformation in metals, size effects are also apparent in elastic deformation of polymers. In the case of polymers, such notions are not applicable and different explanations have been suggested in literature. Nikolov *et al.* consider

size-dependent elastic deformation in polymers and develop a micro-mechanical model for strain gradient elasticity for polymers based on Frank elasticity [54]. Frank elasticity assumes a material has a nematic (no positional order but tendency toward the same direction) molecular structure [75]. It is well established that deformation of nematic liquid crystals can be described by the Frank energy originating from molecular interaction forces and described by crystal rotational gradients during deformation [76].
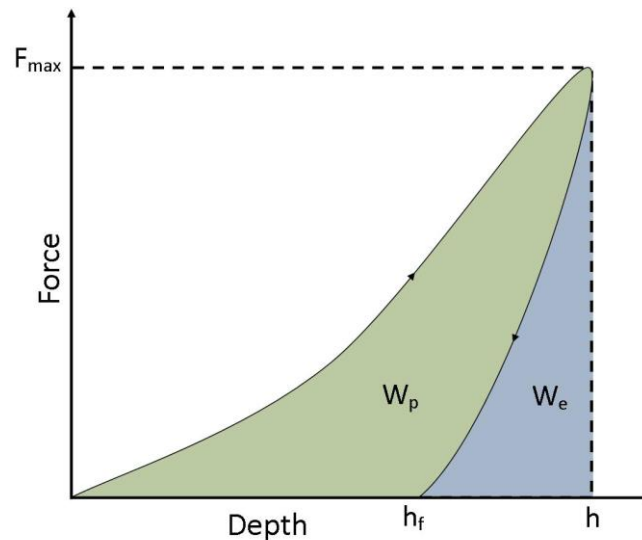


Figure 2.3 - Typical indentation force curve illustrating both a plastic and an elastic region.

Frank elasticity has also been demonstrated in polymers by a number of authors [77 - 79] and is attributed to the small, but non-negligible bending stiffness of the polymer chains and their interactions. Size dependence in polymers is therefore accounted for by Frank elasticity as rotational gradients vary depending on the strain applied [80]. Similar to strain gradient plasticity theory, an increase in rotation gradient is described with decreasing indentation depths and beam diameter during three-point bending. For indentation size effects in polymers, Han *et al.* take this further and develop a model that includes elastic size effects due to rotational gradients in elastic-plastic materials [80]. They highlight that in the absence of indentation size effects, the total work $W$ under an indentation loading curve shown

in *Figure 2.3* is commonly divided into the elastic work component $W_e$ and plastic work component $W_p$ as shown in equation 2.1.

$$W = W_e + W_p \qquad [2.1]$$

They then go on to stipulate that Frank elasticity is usually applied to liquid crystals where $W_e$ and $W_p$ are usually neglected [80]. The same cannot be done in solids and highlight that Frank energy is independent of the classical notation of elastic and plastic deformation. They therefore suggest adding Frank energy $W_f$ to the total work $W$ as shown in equation 2.2.

$$W = W_e + W_p + W_f \qquad [2.2]$$

Since an additional term is added to the work $W$, the area below the load-displacement curve in *Figure 2.3* will increase yielding higher indentation forces for the same indentation depth.

Based on this suggestion, a depth-dependent hardness model was deduced as shown in equation 2.3.

$$H = H_0 \left(1 + \frac{c_l}{h}\right)^{\gamma} \qquad [2.3]$$

Where: H : Depth dependent hardness

$H_0$ : Macroscopic hardness

$c_l$ : Length scale parameter

$h$ : Indentation depth

$\gamma$ : Fitting parameter that should be in the interval $\gamma \in [0,2]$

When $\gamma = 1$, the hardness model is shown in equation 2.4

$$H = H_0 \left(1 + \frac{c_l}{h}\right) \qquad [2.4]$$

A further discussion of the size dependency in polymers is provided by Han *et al.* who, after experimental investigation, conclude that these are strongly dependent on

the bending rigidity of the molecular chains of the polymers [81]. The authors highlight that polymers such as ultra-high molecular weight polyethylene (UHMWPE) and polytetrafluoroethylene (PTFE) have a homogeneous and highly flexible molecular structure and do not contain any rigid components. As Frank elasticity assumes the existence of such components, it does not apply in these polymers. They then demonstrate that when UHMWPE and PTFE were indented on a range of 20 nm to several micrometres, no indentation size effects were observed. Tjernlund *et al.* also observe a relationship with polymer molecular weight while Lam *et al.* demonstrate a relationship with crosslink density [82, 83]. These observations are predicted by Frank elasticity and therefore corroborate the link between Frank elasticity and size effects in polymers.

Various groups attempt to provide different rationales for size effects in polymers. Lim *et al.* hypothesise that friction and adhesion between an indenter and the polymer during nano-indentation cause size effects but this does not explain size effects observed in beam bending [84]. A further hypothesis states that variations in material properties at different thickness caused the indentation size effects [85, 86]. Lam *et al.* test micro-beams in tension and no variation in tensile stiffness was observed disproving a variation in mechanical properties at different thickness [87]. Zhang *et al.* attribute size effects to changes in surface roughness, but the lack of indentation size effects on UHMWPE and PTFE could not be explained by this hypothesis [88, 89]. Indentations were also carried out on silicone samples with very low surface roughness and, contrary to their hypothesis, size effects were observed at indentation depths shallower than 100 μm.

Size effects have been widely reported and described in the literature both in metals and in polymers. These effects are observed on the sub-micrometre range and could have a considerable influence at the cellular scale.

## 2.3. Cell - Scaffold Interactions

The primary intention of artificial scaffolds is to mimic the complex functions of the extracellular matrix. This does not only include the structural support required for cells to attach and proliferate but must also take into consideration the bulk mechanical properties required by the tissue to carry out its function. As cells are in direct continuous contact with the extracellular matrix (ECM), the latter also provides bioactive signals to the residing cells to mediate their functions. These signals consist of chemical (with the ECM acting as a reservoir for growth factors), as well as topographical and mechanical cues. Understanding the interactions between cells and scaffolds is therefore crucial as these have been shown to possess considerable impact on the survival of the cells and ultimately, the effectiveness of the engineered tissue [90].

### 2.3.1. Cell adhesion

The overall cell structure involves a cytoplasm which is surrounded by a lipid bilayer known as the plasma membrane [91]. A number of organelles, each having a different responsibility, are found within the cytoplasm with the largest intracellular organelle being the nucleus which contains genomic DNA and governs cell activities. Apart from maintaining cell shape, the plasma membrane is responsible for monitoring external signals through receptors that communicate with other proteins within the cell. Throughout the cytoplasm is the cytoskeleton which is a three-dimensional protein network and provides a number of functions [92]. Amongst others it acts as a structural scaffold to give the cell its shape, it provides a transport system between the various organelles within the cell, mediates cell division and permits cell motility. The constituents of the cytoskeleton are usually divided into three elements: actin microfilaments, tubulin microtubules and other intermediate filaments made up of various other proteins. Intermediate filaments vary depending on cell type and generally support the nucleus and nuclear membrane. They maintain cell shape, provide structural support and promote barrier formation. Unlike intermediate filaments, both microfilaments and microtubules serve as an intra cellular transport system and play an important role in mitosis. Microtubules

extend throughout the cell and provide passage to proteins and organelles. They are also responsible for building cilia and flagella in certain cell types. Actin microfilaments are responsible for organising the plasma membrane by an actin rich layer just below the membrane. They also play a role in muscle fibre contraction and link certain cell types together in adherence junctions. Actin microfilaments also form structures critical for cell motility: lamellipodia and filopodia. Lamellipodia are at the leading edge of the cell and are formed by a mesh like network of actin filaments in the cytoplasm. Filopodia are interspersed on the edge of these lamellipodia and are rod-like structures which are thought to act as sensors as the cell migrates [93]. These filopodia are usually composed of between 20 and 30 filaments of actin producing a diameter of about 200 nm and can protrude to between 1 μm and 5 μm as illustrated in *Figure 2.4* [94]. Focal adhesions form on both lamellipodia and filopodia and are required for cell migration. This is not an aimless process and it is clear that cell migration is directed by both chemical and mechanical cues.

The cell plasma membrane contains integrins that are essential in cell-scaffold and cell-cell adhesions. Integrins adopt a shape that resembles a globular head and two legs on the outside of the cell but subunits traverse the plasma membrane and terminate in the cytoplasm [95]. These are then responsible for large signalling complexes within the cell that allow it to respond to the extracellular environment [96, 97]. Integrins have been shown to interact with cellular proteins such as talin and vinculin which in-turn, connect to the actin microfilament network as illustrated in *Figure 2.4* [98, 99].

When materials are implanted, they are immediately coated with proteins present in blood and interstitial fluid. Cells will therefore only sense the implanted materials through this absorbed protein layer. Amongst this array of proteins are proteins capable of mediating cell attachment and spreading including: fibronectin, laminin, concanavalin A, chondronectin and vitronectin [100]. Cell integrins bind to certain specific motifs present on these proteins such as the arginyl-glycyl-aspartic (RGD) tripeptide motif via their globular heads as illustrated in *Figure 2.4*. As part of the cellular response, this binding also triggers changes in the integrin conformation,

affinity and clustering causing an increase in integrin recruitment. This leads to the formation of anchoring complexes on the filopodia and lamellipodia and forms larger focal adhesion plaques with increased intracellular activity [101]. The strength of the adhesions in-turn contribute to the larger processes such as cell pulling which is an integral part of cell migration and survival. Cell adhesion is a complex process involving several adhesion molecules and loss of cell anchorage is usually followed by anoikis (adhesion-mediated apoptosis) [102].
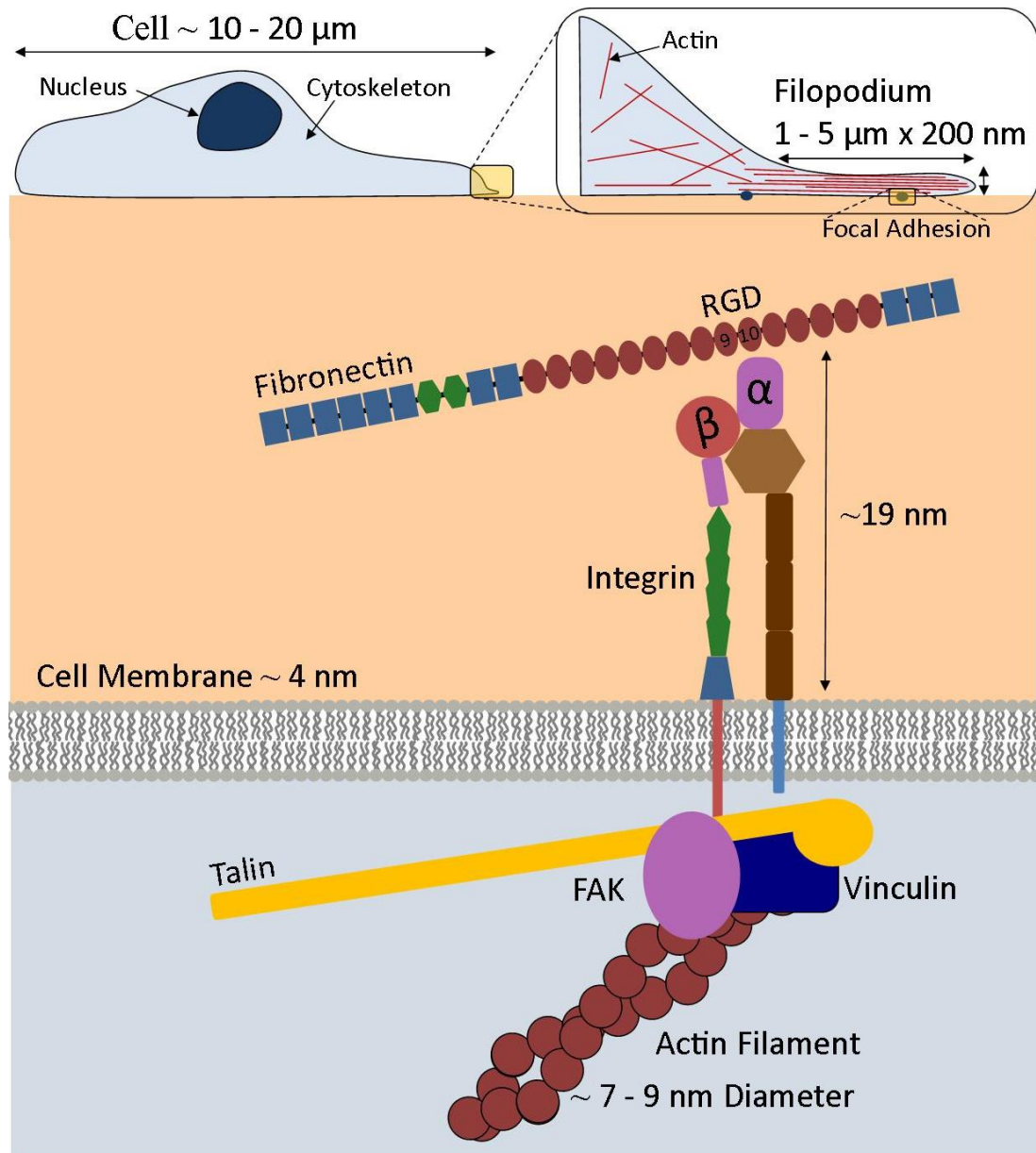


Figure 2.4 - A simplified illustration of size scales (cell down to cell - substrate interactions). Image not to scale.

Cell-scaffold interactions are primarily governed by binding of these integrin receptors on cells to RGD motif sequences present on surface proteins such as collagen, fibronectin and fibrinogen on the scaffold [103 – 105]. These interactions, in turn produce cell type-specific responses that influence adhesion, motility, differentiation and ultimately apoptosis. Arnold *et al.* use gold nano-dots, each having a diameter of less than 8 nm, coated with a cyclic RGDfk peptide [106]. Since integrins are about 19 nm in length, this meant that only one integrin could bind to each nano-dot. These dots were then positioned on PEG substrates at different spacing intervals. The authors demonstrate that spacing higher than 73 nm between each nano-dot reduced the formation of focal adhesion complexes and actin fibres. This phenomenon was attributed to the restriction of integrin clustering which is necessary for the formation and maintenance of focal adhesion complexes and consequently, cell attachment and migration. Apart from surface proteins, chemical signals, also known as chemotaxis, have been shown to steer embryonic differentiation and development [107]. These signals continue to play a crucial role in tissue development, wound healing, axonal guidance and other instances involving cellular migration and differentiation [108]. Our understanding of chemotaxis in tissue engineering is continuously growing with a number of bioactive factors known to induce cell type-specific responses together with a number of molecules whose functions are less understood.

The physicochemical characteristics of the biomaterials used in the fabrication of artificial scaffold such as the surface roughness [109], surface charge [110], crystallinity [111] and hydrophobicity [112] have also been shown to influence cell behaviour. These characteristics occasionally influence cell-scaffold interactions directly or, indirectly affect them by varying the affinity of proteins to the scaffold [113 – 114].

## 2.3.2. Topographical cues

Even though cells are typically tens of micro-metres in diameter, sub-cellular features used in cell adhesion and motility such as filopodia and focal adhesion sites are usually on the nano-scale. Cells therefore make contact with both nano- and micro- scale extracellular topographical features, including pits, protrusions and grooves when *in-vivo* [115]. When investigating the topographical features of endothelial vascular basement membranes, Liliensiek *et al.* describe a complex meshwork consisting of pores and fibres in the sub-micrometre and nanometre scale which varied depending on the location and the physical property of the vessel [116]. These and numerous other topographical features in the ECM may be implicated in the regulation of cell behaviour [117 – 120].

Numerous studies using fabricated topographical features have been carried out to obtain a better understanding of how these influence cell behaviour and in an attempt to control cell behaviour. Selhuber-Unke *et al*. demonstrated that cellular adhesion was reinforced if the distance between integrin molecules was less than 70 nm [121]. It was therefore inferred that nano-feature spacing should not exceed 70 nm if focal adhesions were to be maintained. When nano-protrusions are investigated, a number of authors report an increase in cell adhesion when protrusion height was below 70 nm [122 – 125] When protrusion height is increased further, a decreased focal adhesion formation was observed. Dalby *et al*. demonstrate that on polystyrene surfaces with protrusions of 95 nm, immortalised human fibroblasts initially produced a larger number of filopodia [126]. After 1 week in culture, cells grown on a flat, control surface were confluent while fibroblasts on protrusions were still isolated and were stellate in appearance.

Cellular response to nano-pits has also been investigated by culturing cells on substrates with pits of differing diameter and spacing. Biggs *et al.* demonstrate that nano-pits with highly ordered symmetry reduced cell adhesion while introducing a deliberate disordering increased cellular adhesion size [127]. Park *et al.* used hollow, vertically oriented, titanium dioxide nanotubes with diameters between 15 nm and

100 nm [128]. They demonstrated that nanotubes with diameters larger than 70 nm did not support focal adhesion formation leading to anoikis while reducing fibre diameters enhanced cellular activity as illustrated in *Figure 2.5*.
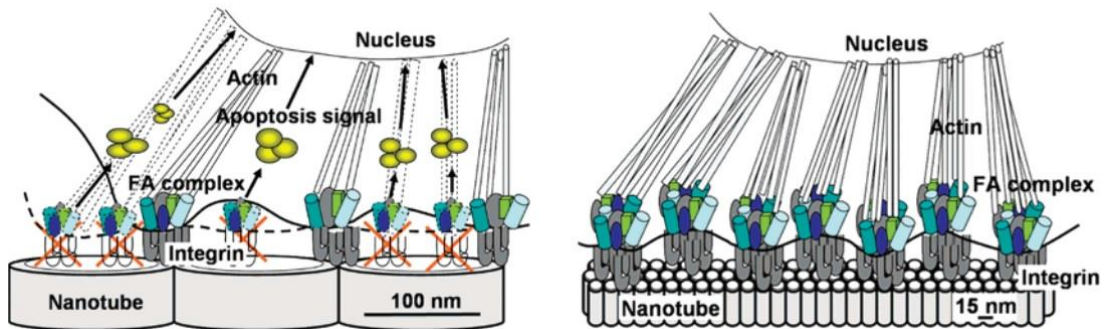


Figure 2.5 - Model showing different spacing of focal adhesion complexes on nanotubes with different diameters. Reproduced from Park *et al.* [128].

The effect of nano-scale grooves has also been demonstrated in a number of publications. Unlike nano- protrusions or pits, nano-grooves have been shown to cause cellular alignment through contact guidance [129]. This is caused by simultaneously providing ledges which disrupt integral binding and planar areas which allow integral binding and hence focal adhesions. Such groves are also present in extracellular matrices and enhance tissue organisation. Alignment to grooved substrates has been observed in a number of cell types including fibroblasts, osteoblasts, nerve cells and MSCs. Apart from promoting cell alignment, Chou *et al.* [130] demonstrate that such surface topography doubled the secretion of fibronectin in human fibroblasts while Dalby *et al.* [131] demonstrate an over-expression in a multifunctional signal adaptor protein (RACK 1) which positively regulates cell adhesions. Crouch *et al.* investigate the behaviour of human dermal fibroblasts on grooved surfaces with regards to aspect ratio between groove depth and width [132]. They conclude that even aspects ratios as shallow as 0.05 were sufficient to induce 80 % cell alignment while an aspect ratio of 0.16 was sufficient to produce 95 % alignment.

When materials are processed for use as a cell scaffold, topographical features can be left over from the fabrication process. When roughness is varied on the nano-scale, the effective surface area available for protein attachment can be drastically altered [133, 134]. Due to the inherent difficulties of characterising scaffolds on these scales, nano-scale topographical features and physiochemical properties are sometimes omitted and research is focused on their micro- to milli- scale equivalents. Even though these micro- and nano- scale topographies have been shown to influence cell functions, these features are sometimes left uncharacterised to the detriment of scaffold efficacy.

### 2.3.3. Mechanical cues

Apart from blood cells, most cell types are anchorage-dependent and cannot survive in a fluid suspension even if soluble proteins and other growth hormones are added to the solution to engage cell adhesion molecules [135, 136]. The distinct difference between fluids and solids is that solids have the ability to resist sustained forces applied upon them [137]. Even though this is a rudimentary observation, it emphasises the importance of substrate mechanical properties in tissues.

Numerous reports in the literature have demonstrated that cells apply traction forces on the scale of a few tens of nano-newtons [138 – 140]. Tan *et al.* described a technique in which cells were cultured on arrays of elastomeric, microneedle-like posts with controllable geometry and therefore compliance [139]. Cells were shown to attach and spread across the posts and the deflection of posts was measured using standard microscopy techniques. This deflection was then interpreted as traction force applied by the cells and varied depending on the size of the focal adhesions. Yang *et al.* describe another technique to measure cell traction fields using a thin polyacrylamide gel embedded with fluorescent beads [140]. The bead displacement was computed between "null-force" and "force-loaded" images from which cell traction forces were calculated based on the theory of elasticity. Curtis *et al.* described another method for measuring cell forces in which cells were grown on a photoelastic substrate [138]. Forces applied by cells caused changes in birefringence, which were measured and recorded by a polarizing microscope. All the techniques

mentioned above require prior knowledge of the mechanical properties of the substrates as cell traction forces were calculated indirectly by measuring substrate displacements.

As cells have been shown to apply forces on the underlying substrate, deformations that are inversely proportional to the substrate stiffness will also occur, as shown by Wen *et al.* in *Figure 2.6* [141]. The degree of substrate deformation on application of force (compliance) has been shown to influence cellular activity. Cellular mechanotransduction, the mechanism by which cells convert mechanical signals into biochemical responses was also investigated by Wang *et al.* They applied mechanical stress directly to various cell membrane receptors using a magnetic twisting device [142]. When magnetic beads were coated with a synthetic peptide containing the RGD sequence to bind directly to integrin receptors on cells, a stiffening response was observed. In contrast, when magnetic beads were coated with non-specific cell attachment ligands, the cell membrane stiffening observed was much lower. They then go on to conclude that integrin β1 might act as a mechanoreceptor and transfers mechanical signals to the cytoskeleton through a specific molecular pathway. Hughes *et al.* take this further and use magnetic particles to apply highly localised forces to distinct regions of the TREK-1 ion channel structure [143]. Amongst sensitivity to a diverse range of stimuli, TREK-1 channels have been shown to be mechanosensitive channels and have been implicated in mechanotransduction pathways in a number of tissues. The authors conclude that direct force application to the extracellular loop region of the TREK-1 channel structure resulted in changes to the whole-cell current and thus implicating this region in mechano-gating. They hypothesise that this region may regulate sensitivity to mechanical forces by acting as a "tension spring" which sets the level of mechano-sensitivity of the channel.

In an attempt to obtain a better understanding of the cellular pathways involved in cell-substrate sensing, researchers have also used a combination of inhibition and knockout cell lines. Jiang *et al.* demonstrate that knocking out elements of integrin adhesion such as talin1 and integrin β1 did not affect spreading of fibroblast cell lines [144]. Focal adhesion kinase (FAK) is a protein activated by both growth

factors and integrins during migration and functions as a receptor and regulator in cell motility [145]. It is involved in downstream signalling and can promote changes in actin and microtubule structures. When Jiang *et al.* cultured FAK knockout fibroblasts, they observed that cells had a significantly smaller spread area [144]. Such complex force-sensing mechanisms within the cell have been shown to influence a number of cellular responses including spread area [146], migration speed [147], focal adhesion formation [148], proliferation [147], apoptosis [149] and cell modulus [150]. Ingber also highlights that mediators of mechanotransduction involve a number of cellular components, molecules and extracellular structures [151]. These include the proteins present on the extracellular matrix, cell – substrate adhesion complexes involving integrins focal adhesions, cytoskeleton filaments and nuclear structures.
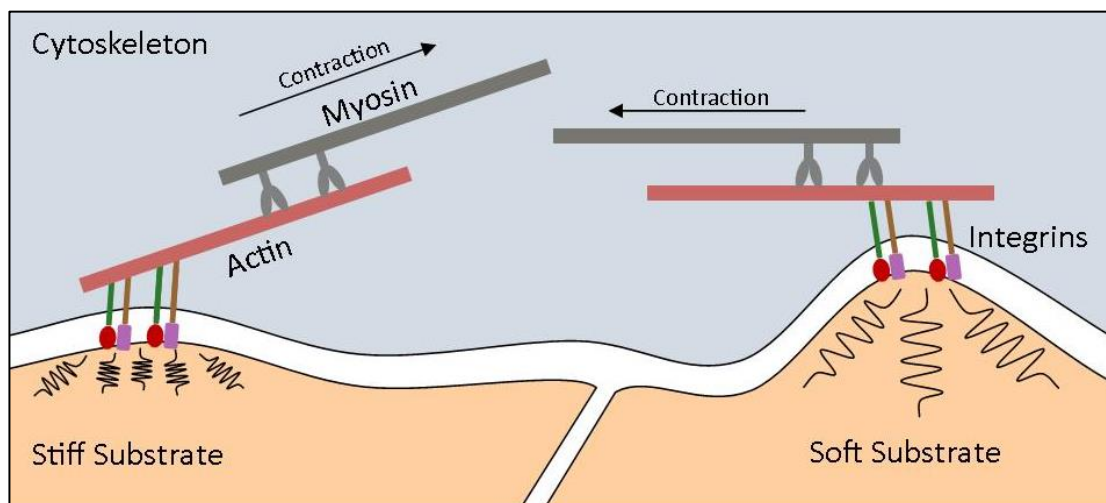


Figure 2.6 - Schematic of a cell deforming a stiff and soft substrate by pulling through actin - myosin contractions. Based on Wen *et al.* [141].

Lo *et al.* demonstrate that extracellular matrix mechanical properties have a clear influence on cell proliferation by demonstrating 3T3 fibroblasts migrating preferentially towards stiffer substrates and term the mechanism of rigidity-guided cell movement as "duro-taxis" [152]. In another study by Engler *et al.*, the effects of matrix elasticity on stem cell lineage are investigated [153]. Amongst other conclusions, they show how cell lineage is clearly dependent on matrix stiffness with stem cells differentiating into neuronal cells on soft scaffolds and into osteoblasts when the scaffold stiffness is increased as illustrated in *Figure 2.7*.
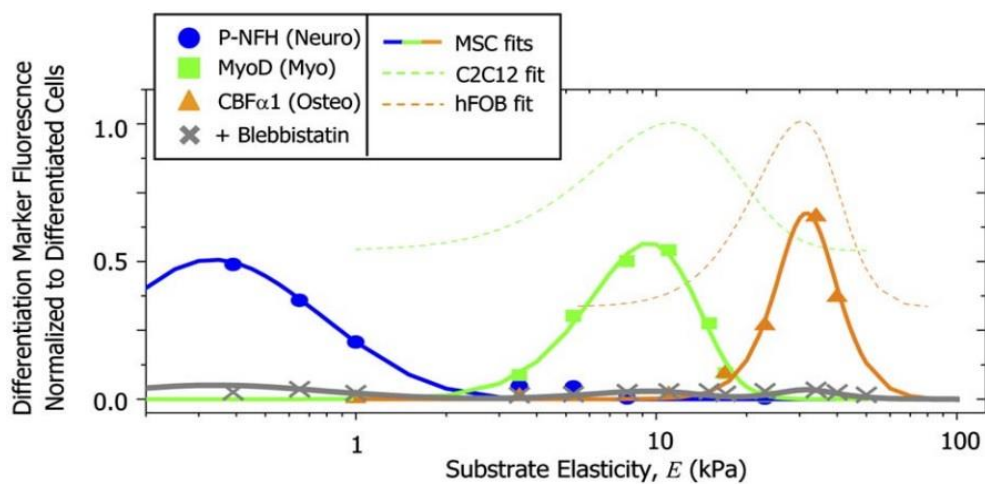


Figure 2.7 - Differentiation marker expression on various substrate elasticities indicating a maximal lineage specification at the elasticity of the respective tissue type. Reproduced from Engler *et al.*[153].

A number of authors have also investigated cell migration speed with changes in the substrate modulus. Bangasser *et al*. argue that cell speed may be biphasic with respect to substrate stiffness as a number of publications have shown an increase in speed with substrate stiffness while others have shown the converse [154]. ECM stiffness has not only been shown to modulate proliferation and survival but in a study by Ulrich *et al.*, it was shown that rigid ECMs increase the spread of tumour cells in tissues [135]. When the scaffold stiffness was lowered to mimic that of healthy matrices, the viability of tumour cells appeared to be significantly reduced. In a further study, Paszek *et al.* state that tissue stiffness can be used to predict the presence of a cancerous growth [155]. They demonstrate that a slight increase in

ECM rigidity changes tissue architecture promoting the growth of cancerous cells [155]. These findings therefore emphasise the need for closer analysis of mechanical properties in artificial scaffolds to mimic the mechanical properties of the cell's native extracellular matrices.

In a study by Trappmann *et al.,* the influence that various extracellular matrix properties have on stem-cell fate is discussed [156]. They note that by simply varying bulk mechanical properties of polydimethylsiloxane (PDMS) substrates, the spreading of cells on collagen or fibronectin was not altered. On the other hand, similar to observations made in previous publications, when cells were cultured on polyacrylamide (PAAm) hydrogels with varying stiffness, their shape was highly dependent on substrate stiffness [153, 157]. Keratinocytes were observed to adhere but not spread on gels with moduli of around 1 kPa. When cells were cultured on stiffer gels, they adopted spindle-shape morphology and were able to spread more as the modulus was further increased. However, time-lapse imaging demonstrated that these cells sent out protrusions indicating dynamic interaction even on the softest gels investigated. Trappmann *et al.* observe that the change in bulk mechanical properties in these gels is brought around by a decrease in pore size within the structure. They later conclude that changes observed in cell behaviour are caused by a change in the density of anchorage points available for collagen as shown in the *Figure 2.8* [156].

When traction forces originating in the cell cytoskeleton were applied onto attached collagen, feedback consisted of movement of the collagen segment coupled with the movement of PAAm gel segments. The authors continued to alter the anchorage points and thus reduced the effective length of the collagen resulting in an effect that mimics the stiffening of the substrate. They concluded that the interfaces between cells and ECM are different on different substrates and must be taken into account for optimal cell control. Wen *et al.* take this further and investigate similar hydrogels with varying porosity and stiffness [141]. They conclude that stem cell differentiation was regulated by substrate stiffness and was independent of protein tethering and substrate porosity. It is however noted that authors in both these

publications had to go to great lengths to confirm this observation as altering substrate stiffness was indirectly achieved by altering the hydrogel porosity (and therefore topography).
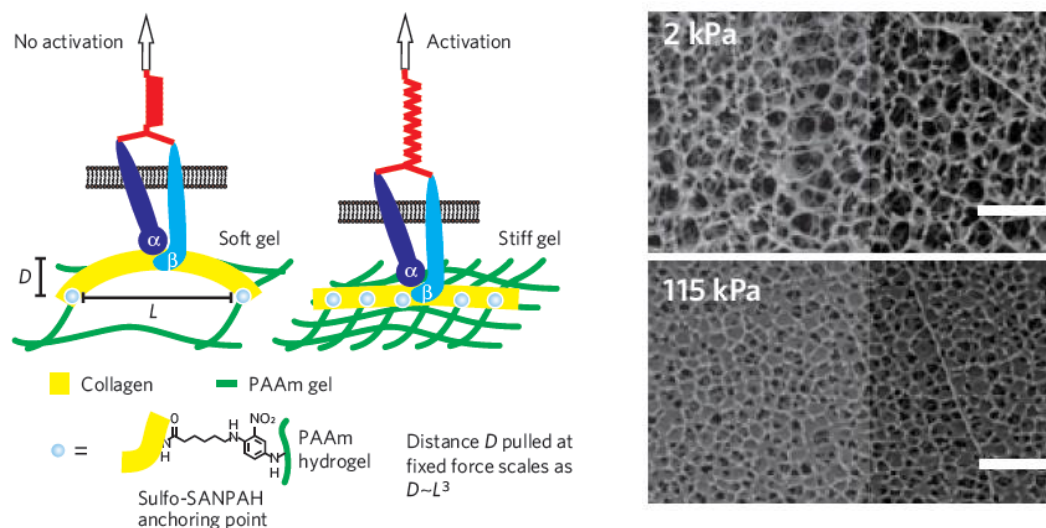


Figure 2.8 - Schematic diagram showing anchorage of collagen fibres on PAAm gel and a cell attached to the collagen fibre. The stiff gel allows for less movement and triggers activation of cell receptors (left). Differences in porosity observed in gels of different substrate stiffness (left). Reproduced from Trappmann *et al.* [156]

## 2.3.4. Cells cultured on electrospun scaffolds

Electrospinning is widely used in the manufacture of cellular scaffolds and can produce scaffolds comprising of fibres with a wide range of fibre diameters (from less than 100 nm up to a few microns) and with varying degrees of alignment. Cell function, proliferation and orientation can therefore be altered as discussed in *Section 2.3.2* by varying topographical cues such as fibre diameter and alignment.

Chen *et al.* investigate the role of fibre diameter in electrospun polycaprolactone (PCL) scaoffolds on the adhesion and proliferation of 3T3 fibroblasts [158]. The lowest cell attachment was observed on the smallest electrospun fibres with a fibre

diameter of 117 nm. These scaffolds were however the only scaffolds to contain a large number of bead defects on the fibres and the authors conclude that beaded scaffolds considerably reduced growth kinetics. When fibroblasts were cultured on a range of scaffolds with fibre diameters ranging from 428 nm to 1,051 nm, cell attachment and proliferation was higher on scaffolds with smaller diameters. In a further scaffold having an average fibre diameter of 1,647 nm, a bimodal fibre distribution was reported. Cell proliferation was observed to increase when compared to scaffolds with smaller fibre diameters. The converse was also observed by Sisson *et al.* when osteoblastic MG63 cells were cultured on electrospun gelatin [53]. The authors demonstrated that cell viability was initially (3 days) similar on electrospun substrates of 110 nm ± 40 nm and 600 nm ± 110 nm. At later time points (day 5 and day 7), cell proliferation appeared to increase on scaffolds with larger fibre diameters. Noriega *et al.* suggested that there exists an interrelationship between scaffold fibre diameter and gene expression activation [159]. They demonstrated that when chondrocytes were cultured on electrospun chitosan matrices with a mean fibre diameter of 300 nm, a higher ratio of collagen-II/collagen-I was noted when compared to cells cultured on scaffolds with a mean fibre diameter of 1,000 nm. This ratio is often considered to be a marker for chondrocytes phenotype and their observations suggested that cells preserved a more differentiated phenotype on scaffolds with a lower mean fibre diameter [160]. Li *et al.* demonstrated that chondrocyte proliferation was supported on both micro- and nano- fibres with a higher rate seen in cultures on nano-fibrous scaffolds [161]. This observation was made despite the fact that chondrocytes had a rounded morphology on nano-fibrous scaffolds compared to an organised actin cytoskeleton and well-spread morphology when cultured on micro-fibrous scaffolds. Chondrocytes cultured on nano-fibrous scaffolds also demonstrated a higher expression of collagen type II and IX, aggrecan and cartilage proteoglycan link protein when compared to cells cultured on micro-fibrous scaffolds indicating a strong influence of fibre diameter on cellular gene expression.

Apart from fibre diameter, a number of researchers have also investigated the influence of fibre alignment on cell behaviour. Whited *et al.* cultured endothelial

cells on electrospun scaffolds with varying degrees of alignment [162]. They demonstrate that cell alignment increased as the degree of fibre alignment was increased leading to a fully aligned endothelium on scaffolds with highest fibre alignment. The authors also demonstrated that actin was oriented parallel to the direction of electrospun fibre alignment mimicking actin organisation of native endothelial cells. Wang *et al.* investigated neurite outgrowth and Schwann cell migration while varying both fibre diameter and degree of fibre alignment [163]. They demonstrate that aligned electrospun fibres directed neurite outgrowth to varying degrees depending on both fibre alignment and diameter. Neurite extensions and Schwann cell migration was not promoted extensively on aligned scaffolds with fibre diameters of 293 nm ± 65 nm. The converse was observed on scaffolds with larger fibre diameters (1325 nm ± 383 nm) with long, directed neurite extension and Schwann cell migration being observed. The authors conclude that fibre diameter is an important parameter when constructing aligned fibres for neurite outgrowth.

Multiple authors have demonstrated that both fibre diameter and alignment are associated with a change in cellular behaviour. The response is also cell type dependent and cannot be translated between scaffolds of different materials as these would display different topographical and chemical characteristics.

## 2.4. Objectives

A clear relationship between fibre diameter and cell behaviour has been reported in a number of publications as reported in *Section 2.3.4*. This change in fibre diameter has been associated with a change in contact area and other topographical cues. Size effects, discussed in *Section 2.2.3,* have been shown to act on the micro – nano scale and would therefore alter the effective modulus of the substrate on the cellular scale. It was hypothesised that this could in turn influence cell behaviour through mechanosensitive mechanisms described in *Section 2.3.3.* A review of the literature reveals no clear reporting of this relationship. The aim of this work, therefore, was to apply advanced material analyses techniques to investigate the influence of nano-mechanical properties in cell-scaffold interactions. To this end, scaffolds that demonstrated similar chemical properties and surface morphology while presenting different nano-mechanical properties were manufactured. Scaffolds were characterised on the cellular scale to ensure that the nano-mechanical properties were the sole variable influencing cell behaviour.

Polyurethane was used for the manufacture of these scaffolds as intrinsic mechanical properties could be altered while maintaining the same chemical intermediates. Scaffolds were fabricated using solvent-casting and electrospinning from a range of polyurethane grades with different intrinsic mechanical properties. The first aim, therefore, was to analyse the mechanical properties of these scaffolds on the macro – nano scale using bulk tensile testing, a dedicated nano-indentation system and AFM indentation. Small changes in topographical features have been shown in *Section 2.3.2* to alter cell behaviour. The aim of the following section was therefore to investigate whether changes in the fabrication parameters affected the resulting scaffold topography, nano mechanical properties or chemical domain structure.

Nano-mechanical properties of electrospun fibres are shown to vary depending on fibre diameter and on mode of loading. In order to fabricate scaffolds for the investigation of the influence of nano-mechanical properties on cell behaviour, the following section aimed to produce electrospun mats with diverse nano-mechanical properties. Initially, defect free electrospun mats were manufactured with different

fibre diameter distributions and hence nano-mechanical properties. This was followed by the fabrication of electrospun mats from two different grades of polyurethane with fibre diameters on the same range. Such scaffolds had similar topography and chemistry but different mechanical properties. The final objective of this section was to use dual spinning and fabricate an electrospun scaffold with bi-modal nano-mechanical properties. Such scaffolds could be used in the investigation of the influence of nano-mechanical properties on cell behaviour.

Similar to metals, polymeric biomaterials are susceptible to chemical reactions that could lead to unintended degradation of the mechanical or topographical characteristics of the original material. Such changes have been shown to varying degrees in highly oxidative environments on a range of polyurethanes by Meijs *et al.* [164]. Changes to surface roughness on the nano-scale have also been reported to alter cell behaviour by various authors. In an investigation of the influence of nano-mechanical properties on cell behaviour, it has to be ensured that nano-mechanical cues are the only variables effecting cell behaviour. The objective of the following section was therefore to investigate whether exposure to a physiological environment could alter the surface properties of polyurethanes on the nano-scale. Specimens were stored in a physiological solution and an oxidative solution mimicking inflammation for an extended period of time. Topographical changes were monitored by means of AFM over the period of immersion to investigate whether physiological environments were sufficient to alter the surface topography.

Cell adhesion is heavily influenced by the surface properties of the substrate and loss of cell anchorage is usually followed by anoikis [102, 165]. The final objective was to perform an initial assessment of cell attachment on the range of polyurethanes being used. The activity of three distinct cell types on both solvent-cast and electrospun forms was investigated. This study could therefore confirm the possibility of culturing cells on the various forms of polyurethanes for use in an investigation into the influence of nano-mechanical properties on cell behaviour.

# Chapter 3

# Materials and Methods

## 3.1. Overview

This *Chapter* outlines experimental theory and describes the exact methodologies used in this study.

## 3.2. Materials

### 3.2.1. Polyurethane chemistry

Polyurethanes were chosen as the materials to be investigated for their wide range of macro-mechanical properties while maintaining similar chemistry [40]. Polyurethane substrates could also be manufactured using both thermal and chemical process while a double melting point could provide an insight into the resulting domain structure [166]. Polyurethanes fall in two major categories: thermosetting polyurethanes do not melt when heated, whereas thermoplastic polyurethanes are hard when cooled but soft and malleable when heated.

Thermoplastic polyurethanes are block copolymers composed of two distinct segments shown in *Figure 3.1*. The hard segment (HS) is composed of di-isocyanate and a chain extender which is usually a low molecular weight diol or diamine [167]. Di-isocyanates are organic compounds that contain two isocyanate functional groups with each having the formula R-N=C=O. These di-isocyanates can be either aromatic or aliphatic which considerably affects the properties of the final polymer. Aliphatic di-isocyanates have a greater resistance to degradation than aromatic di-isocyanates but this usually results in lower mechanical properties [168]. The soft segment (SS) is usually a polyol, which is an alcohol containing multiple hydroxyl functional

groups. These can therefore be polyester, polyether, polycarbonate, polyolefin or hydrocarbons.
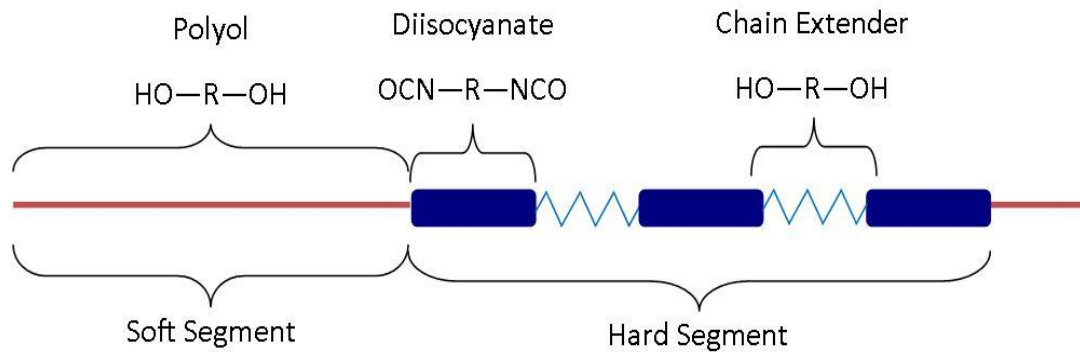


Figure 3.1 - Schematic diagram of polyurethane showing both soft and hard segments as well as their constituents.

The hard segments and soft segments are immiscible and tend to aggregate into soft segment-rich domains and hard segment-rich domains. HS domains are rigid and act as "virtual crosslinkers" to the relatively softer SS domains as shown in *Figure 3.2* [167]. Modifying the ratio of HS to SS while keeping the same chemical intermediates, causes a substantial change in mechanical properties of the resulting polymer. The same intermediates with 15 - 40 wt/wt% HS creates a rubbery elastomer while a hard load bearing polymer can be formulated with a HS content of over 65 wt/wt%. This suggests that materials with considerably different mechanical properties but similar chemical biocompatibility can be manufactured since the same intermediates are used when formulating the polymers [40].
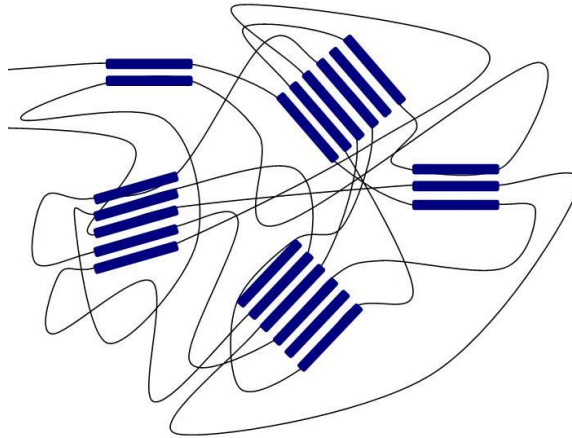
Figure 3.2 - Solidified thermoplastic polyurethane showing separation of hard and soft segments into different phases.

The chemistry of the soft-segment also determines the stability of the resulting polyurethane. When degradable polyethers such as poly(ethylene oxide) (PEO) or poly(lactic acid) (PLA) are used in place of the soft segments, the overall structure of polyurethane degrades rapidly. Rates of degradation can be determined by changing the molecular weight of the soft segment or by altering the chemistry completely [169]. The use of degradable polyurethanes and degradable polymers in general is on the rise since these can degrade *in vivo* and give way for cells to rebuild their own extracellular matrix and thus eventually restoring function without the involvement of an artificial polymer. The main disadvantage of degradable polyurethanes is that even though the majority of soft segments materials used are known to be biocompatible, degradation of such polymers also releases the components of both the di-isocyanate and the chain extenders. The biocompatibility of the materials used in these components is not completely understood and research is still being conducted to determine which of these are safe for use *in vivo* [170]. This has not halted a number of biomedical products from being manufactured from degradable polyurethane in numerous applications including cardiovascular [171 – 175], musculoskeletal [173, 176 – 178] and nerve regeneration [179, 180].

*Table 3.1* demonstrates some of the chemical intermediates used in the manufacture of thermoplastic polyurethane. With this wide range of possible combinations, specific polyurethane makeups have to be investigated individually in order to ensure that the characteristics are representative of the polymer in question.

| Component | Type | | Chemical compound | |
|---|---|---|---|---|
| Soft Segment | Polyol | | Poly(ethylene oxide) (PEO) | [181] |
| | | | poly(ether ester) | [182] |
| | | | Poly(propylene oxide) (PPO) | [183] |
| | | | Poly(tetramethylene oxide) (PTMO) | [184] |
| | | | Poly(caprolactone) (PCL) | [185] |
| | | | Poly(lactic acid) (PLA) | [186] |
| | | | Poly(epsilon-caprolactone) | [187] |
| | | | Poly(ethylene adipate) (PEA) | [188] |
| | | | Diamer acid (DA) | [189] |
| | | | Poly(carbonate) (PCU) | [190] |
| | | | Polyisobutylene (PIB) | [191] |
| | | | Hydroxyl Terminated Polybutadiene (HTPBD) | [192] |
| | | | Poly(dimethylsiloxane) (PDMS) | [193] |
| Hard Segment | Di-isocyanate | Aromatic | Methylene diphenyl diisocyanate (MDI) | [194] |
| | | | 2,4-toluene diisocyanate (TDI) | [194] |
| | | Aliphatic | 4,4′-methylene bis(cyclohexyl isocyanate) (HMDI) | [192] |
| | | | 1,6- hexamethylene diisocyanate (HDI) | [195] |
| | | | 1,4-butane diisocyanate (BDI) | [190] |
| | | | Isophorone diisocyanate (IPDI) | [187] |
| | | | L-lysine ethyl ester diisocyanate (LDI) | [196] |
| | Chain Extender | Diols | DL-lactic acid and Ethylene glycol (EG) | [197] |
| | | | 1,2-ethanediol (EG) | [198] |
| | | | 1,4-butanediol (BD) | [199] |
| | | | 2-amino-1-butanol (2AB) | [185] |
| | | | 1,6-hexanediol (HD) | [198] |
| | | | Diurea diol | [200] |
| | | Others | Aliphatic diamines | [201] |
| | | | Aromatic diamines | [201] |
| | | | Amino acids | [202] |

Table 3.1 - Table showing the wide variety of monomers commonly used in the manufacture of thermoplastic polyurethane adapted from Juan *et al.* [203].

## 3.2.2. Polyurethanes used in this work

A series of medical-grade thermoplastic polyether-urethane – $b_9{}^{TM}$ series (*Biomer Technology Ltd., Runcorn, UK*) was provided for use in this project. The polymers being investigated were a class of chemically-inert, medical-grade poly(ether) urethanes. The manufacturer states that these polymers are biocompatible, show low temperature flexibility, a wide dynamic range of hardness and can be processed in a variety of manufacturing methods.

More specifically, the polyurethane range provided was made up of 6 grades of an aromatic medical-grade poly(ether) urethanes termed Z1A1, Z3A1 (Mn - 143,566 Mw - 272,857), Z4A1, Z6A1, Z9A1 and Z9A1 (Mn - 100KD Mw - 197KD), composed of 4,40 -diphenylmethane diisocyanate, 1,4 butane diol and polyether diol. The intermediates used in the formulation of each polymer grade were all the same. The differences between each grade arise from a change in the hard segment length. Polymers with lower grade numbers had shorter HS chain lengths and thus create a difference in the ratio of HS to SS within the polymer. This was established as the molecular weight was lower in polymers with higher grade numbers. This change in the ratio of soft to hard segments within the polymers caused a substantial shift of mechanical properties while maintaining a similar chemistry. Z9A1 was therefore the hardest material while Z1A1 was the softest material in the range.

## 3.2.3. Solvents

The solvents used in these experiments were as follows: dimethylformamide (DMF) (>= 99.8 %), dimethylacetamide (DMAC) (99.8 %), tetrahydrofuran (THF) (>= 99.9 %) all supplied by Sigma-Aldrich, Poole, UK. These solvents were used since they are the solvents that are most commonly reported for electrospinning of polyurethane [204 - 208].

### 3.2.4. Preparation of polymer dispersions

Melt-processed polymer beads provided by *Biomer Technology Ltd.* were weighed and dried in a vacuum oven at 70 $^o$C for 2 hours in a clean 100 ml glass bottle. Solvent was then measured and added to the beads in an exhaust fume cabinet, sealed and agitated over rollers for up to 3 days at room temperature. Solution concentrations were always calculated as a percentage of weight of polymer per weight of solvent.

## 3.3. Solvent-Cast Films

### 3.3.1. Process overview

Polymers can be processed using a wide variety of techniques that exploit their chemical, thermal or mechanical behaviours [209]. Solvent-casting is a standard technique that exploits chemical properties of polymers to produce thin, homogenous films.

The main prerequisite for the production of solvent-cast films is identifying a volatile solvent or solvent system that can dissolve the polymer. Once this has been established, polymer is mixed at a set ratio to the solvent system in a non-reactive, sealed container and allowed to dissolve over a set period of time. The resulting solution is then transferred into a non-reactive open container and the solvent removed by evaporation using an elevated temperature and vacuum. This technique therefore creates two distinct surfaces, the air interface and the glass interface as shown in *Figure 3.3*. These two surfaces have previously been shown to exhibit different topographical and chemical properties and in turn influence cell adhesion and proliferation [210]. The solvent-casting process is similar to electrospinning, in which an initial solution of polymer and solvent is drawn out into a long fibre and the solvent evolved by a process of evaporation.
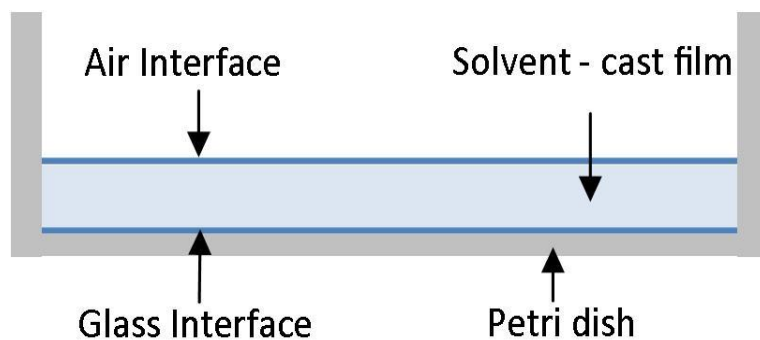
Figure 3.3 - Schematic diagram of solvent-cast film production highlighting the two different surfaces.

## 3.3.2. Vacuum oven

A vacuum oven (*Cole Parmer, StableTemp, London, UK)* was used in the manufacture of solvent-cast films. The oven could reach a temperature of 280 $^o$C and was connected to a vacuum pump that could produce a vacuum of -100 KPa. Fumes produced during the manufacture of solvent-cast films were safely sealed within the oven chamber for the duration of the solvent-casting process. Once this was completed, the air inside the chamber could be pumped out through an exhaust fume cabinet and circulated with clean air.

## 3.3.3. Preparation of solvent-cast films

Glass petri dishes with 10 cm diameter were washed in distilled water followed by a solution of sodium dodecyl sulphate (SDS) (*Sigma-Aldrich - UK*) in distilled water, rinsed in ethanol and then wiped dry using a lint-free cloth. At least 15 ml of polymer solutions was then transferred into the glass petri dishes in an exhaust fume cabinet to produce films of at least 0.2 mm. Petri dishes were then moved into a vacuum oven at 65 $^o$C, -80 kPa for a further 2 days in order to ensure that the solvent was completely evolved as vapour from the sample.

To ensure that solvents dispersed in the vacuum oven were completely removed, clean air was pumped through a 50 μm filter into the chamber and out through an exhaust fume cabinet. Clean air was then allowed to circulate for at least 2 hours

before opening the oven door to remove the samples. Thereafter, they were removed from the petri dish and rinsed in distilled water. The solvent-cast films were then rinsed in distilled water and cleaned using an ultrasonic cleaner in distilled water for 15 minutes. Samples were then dried using clean compressed air and stored for subsequent characterisation.

## 3.4. Electrospinning

Electrospinning is a highly versatile technique used in the manufacture of fibrous scaffolds for tissue engineering. As outlined in *Section 2.2.3*, size effects are predominant on the nano-scale and strain gradient theory suggests that a reduction in fibre diameter causes an increase in the fibre modulus. Fibrous scaffolds were therefore investigated as these manifest strain gradient plasticity which could have an impact on cell mechanotransduction.

### 3.4.1. Electrospinning principles

One of the most attractive attributes of electrospinning is that it can be set up using only a few pieces of standard equipment. A syringe is used as a reservoir of the polymer solution while a high potential DC generator supplies a potential difference between the polymer solution and a surface used to collect the resulting fibres as shown in *Figure 3.4*. Some standard additions to this setup include a separate motor that rotates the collector and a syringe actuated by a linear motor to maintain a fixed polymer feed rate [211].

The fibrous mat created on the collector is generally composed of a continuous nano-fibre arranged in a random manner brought around by the high electrical instability in the electrospun fibre [212]. A substantial number of variables that determine the quality of fibres produced can immediately be seen, making the process highly unpredictable.
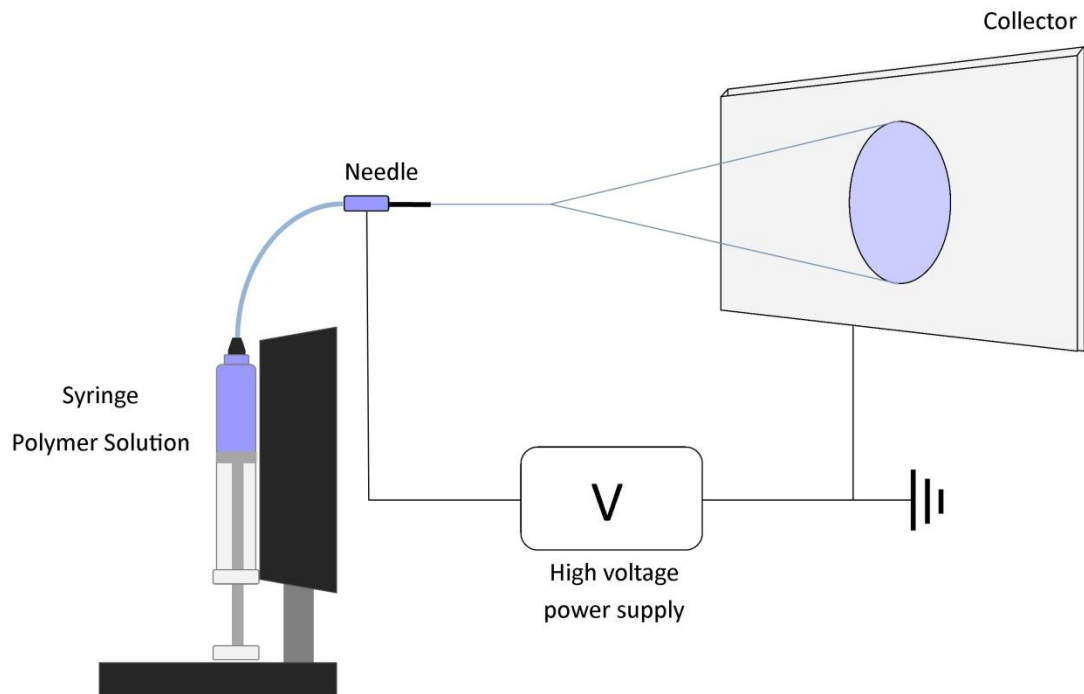
Figure 3.4 - Illustration of a basic electrospinning setup

## 3.4.2. Process description

Electrospinning is initiated by a solution droplet being slowly pumped out of a needle at a set feed rate. An electric field that is high enough to counteract the surface tension of the solution is applied causing the droplet to elongate and assume a cone-like shape. From this "Taylor cone", a narrow jet of liquid is ejected in the direction of the electric field potential [213]. The surface area of the jet is then increased to accommodate the large build-up in charge by producing a thin, long fibre travelling towards the collector [211, 214]. This jet can then split into two or more fibres as the radial forces from the charge applied become large enough to overcome cohesive forces. Due to their similar charge, these resulting smaller jets repel each other contributing to lateral velocities and chaotic trajectories. Fibres are also accelerated towards the collector causing them to become thinner and speed up solvent evaporation [215]. Electrostatic interactions between the externally applied electric field and the surface charges on the jet cause it to bend rapidly to increase the surface area, producing a whipping instability region [50, 216, 217].

### 3.4.3. Process variables

The morphological properties of the final fibrous mats produced by electrospinning are highly dependent on a number of variables [218]. Solution-dependent variables are governed by the solvent system used and the concentration of polymer in the solution. These two variables influence solution conductivity, viscosity and volatility of the solvent system used. Process-dependent variables include the solution feed rate, electric field applied, distance of tip from collector and the rotational speed of the collector amongst others. Environmental factors are another set of variables that affect the resulting structure. An increased environmental temperature leads to faster evaporation of the solvent while a change in atmospheric humidity will make the resulting fibres thicker or thinner, depending on the chemical nature of the polymer [219]. Because of this large number of variables, it is very challenging to create a predictive model that would factor in all these variables and foretell the final properties of the fibrous mat produced [212, 220].

The general trends resulting from altering certain parameters on the final product are discussed in the following section. Since no quantitative data is available to help predict these results, electrospinning is sometimes considered as much an art as it is a science [50].

### 3.4.3.1. Polymer concentration

Polymer concentration is typically the dominant factor in electrospinning due to its direct relationship with solution viscosity. This factor not only determines fibre diameter but also the stability of the Taylor cone which in turn determines whether any fibres are produced from the solution. Polymer concentration is considered as the most important factor affecting fibre diameter, where an increased concentration generally increases diameter. It is important to note that this relationship is not linear and that a threshold value of viscosity has to be exceeded for electrospinning to be possible [50, 221].

### 3.4.3.2. Solvent system

Since solvent usually encompasses around 80 % of the solution, the solvent system used also has a substantial impact on the resulting solution viscosity, conductivity, surface tension and rate of solidification due to the solvent's volatility. Changing the solvent therefore impacts multiple factors that would in turn affect the product's fibre diameter [212, 222]. Changing the solvent system usually means that other parameters, such as the applied potential and polymer concentration, would have to be changed in order to facilitate electrospinning. This therefore means that it is very difficult to extrapolate the direct effect the solvent would have on the final electrospun mesh by formulating experiments where the only variable is the solvent used [50]. A blend of solvents is sometimes also used in order to take advantage of certain aspects of each solvent.

Solvent volatility is a very important parameter since solid nanofibres are only formed when the solvent has completely evaporated from solution. The boiling point of the solvent together with the tip-to-collector distance determines whether the solvent is completely evaporated when the fibre reaches the collector. If the solvent does not evaporate before reaching the collector, wet fibres may fuse and form a reticular mat as shown in *Figure 3.5*. On the other hand, if the solvent is too volatile, the fibres produced usually appear to be wrinkled and instability of the Taylor cone could cause needle blockages [50].

### 3.4.3.3. Collector

The collector geometry does not only affect the general shape of the final fibrous mat but can also help control fibre diameter and fibre alignment [223]. Stationary metal plates are the simplest collectors and are also very commonly used. Apart from being inexpensive and easier to operate, this method is also used when a completely random and unaligned mesh is required. When a tubular rotating drum is used, the angular velocity and direction of rotation are another two variables that can be modified. The direction of rotation together with the height of the needle relative to the drum can change the resulting morphology of the fibres while rotating the drum at an angular velocity above a certain threshold results in aligned fibres. A rotating collector would also increase the rate of evaporation of the solvent and thus changing the morphology of the fibres [211]. Aligned fibres can also be produced by altering the shape of the collector. When electrospinning is carried out on two parallel plates, charged to the same voltage, fibres have been shown to align perpendicularly between the two plates [224]. As the electrospun fibres approach the plates, fibres form across the gap due to electrostatic interactions [225].

The collector material is another variable that influences the resulting fibre mesh with the electrical conductivity of material used being the most important property. If the material used is not sufficiently conductive, the process could be interrupted with nanofibres being redirected onto a more conductive surface [212].

### 3.4.3.4. Applied voltage

The high potential difference between the polymer solution and the collector is the driving force in electrospinning. The applied voltage has to be high enough to overcome the surface tension of the solution to form a Taylor cone and initiate the electrospinning process. In general, increasing the electric field accelerates the fibres further and leads to smaller diameters as well as encouraging faster solvent evaporation, yielding drier fibres [226 – 228]. The polarity between the polymer solution and the collector has also been shown to influence the resulting electrospun mat. A number of publications have shown the effect of changing electrospinning

polarity on the resulting fibre morphology [229, 230]. These differences have been shown to vary depending on the polymer and solvent system used. Ali *et al.* have shown substantial changes in fibre diameter, deposition area as well as critical voltage when electrospinning polyacrylonitrile (PAN) [229]. They demonstrate that a positively charged needle and a grounded collector produced fibres with smaller diameters, had a lower critical voltage and an increased deposition area. Kilic *et al.* demonstrate that when the needle had a higher voltage when compared to the collector, thinner and more homogenously distributed fibres were produced when electrospinning PVA [230]. Tong *et al.* take this further and investigate whether changing the polarity used for electrospinning altered cell behaviour on the resulting scaffolds [231]. They highlight that the different electrospinning polarities result in either a negatively or a positively charged scaffold and that such charges have been shown to influence cell behaviour [110, 223]. Tong *et al.* demonstrate that when the electrospinning source is negatively charged with respect to the collector, the response of MC3T3-E1 cells was enhanced in terms of proliferation, alkaline phosphate activity and mineralization [231].

### 3.4.3.5. Polymer feed rate

For a stable nano-fibre to be produced, the rate at which solution is made available for electrospinning should match the rate of removal of solution from the tip. This means that for a given feed rate, a corresponding voltage needs to be applied. Increasing the feed rate increases the fibre diameter to a certain extent, after which wet fibres are formed if the feed rate is too high for a given voltage. When the polymer feed rate is too low, an unstable Taylor cone is formed that results in a variation in fibre diameters within the same electrospun mat [46, 227].

### 3.4.3.6. Tip to collector distance

The distance between the needle tip and the collector defines both the strength of the electric field on the tip as well as the distance available for the solvent to evaporate before it reaches the collector [233]. Increasing this distance generally reduces the resulting fibre diameter, as literature indicates that fibres are continuously being stretched until they reach the collector [46]. If the gap is too wide, the electric

potential might not be sufficient to produce a Taylor cone, therefore halting electrospinning completely. The converse usually leads to wet fibres being deposited onto the collector producing a network of fused nanofibres [46, 221].

Since these parameters are all interlinked, modifying one parameter does not always result in a linear response in fibre production. These variables must therefore be considered collectively and not as separate entities making it difficult to produce a table that demonstrates what changing one variable does to the resulting fibrous mat.

### 3.4.4. Electrospinning setup

The potential difference in the electrospinning setup used was provided by two high voltage power supplies (*Brandenburg,* Alpha III, *Dudley, UK*) that were capable of producing up to 25,000 V each. One of the power supplies was connected to the collector which could either be held stable or rotated at a fixed speed up to 3000 RPM. Another high voltage power supply was connected to a needle which was in turn connected to an infusion pump (*Harvard Apparatus, PHD 2000, Kent, UK*) that could deliver polymer at a fixed rate from 0.0001 µl/hr to 220 ml/min as shown in *Figure 3.6*. This stationary infusion pump housed the syringe which acted as the polymer reservoir. The position of the needle could be controlled using a linear motor across the length of the collector to produce films of a specified length. The distance between the needle and the collector could be set manually and could not be altered during electrospinning.

Even though electrical current was highly limited, safety was still a key concern as the system utilised high voltages and toxic solvents during use. Protective measures included an insulating cage, an emergency stop button and various sensors that ensure the safety of the user as described in previous work by *Whitto*n [234]. The rig itself was designed to slide into an exhaust fume cupboard and could not be operated if the shutter of the fume cupboard was not completely closed.

The setup allowed two polymer solutions to be electrospun concurrently. This could be used in a number of applications. The production of a thick scaffold could be sped

up by electrospinning the same polymer solution via a manifold and multiple nozzles. The same polymer grade with different solution concentration could be used to produce scaffolds with two different fibre diameters. Two different grades of polymer could be electrospun at the same time creating a scaffold with a mix of nano-mechanical properties but one bulk mechanical property. A resorbable polymer could be electrospun along alongside a bio-stable polymer allowing for variation in scaffold porosity. Aligned fibres could also be produced using a parallel plate setup. This consisted of two parallel plates with a variable distance from each other, both connected to the same voltage. With all these systems in place, the electrospinning rig was very versatile while being safe to operate.



Figure 3.6 - Photograph of electrospinning rig:  1) Needle; 2) Collector; 3) Infusion pump; 4) Syringe; 5) Emergency stop button; 6) Security key; 7) Power supplies.

### 3.4.5. Preparation of electrospun mats

#### 3.4.5.1. Electrospinning of Z1A1

The polymer with the lowest bulk modulus, Z1A1, was electrospun using an iterative method to determine the range of electrospinning parameters that produced mats with least defects. In order to investigate the reproducibility of the electrospinning technique under similar conditions, five samples were produced consecutively using the same parameters. Z1A1 samples were successfully produced from solutions of 8 wt/wt % Z1A1 in DMF. All five samples were produced at a fixed potential difference of 15 kV and a tip to collector distance of 15 cm. The polymer feed rate was kept constant at 0.38 ml/hr. The collector used was an 8 mm stainless steel rod that was spun at 1000 RPM to manufacture a tubular scaffold that was later split across its length to produce a rectangular scaffold allowing for easy removal of the sample. Traverse movement was limited to 15 cm to reduce variations in the final scaffold. Samples were imaged and stored at 20 $^o$C +/- 5 $^o$C in aluminium foil.

In order to produce electrospun mats with different nano-mechanical properties, samples were produced from the same material (Z1A1) but with a different fibre diameter distribution. To accomplish this, a new set of parameters that produced homogenous electrospun mats with a low number of imperfections had to be established. A solution of 7 wt/wt % Z1A1 in DMF was used with a fixed voltage difference of 18 kV and a tip to collector distance of 15 cm. The polymer feed rate was kept constant at 0.5 ml/hr. A further set of samples was manufactured with smaller fibre diameter distributions from a 5 wt/wt% solution of Z1A1 in DMF with a fixed voltage difference of 18 kV and a tip to collector distance of 15 cm. The polymer feed rate was kept constant at 0.5 ml/hr.

Electrospinning of polyurethane was carried out with high potential on the polymer solution when compared to the collector. Publications reporting electrospinning of polyurethane all describe using this polarity [205 – 207, 235 – 239]. When attempted, electrospinning of defect free films with the opposite polarity was not

successful. An investigation into this observation was not pursued as it was beyond the scope of this study.

### 3.4.5.2. Electrospinning of Z6A1

Electrospun mats were then manufactured from Z6A1 in an attempt to manufacture scaffolds with different mechanical properties while maintaining a similar fibre diameter distribution. After an iterative process to determine parameters that produced a homogenous mat, a solution of 17 wt/wt % of Z6A1 in DMF was used in order to obtain a solution with similar viscosity to Z1A1 solutions. A fixed voltage of 20 kV was used at a tip to collector distance of 18 cm and the polymer feed rate was kept constant at 0.5 ml/hr.

### 3.4.5.3. Electrospinning of PCL

To manufacture electrospun mats from a resorbable material, polycaprolactone *(PCL, $M_n$ 80,000, Sigma-Aldrich)* was used. After an iterative process, defect free mats were manufactured from a 10 wt/wt % solution in DMF:chloroform 1:9. A distance of 15 cm, a voltage of 20 kV and a constant polymer feed rate of 0.5 ml/hr was used.

### 3.4.5.4. Summary

In summary, seven different sets of parameters were used to electrospin samples for the purposes of these experiments as shown in *Table 3.2*.

|  | Polymer | Solvent | Concentration ( wt/wt % ) | Potential difference ( kV ) | Distance ( cm ) | Flow Rate ( ml/hr ) |
|---|---|---|---|---|---|---|
| a) | Z1A1 | DMF | 12 | 20 | 15 | 0.4 |
| b) | Z1A1 | DMF | 8 | 15 | 15 | 0.38 |
| c) | Z1A1 | DMF | 7 | 18 | 15 | 0.5 |
| d) | Z1A1 | DMF | 5 | 18 | 15 | 0.5 |
| e) | Z6A1 | DMF | 17 | 20 | 18 | 0.5 |
| f) | Z6A1 | DMF | 15 | 15 | 13 | 0.4 |
| g) | PCL | DMF: Chloroform | 10 | 20 | 15 | 0.5 |

Table 3.2 - Table showing different electrospinning parameters used to produce both Z1A1 and Z6A1 samples.

### 3.4.5.5. Dual spinning of Z1A1 and Z6A1

In order to demonstrate the possibility of having a single electrospun mat manufactured from the *Biomer b₉*™ polyether-urethane range with two different nano-mechanical properties, dual spinning was used. Since Z1A1 had a wider range of parameters which successfully produced electrospun fibres, electrospinning of both polymers simultaneously was performed by first electrospinning Z6A1 and finding a solution of Z1A1 that electrospun at the same parameters while producing fibres of similar size. After a number of iterations, it was concluded that it was not possible to achieve this goal without adding THF to the Z6A1 solution. THF considerably increased the ease at which electrospun fibres were produced from Z6A1 and a wider selection of fibre diameters was made available even when added in small quantities.

Polymer dispersions of both Z1A1 and Z6A1 were made following standard procedures described in *Section 3.3.3*. For Z1A1, a solution of 8 wt/wt% in DMF was prepared while a solution of 15 wt/wt% in 70:30 DMF:THF was prepared for Z6A1. Initially, both polymers were processed alone. Z1A1 spun successfully at 15 kV and 20 kV with tip to collector distances between 12 cm and 17 cm and a feed rate of around 0.5 ml/hr. Z6A1 spun at 12 kV – 20 kV, tip to collector distance between 12 cm and 15 cm and feed rates of around 0.3 ml/hour. Both solutions spun simultaneously with few imperfections at 22 kV, 14 cm tip to collector distance at a feed rate of 0.2 ml/hr. The two nozzles were moved in traverse to the collector producing areas with fibrous meshes consisting of the individual polymers and areas that overlapped and consisted of a mix of Z1A1 and Z6A1 nano-fibres as shown in *Figure 3.7*.
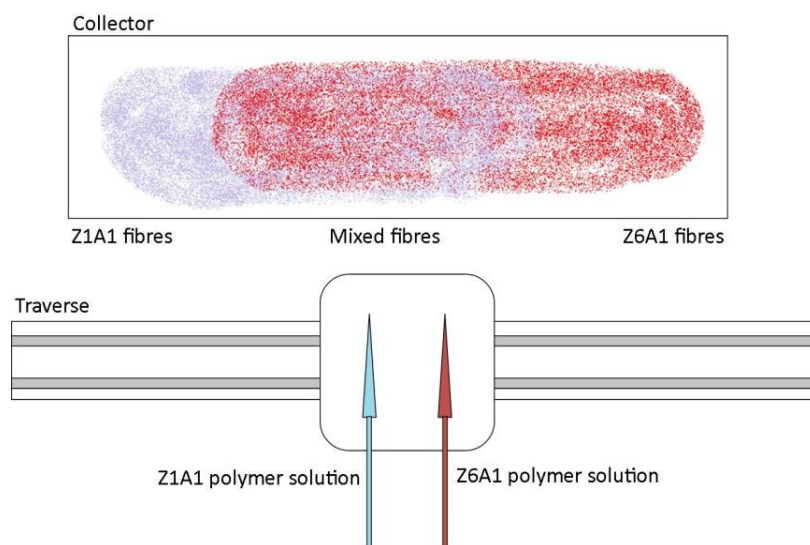


Figure 3.7 - Illustration of the dual spinning setup.

## 3.5. Topographical Characterisation

### 3.5.1. Topographical characterisation by scanning electron microscopy

In order to investigate topographical characteristics on the micro-scale, scanning electron microscopy (SEM) was used as this provided relatively quick and reliable characterisation on the scales of interest. The basic principles in SEM involve an electron gun that produces an electron beam which is accelerated down a column towards a specimen. When this focused beam reaches the specimen, amongst other interactions, secondary electrons are knocked loose from the surface of the sample. The electron beam is rastered across the surface and the intensity of these secondary electrons is detected. To ensure that the electron beam interacts with the sample rather than air, the process has to take place inside a partial vacuum. Samples must also be conductive but since the electron beam only interacts with the surface of the sample, a thin conductive layer can be deposited on the specimen by a process of sputter coating.

#### 3.5.1.1. Scanning electron microscope

A table-top scanning electron microscope (SEM, *Hitachi TM1000, Krefeld, Germany*) was used to obtain surface images on the micro-scale and is shown in *Figure 3.8*. Since electrospinning relies on a considerable number of variables, an iterative process was used to produce films with low defects and to a required fibre specification. The *Hitachi TM1000* was suited for this process as very little sample preparation was required and an image could be acquired within minutes, and thus facilitating the acquisition of correct electrospinning parameters. This SEM had a fixed accelerating voltage at 15 kV and allowed for magnifications from x100 up to x10,000. The sample chamber could accommodate samples of up to 70 mm in diameter while the movement range was set at 15 mm x 18 mm.

A sputter coater was used to deposit a thin film of gold on the sample. This prevents charge build-up on the sample as well as increasing the signal to noise ratio and thus resulting in a sharper image with higher contrast.



Figure 3.8 - Photograph of the scanning electron microscope - Hitachi TM-1000

### 3.5.1.2. Fibre diameter distribution calculation

Electrospun samples were gold-coated using the sputter coater to increase their conductivity. The equipment manual stipulated that the thickness of the coating can be calculated using *Equation 3.1*.

$$d \cong I \times V \times t \times k \qquad [3.1]$$

Where: d    is the thickness of the film in Angstroms

       I    is the reading in current in milliamps on the meter

       V    is the voltage used in kilovolts

       T    is the time of the discharge in minutes

       k    is a constant which is 5 for argon and 2 for nitrogen and air.

Samples from electrospun specimens were mounted onto an SEM sample holder using conductive tape. Samples were sputter coated in argon five times in bursts of 15 second each at 20 mA and 1.2 kV to avoid overheating and melting the fibres. Using this procedure a coating thickness of approximately 150 Angstroms was deposited onto each specimen.

Samples were then mounted into the *Hitatchi TM-1000* SEM for imaging. Representative images were obtained at various magnifications and in various locations across the sample. The standard procedure of measuring fibre diameter distribution within an image has traditionally involved manual selection and measurement from SEM micrographs by using line tools in image analysis software such as *ImageJ*. This technique was however slow and open to operator bias. Fibres with diameters smaller or larger than those expected might be avoided by the operator and thus creating a fibre diameter distribution that was not representative of the actual scaffold. To avoid this, images were loaded onto the image analysis software *ImageJ* and a fibre diameter distribution from each image was obtained using the extension *DiameterJ*. This tool was used as it was a validated nanofiber diameter characterisation tool that was able to locate fibres as well as analyse their diameters at every pixel along their length [240]. Images are first transformed into binary black or white images by thresholding and a selection of eight images with different thresholding parameters presented to the user. The user then selects the most appropriate threshold image and the centreline of each fibre was determined automatically as illustrated in *Figure 3.9*. The areas where fibres intersect are removed to avoid artificially increasing fibre diameter measurements. This was then followed by a calculation of the distance between the centrelines and the edges of each fibre. A table showing fibre radii (in pixels) and their occurrence was then automatically populated. This was then converted to fibre diameter (in μm) using the defined pixel size at the set magnification. When comparing to manual measurements, Hotaling *et al.* conclude that *DiameterJ* provides an efficient, unbiased and accurate way to calculate fibre diameters in electrospun mats [240].
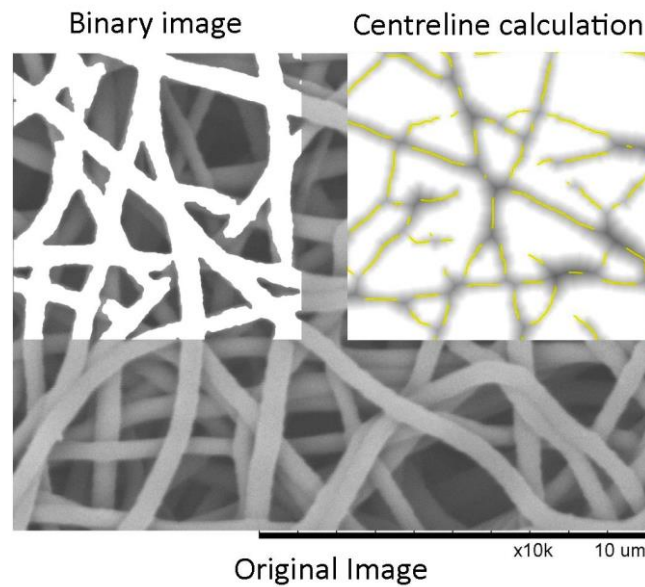
Figure 3.9 - Different steps involved in *DiameterJ* processing to obtain fibre diameter distribution. The original image is transformed into a binary image (black has been removed from this image for easier comparison). The centreline of each fibre is then calculated and areas of intersection removed to avoid artificially increasing fibre diameter measurements.

In order to obtain a representative fibre diameter distribution, samples were taken at five different locations across each specimen and at three SEM micrographs obtained at each location at x10,000. Fibre diameter distribution was then calculated using *DiameterJ* for each micrograph individually. Fibre diameter occurrence from all images per location was then pooled together to create an averaged fibre diameter distribution for each location as shown in *Figure 3.10*. To avoid presentation of data for each pixel length, fibre diameters were binned into 0.1 µm bins across the whole range of fibre diameter. As the number of points analysed was not limited, data was then normalised for ease of presentation.
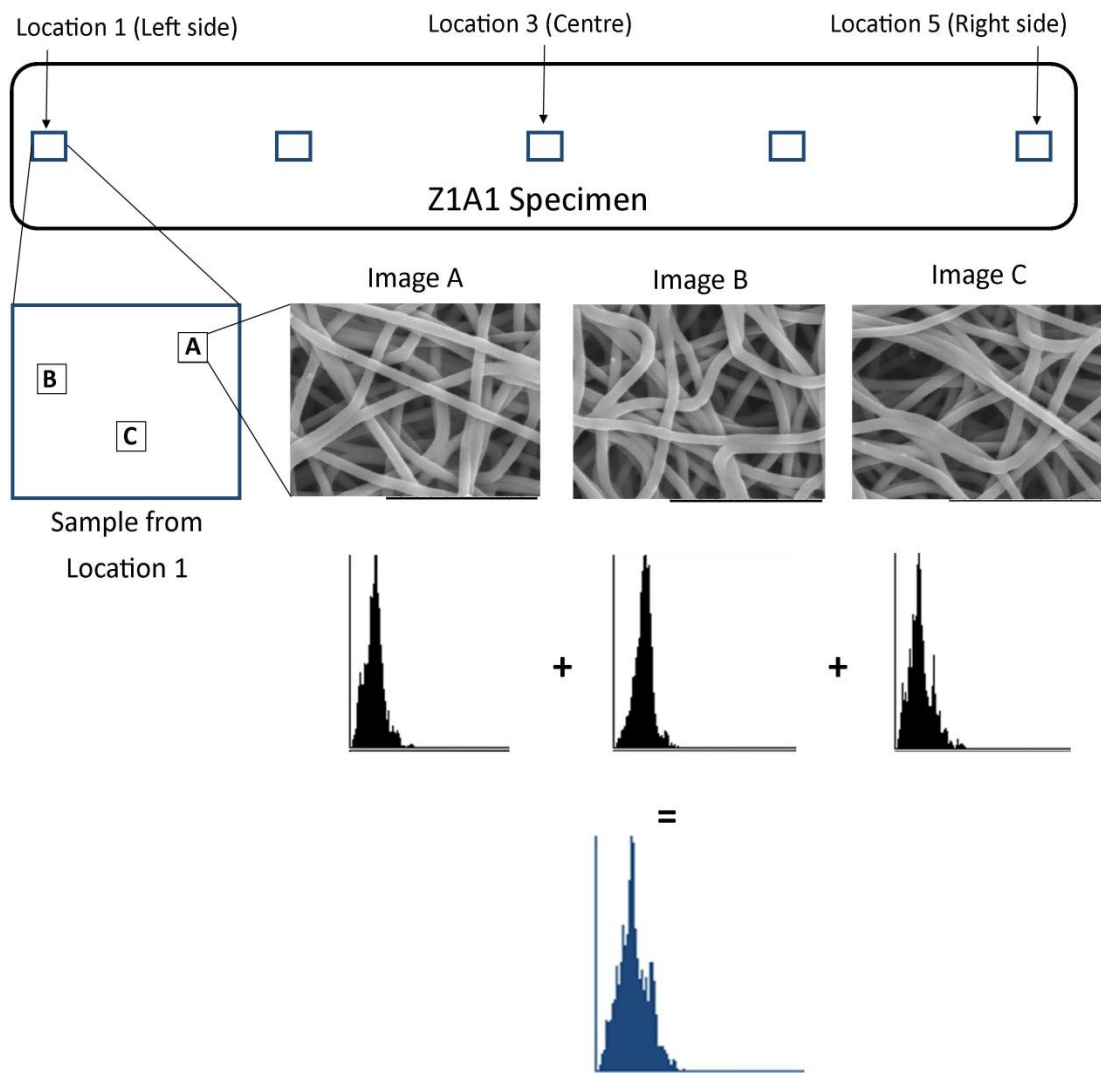
Figure 3.10 - Representation of how fibre diameter distribution was calculated for electrospun specimens. Five samples were taken from each specimen at different locations. Three SEM micrographs were obtained for each sample and their fibre diameter distribution. Data from each image was then pooled together to obtain a final fibre diameter distribution representative of the sample location.

The resulting mean fibre diameter was calculated using the standard mathematical calculation:

$$\bar{x} = \frac{\Sigma(f.x)}{\Sigma f} \qquad [3.2]$$

Where    $\bar{x}$ = mean

f = frequency

x = bin midpoint

Standard deviation $\sigma$ was then calculated using:

$$\sigma = \sqrt{\frac{\Sigma f.(x - \bar{x})^2}{\Sigma f}} \qquad [3.3]$$

Fibre diameter was always presented as mean ± standard deviation.

## 3.5.2. Topographical characterisation by AFM

### 3.5.2.1. Atomic force microscopy

The atomic force microscope (AFM) was developed in 1985 by *Binning, Quate* and *Gerber* and was made commercially available in 1989 [241]. An accurate, three-dimensional representation of the surface can be produced from a vast range of surfaces including metals, polymers, composites and biological samples. Images can also be obtained in air at standard temperature and pressure or while submerged in a liquid, unlike electron microscopes which require a partial vacuum [64, 242].

### 3.5.2.2. Working principles

Atomic force microscopes generate images from a sample surface by moving a probe over the surface in a raster manner. As the sample moves, the probe records the height change in the surface and an image of the surface is slowly built up [64, 243].
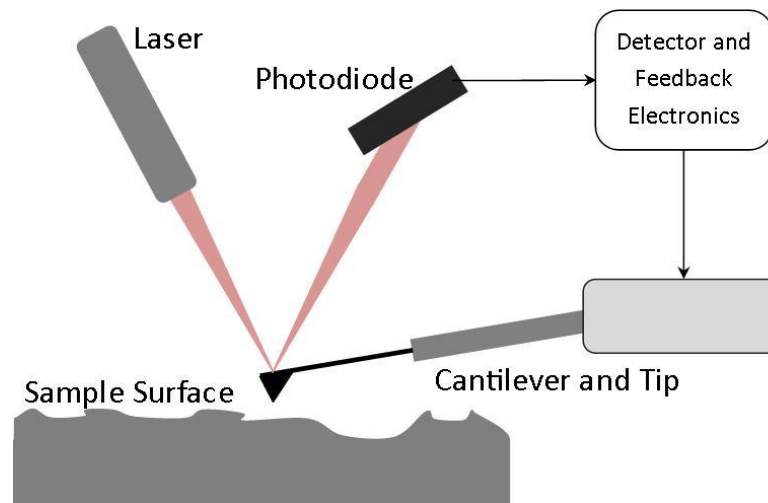
Figure 3.11 - Schematic diagram showing AFM basic operation principle.

Atomic force microscopes use a cantilever usually made out of silicon or silicon nitride with a tip of only a few nanometers in diameters at the far end of the cantilever. A laser is aimed onto the cantilever and a photodetector tracks any movement brought around by a change in height of the sample surface [244, 245]. The operator can adjust feedback controls that attempt to maintain a constant force between the cantilever and the surface by adjusting the height of the cantilever relative to the sample. This is done in order to minimise the deflection of the tip and to increase the accuracy of the final image. The data obtained from the photodetector is manipulated by computer software to build up a three-dimensional image of the surface [246].

### 3.5.2.3. Imaging methods

In an ideal environment, when the cantilever is relatively far away from the surface, no force is detected (*Figure 3.12* a). As the cantilever approaches the surfaces, *van der Walls* forces attract the cantilever towards the surface when the distance is on the scale of a few tens of angstroms (*Figure 3.12* b). If the cantilever is brought further towards the surface, repulsive forces take over and increase asymptotically as distance between the cantilever and surface is reduced (*Figure 3.12* c). AFM imaging can be carried out in both repulsive and attractive regimes and is usually separated into two major modes of operation: contact mode and tapping mode.
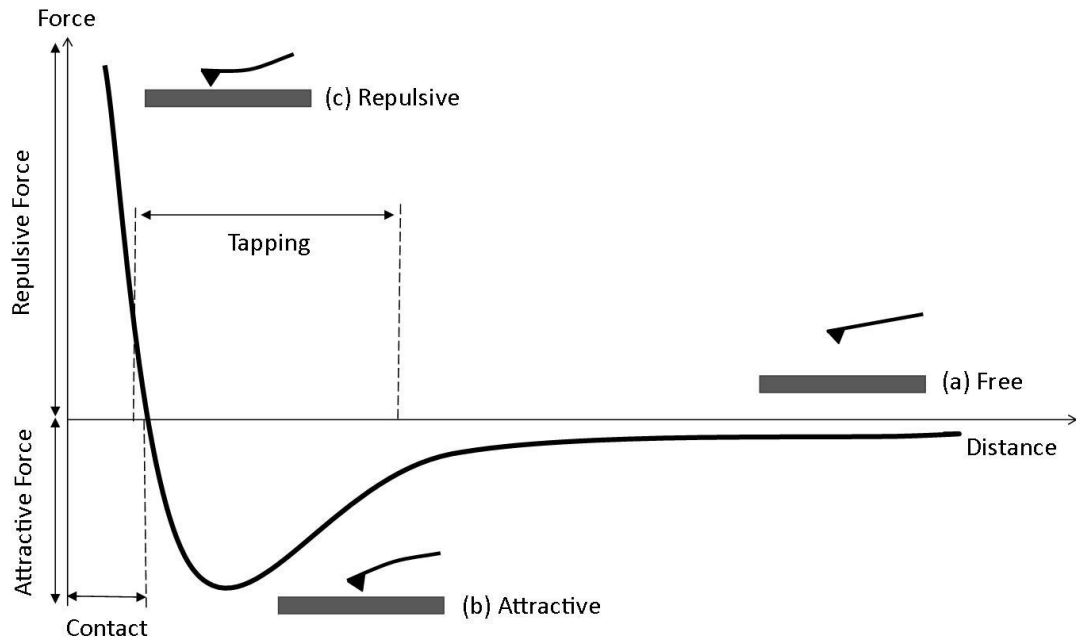
Figure 3.12 – Ideal representation of tip-sample force curve.

**Contact mode**

This mode is the primary mode of operation in AFM as it requires less control when compared to tapping mode. The tip is maintained in the repulsive region by moving the cantilever close to the surface. A feedback loop is used to maintain a constant force on the cantilever by adjusting the height of the sample while the sample is moved in a raster manner [247]. The spring constant of the cantilever has to be sufficiently lower than that of the surface to allow the cantilever to bend rather than the surface. In very soft samples, the nano-scale forces applied between the surface and the cantilever can sometimes be enough to alter the sample surface [243]. This mode is also useful in surface analysis of samples submerged in a liquid as constant "contact" is kept with the surface.

**Lateral force microscopy**

When operating in contact mode, deflections in vertical direction are translated into topographical information. The frictional coefficient of the surface causes deflections in the horizontal direction and these are used in lateral force microscopy (LFM) together with cantilever's lateral spring constant to map the frictional coefficient of the surface being investigated [248]. LFM is therefore useful for studying heterogeneous compounds on the same surfaces. Unlike contact imaging, LFM requires a four-quadrant photodetector since both the horizontal and vertical deflections have to be monitored simultaneously as illustrated in *Figure 3.13* [249]. This means that topographical images can be overlaid with frictional force data for better analysis since topographical features will inevitably also produce changes in the lateral signal.
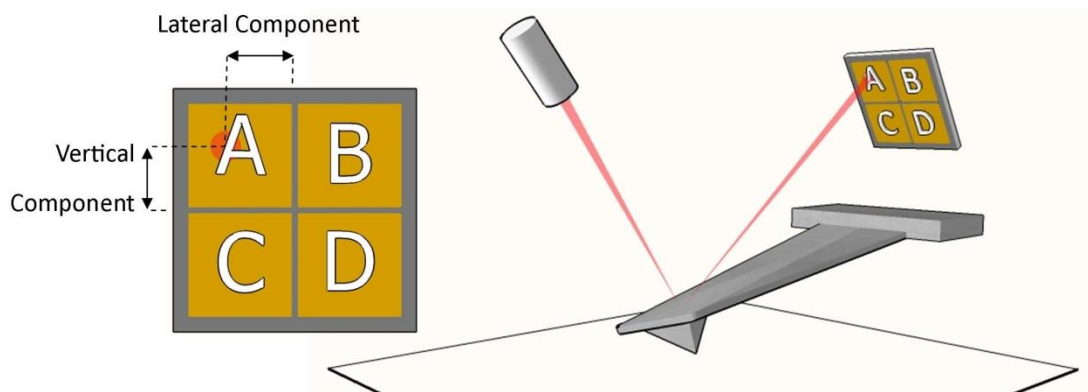


Figure 3.13 - Illustration of LFM and four quadrant photodetector

**Tapping mode**

In tapping mode, the cantilever is oscillated at its natural frequency using a further piezoelectric element. The cantilever is kept in intermittent contact with the surface and a feedback loop works to maintain constant oscillation amplitude, and hence force, between the surface and the sample. A system is also put in place that monitors changes in the amplitude due to the *van der Waals* forces that the surface has on the tip [243]. This method is therefore useful when imaging soft biological samples or samples that are loosely held on the substrate as lateral forces are virtually eliminated [246].

Intermittent contact AFM therefore encompasses two distinct frequencies. Piezoelectric components drive the cantilever to vibrate at a set frequency and amplitude, while laser optics monitors the actual vibration characteristics adopted by the cantilever as shown in *Figure 3.14*.
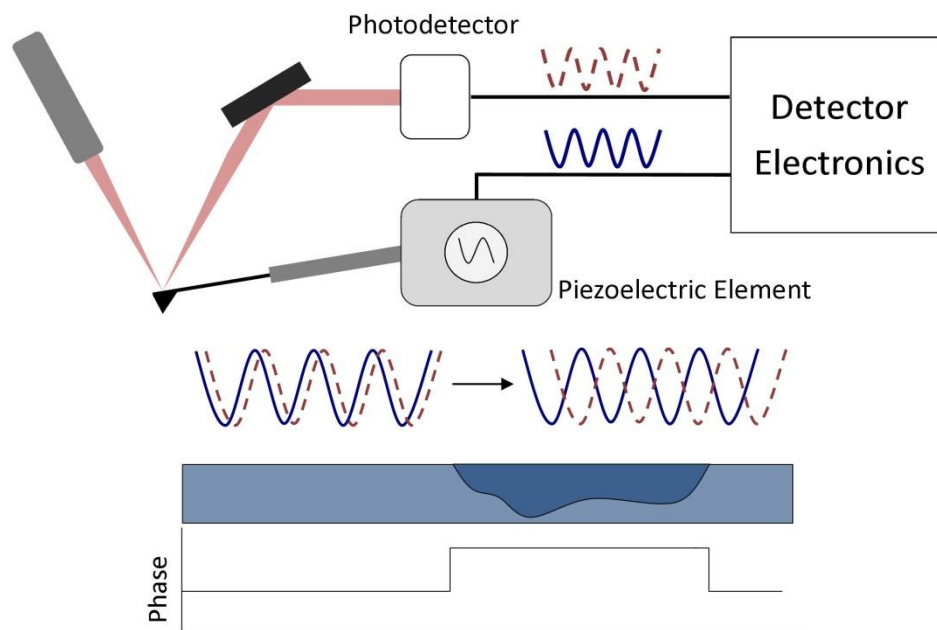


Figure 3.14 - Schematic diagram showing differences in phase readings when scanning surfaces of different surface properties even though there is no change in topography.

Changes in the oscillation amplitude are used to measure topographic variation in the sample and can build up a topographical image of the surface being scanned. The difference in phase between the piezoelectric drive signal and the actual cantilever oscillation is also monitored and is sensitive to variations in surface material properties [250]. The difference in phase angle is known as the phase shift and the images recording these phase shifts during tapping mode are called phase contrast images. A number of publications link changes in phase to surface adhesion [251], mechanical properties [252] and charge [253] but it was shown that phase shift alone cannot be used to quantify these differences [254]. Phase changes can be considered as a measure of the energy dissipation between the tip and the sample and therefore depends on a number of factors including the surface properties mentioned earlier as well as the contact area [64]. As the contact area is also dependant on topographical

features, these can indirectly affect the phase reading and appear as a change in phase when no changes in surface properties are present. Topographical data is therefore sometimes "leaked" into the phase contrast image causing ambiguous interpretation. This is usually avoided by overlaying phase images onto topographical images. The phase image produced by AFM software has the same resolution as the topography image. The former is usually used as a contrast enhancement as it highlights edges and is usually not affected by relatively large height differences. Phase imaging is useful when analysing bi-phasic materials as different domains that are usually undetected by conventional topographical analysis can be revealed in the phase image [250, 255].

### 3.5.2.4. AFM artefacts

All scientific measurement instruments are susceptible to undesirable artefacts that are generated during one of the many stages of data collection and manipulation. Since AFM involves a complex setup that comprises of both mechanical and electronic components, it is important to understand the data that is produced so as not to misinterpret the results obtained [243, 245].

**Vibrations**

A common source of artefact in AFM is vibration from an external source that causes the cantilever in the microscope to vibrate at an undesired frequency. Acoustic vibration is a common source of artefacts and is usually minimised by having the equipment in a sound-proof chamber. Buildings usually vibrate a very low frequency over a distance of several microns. To counteract this issue, AFMs are usually installed on a lower floor towards the core of the building. Active vibration isolation tables are also sometimes installed in order to reduce vibrations originating from nearby sources [256].

**Probe artefacts**

One of the main causes of artefacts in atomic force microscopy is the cantilever tip used. Since this is a physical object with a finite tip diameter and shape, the AFM

image will not always reflect the true shape of the sample surface being scanned. A convolution of the probe geometry and the shape of the features being imaged is usually presented to the user caused by mechanisms shown in *Figure 3.15*. The size of these artefacts is only important when the size of the feature being scanned has a similar size to the cantilever tip diameter [257]. Typical probes have a tip diameter of around 10 nm but probes with tips that are made of carbon nanotubes or tungsten spikes with tips of 2 nm in diameter are commercially available [247].
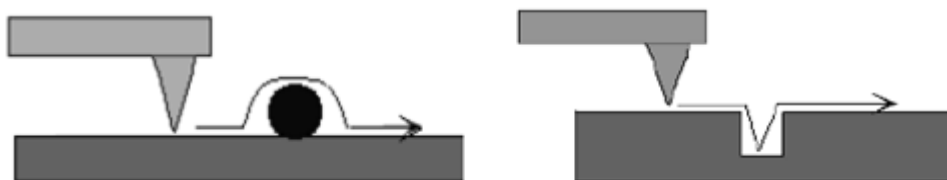


Figure 3.15 - When the AFM tip moves over a fibre or sphere attached to the surface, the data obtained would show broadening of the features in the final image (left). When the probe moves into a pore, the width of the probe does not allow for an accurate scan of the feature, resulting in a convoluted and narrower image (right). [256]

Cantilevers are commonly made out of silicon nitride making them fragile and easily chipped during normal use. This changes the convolution between the tip and the surface since a new tip shape would be produced [256].

**Other common artefacts**

A common artefact in atomic force microscopes is the angle between the probe and the surface. This angle is determined both by the angle at which the cantilever is mounted in the holder as well as the angle of the sample. Electrostatic surface charge can also build up on non-conductive surfaces altering the image obtained. This is usually solved by grounding both conductive and non-conductive samples to eliminate the build-up of charge [244, 257, 258].

### 3.5.2.5. Atomic force microscope

A stand-alone AFM (*Asylum Research, Bio-MFP-3D, Santa Barbara, CA, USA*) was used for analysis of various samples on a micro- to nano-meter scale. Imaging could be done both in contact and in tapping mode, in air or submerged in liquid. An inbuilt optical camera could also be used to locate desirable positions for the AFM to scan while giving the option to image both from the top and bottom for translucent samples. As well as surface imaging, this AFM could be used in *Force Mode* where the sample's nano-mechanical properties could be determined by means of indentation. A Class I laser system was used to accurately monitor any movements of the cantilever for precise measurements of the cantilever position. The system uses accurate piezoelectrics to measure exact positions and automatically corrects for hysteresis and creep. The AFM stage allowed for a 90 μm x 90 μm X-Y scan size with an average deviation of 0.5 nm. The Z travel range was limited to 12 μm with a lower average deviation of 0.06 nm allowing for accurate measurement of forces. The proprietary software provides complete control over the AFM and various additional features that make the system highly versatile and adaptable. To avoid unwanted noise while obtaining measurements, a vibration isolation table was used along with an acoustic isolation enclosure as shown in *Figure 3.16*.



Figure 3.16 - Photograph of the AFM on a vibration isolation table inside an acoustic chamber. 1) AFM head; 2) Movement table; 3) Light source and camera controls; 4) Vibration isolation table; 5) Acoustic enclosure.

### 3.5.2.6. Measurement of surface roughness

The surface morphology of solvent-cast films was investigated using the *Asylum Research MFP-3D* AFM. Topographical images were obtained in contact mode using *AR-iDrive-N01 L* tips with low modulus for increased sensitivity. Unless otherwise specified, all scans were 50 μm x 50 μm at 0.5 Hz with 256 points and lines which allowed for a good compromise between scan time and image quality. Images were then flattened in both X and Y axis in order to reduce alignment artifacts and roughness $R_{RMS}$ was recorded from each image. Three images were obtained per sample and a mean and standard deviation of roughness was calculated.

### 3.5.2.7. Phase imaging of solvent-cast films

In order to investigate whether the different polymer micro-phases can be resolved, the *Asylum Research MFP-3D* AFM was used in intermittent contact mode using an *AC 160TS* cantilever. Using this setup, a phase image that reveals changes in surface properties was obtained. To better interpret the results obtained, the phase image was overlaid onto height data resulting in an image where the three-dimensional height indicates the changes in height of the surface whereas changes in phase are indicated by colour mapping. Images of various sizes were obtained at a number of locations but a minimum of 256 points and lines was maintained to preserve image quality.

### 3.5.2.8. AFM imaging of electrospun mats

The surface topography of the resulting electrospun mats was investigated using the *Asylum Research MFP-3D* AFM. Topographical images were obtained both in contact mode and in intermittent contact mode. Contact mode images were obtained using *BL-TR400PB – L* tips with low modulus for increased sensitivity while intermittent contact imaging was performed using *AC 160TS* cantilevers. These cantilevers were stiffer than the former making them more suitable for intermittent imaging. Images of various sizes were obtained at a number of locations but a minimum of 256 points and lines was maintained for an increased image quality.

## 3.6. Macro-mechanical Characterisation

### 3.6.1. Vertical load frame system

The load frame system (*Bose, Electroforce 3200, Eden Prairie, MN, USA*) was used to evaluate the bulk mechanical properties of samples manufactured for use in this project. This system was set up for testing of soft materials with force transducers ranging from a maximum of 450 N to 22 N. A large selection of clamps was available to perform a variety of tests on samples with different requirements. The tests could be performed in dry conditions or submerged in a heated saline bath to mimic the environment required. The included software allowed the user to define a series of test conditions while recording the resulting forces.



Figure 3.17 - Photograph of the Bose Electroforce 3200 load frame system

### 3.6.2. Bulk mechanical characterisation

Three samples were obtained from each specimen to be tested. The nominal dimensions of each sample were 5 mm x 30 mm whereas the actual dimensions were later assessed individually. The actual width of each sample was measured using an upright microscope with digital position readout. This was accomplished by

obtaining three relative x- and y- coordinate readings from the two sides of the sample followed by a simple trigonometric calculation to obtain the width of each sample. This technique eliminated the possibility for the sample buckling under the compression of Vernier callipers. The thickness of solvent-cast films was measured directly using a micrometer screw gauge while the thickness of electrospun mats had to be measured indirectly as these could easily be compressed if the same technique was used. Each sample was mounted vertically in a scanning electron microscope and the mean thickness was measured from four different positions using *ImageJ*.

The distance between the grips determined the sample gauge length and was accurately measured using Vernier callipers. Each sample was tested using the *Bose Electroforce 3200* set up for tensile testing. Samples were subjected to 5 % strain to ensure no plastic deformation. The tensile modulus was calculated from the gradient of the stress-strain loading curve between 20 % and 80 % of the maximum stress. The mean modulus for each sample was then calculated from three loading cycles performed on each sample.
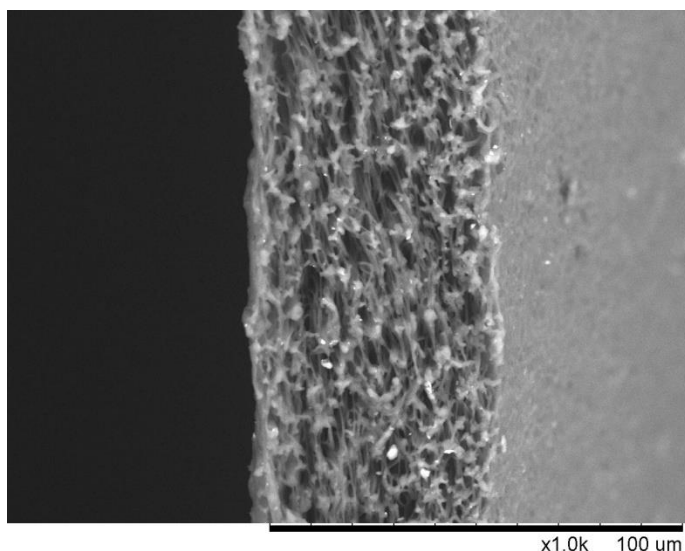


Figure 3.18 - SEM micrograph showing the cross-section of a fibrous scaffold used to calculate sample thickness

## 3.7. Nano-mechanical Characterisation

### 3.7.1. Nano-indentation

Mechanical indentation is a versatile technique used to investigate compressive mechanical behaviour of materials by loading samples under investigation with a known force and measuring the resulting deformation. Traditionally, indentation tests investigated plastic behaviour and involved a single fixed load on an indenter with defined geometry. This, then results in a permanent imprint on the surface which could either be measured using conventional techniques or using microscopy, depending on which scale was being investigated. Advances in this technology have meant that indentation can now be carried out to specific forces or displacements while being measured over the entire loading and unloading cycle. Nano-indentation has been made possible with the development of transducers sensitive down to the nano-scale, thus enabling the analysis of mechanical behaviour of materials micro- and submicro-metre range.

Nano-indentation is considered as one of the most convenient methods of the nano-mechanical characterisation techniques. Systems which control displacement and forces applied from the sub-micron to the micron scale are readily available, thereby allowing the surface compliance and stiffness to be measured [86].

Sample preparation is minimal; the main requirement being that the surfaces being tested is flat on the corresponding scale [259]. Samples should also be mounted on a relatively hard surface and the thickness of the sample has to be at least 10 times that of the depths of indents performed. Nano-indentation can also be performed using different loading conditions, dwell times and indenter tip shapes.

Indenter tips are usually made of materials such as fused silica or diamond as these have a much greater stiffness than the sample being indented. The overall indenter tip shape as well as the specific tip geometry has a substantial influence on the resulting measurements. Spherical geometries generally have a radius of curvature on the range of a few millimeters, making it difficult to investigate localised changes in

nano-mechanical properties. Three-sided pyramidal tips are relatively easy to manufacture, and are commonly used on metals, polymers and stiff biological materials. The angle that the faces make relative to a normal plane can be customised depending on the requirements of the experiment. Shallow angles result in sharp tips that might tear nanostructures within the sample rather than deform them elastically while giving rise to an elevated amount of stress concentrations. On the other hand, larger angles might result in problems similar to those experienced with spherical tips. Berkovich tips and cubed corner tips are two examples of three-sided pyramidal tips with a defined open angle at $65.3^o$ and $35.3^o$ respectively. Berkovich is the most common tip shape. Its steep angle minimises the influence of friction and makes it difficult to damage [260, 261].

Nano-indentation is usually carried out using a dedicated system with force and displacement transducers perpendicular to the surface, however, such calculations can be carried out using atomic force microscopy. In AFM, the position of the probe can be accurately controlled while the relative position of the cantilever is recorded by means of a laser as explained in *Section 3.5.2.1*. The nominal mechanical properties of the cantilever are usually provided by the manufacturer as the shape and material used are known but, the actual values within a batch of probes usually varies considerably. Actual values of cantilever spring constants can easily be calculated by lowering the probe over a rigid surface such as fused silca and measuring the displacement of the cantilever [262, 263].

With *a priori* knowledge of these variables, nano-indentation can be carried out using AFM at specific locations after an image of the surface is obtained. The main advantage of AFM nano-indentation is that the degree of indentations can be controlled according to which cantilever probe is used. Stiff cantilevers can be used to nano-indent stiffer materials successfully while the deflection for a given force might not be enough if softer materials are indented. Soft cantilevers can be used for relatively soft materials, whereas indenting harder materials would result in a large cantilever deflection with very low indentation.

Different cantilevers have different tip geometries thus preventing direct comparison on data obtained from indentations performed from two different cantilevers. Cantilever tips are also very susceptible to damage and wear during use in surface imaging which changes the tip shape and the resonant frequency. This, together with the fact that the original tip geometry of every cantilever cannot be accurately characterised, makes AFM nano-indentation an unreliable technique to collect absolute measurements of sample mechanical properties when compared to Berkovich tip indentation.

Another factor affecting nano-indentation is the water condensation present on all surfaces exposed to water vapour present in the atmosphere. Capillary action between the AFM tip and the sample being tested causes adhesion which becomes more significant as the forces being applied are reduced to the nano-newton scale. Chambers with controlled atmospheres are sometimes used to counteract this problem when extremely low force nano-indentation is being performed. As previously explained in *Section 2.2.3* the smaller the indentation depth, the more predominant size effects become, making it more challenging to obtain reliable data.

### 3.7.1.1. Models of indentation

Conventional indentation of metal surfaces involves measuring the resulting plastic deformation made by the indenter on the surface. *Doerner and Nix* (1986) [264] developed the first method for interpreting data from depth-sensing indentation instruments to calculate a value of Young's modulus as well as a value for hardness from indentations to depths less than a micron.

*Oliver and Pharr* (1992) [265] developed what has become the most cited analysis technique through advancing Hertz's [266] contact theory by linking *Sneddon's* relationship [267] which describes the relationship between unloading contact stiffness, contact area and elastic modulus. The Oliver-Pharr model is used in conjunction with sensitive displacement and force sensors that collect data continuously while indentations are performed. The model is then applied to the unloading curve as it assumes pure elastic recovery.
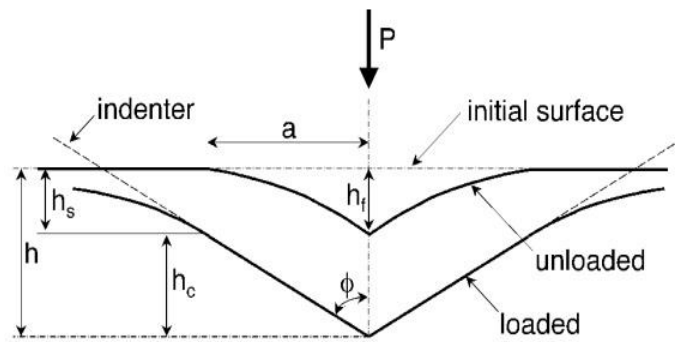
Figure 3.19 - Schematic diagram showing original, loaded and unloaded surface indicating that measurements made from unloading are purely elastic. Reproduced from Oliver *et al.* [268].

*Figure 3.20* illustrates a typical loading and unloading curve obtained from a single indentation. The important parameters obtained from this curve are the maximum load, maximum displacement, the elastic unloading stiffness *dP/dH* and the final depth after the indenter is fully unloaded [268].
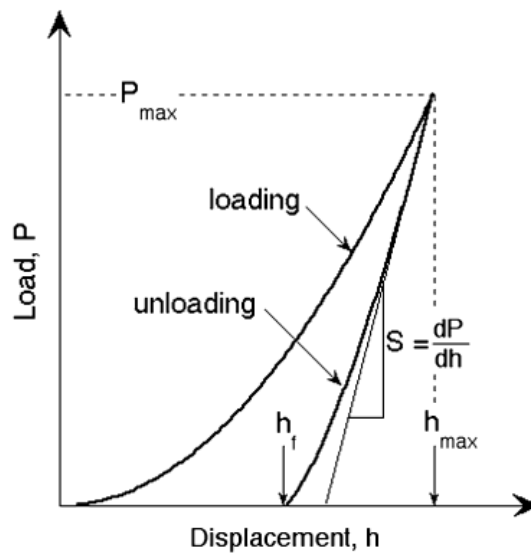


Figure 3.20 - Loading and unloading curves in nano-indentation Reproduced from Oliver *et al.* [268]

The contact area relative to the depth of indent can be calculated since the geometrical shape of the tip is well-defined. The Oliver-Pharr method calculates a value for Young's modulus using the gradient at the maximum contact depth:

$$S = \frac{dP}{dh}$$ [2.1]

The effective modulus $E_{eff}$ was found by:

$$E_{eff} = S \frac{\sqrt{\pi}}{2\sqrt{A}}$$ [2.2]

Where A is theoretical predicted the contact area at the contact depth for a fixed indenter shape.

$E_{eff}$ is the compound modulus of both the specimen and the indenter as both are assumed to deform.

The Young's modulus of the specimen E is found using:

$$\frac{1}{E_{eff}} = \frac{(1 - v^2)}{E} + \frac{(1 - v_i^2)}{E_i}$$ [2.3]

Where: v is the Poisson's ratio of the specimen

$v_i$ is the Poisson's ratio of the indenter

$E_i$ is the Young's Modulus of the indenter

One of the assumptions in nano-indentation is that the material deforms linearly around the indentation tip. In some occasions, the material piles up thus considerably increasing the actual contact area leading to an artificial increase in the Young's modulus calculated [265].
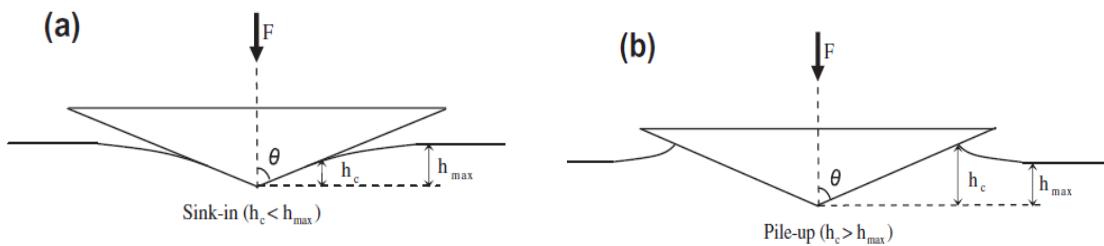


Figure 3.21 - Illustrations of the two modes of indentation: sink-in vs pile-up Reproduced from Oliver *et al* [265].

### 3.7.2. Apparatus - dedicated nano-indenter

The nano-mechanical properties of solvent-cast polyurethane films were investigated using a nano-indentation system (*Asylum Research, MFP NanoIndenter, Santa Barbara, CA, USA*). This system used the same vibration and acoustic isolation systems as the AFM described in *Section 3.5.2.5*. A separate optical camera was used to allow for imaging of the sample and indenter simultaneously. The system allowed for a maximum load of 4 mN with a Z-travel range of 12 μm. The following nano-indenter tip geometries were available: a Berkovich tip, a cube corner tip and a diamond flat punch. The accompanying software facilitated analysis with tools such as inbuilt options for Hertz and Oliver-Pharr calculations as outlined in *Section 3.7.1.1*.

### 3.7.3. Indentation of solvent-cast films using the dedicated nano-indenter

Standard calibration procedures were performed before testing was initiated to confirm the accuracy of the data obtained subsequently. The thickness of each sample was substantially higher than 10 times the maximum indentation depth in order to avoid substrate effects during testing [269]. Samples were mounted onto a glass slide using two-part epoxy resin in order to create a rigid bond and to avoid movement during testing. Unless otherwise stated, indentations were carried out on the glass interface.

Indentation was carried out using a dedicated nano-indenter with a fused silica Berkovich tip to a specified depth. The rate of indentation was kept constant throughout all the experiments performed. The surface approach speed, the indentation rate and the rate of retraction chosen were 100 nm/second as this produced a satisfactory compromise between indentation data resolution and indentation time. The Oliver-Pharr method was used to determine the elastic moduli of the samples by taking the first 40 % of the retraction curve and a standard Berkovich contact area function was assumed.

### 3.7.4. Nano-indentation of solvent-cast films using AFM

AFM nano-indentation was carried out using the *MFP-3D* AFM and BL-TR400PG-L cantilevers for nano-indentation. Standard calibration techniques were used and a real value for cantilever stiffness was obtained.

Samples were fixed onto a glass slide using epoxy resin to avoid sample movement during testing. Indentations were then performed at a fixed rate of 100 nm/second to specified depths. An area of 90 μm x 90 μm was indented 100 times in a raster manner shown in *Figure 3.22a.* Moduli from each indent were calculated using Oliver-Pharr from the first 40 % of the retraction curve and a conical tip shape with nominal tip radius was used for contact area measurements. A graph of modulus and location was plotted as shown in *Figure 3.22b.* Moduli were then split into 25 bins across the whole range and Gaussian curve fitting was applied as shown in *Figure 3.22c.* This process was performed automatically by the AFM software and was only used when multiple indentations were performed in the same area using AFM. The mean and standard deviation was then derived from the resulting distributions.

### 3.7.5. Nano-indentation of electrospun fibres using AFM

Indenting specific fibres could only be performed using AFM nano-indentation. Using AFM, the centre of an individual fibre could be located by imaging the surface before indenting. Since the surface area of a Berkovich tip was large relative to the morphology of the surface features, indenting such films using a Berkovich tip, would also mean that more than one fibre would make contact with the tip surface at the same time contributing to artefact. After electrospinning a thin film of polymer onto aluminium foil, the AFM was used to locate individual fibres attached directly on the aluminium foil. This was performed in an attempt to ensure that the derived quantities (effective modulus) were based on the nano-indentation of a single fibre rather than the compound effect of nano-indentation and the movement of the electrospun mesh as a whole. Fibres were scanned in intermittent contact mode using an *AC 160TS* cantilever to determine the precise point of indentation. These were

then carried out using the AFM probe to a fixed cantilever displacement of 200 nm. Oliver-Pharr was then used to calculate the modulus for each indent from the first 40 % of the retraction curve.

a)

b)

c)
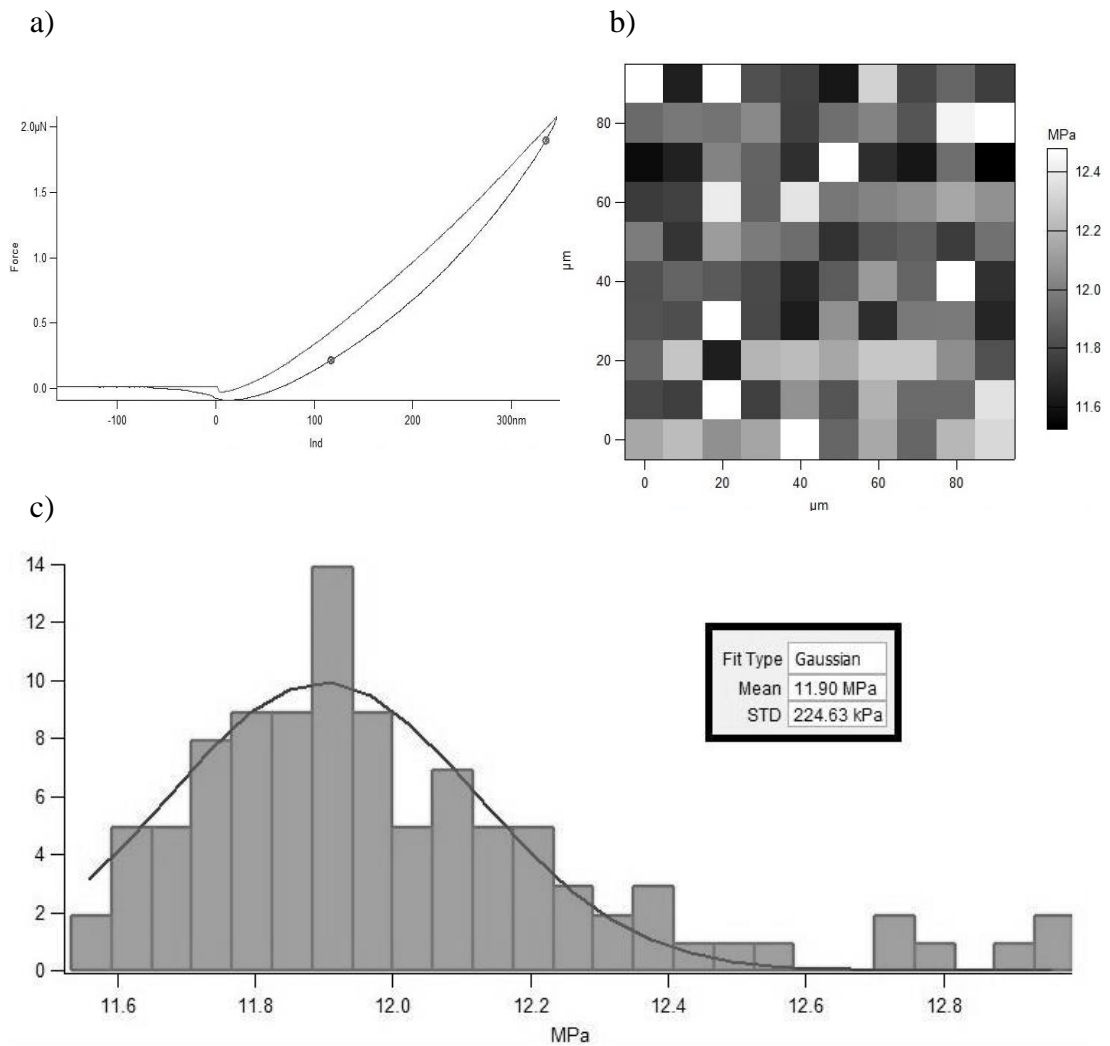
Figure 3.22 - a) Graph obtained from one indent at 350 nm on Z6A1, b) Grid of 10 x 10 indents showing variation of modulus calculated of a 90 μm square at one indentation depth, c) Bar chart showing distribution of moduli overlaid by a Gaussian distribution curve

## 3.8. Thermal characterisation

### 3.8.1. Differential scanning calorimetry

Differential scanning calorimetry (DSC) is a technique used for direct measurement of a sample's specific heat capacity and how this varies with a change in temperature. A sample of known mass is heated at a fixed rate and changes in heat flow are tracked as changes in the material heat capacity. This therefore allows for the detection of various thermal transitions such as phase changes, material curing temperatures, glass transition temperatures and melting temperatures [270 – 272].

The working principal of this technique involves a closed feedback loop that tries to maintain the sample at a set temperature while measuring the power needed to do this against a reference sample with known thermal properties. The rate at which the sample is heated can therefore be controlled precisely allowing for accurate enthalpy and heat capacity measurements. *Figure 3.23* shows a typical DSC graph with temperature on the x-axis and heat flow on the y-axis. During testing, endothermic peaks are formed when the test sample absorbs more heat, making it cooler than the reference and thus causing a downward-facing peak. The converse is true when exothermic events occur, leading to a positive-pointing peak [271].
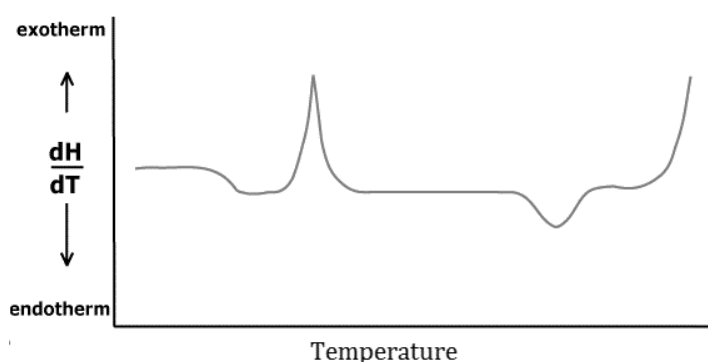


Figure 3.23 - Typical DSC thermogram

DSC therefore has uses in a wide array of applications with polymer processing being one of the major fields. The main observations to be made when polymers are tested using DSC are glass transition and melting temperatures, both seen as endothermic peaks and crystallisation temperatures seen as exothermic peaks.

## 3.8.2. Apparatus - differential scanning calorimeter

A DSC (*Mettler DSC822e, Columbus OH, USA)* was used for thermal analysis. This DSC had temperature range of -150 $^o$C to 700 $^o$C while maintaining high temperature accuracy at $\pm 0.2$ $^o$C. The operation of DSC involves measuring and recording difference between heat flows to and from (endothermic vs exothermic reactions) a given sample and to a reference crucible.

## 3.8.3. Methodology

The mass of each sample was recorded to $\pm 0.01$ mg and sealed in an individual DSC pan. The accompanying DSC software was then used to setup the parameters for the test. Each sample was heated at a fixed rate of 10 $^o$C/min from 50 $^o$C to 170 $^o$C. Samples were then allowed to cool down to room temperature independently. The rate of heating was kept constant across all experiments to reduce errors owing to equipment response time.

# Chapter 4

# Polymer Processing and Characterisation

## 4.1. Introduction

It is well known that cells apply loads on the nano-newton scale during movement [138]. In order to better understand the forces that cells encounter while moving on a scaffold, it is necessary to understand how substrates behave on such scales. Literature outlined in *Section 2.2.3* demonstrates that size effects have a strong influence at the scale of interest. Whereas the characterisation of bulk mechanical properties of an artificial implant may be helpful in understanding how the implant will act under external loading, it does not give insight into what mechanical properties the cells will encounter.

The range of polymers made available by *Biomer Technology Limited* has not been previously investigated on the micro – nano scale. This *Chapter* reports the results of a systematic investigation into the influence of a number of processing parameters on the topographical and mechanical properties of the resulting specimens. The first section focuses on the investigation of the mechanical properties on various scales of the different grades of the *Biomer $b_9$* poly(ether) urethane range. Macro-scale, tensile moduli will be investigated to observe differences in mechanical properties between the different polymer grades. Indentation to a fixed depth of 1.5 μm will then be carried out to confirm whether the differences in bulk mechanical properties hold on the micro-scale. Indentations will then be performed to various depths down to the

nano-scale to investigate size-effects during nano-indentation on the various polymer grades.

Small changes in surface topography or mechanical properties can produce different cell stimuli which could in turn alter cell behaviour [156]. The subsequent section will therefore investigate whether the solvent system used in the initial polymer solution has any effect on the resulting scaffold topography, nano-mechanical properties or domain structure. Such observations can be used to inform further experiments into the investigation of the influence of nano-mechanical properties on cell mechanotransduction.

Since polyurethane is a bi-phasic polymer, changes in the domain structure could influence the resulting nano-mechanical properties. The final section focused on the influence of the processing technique on the resulting microstructure. Differential scanning calorimetry was used to investigate the degree of phase separation in melt-processed, solvent-cast and electrospun mats. AFM phase imaging from was then used in an attempt to visualise the different micro-domains found in both solvent-cast films and electrospun fibres.

## 4.2. Results

### 4.2.1. Mechanical characterisation of polyurethane grades

Mechanical characterisation on the various grades of *Biomer Technology Limited* b$_9$™ polyether-urethane range was first carried out in both solvent-cast and electrospun form. Manufacturer supplied mechanical specifications were performed on melt-processed forms and to relatively high strains. In *Section 4.2.1*, the bulk, tensile moduli of solvent-cast films and electrospun mats are investigated. This was then followed by an investigation using indentation to the micro – nano scale. Characterisation on such scales was essential to identify mechanical properties encountered by cells during mechanotransduction.

#### 4.2.1.1. Bulk tensile moduli of solvent-cast films

Tensile macro-mechanical characterisation was first performed on the complete range of solvent-cast films from various *Biomer Technology Limited b₉* polyurethane grades. Solvent-cast films were produced from the complete range of polyurethane grades available (Z1A1, Z2A1, Z3A1, Z4A1, Z6A1, Z9A1) from solutions of 15 wt/wt% in DMF using the solvent-casting methodology described in *Section 3.3.3*. Three samples from each polymer specimen were subjected to 5 % strain using the *Bose Electroforce 320*0 as outlined in *Section 3.6.2*. The results obtained from tensile testing of the complete range of polyurethane grades were shown in *Figure 4.1* as a mean and standard deviation from three discrete samples for each polymer grade. A clear difference in tensile modulus can be observed between the different polyurethane grades.
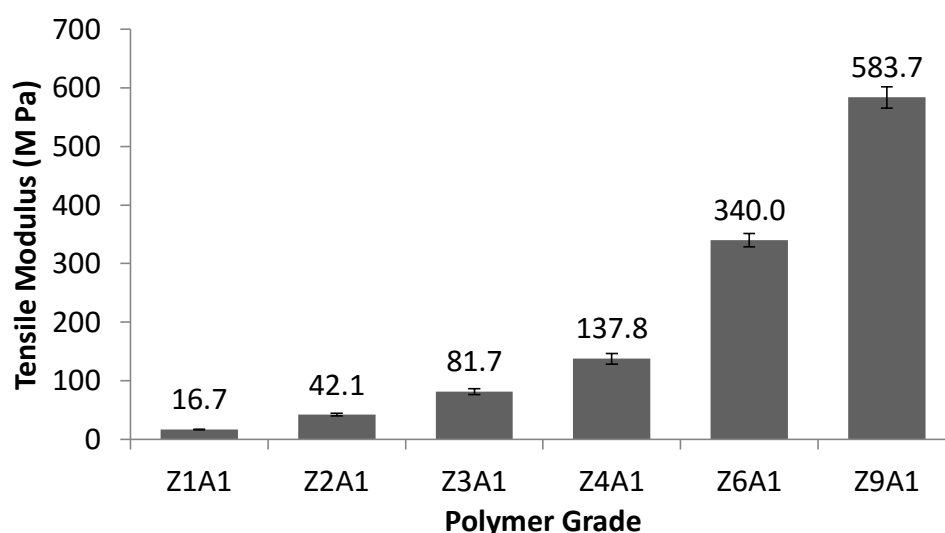


Figure 4.1 - Graph showing mean and standard deviation of tensile modulus for the range of polyurethane grades available (n = 3).

#### 4.2.1.2. Bulk tensile moduli of electrospun mats

The bulk tensile mechanical properties of electrospun mats manufactured from two grades of polyurethane were investigated in tension following the methodology outlined in *Section 3.6.2*. Z1A1 and Z6A1 electrospun mats were manufactured using parameters sets *b)* and *e)* outlined in *Table 3.2* as these were later shown to have fibre diameter distributions within the same range (0.45 µm ± 0.11 µm for Z1A1 and

0.58 μm ± 0.27 μm for Z6A1). *Figure 4.2* illustrated a representative stress-strain curve from both Z1A1 and Z6A1. It is important to note that stress was plotted on a different axis for the different polymer grades. The signal to noise ratio in the presented Z1A1 loading curve appears to be much lower as the force required to strain Z1A1 were much less than that in Z6A1. The resulting moduli were 0.895 MPa ± 0.031 MPa (n = 6) for Z1A1 and 77.129 MPa ± 5.142 MPa (n = 6) for Z6A1.
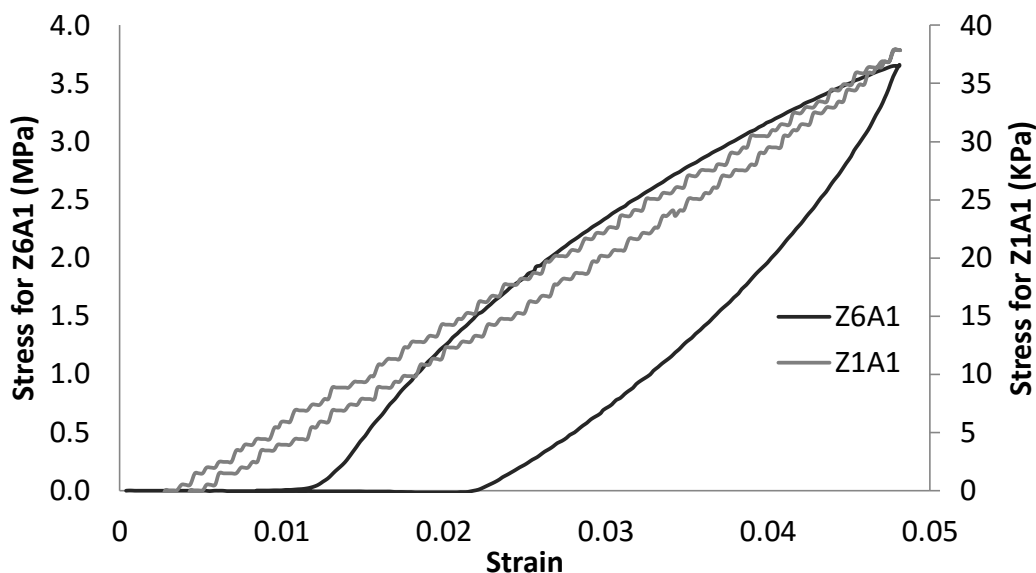


Figure 4.2 - Graph showing typical stress-strain curves obtained during tensile testing of electrospun mats of Z1A1 and Z6A1

The surface of each sample was analysed by means of SEM in order to determine whether or not the test specimens were subject to any permanent deformation following these tests. A representative image before and after tensile testing of an electrospun Z6A1 mat is shown in *Figure 4.3*.
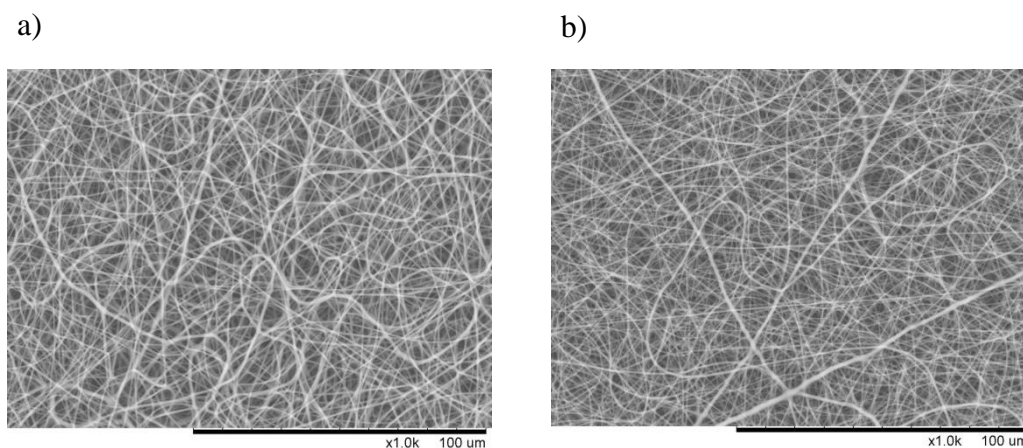
Figure 4.3 - SEM micrographs of Z6A1 electrospun mat before (a) and after tensile testing (b). Both images were obtained at x1,000.

### 4.2.1.3. Indentation using a Berkovich tip nano-indenter

The mechanical properties of this family of polyurethanes under indentation load were then investigated using a dedicated nano-indentation system. Solvent-cast films were manufactured from the complete range of polyurethane grades available using standard procedures described in *Section 3.3.3* from a solution of 15 wt/wt% in DMF. Samples were then indented using a dedicated nano-indentation system following the methodology described in *Section 3.7.3*. Since applying a fixed indentation force on the range of polymers would result in varying of indentation depths, tests were performed to a fixed depth of 1.5 µm. As explained in *Section 2.2.3* if indentations were performed to a fixed force, and therefore different depths, indentation size effects would influence the resulting moduli by producing artificially higher results in stiffer samples as the indentation depth would have been decreased. However, this approach meant that Z9A1 could not be tested as a 1.5 µm indent would require a force larger than the 4 mN that the system could apply. Five indentations were performed at different locations on each sample and a mean and standard deviation of the modulus was calculated and shown in *Figure 4.5* below. *Figure 4.4* demonstrates representative loading and unloading curves on Z1A1, Z3A1 and Z6A1.
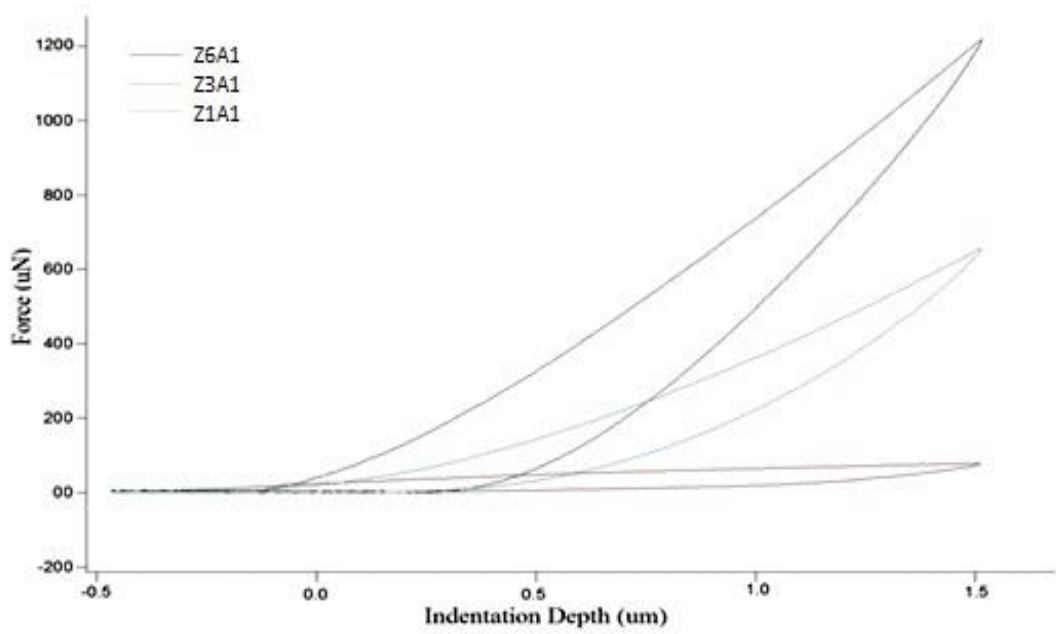
Figure 4.4 - A graph showing the indentation curves for three polymer grades (Z1A1, Z3A1 and Z6A1) to a depth of 1.5 μm
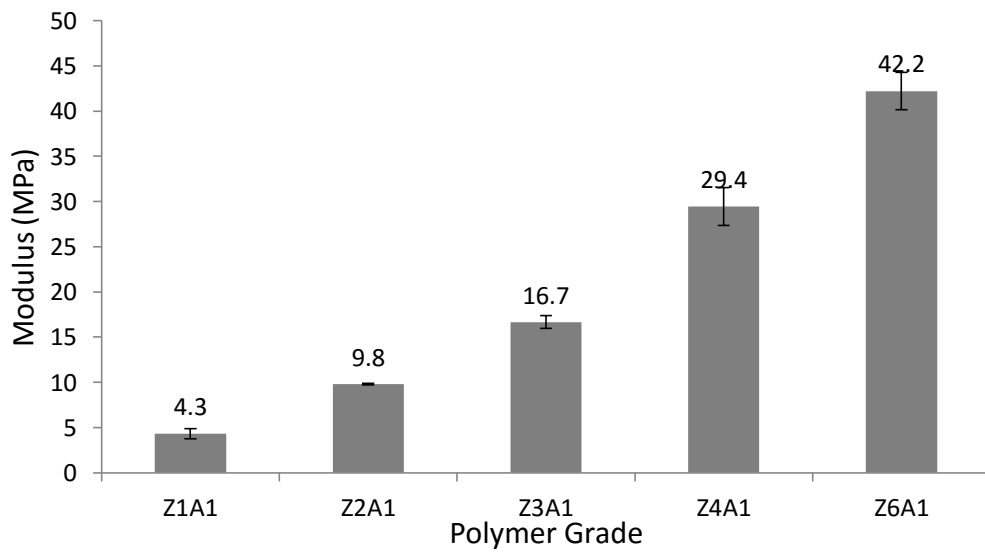


Figure 4.5 - Graph of the resulting mean moduli and standard deviations measured from nano-indentation of various polymers at a fixed depth of 1.5 μm (n = 5)

The nano-mechanical properties of solvent-cast films were then investigated by nano-indentation. To investigate indentation size effects, three polymer grades were indented to varying depths between 100 nm and 2000 nm using the dedicated indentation system following the protocol described in *Section 3.7.3*. Z1A1, Z3A1 and Z6A1 samples were each indented to 100nm, 150 nm, 200 nm, 300 nm, 400 nm, 500 nm, 750 nm, 1000 nm, 1500 nm and 2000 nm. Each indent was performed on a different location and the mean modulus from three indents is represented in *Figure 4.7*. *Figure 4.6* below illustrates indents performed to a different depth on the same sample. The Oliver-Pharr method was used to obtain a value for indentation modulus from the first 40 % of the unloading curves obtained.
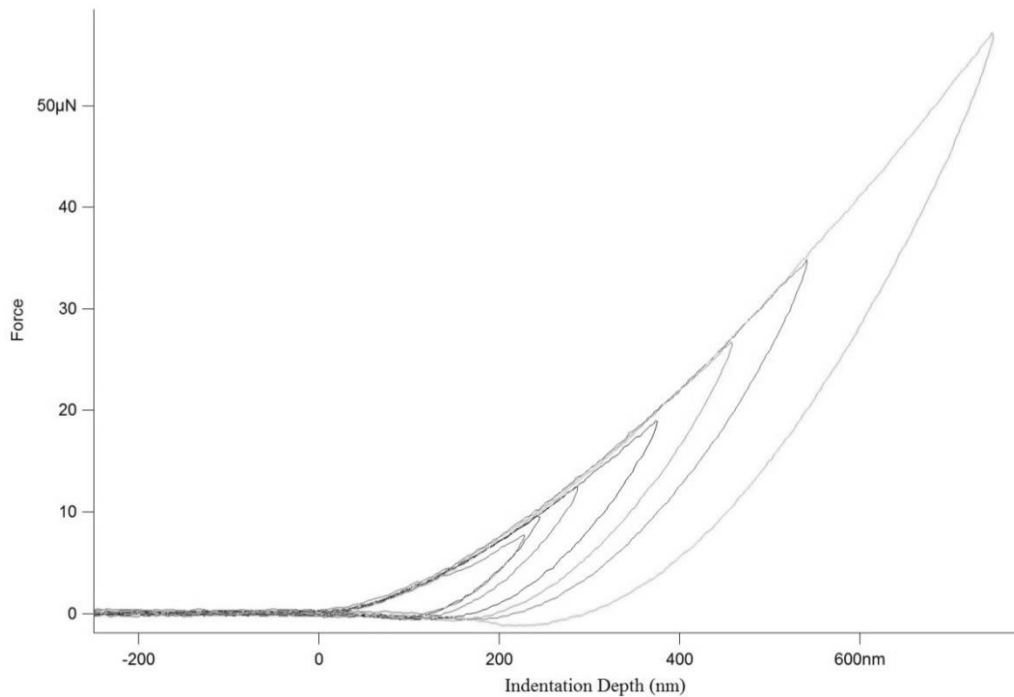


Figure 4.6 - Graph of force against indentation depth obtained when indenting Z1A1. Each curve represents a complete indentation cycle (loading and unloading) to varying depths.
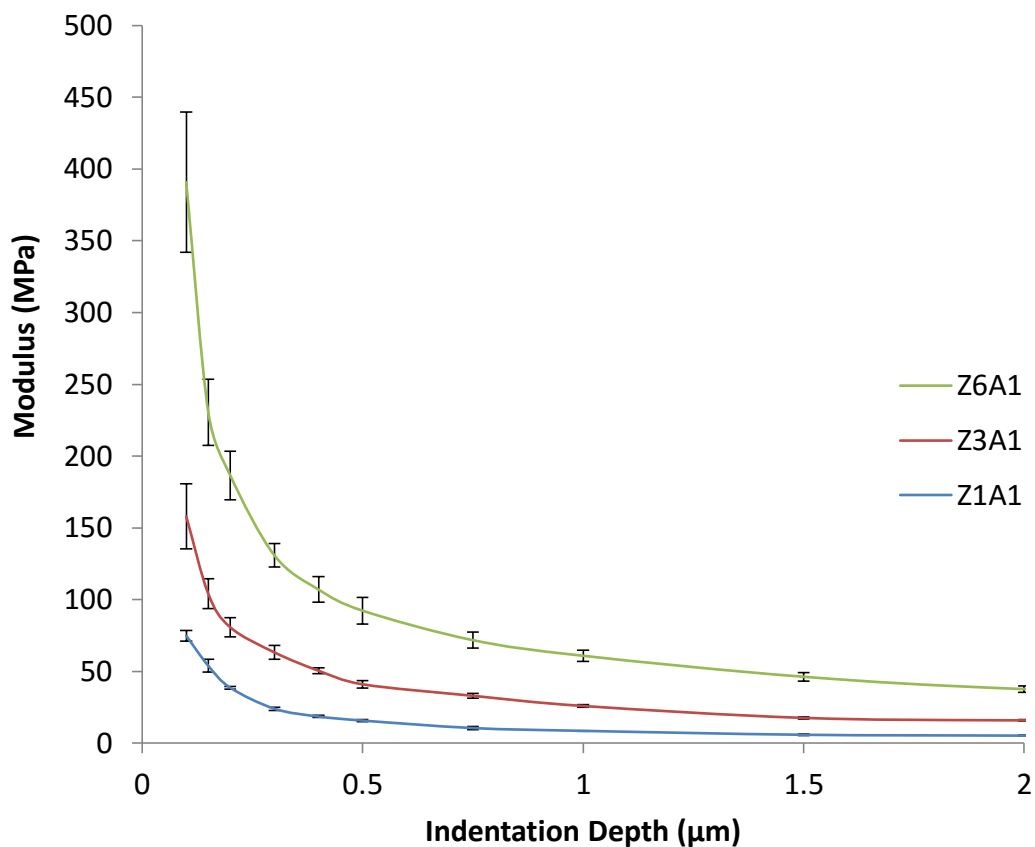
Figure 4.7 - Graph showing indentations in Z1A1, Z3A1 and Z6A1 at indentation depths between 100 nm and 2000 nm showing mean and standard deviation (n = 3).

### 4.2.1.4. Nano-indentation of solvent-cast films using AFM

A similar experiment was carried out using an AFM in force acquisition mode following the methodology described in *Section 3.7.4*. Solvent-cast films were manufactured from Z1A1 and Z6A1 using standard procedures described in *Section 3.3.3* from a solution of 15 wt/wt% in DMF. These were indented then to various depths to a range of between 30 nm and 300 nm (30 nm, 50 nm, 100 nm, 150 nm, 200 nm, 250 nm, 300 nm). This indentation depth range was considerably lower than the range investigated using the dedicated nano-indenter since the former was limited by indenter shape and stiffness. Graphs showing the calculated moduli at a set indentation depth were then plotted from this data as shown in *Figure 4.8*. It is

important to note that modulus scale in this figure is different for the polymers investigated with indentations on Z6A1 resulting in much higher moduli.
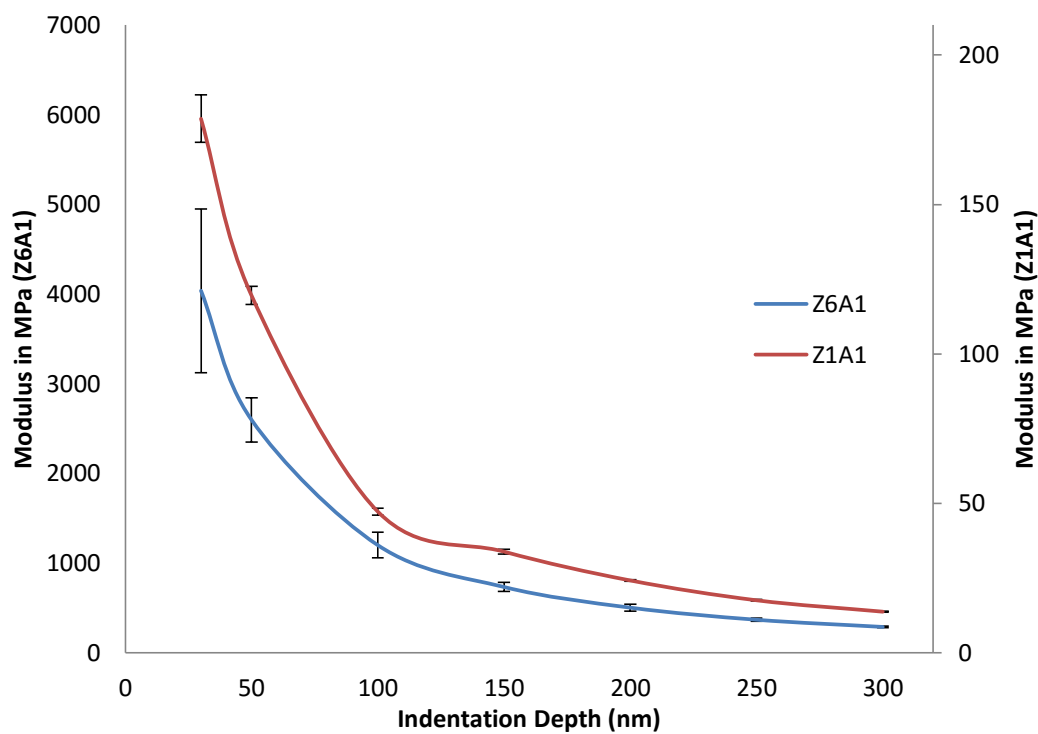


Figure 4.8 - Graph of nano-indentation at various depths on Z1A1and Z6A1 solvent-cast films using AFM showing mean and standard deviation (n = 100).

## 4.2.2. Nano-indentation of electrospun fibres using AFM

Individual fibres of both Z1A1 and Z6A1 polyurethane grade were indented using an AFM probe as outlined in *Section 3.7.5*. *Figure 4.9* demonstrates AFM images of both Z1A1 and Z6A1 fibres and the locations at which they were indented. To reduce errors brought around by substrate movement, indentations performed in areas where fibres overlap were omitted. *Figure 4.9* also includes representative indentation curves from nano-indentation on both Z1A1 and Z6A1 and the resulting mean and standard deviation of modulus from six discrete indents on each polymer. Even though an accurate comparison was not possible, a clear difference in moduli was still observed when indenting electrospun fibres.



a)

Z1A1 Fibres        Z6A1 Fibres

b)

c)        173 MPa +/- 55 MPA        10544 MPa +/- 6284 MPa
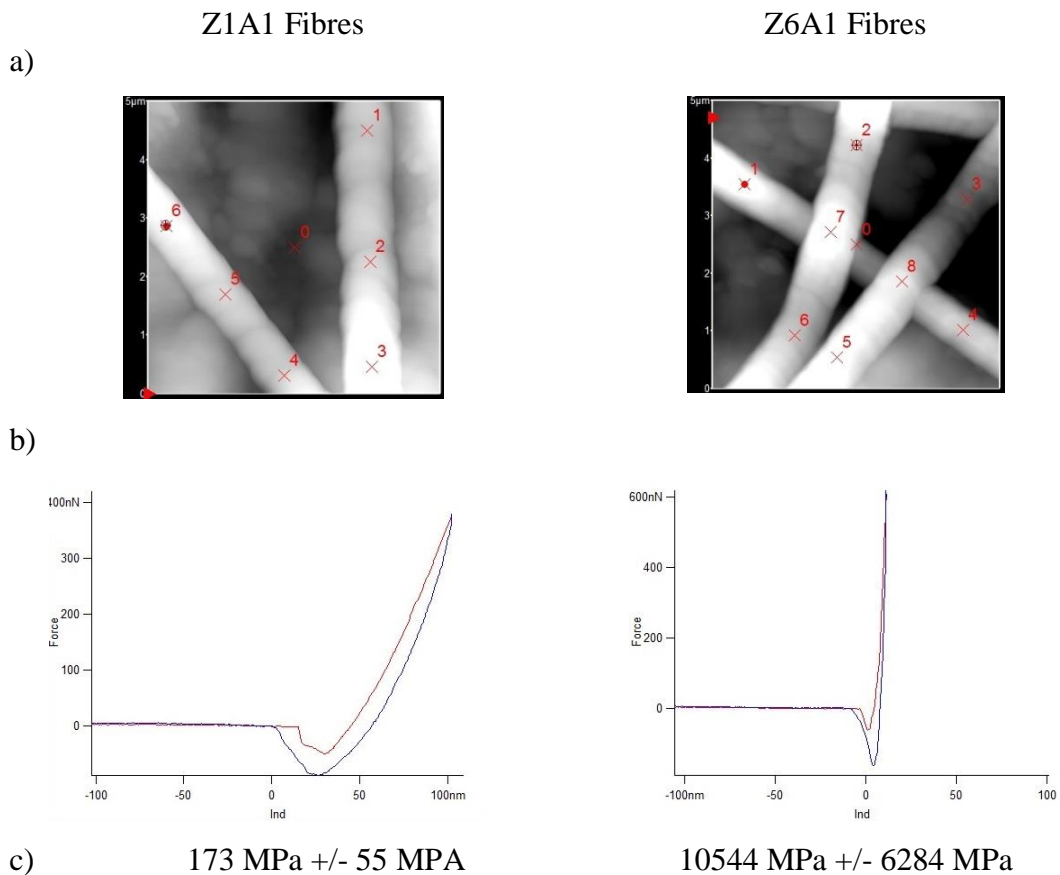
Figure 4.9 – a) AFM images of both Z1A1 and Z6A1 fibres (5 μm x 5 μm) with indentation locations. b) Representative indentation curves from nano-indentation on both Z1A1 and Z6A1. c) Mean and standard deviation of modulus calculated using Oliver-Pharr (n = 6).

## 4.2.3. Influence of solvent system used

Topographical and nano-mechanical changes on the scale at which cells mechanosense can alter cell behaviour [90, 156]. An investigation was carried out to determine whether the solvent system used in the initial polymer solution had any effect on the resulting specimen. Analysis in this section was performed on solvent-cast films as understanding nano-scale interaction in electrospun fibrous meshes can be simplified by understanding interactions on solvent-cast films since the variables in the manufacturing process are fewer and more manageable. Solvent-cast films are also homogenous structures meaning that intra-sample variability is likely to be much lower than in electrospun fibres. Only solvents used in the electrospinning of polyurethane were therefore investigated.

### 4.2.3.1. Surface roughness

Z3A1 solvent-cast films were produced from solutions of 15 wt/wt % of Z3A1 in DMF, DMAC and 75:25 (V/V) of THF:DMF following the standard methodology outlined in *Section 3.3.3*. The surface topography of the resulting solvent-cast films was investigated using AFM. The images presented were 50 µm x 50 µm in length and width with a Z-range of 1 µm. This range was chosen over a more representative Z-range as the former made differences in height more distinguishable as demonstrated in *Figure 4.10.*

a)                                              b)
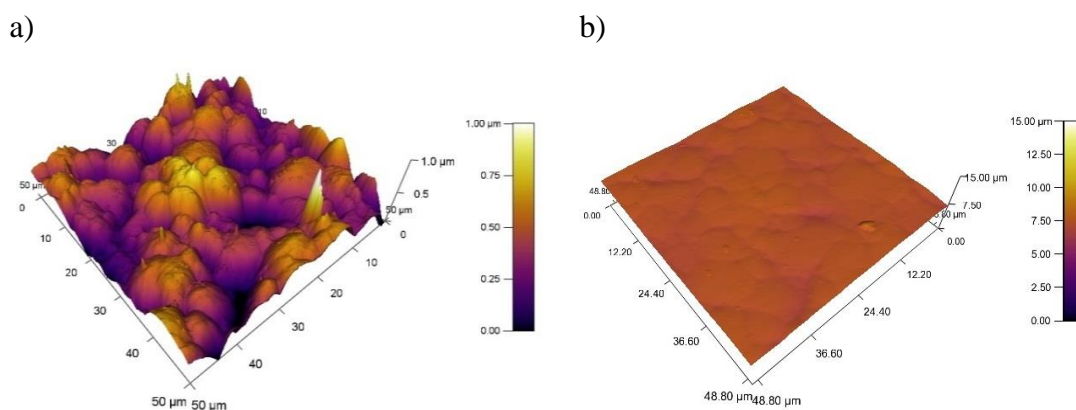


Figure 4.10 - AFM image of air interface with 1 µm Z-range (a) and the same image with 1:1 Aspect ratio (b). Pseudo-colour representing height was added to the images to increase contrast.

The differences between the glass interface and the air interface were investigated together with the influence of different solvent systems on the resulting surface morphology. A representative image for each variable is shown in *Figure 4.11* below.
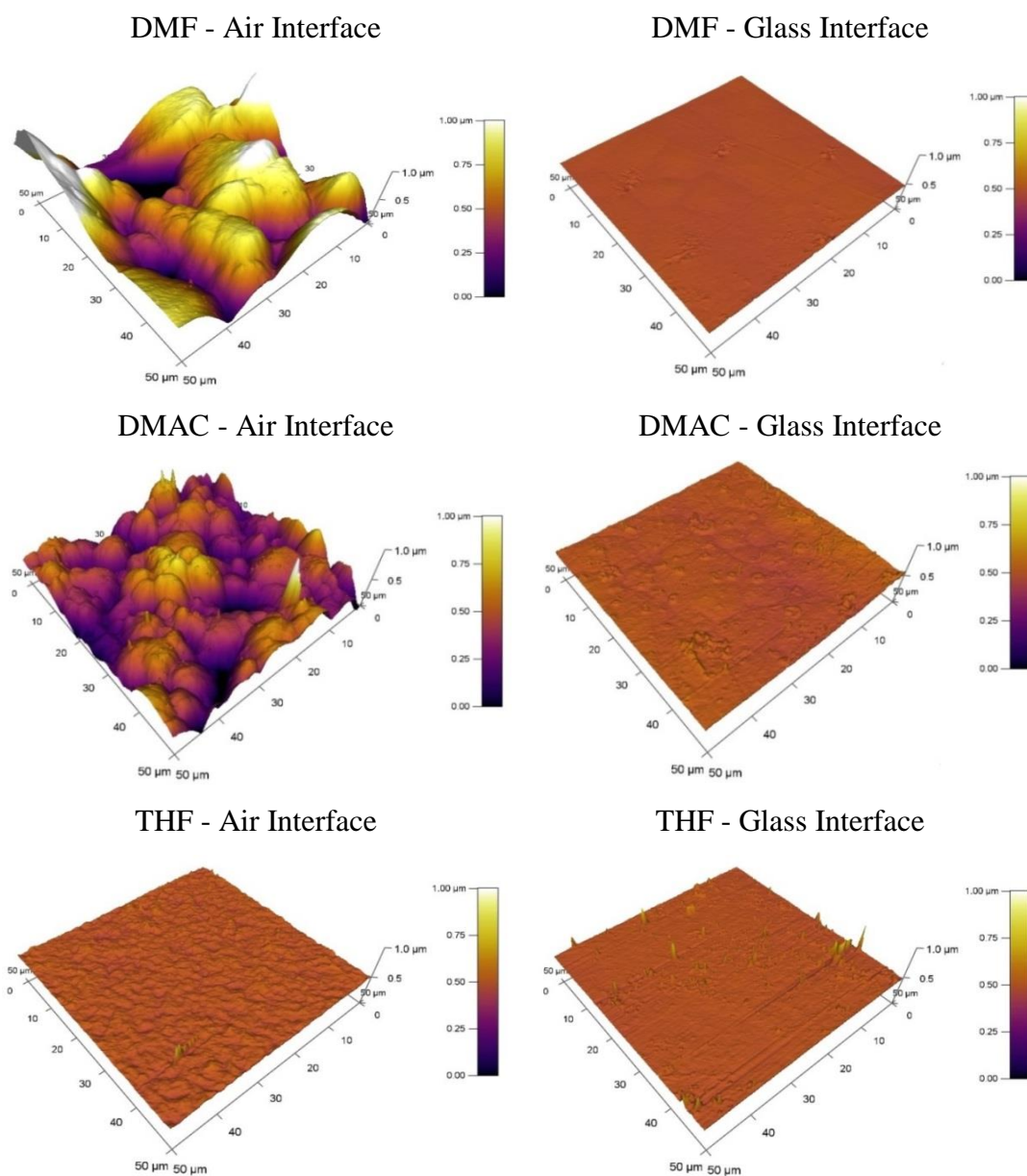


Figure 4.11 - Representative AFM images at 50 µm x 50 µm obtained from various Z3A1 solvent-cast films. Pseudo-colour representing height was added to increase contrast.

The surface roughness was calculated following the methodology outlined in *Section 3.5.2.6*. Two sets of three solvent-cast films were fabricated using the same process variables in order to investigate inter-sample variability. The resulting mean and standard deviation of roughness was plotted in *Figure 4.12* below.
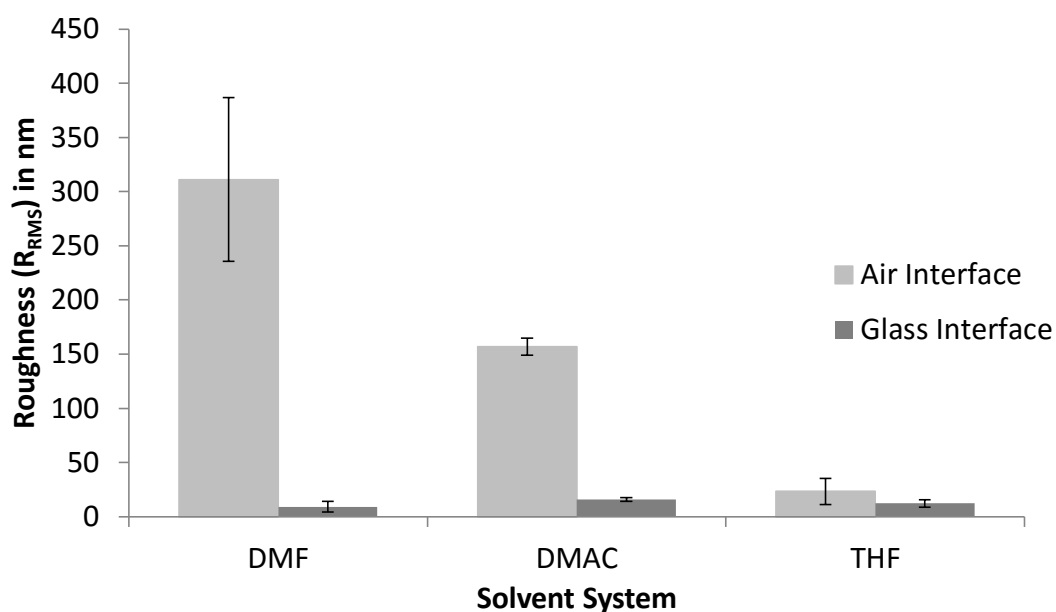


Figure 4.12 - Chart showing the mean and standard deviation of roughness $R_{RMS}$ calculated from a series of $50\,\mu m$ x $50\,\mu m$ images after two-dimensional flattening (n = 6).

### 4.2.3.2. Nano-mechanical properties

Nano-indentations were carried out on Z3A1 solvent-cast films produced from different solvent solutions, including DMF, DMAC and THF, to investigate whether the solvent system used had an impact on the resulting nano-mechanical properties. The methodology outlined in *Section 3.7.3* was followed and Z3A1 samples were indented four times each to depths of $2\,\mu m$, $1.5\,\mu m$, $1\,\mu m$, $0.75\,\mu m$, $0.5\,\mu m$, $0.25\,\mu m$ and $0.1\,\mu m$. The mean and standard deviation on the resulting indentation modulus was then plotted in *Figure 4.13* below. Two-tailed, un-paired, student t-tests performed at each indentation depth between both variable indicated no statistical difference (p > 0.05).
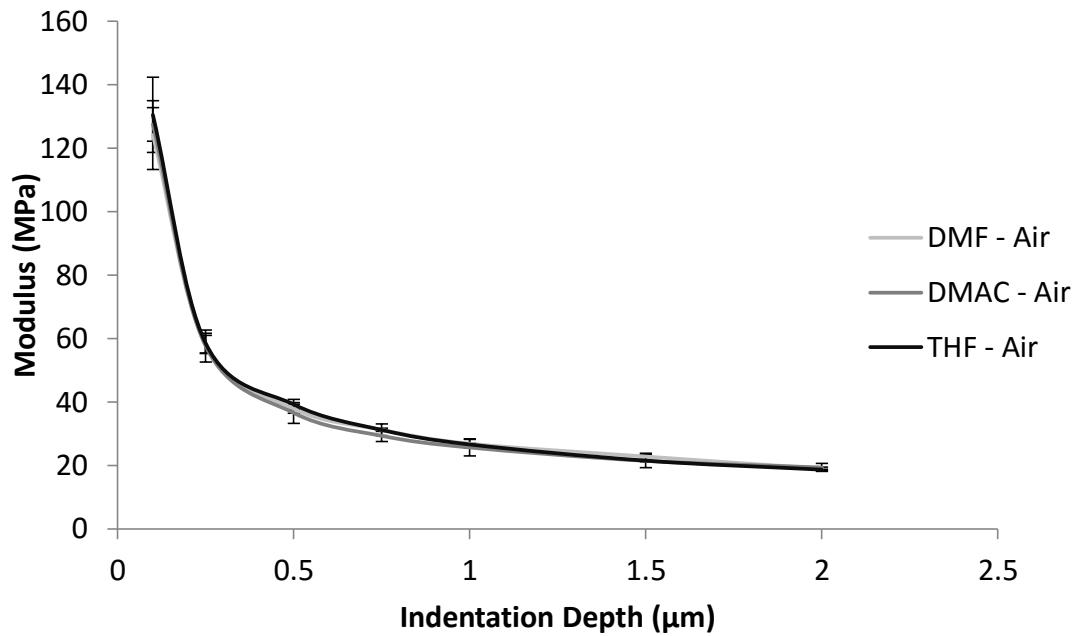
Figure 4.13 - Plot of mean and standard deviation of modulus against indentation depth for nano-indentation of Z3A1 solvent-cast films from DMF, DMAC and THF (n = 4).

A similar procedure was then carried out on both the air interface and the glass interface to investigate any differences in nano-mechanical properties as morphological analysis demonstrated that the two interfaces were distinctly different. The methodology outlined in *Section 3.7.3* was followed and Z3A1 samples were indented four times each to depths of 2 μm, 1.5 μm, 1 μm, 0.75 μm, 0.5 μm, 0.25 μm and 0.1 μm. The mean and standard deviation of the resulting indentation modulus was then plotted in *Figure 4.14* below. Two-tailed, un-paired, student t-tests performed at each indentation depth between all three variables indicated no statistical difference ($p > 0.05$).
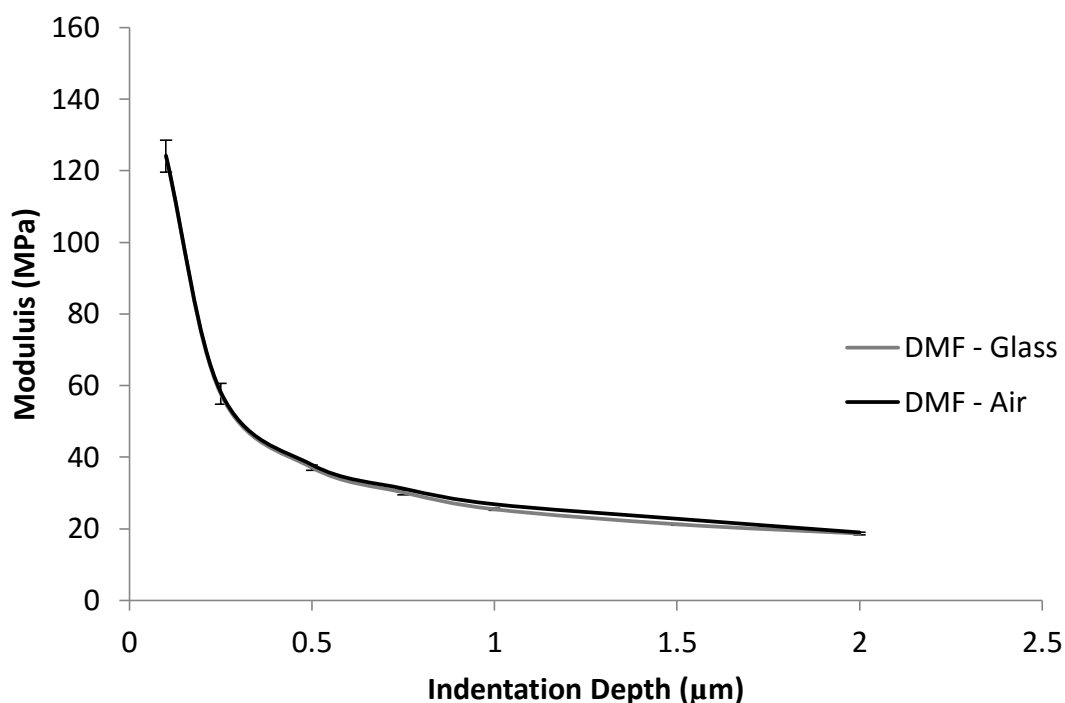
Figure 4.14 - Plot of mean and standard deviation of modulus against indentation depth for nano-indentation of Z3A1 on both the air interface and the glass interface at a range of depth between 0.1 µm to 2 µm (n = 4).

### 4.2.3.3. Thermal characterisation

Z3A1 solvent-cast films from DMF, DMAC and solution of THF:DMF 75:25 (V/V) (Figure 4.16*)* as well as Z6A1 solvent-cast films from DMF and DMAC (*Figure 4.15)* were manufactured using the methodology previously outlined in *Section 3.3.3*. Samples were then prepared for DSC to investigate any differences in the resulting microstructure using the methodology described in *Section 3.8.3*. When DSC analysis was performed on solvent-cast films produced from various solvents, no clear difference was observed on the resulting thermograms.
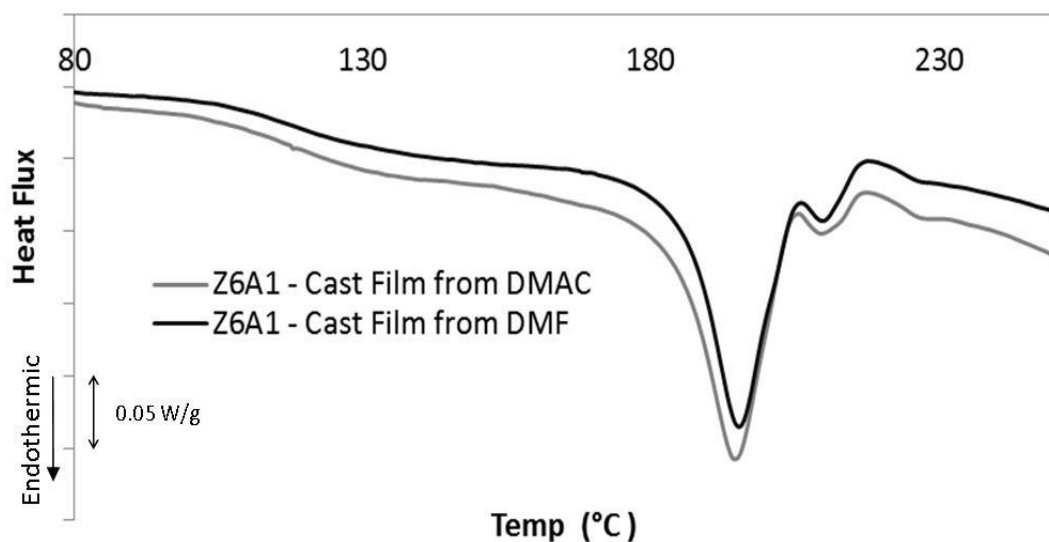
Figure 4.15 - DSC thermograms showing melting endotherms obtained from Z6A1 solvent-cast films manufactured from DMAC and DMF.
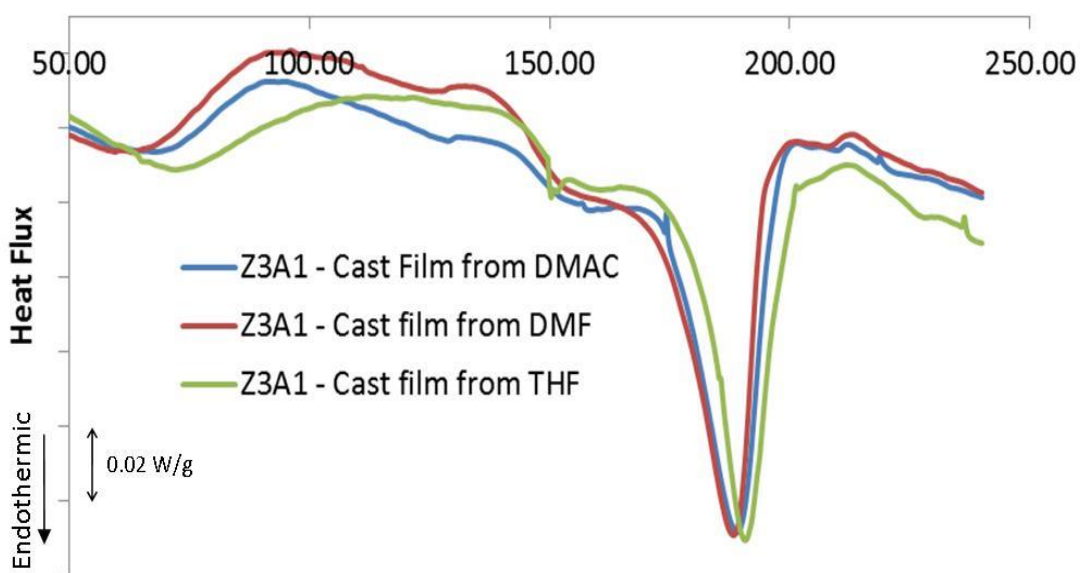


Figure 4.16 - DSC thermograms obtained from Z3A1 solvent-cast films manufactured from DMAC, DMF and THF showing the meting points of the polymer grade

## 4.2.4. Influence of processing technique on resulting microstructure

Polyurethane is made up of two distinct segments that are immiscible and aggregate into soft segment-rich domains and hard segment-rich domains. This domain structure is highly dependent on the processing technique used and can influence the resulting surface properties [273]. The influence that the processing technique has on the resulting microstructure was investigated using both a thermal characterisation technique (DSC) and phase imaging using AFM.

### 4.2.4.1.  Thermal characterisation

Melt-processed, solvent-cast and electrospun forms of two polyurethane grades (Z1A1 and Z6A1) were investigated by DSC using the methodology described in *Section 3.8.3*. Thermographs in *Figure 4.17* demonstrated changes in the endothermal peaks obtained from the different forms of Z6A1. This indicated distinct differences in micro-phase separations when the same polymer is processed using different techniques.
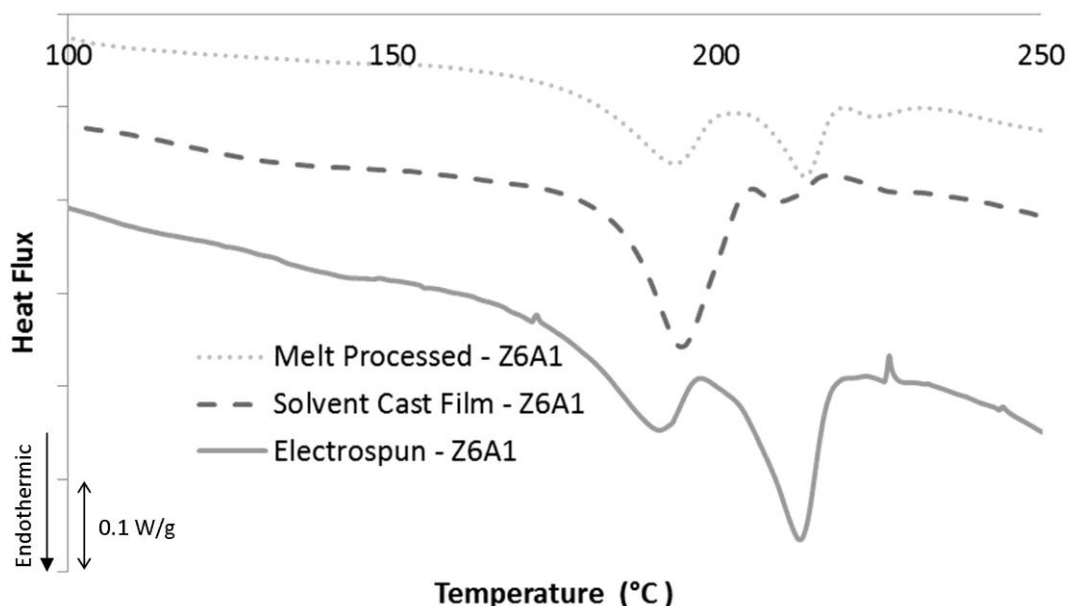


Figure 4.17 - DSC thermograms obtained from melt-processed, solvent-cast and electrospun Z6A1 samples.
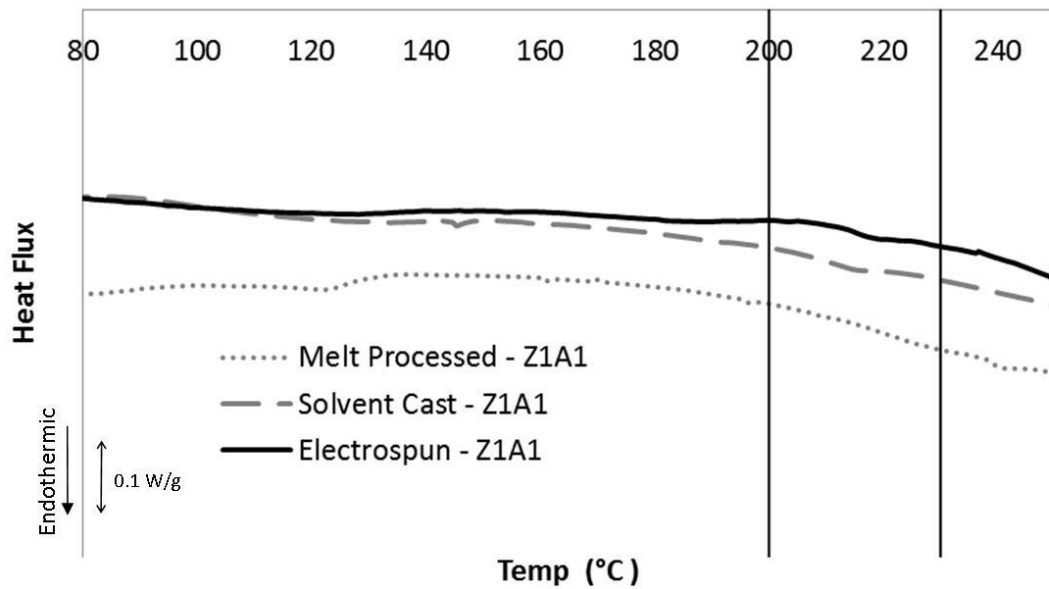
Figure 4.18 - DSC thermograms obtained from melt-processed, solvent-cast and electrospun Z1A1 samples

In *Figure 4.18,* Z1A1 demonstrates no clear disordering of HS crystallites which indicated that the material was amorphous and contains untraceable amounts of hard segment. Small peaks can be seen throughout the thermographs which were related to disordering of micro-domains within the sample.

A sample of solvent-cast Z6A1 was heated at 10 $^o$C/min to 240 $^o$C, allowed to cool down to 60 $^o$C and heated one more time at the same rate to 240 $^o$C. The resulting thermographs were graphed in *Figure 4.19* below and demonstrate distinct changes in the microstructure.
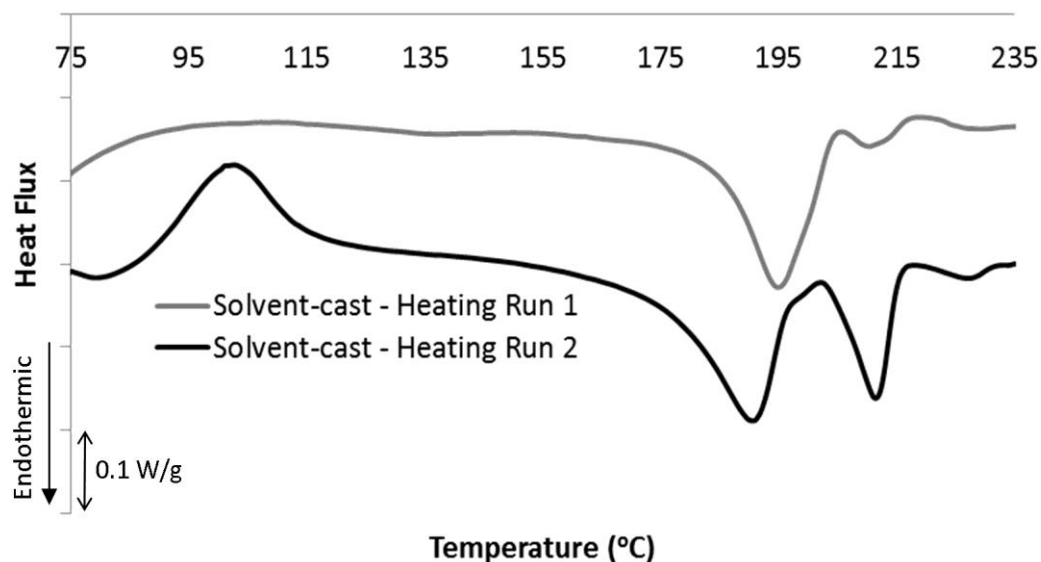
Figure 4.19 - DSC thermogram showing two heating runs of a solvent-cast Z6A1 sample. Sample was heated to 240 $^{\circ}$C, allowed to cool down to 60 $^{\circ}$C and heated one more time at the same rate to 240 $^{\circ}$C

### 4.2.4.2. Phase imaging

**Phase imaging of solvent-cast films**

In an attempt to investigate the different micro-phases present in polyurethane, AFM was used in intermittent contact mode as outlined in *Section 3.5.2.7*. The size of these phases could be used to inform mechanical behaviour of these polymers. An image that plots the phase difference between the drive frequency and the actual tapping frequency was obtained. These images indicate changes in surface properties and should be analysed in conjunction with the cantilever height as changes in height sometimes cause a shift in phase as outlined in *Section 3.5.2.3*. Both Z1A1 and Z6A1 solvent-cast films produced from 15 wt/wt % in DMF as outlined in *Section 3.3.3*. Results presented show both the topographical height image alone as well as the topographical height overlaid with phase difference.

**Z1A1**

*Figure 4.20* demonstrates a relatively large scale AFM image obtained from a Z1A1 solvent-cast film from 15 wt/wt % Z1A1 in DMF. When analysing such images it was important to take into consideration the height data in conjunction with phase data as edges usually show up as a difference in phase due to the change in topographical gradient. In Z1A1, 20 µm images only revealed a steep change in phase on the edges of features meaning they can easily be discarded as artefact.

Z1A1 – Height                    Z1A1 – Height with phase overlay
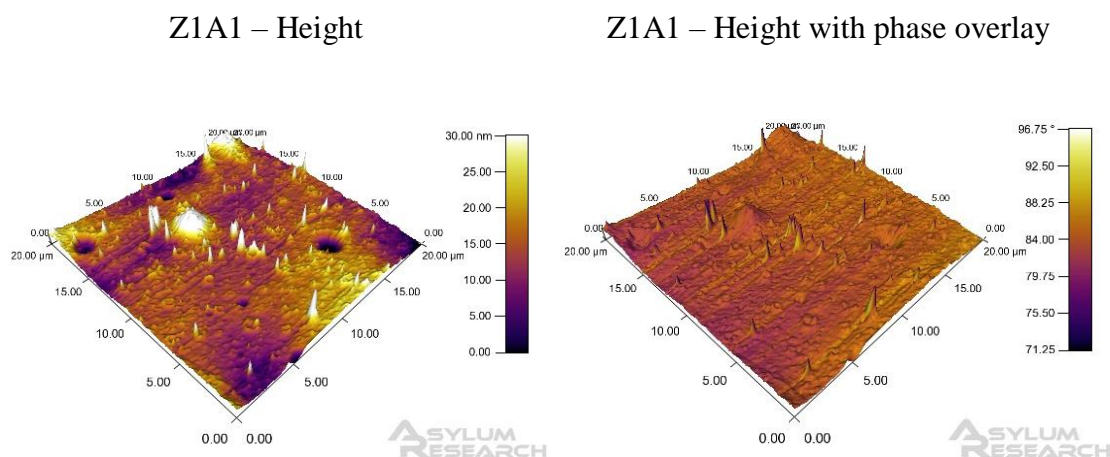


Figure 4.20 - Images obtained using AFM for both height and phase data from Z1A1 solvent-cast films. Both images were 20 µm x 20 µm.

In an attempt to investigate the different scales of surface topography, *Figure 4.21* represents images obtained from the same solvent-cast film at higher magnification. In 5 µm images shown in *Figure 4.21,* phase changes can be identified in phase only images but when phase was overlaid onto height data, it was apparent that phase changes correspond with edges in the topography.

Z1A1 – Height
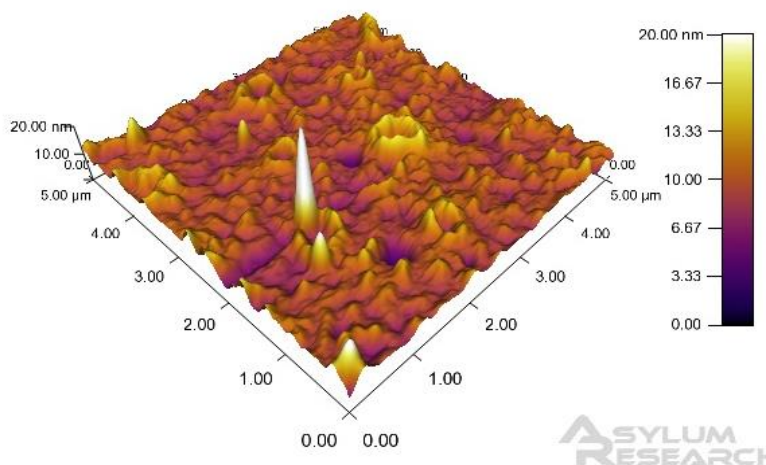


Z1A1 – Height with phase overlay
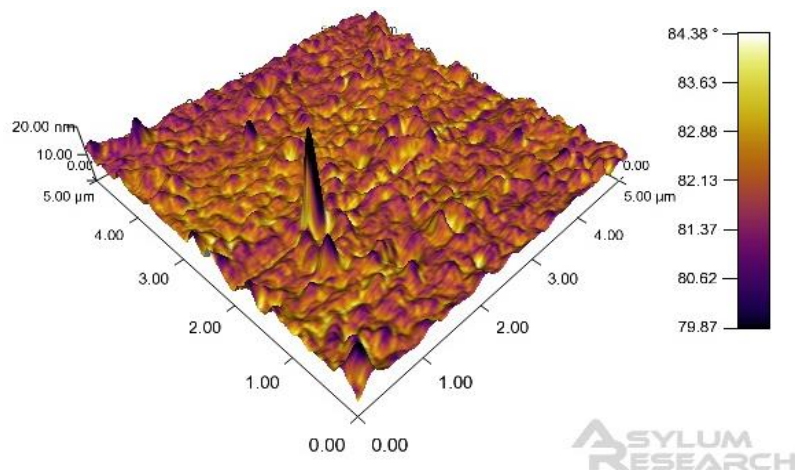


Figure 4.21 - Images at 5 µm x 5 µm obtained using AFM for both height and phase data from Z1A1 solvent-cast films produced from a solution of 15 wt/wt % Z1A1 in DMF.

Further images were obtained at 1 µm x 1 µm from the same Z1A1 solvent-cast film in intermittent contact mode and represented in *Figure 4.22*. Both images presented in *Figure 4.22* consisted of a topographical height image overlaid with a phase image. At this higher magnification, it was not completely clear that the phase changes observed are due to a change in surface gradient. 1 µm images reveal certain areas demonstrating a change in phase value while no clear change in surface gradient was observed.

Z1A1 – Height with phase overlay



Z1A1 – Height with phase overlay
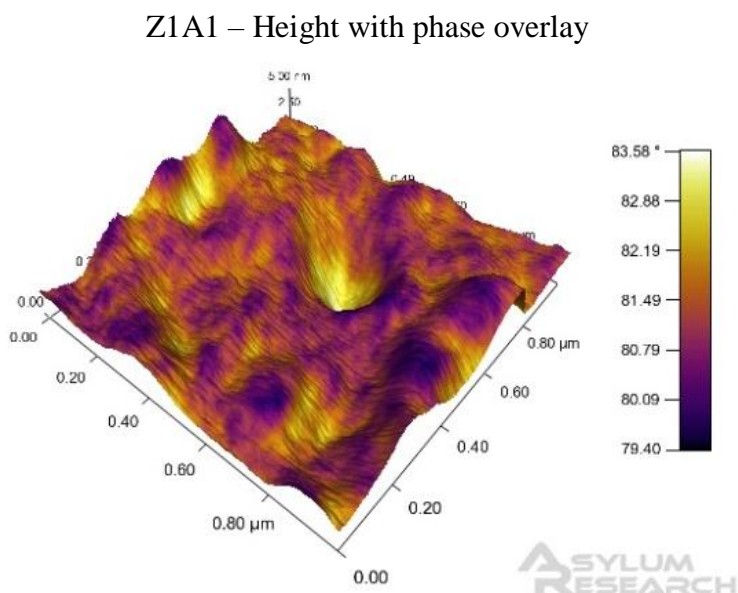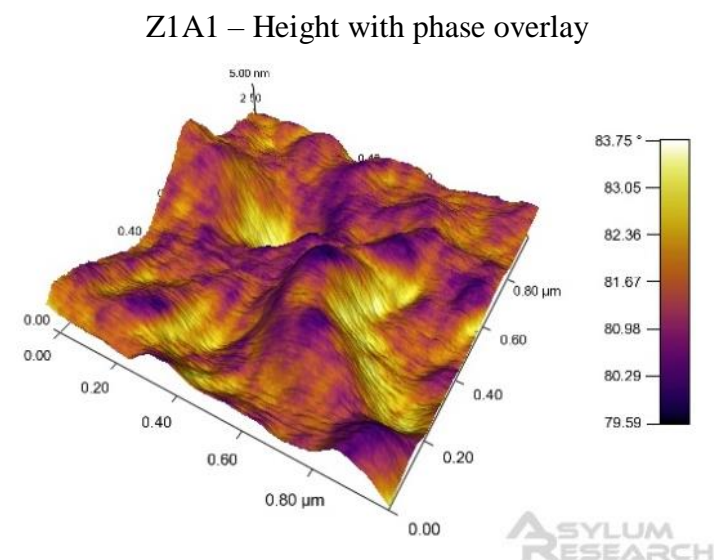


Figure 4.22 - Images at 1 µm x 1 µm obtained using AFM for phase data from Z1A1 solvent-cast films produced from a solution of 15 wt/wt % Z1A1 in DMF.

**Z6A1**

AFM phase images were also obtained from a solvent-cast film produced from a solution of 15 wt/wt % Z6A1 in DMF. *Figure 4.23* shows representative AFM images from both the air interface and glass interface of this solvent-cast film on a relatively large scale of 50 µm x 50 µm. Phase imaging in Z6A1 revealed no distinct difference in either the air interface or glass interface on the 50 µm scale. Changes in phase readings traversing the image in straight lines are caused by changes in phase while that specific line of the raster movement was being scanned and cannot be considered as a change in surface properties.

<table>
<tr><td align="center">Z6A1 – Height<br>(Glass interface)</td><td align="center">Z6A1 – Height with phase overlay<br>(Glass Interface)</td></tr>
</table>



<table>
<tr><td align="center">Z6A1 – Height<br>(Air interface)</td><td align="center">Z6A1 – Height with phase overlay<br>(Air Interface)</td></tr>
</table>
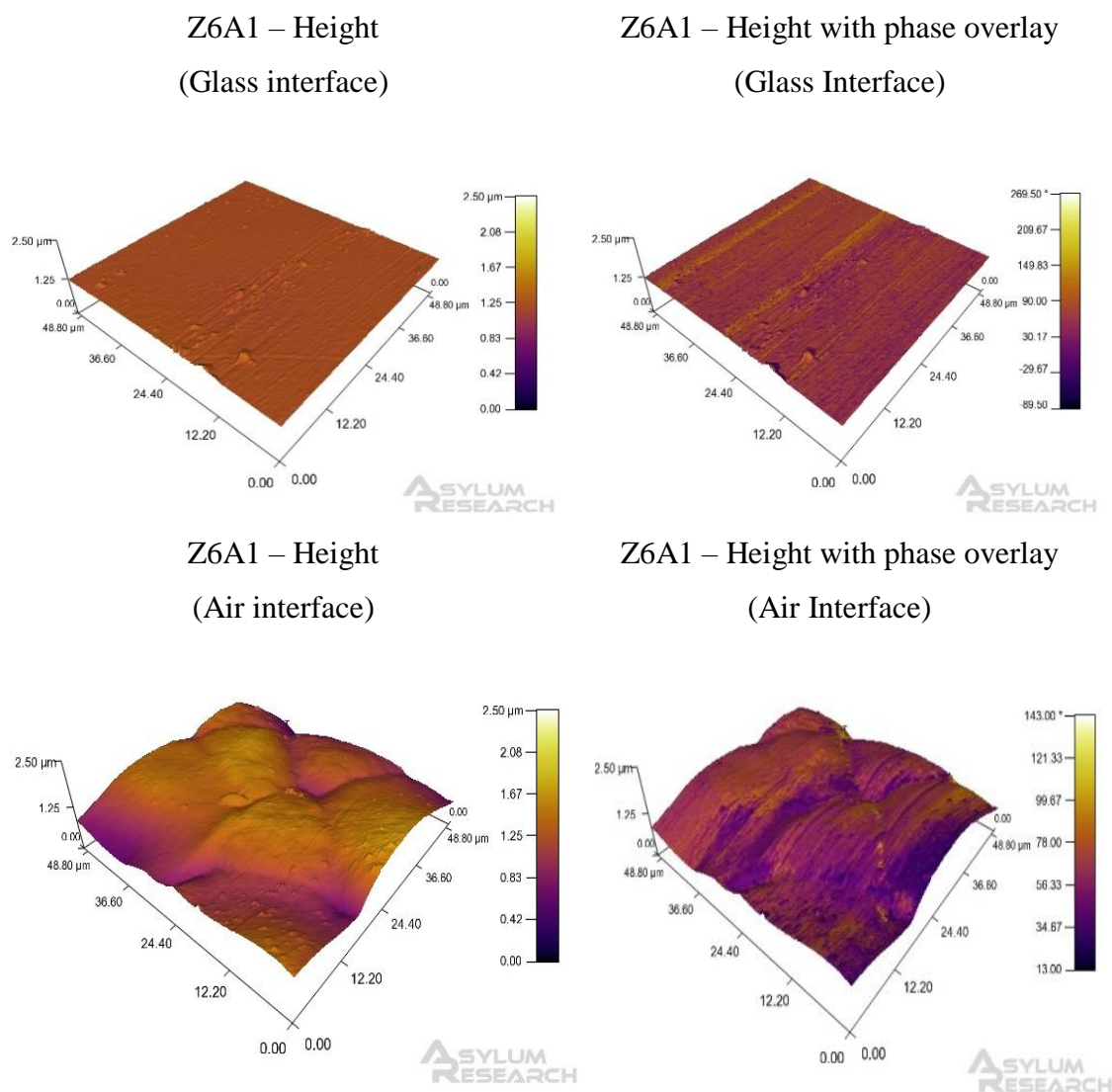


Figure 4.23 - AFM topography and phase images of Z6A1 solvent-cast films on both the glass and air interface. Each image was 50 µm x 50 µm.

AFM images were then obtained at smaller scales in an attempt to distinguish between the different chemical micro phases. *Figure 4.24* represents AFM phase images obtained at both 5 µm x 5 µm and 2 µm x 2 µm.

Z6A1 – Height with phase overlay
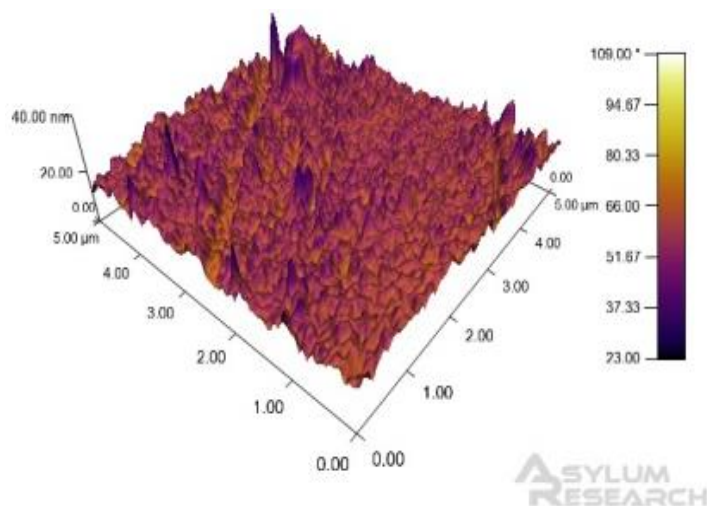


Z6A1 – Height with phase overlay
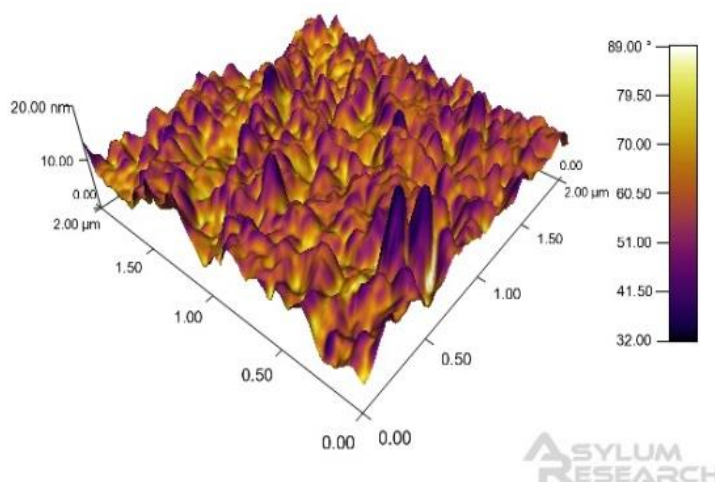


Figure 4.24 - AFM topography and phase images of Z6A1 solvent-cast films produced from a solution of 15 wt/wt % Z6A1 in DMF on the glass interface at 5 µm x 5 µm and 2 µm x 2 µm

Further images were obtained at 1 µm x 1 µm and 0.5 µm x 0.5 µm from the same Z6A1 solvent-cast film in intermittent contact mode and represented in *Figure 4.25*. Both images presented in *Figure 4.25* consisted of a topographical height image overlaid with a phase image. Images obtained from smaller areas, such as those in *Figure 4.24* and *Figure 4.25* demonstrated relationships similar to those observed in Z1A1; peaks had a lower phase, while troughs had a much higher phase value.

Z6A1 – Height with phase overlay



Z6A1 – Height with phase overlay
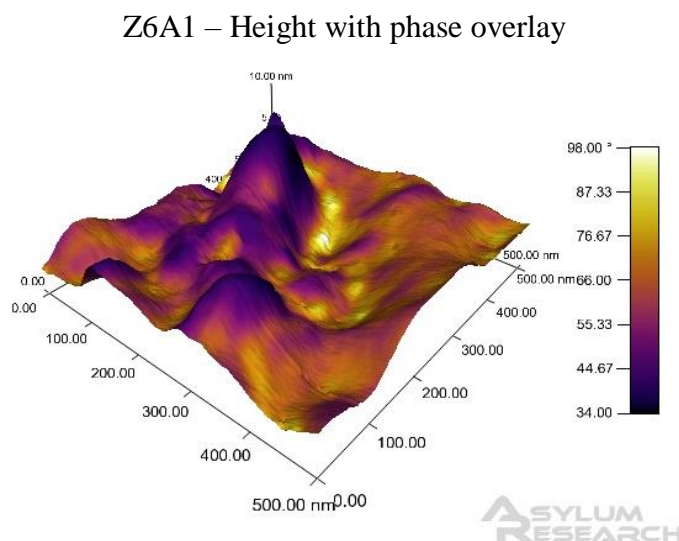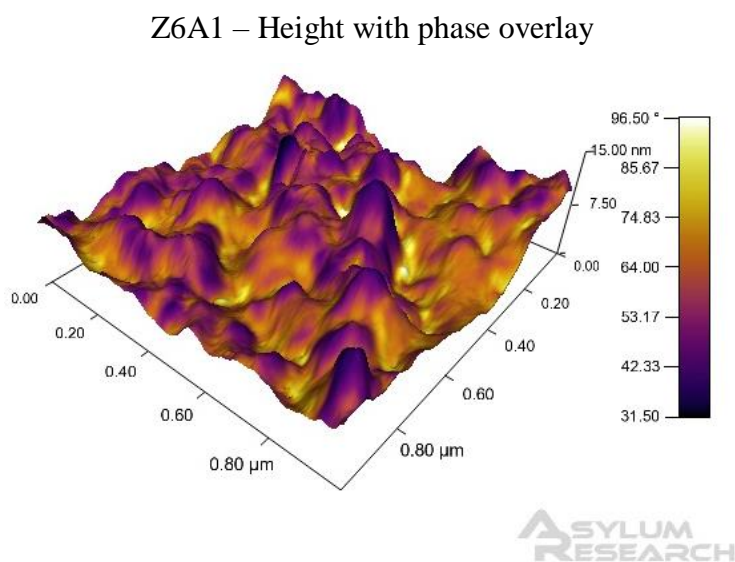


Figure 4.25 - AFM topography and phase images of Z6A1 solvent-cast films produced from a solution of 15 wt/wt % Z6A1 in DMF on the glass interface at 1 µm x 1 µm and 0.5 µm x 0.5 µm

**Phase imaging of electrospun mats**

AFM imaging was then carried out in intermittent contact mode on electrospun Z6A1 fibres as outlined in *Section 3.5.2.8*. This was performed to investigate whether the change in processing technique produced a change in resulting micro-structure. Images were obtained at various locations and at increasing magnifications. Representative images were shown below as height data only and height data overlaid with phase to facilitate interpretation as previously outlined.

a)    b)



c)
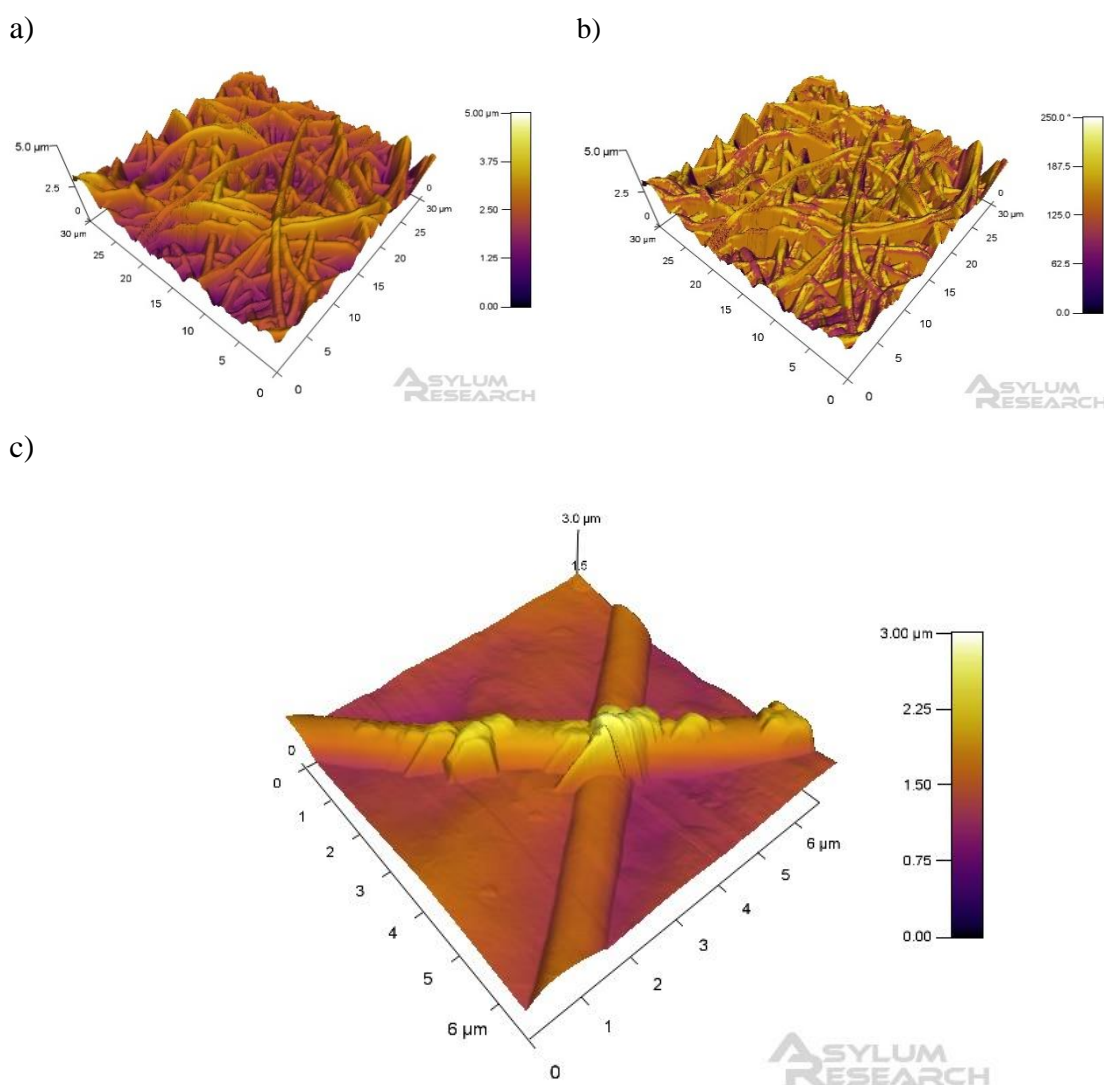


Figure 4.26 - Representative AFM images of electrospun Z6A1 film. a) 30 μm Height image, b) 30 μm Height image overlaid with phase, c) Image of two Z6A1 fibres intersecting on aluminium foil substrate

Figure 4.27 demonstrated representative AFM images of electrospun Z6A1 fibres. Images shown consisted of a height image overlaid by a phase image as previously described. Different magnifications are represented to demonstrate changes at different scales. *Figure 4.28* then shows images from a smaller scale to investigate the changes in phase observed in previous images.

a)
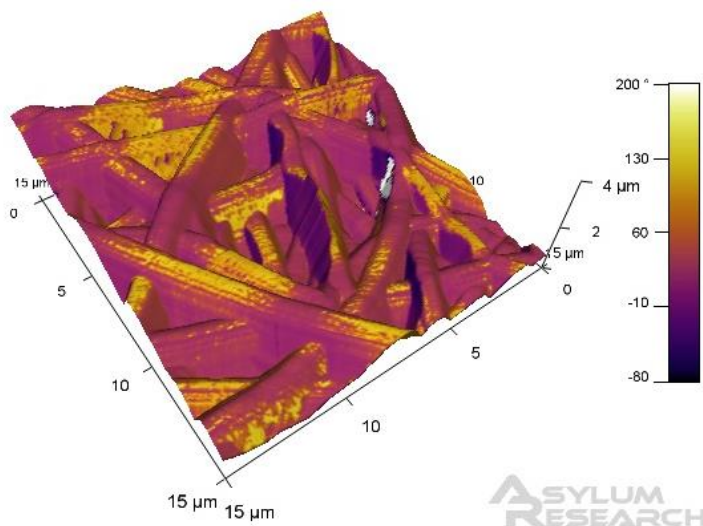


b)
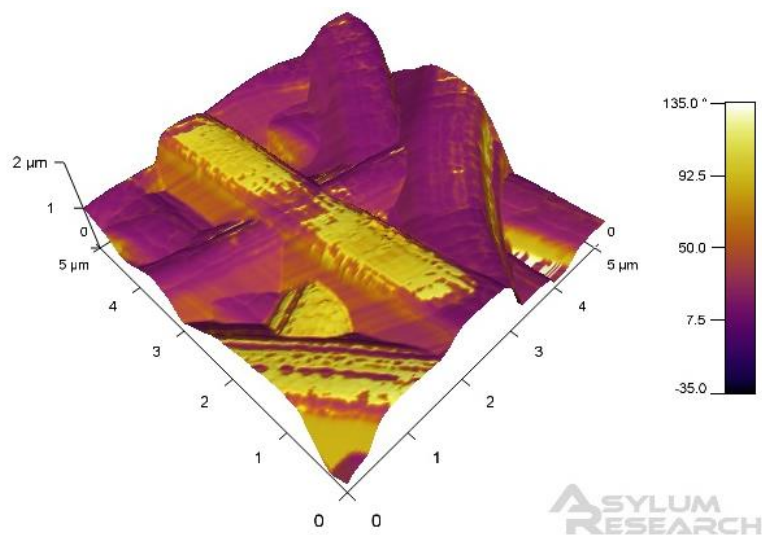


Figure 4.27 - Representative AFM height and phase images of electrospun Z6A1 fibres. a) 15 µm x 15 µm height image overlaid with phase, b) 5 µm x 5 µm height image overlaid with phase

Imaging of Z6A1 electrospun fibres using AFM in intermittent contact mode revealed areas with large changes in phase in *Figure 4.27a*. Some areas on the fibres demonstrated changes in phase that were not immediately apparent to be related to changes in topographical gradients. *Figure 4.27b* illustrates the same phenomenon in greater detail (i.e. at higher magnification) and changes in phase of up to $100^{o}$ were observed on the same fibre.

The changes in phase observed in *Figure 4.27* were further explored in *Figure 4.28* which shows similar scans at increasing magnification. *Figure 4.28a* and *Figure 4.28b* show height only images obtained over a 1.7 µm x1.7 µm area and a 250 nm x 250 nm area. These images reveal slight changes in topographical height across the fibre. To further investigate these changes, a cross-sectional plot demonstrating changes in topographical height was obtained and presented in *Figure 4.29* below. A 16 nm ridge was observed in topographical height with the remaining areas being topographically flat.

a)                                          b)
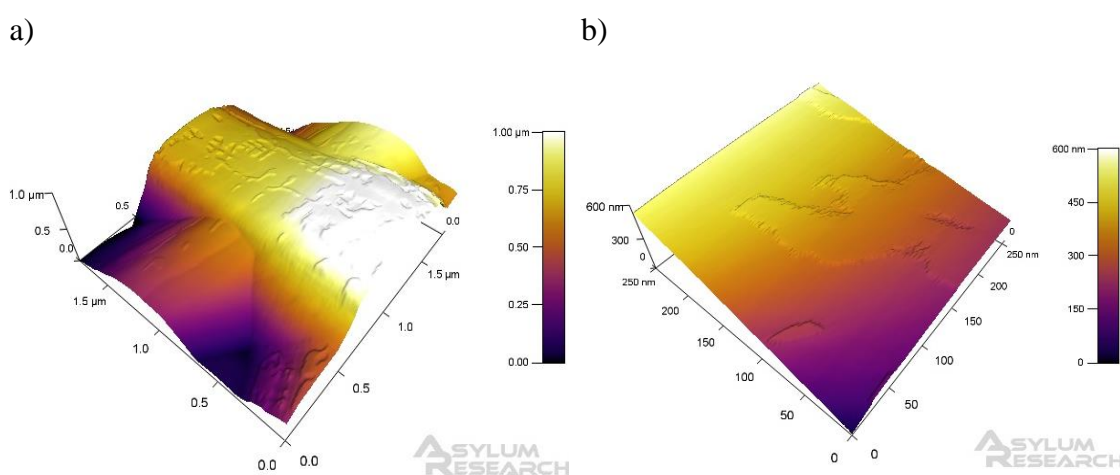


Figure 4.28 - Representative AFM height images of electrospun Z6A1 fibres. a)1.7 µm x  height image,  b) 0.25 µm height image

a)

b)
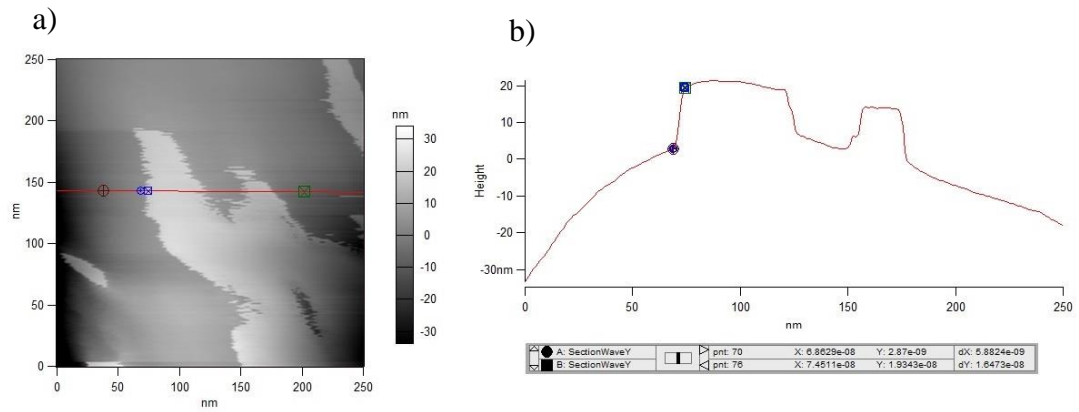


Figure 4.29 - a) 250 nm x 250 nm image of topographical height. b) A cross-sectional plot of changes in topographical height showing a ridge of about 16 nm

*Figure 4.30* then demonstrated the same locations presented in *Figure 4.28* with phase overlaid on topographical height. It was clear that topographically high areas were all linked to an increase in phase of up to 90$^{\circ}$.

a) b)
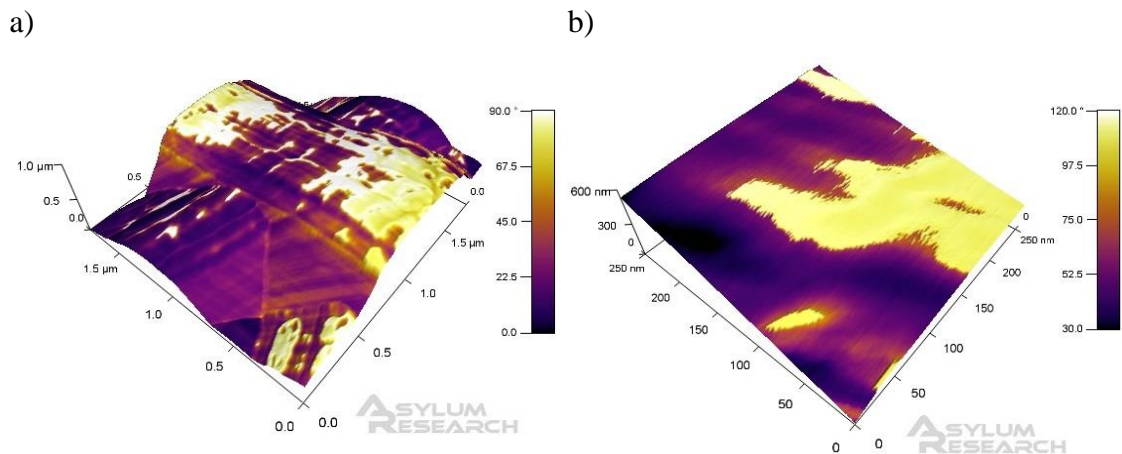


Figure 4.30 - Representative AFM height image overlaid with phase of electrospun Z6A1 fibres. a) 1.7 μm height image overlaid with phase, b) 0.25 μm height image overlaid with phase

An area that demonstrated high changes in phase was scanned twice with a different scanning angle to investigate whether changes in phase were produced by momentary cantilever artefacts. The two resulting images are shown in *Figure 4.31* below and demonstrated no clear differences.
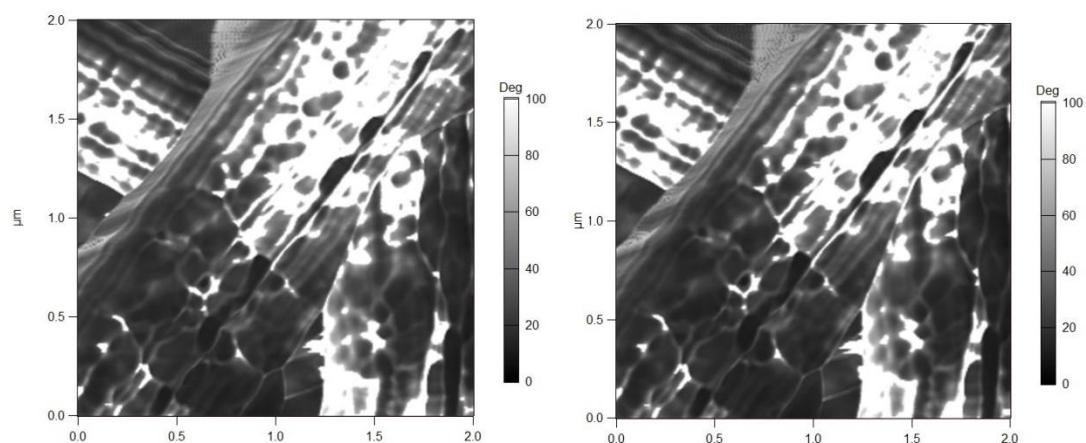


Figure 4.31 - Phase maps of repeated scan using similar imaging variables on Z6A1 electrospun fibres confirming observed phase changes are not caused by momentary artefacts. (2 µm x 2 µm)

## 4.3. Discussion

### 4.3.1. Mechanical characterisation of polyurethane grades

**Bulk tensile moduli of solvent-cast films**

Macro-mechanical moduli obtained from tensile testing of solvent-cast films on the *Bose Electroforce 3200* clearly indicate that the bulk mechanical properties of the various grades increase as the grade number increases as shown in *Figure 4.1*. The manufacturer provided nominal values of tensile moduli are shown in *Table 4.1*. These values were considerably different than those calculated in this experiment and this could be attributed to a number of reasons. The values provided by the manufacturer were calculated from tests of at least 50 % strain when compared to 5 % strain in our experiments. The rate of loading was also different and this may have substantial effect on the resulting tensile properties. A different thermal history of the samples being tested would have resulted in a change in the polymer

microstructure which could in turn also produce differences in tensile properties. The main observation made from this experiment was that even though the chemical intermediates were identical, by varying the ratio of soft to hard segment within each polymer grade, a vast difference in bulk tensile modulus was observed.

| Tensile Modulus (MPa) | Z1A1 | Z3A1 | Z6A1 |
|---|---|---|---|
| 50% elongation | 3.1 | 10.6 | 22.8 |
| 100% elongation | 3.9 | 13 | 23.5 |
| 200% elongation | 5.8 | 20.3 | 33.7 |
| 300% elongation | 10.9 | 32.7 | 56.5 |
| Ultimate Tensile Strength (MPa) | 39.6 | 46.7 | 57.0 |
| Ultimate Elongation % | 555 | 410 | 305 |

Table 4.1 - Mechanical characteristics provided by the polymer manufacturer

**Bulk tensile moduli of electrospun mats**

The width of each sample was measured with the aid of an upright microscope while the thickness of each film was estimated from scanning electron micrographs. Samples were cut using a sharp scalpel and mounted perpendicular to the electron beam in an attempt to obtain an accurate measurement of thickness. Even though this was successful, only a few areas were truly perpendicular to the electron beam and a measure for the thickness had to be obtained from estimation at these points.

Samples with fibre diameter distributions within the same range were loaded in tension using a *Bose Electroforce 3200* and a representative stress-strain curve was demonstrated in *Figure 4.2*. Loading curves obtained from tensile testing of Z1A1 demonstrated a purely elastic relationship and a modulus of 0.895 MPa ± 0.031 MPa (n = 6). When Z6A1 was loaded in tension a degree of viscoelasticity was observed even though the same strain was applied using the same loading rate. Since the individual fibres were stiffer in Z6A1, movement of fibres relative to each other was more predominant in Z6A1 films than in Z1A1 films. On unloading, this movement was delayed due to the effects of friction between fibres. This therefore creates the time-dependent response seen as viscoelasticity in loading curves obtained for Z6A1 electrospun mats. Full viscoelastic characterisation of such films was not performed

as this was beyond the scope of the current experiments. The toe region observed below 1% strain for Z6A1 in *Figure 4.2* was caused by alignment of the whole sample to the direction of strain rather than movement in the electrospun fibres themselves since the corresponding stress at this region is essentially zero. It is however important to note that Z6A1 films were much stiffer than Z1A1 films with a modulus of 77.129 MPa ± 5.142 MPa (n = 6). No obvious changes in the overall morphology of the electrospun mats at the scales investigated could be detected on close inspection of SEM micrographs represented in *Figure 4.3*. In a published research article by *Tetteh et al*, the mechanical properties of electrospun Z3A1 and Z9A1 mats were also investigated [239]. The authors conclude that the mechanical properties of these polymers are also dependant on the solvent system used to manufacture the electrospun mats. This was however attributed to the fact that when the solvent system used was altered, fibre morphology was completely different and uncontrolled for in their experiments. The reported fibre dimeters in this publication were 2.06 μm ± 3.09 μm in Z9A1 electrospun mats produced from DMF only and 1.25 μm ± 1.56 μm in Z3A1 electrospun mats produced from DMF only. The resulting moduli were 60.09 MPa ± 10.1 MPa for Z9A1 and 18.54 MPa ± 2.31 MPa for Z3A1. Comparing results between electrospun mats with completely different fibre morphology is not ideal as these would have different pore sizes, fibre density and consequently, different bulk mechanical properties. Even though an exact comparison was not possible, the moduli reported by Tetteh *et al.* were on the same range as those reported in these results.

**Indentation to a fixed depth**

The absolute values calculated from indentation were shown in *Figure 4.5* and were different to those obtained from the tensile testing in *Figure 4.1*. This can be attributed to the different loading method used leading to a change in the material volumes samples. Even though both set of results refer to an elastic modulus, since the loading method used was different, the absolute values should not be compared. This observation is universally accepted and has been reported in a number of publications [274 - 276]. This meant that relative values of stiffness were more representative than absolute values. *Table 4.2* shows ratios of moduli calculated from

both tensile testing and indentation. The final table shows the ratio of the previous two ratios and thus compares the relative values obtained from the two loading techniques. *Table 4.2* (c) demonstrates that the moduli of different polymer grades increase at nearly the same ratio in tensile testing and indentation testing for polymers between Z1A1 and Z4A1. In the case of Z6A1, the relative increase in modulus calculated in tensile testing was approximately twice that seen in the case of indentation.

a)

|  | MPa | Z1A1<br>16.7 | Z2A1<br>42.1 | Z3A1<br>81.7 | Z4A1<br>137.8 | Z6A1<br>340 |
|---|---|---|---|---|---|---|
| Z1A1 | 16.7 | 1.0 | 2.5 | 4.9 | 8.3 | 20.4 |
| Z2A1 | 42.1 |  | 1.0 | 1.9 | 3.3 | 8.1 |
| Z3A1 | 81.7 |  |  | 1.0 | 1.7 | 4.2 |
| Z4A1 | 137.8 |  |  |  | 1.0 | 2.5 |
| Z6A1 | 340 |  |  |  |  | 1.0 |

b)

|  | MPa | Z1A1<br>4.3 | Z2A1<br>9.8 | Z3A1<br>16.7 | Z4A1<br>29.4 | Z6A1<br>42.2 |
|---|---|---|---|---|---|---|
| Z1A1 | 4.3 | 1.0 | 2.3 | 3.9 | 6.8 | 9.8 |
| Z2A1 | 9.8 |  | 1.0 | 1.7 | 3.0 | 4.3 |
| Z3A1 | 16.7 |  |  | 1.0 | 1.8 | 2.5 |
| Z4A1 | 29.4 |  |  |  | 1.0 | 1.4 |
| Z6A1 | 42.2 |  |  |  |  | 1.0 |

c)

|  | Z1A1 | Z2A1 | Z3A1 | Z4A1 | Z6A1 |
|---|---|---|---|---|---|
| Z1A1 | 1.0 | 1.1 | 1.3 | 1.2 | 2.1 |
| Z2A1 |  | 1.0 | 1.1 | 1.1 | 1.9 |
| Z3A1 |  |  | 1.0 | 1.0 | 1.6 |
| Z4A1 |  |  |  | 1.0 | 1.7 |
| Z6A1 |  |  |  |  | 1.0 |

Table 4.2 - Table showing the relative measurements of moduli obtained from tensile testing and indentation testing. a) Ratios comparing moduli obtained from tensile testing, b) Ratios comparing moduli obtained from indentation testing, c) Table comparing the absolute values obtained from indentation to moduli obtained from tensile testing

**Nano-indentation to varying depths**

The relationship of indentation depth and modulus was examined by varying the depth of indentation and calculating the effective modulus according to the Oliver-Pharr model from the resulting force-indentation curves. *Figure 4.6* demonstrates multiple force curves performed to different indentation depths. The gradient of the retraction curve in indents performed to a larger depth appears to be increasing, indicating an increase in modulus. This is the opposite of what is reported in *Figure 4.7* with indentation moduli decreasing when indentation depths were increased. When calculations are made using the Oliver-Pharr method, the gradient of the retraction curve is not the only parameter affecting the resulting modulus as highlighted in *Section 3.7.1.1*. As the indentation depth is increased, the tip contact area is increased which is taken into consideration by the Oliver-Pharr method and leads to the resulting moduli calculated in *Figure 4.7*.

In *Figure 4.7* nano-indentation shallower than 500 nm demonstrated an increase in moduli measured for all the grades of polyurethane investigated. This phenomenon was explained by size effects and has been reported in *Section 2.2.3*. It is important to note that the apparent increase in elastic modulus with decreasing indentation is observed universally, and is a phenomenon related to the mode of loading rather than the material itself [69].

Similar to what was previously performed in *Table 4.2*, a table showing the ratios of indentation modulus between the different polymer grades at different indentation depths was populated in *Table 4.3*. *Figure 4.32* then plots these ratios on a graph for easier interpretation. An observation made from the calculations in *Figure 4.32* below was that the ratio of moduli observed in shallow indents was similar to the ratio observed in relatively deep indents where size effects do not play a substantial role. This indicates that even in shallower indents on the scale of a few nanometres, a change in intrinsic material modulus would still be observed.

| | Depth (μm) | 0.1 | 0.15 | 0.2 | 0.3 | 0.4 | 0.5 | 0.75 | 1 | 1.5 | 2 |
|---|---|---|---|---|---|---|---|---|---|---|---|---|
| Modulus (MPa) | Z1A1 | 74.7 | 53.2 | 38.5 | 23.9 | 18.3 | 15.3 | 10.4 | 8.3 | 5.9 | 5.1 |
| | Z3A1 | 158.0 | 104.0 | 80.6 | 63.2 | 50.4 | 41.0 | 32.9 | 25.9 | 17.6 | 15.8 |
| | Z6A1 | 390.8 | 230.6 | 186.4 | 130.8 | 107.0 | 92.2 | 71.7 | 60.8 | 46.2 | 37.6 |
| Ratio | Z1A1:Z3A1 | 2.1 | 2.0 | 2.1 | 2.6 | 2.8 | 2.7 | 3.2 | 3.1 | 3.0 | 3.1 |
| | Z1A1:Z6A1 | 5.2 | 4.3 | 4.8 | 5.5 | 5.8 | 6.0 | 6.9 | 7.4 | 7.8 | 7.4 |
| | Z3A1:Z6A1 | 2.5 | 2.2 | 2.3 | 2.1 | 2.1 | 2.3 | 2.2 | 2.4 | 2.6 | 2.4 |

Table 4.3 - Table showing the apparent modulus (mean values – n = 3) as a function of indentation depth for three different polymers along with the ratios of moduli between the different polyurethane grades.
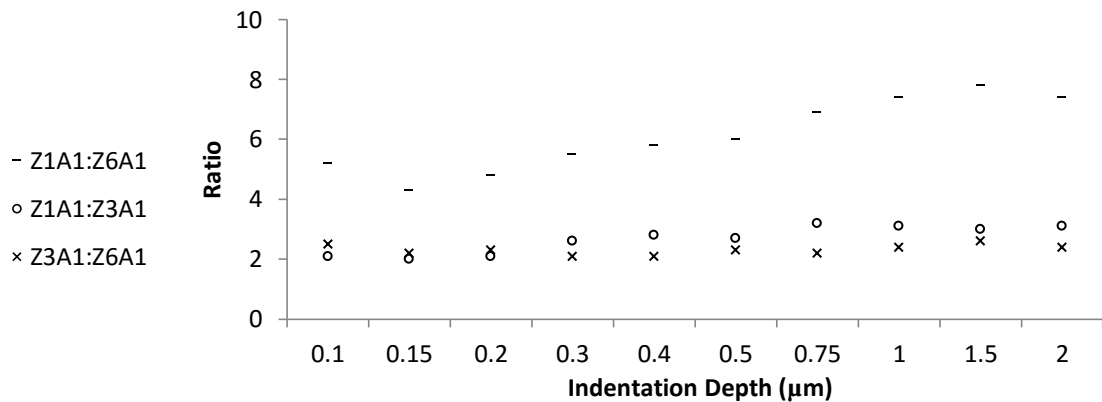


Figure 4.32 - Plot showing the changes in moduli ratios at various indentation depths from three grades of polyurethane.

Nano-indentation was then performed using an AFM cantilever to various depths between 30 nm and 300 nm on both Z6A1 and Z1A1 (*Figure 4.8*). The resulting nano-indentation data was similar to that obtained from the dedicated nano-indentation system with Oliver-Pharr being used to obtain the indentation modulus from each resulting curve. The main difference between the two systems was the scale on which they operate. The dedicated nano-indentation system has a maximum applied force of 4 mN over an indentation distance of 12 μm. When indenting using an AFM, the maximum forces that can be applied are determined by the mechanical and morphological properties of the cantilever used. Cantilevers with higher spring constants are able to apply a larger force when compared to softer

cantilevers but the latter are more sensitive when performing shallower indents or on softer tissue.

The main disadvantage of nano-indentation using AFM was that the geometry of the indentation tip cannot be accurately estimated as cantilevers are considered as disposable consumables and tip shapes may vary from the nominal shape defined by the supplier. Tips are also subject to wear during use in surface imaging which can change the contact area during indentation. This means that even if cantilevers are imaged using SEM before or after indentation, the reliability of the calculated tip shape would still be questionable. Since the estimation of contact area was important in Oliver-Pharr calculations, absolute values of moduli cannot be relied upon when indenting using AFM cantilever tips. The key advantage of AFM indentation was that indentation depths can be performed to a much smaller scale when compared to the dedicated indentation systems due to their increased sensitivity. At these smaller scales, the influence of size effects was highlighted with moduli increasing rapidly as indentation depths are reduced. Both the AFM and the dedicated indentation system were used to indent Z1A1 and Z6A1 at a range of 300 nm to 100 nm. Indentation moduli obtained from these two techniques cannot be directly compared but the ratio at which the moduli increase for each polymer at the range where both techniques were used can be investigated as shown in *Table 4.4*.

| | | Indentation Depth (nm) | | | |
|---|---|---|---|---|---|
| | | 100 | 150 | 200 | 300 |
| **Berkovich** | Z1A1 (MPa) | 74.7 | 53.2 | 38.5 | 23.9 |
| | Z6A1 (MPa) | 390.8 | 230.6 | 186.4 | 130.8 |
| **AFM** | Z1A1 (MPa) | 47 | 32 | 23 | 14 |
| | Z6A1 (MPa) | 1200 | 674 | 489 | 310 |

| | | | | | |
|---|---|---|---|---|---|
| **Berkovich / AFM** | Z1A1 | 1.6 | 1.7 | 1.7 | 1.7 |
| | Z6A1 | 0.3 | 0.3 | 0.4 | 0.4 |

Table 4.4 - Table showing mechanical properties calculated by nano-indentation using a Berkovich tip and an AFM tip and a table showing the ratios between the two sets of values.

The ratio of modulus calculated for AFM tip and Berkovich indentation appears to be constant since the ratio between the two values obtained at a specific depth was constant (1.7 for Z1A1 and 0.4 for Z6A1). Since nano-indentation using a dedicated Berkovich nano-indenter produces more reliable results, indentation moduli obtained by AFM can be shifted by the magnification factor described above to create a continuous curve with indentations ranging from 30 nm to 2 μm.

When moduli obtained at various indentation depths are plotted on a log-log graph, a linear relationship can be observed as shown in *Figure 4.33*. This indicates that the relationship between indentation modulus and indentation depth for the range that was investigated takes the form of $y = ax^k$ where *log a* was the y-intersect (on the *log y* - axis) and *k* was the gradient. These two equations also indicate that if the indentation depth was reduced further, the resulting modulus would still demonstrate an intrinsic difference between the two polymer grades.
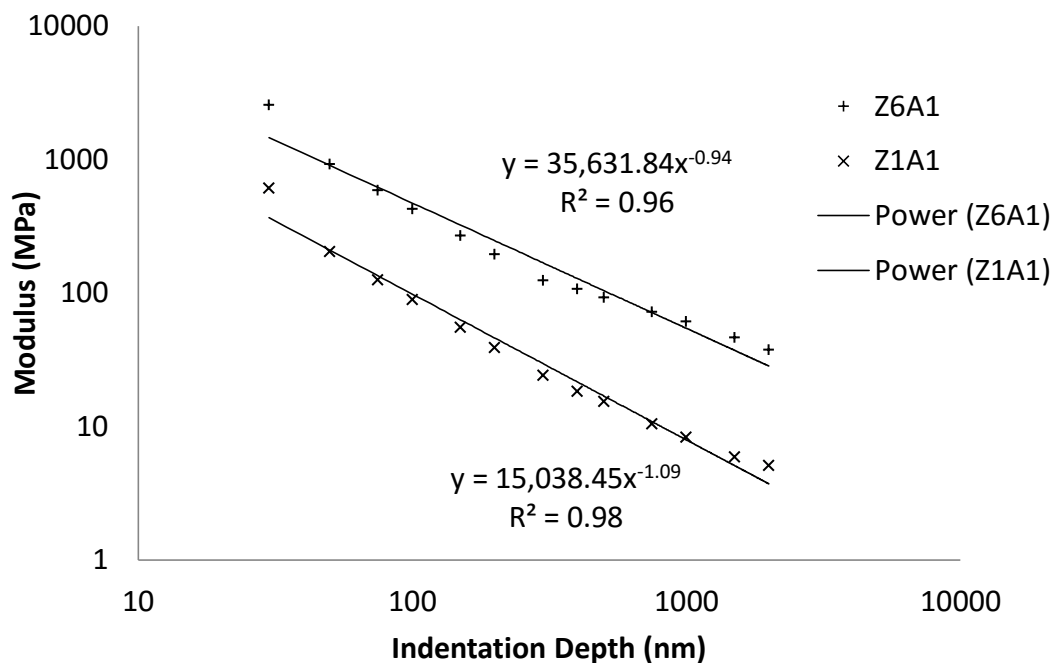


Figure 4.33 - Log-log graph of indentation depth plotted against modulus for both Z6A1 and Z1A1 demonstrating a logarithmic (power) relationship.

Another factor that has to be considered is the influence on surface roughness on these measurements. Even though nano-indentation was always carried out on the glass-interface, the radius of curvature of the indenter (AFM or dedicated indentation system) might have altered the area of contact depending on the roughness of the surface being investigated. In AFM, BL-TR400PG – L with a radius of curvature of 42 nm ± 12 nm cantilevers were used. This is considerably larger than the surface roughness (9.2 nm ± 4.8 nm RMS in *Figure 4.13*) and meant that these artefacts were not predominant in the results.

### 4.3.1.1. Nano-indentation of electrospun fibres

Nano-indentation of electrospun fibres could only be performed by AFM since it was not possible to scan the surface with the dedicated nano-indentation system. Using AFM, an image of the area of interest could be obtained and specific locations could be selected for nano-indentation. The resulting moduli from AFM nano-indentation show a clear distinction between the two polymers. The values obtained for Z6A1 however could not be directly compared to those obtained for Z1A1 as the indentation depth was much shallower in Z6A1. The cantilever being used to make the scan (*AC-160 TS*) was not stiff enough to indent Z6A1 to the same depth that Z1A1 was indented. Conversely, the cantilever was not sensitive enough to obtain a graph when Z1A1 was indented to the same depth as was allowed on Z6A1 fibres. As previously described by size effects, indents at a shallower depth will produce higher values of moduli meaning that comparing these two sets of data was not possible. However, since the same cantilever displacement was applied using the same cantilever resulting in a much deeper indent in Z1A1 than in Z6A1, it could easily be concluded that Z6A1 nano-fibres are still stiffer than Z1A1 nano-fibres. This meant that even though absolute values of nano-indentation are difficult to obtain, it was still possible to observe changes in nano-mechanical properties if the same cantilevers were used.

Finding a cantilever that has the stiffness needed to indent both polymers to a reasonable depth while having enough sensitivity to produce reliable values of moduli on both materials was challenging and as previously described, using

different cantilevers for different materials produces unreliable results. Since the same force was applied on both materials and this resulted in a different indentation depth, we could conclude that one material was stiffer than the other but the amount by which the stiffness varies could not be calculated reliably.

The cantilever used for intermittent mode imaging and nano-indentation of electrospun fibres *(AC 160TS)* had a nominal spring constant of 42 N/m and a length of 160 μm while the much softer cantilever used for contact mode scanning and solvent-cast film indentation *(BL-TR400PB – L)* had a nominal spring constant of 0.02 N/m and a length of 200 μm. The indentation depths produced by these two cantilevers when the same force was applied would therefore be on a different scale when indenting the same material. As explained and demonstrated in previous sections and by size effect theories, indentations at different depths cause a change in the resulting modulus. This meant that moduli generated by indenting materials by these two different cantilevers cannot be directly compared since the depth of indent produced was on a different range.

Another factor that has to be considered was the difference in nominal cantilever tip shape. The tip radius was very different in these two cantilevers with 9 nm ± 2 nm for *AC160TS* and 42 nm ± 12 nm for *BL-TR400PG – L* cantilevers. Polyurethane consists of a pseudo-crystalline structure with hard and soft segments. Indenting using a tip with a larger radius of curvature could mean that more crystals would have to be recruited and deformed by nano-indentation.

## 4.3.2. Influence of solvent system used

### 4.3.2.1. Effect of solvent system on roughness

On the macro scale, the glass interface was reflective and looked polished when seen with the naked eye. AFM topographical results in *Figure 4.12* demonstrated a clear difference between the air interface and glass interface for all solvent systems with the glass interfaces demonstrating much lower surface roughness. AFM images

shown in *Figure 4.11* demonstrated that this surface was being generally smooth with few imperfections caused by heterogeneities on the glass petri dish.

A marked difference between the air interfaces for all three solvent systems was also seen as shown in *Figure 4.12* with DMF leaving a rougher surface than DMAC. The solvent-cast film manufactured from 75% THF and 25% DMF formed numerous macro-scale imperfections on the surface unlike the other two cast films that were macroscopically flat. This solvent-cast film however, demonstrated the lowest micro-scale roughness with values comparable to those observed on the glass interface. It was hypothesised that rapid evaporation of THF left behind a viscous solution of polymer in a relatively small amount of DMF. Bubbles formed by the evaporation of DMF solidified before enough pressure was present to deflate them resulting in the surface observed.

Roughness measurements were calculated from two sets of different solvent-cast films that were manufactured consecutively using the same process parameters. The resulting solvent-cast films did not demonstrate substantial inter-sample differences and the standard deviation plotted in *Figure 4.12* rises from intra-sample variation. This standard deviation was larger in DMF solvent-cast films. Since features in these solvent-cast films are larger than those observed in solvent-cast films produced from DMAC or THF, it was difficult to obtain a representative average surface roughness without scanning a larger area. In such surfaces, at least 10 features should be visible to obtain an accurate measure of roughness. This could not be achieved in DMF solvent-cast films as the AFM system used in these experiments only allowed for 90 µm x 90 µm images. The purpose of this experiment was, however, still met since the main intention was to determine whether different solvents influence the resulting surface morphology.

A review of the literature confirms that little is known about the micrometre-sized structures observed on the solvent-cast films. Xu *et al*. hypothesise that the structures observed by atomic force microscopy originate with the nucleation of hard segment domains within the polyurethane solution [277]. These segments grow with time and

consist of both hard and soft segments. They emphasise that further work has to be done to better test their hypothesis as it could not be confirmed by the techniques they used. KoJoi *et al.* emphasise that the morphology of solvent-cast polyurethane films depends on the ratio of hard and soft segments as well as the preparation conditions [278]. Their results suggest that the structures seen under AFM are composed of a hard segment-rich phase in a matrix of a soft segment-rich phase. Another observation made in this journal was that in thin, 7 μm films, these structures are not observed even though they were prepared from the same solution. This observation was attributed to the fact that as the film thickness decreased, there was less space for the hard segment to crystallise and thus forming smaller features.

Even though a substantial difference in surface roughness was observed when a different solvent system was used, the relationship between these two variables is not discussed in literature. It was hypothesised that the difference in boiling point between DMF (153 $^{o}$C) and DMAC (163 $^{o}$C) might have varied the amount of time available for nucleation points to form before all the solvent was evaporated. This would have permitted more time for nucleation points to form in DMAC solvent-cast films and this resulting in more nano-features with a smaller size. Further work has to be performed to confirm this hypothesis. Solvents with different boiling points could be used in order to obtain a relationship between boiling point and surface roughness. Pyridine (boiling point 115.2 $^{o}$C), dimethyl sulfoxide (DMSO) (boiling point 189 $^{o}$C) and N-methyl-2-pyrrolidone (NMP) (boiling point 202 $^{o}$C) are all listed as solvents for polyurethane and could be used in such an experiment. These solvents were not used in the current experiments as DMF, DMAC and THF are the solvents that are most commonly used for electrospinning of polyurethane [204 - 208]. Since the aim of this experiment was to investigate whether the different solvents would produce a change in electrospun fibre morphology, investigating further solvents would have been beyond the scope of this experiment.

### 4.3.2.2. Effect of solvent system on indentation modulus

Nano-mechanical properties obtained by nano-indentation at different depths appeared to be unaltered when studies were carried out on either the glass interface

or the air interface as shown in *Figure 4.14*. Similarly when solvent-cast films produced from different solvents were tested, nano-mechanical properties appeared to be unchanged as shown in *Figure 4.13*. This indicates that the difference in surface topographies outlined in *Section 4.3.2.1* could not linked to a change in nano-mechanical properties on the scale being investigated. Even though the different solvents produced substantial changes in surface topography, AFM nano-indentation did not demonstrate any changes in indentation modulus. This therefore highlights the fact that this scale of the surface roughness did not influence the AFM cantilever contact area during nano-indentation calculations using the Oliver-Pharr method.

## 4.3.3. Influence of processing parameters on the resulting chemical microstructure

### 4.3.3.1. Differential scanning calorimetry

Thermoplastic polyurethane elastomers are linear multi-block copolymers containing two segments- a soft segment (SS) and a hard segment (HS) [166]. The HS domains act as a cross-linker to SS domains that in turn produce flexibility in the elastomer. The two segments are thermodynamically immiscible at low temperatures resulting in phase separation. This phase separation is usually incomplete resulting in a domain structure of soft segment-rich and hard segment-rich domains [167]. The mechanical and topographical properties of polyurethanes are therefore not only determined by the ratio of HS to SS. They are also influenced by the manufacturing conditions and thermal history as these have been shown to influence micro-phase structures [40, 166, 273, 279].

Using DSC, disordering of crystallites is observed as endothermic behaviour. Seymour *et al.* suggests that two endothermic peaks are characteristic to thermoplastic polyurethane and are termed as *Type I* and *Type II* endotherms. The low temperature endotherm *(Type I)* is caused by HS crystallites with relatively short order and therefore indicating a higher degree of phase mixing. *Type II* is caused by HS crystallites with long range order and therefore a higher degree of phase

separation [280]. *Table 4.5* summarises the two endotherms that are observed during melting of polyurethanes.

| Type | Endotherm | Indication |
|---|---|---|
| Type I | Lower temperature | More phase mixing |
| Type II | Higher temperature | More phase separation |

Table 4.5 - Summary of endotherms observed when polyurethanes are analysed using DSC.

An increased degree of phase mixing results in a decrease in the mobility of phases within the superstructure and therefore causes an increase in mechanical properties. This highlights the fact that in polyurethanes, the resulting mechanical properties are not only defined by the chemical composition but also rely heavily on the manufacturing process used. *Figure* 4.17 illustrates DSC thermograms obtained from various forms of Z6A1. The first endotherm (below 200 $^{\circ}$C) indicates to disordering of *Type I* crystals and the second (between 200 $^{\circ}$C and 230 $^{\circ}$C) indicates disordering of *Type II* crystals. The first two endotherms are termed as the multiple melting points of the material [167]. As outlined in *Table 4.5, Type I* crystals indicate a higher degree of phase mixing while *Type II* crystals indicate a higher degree of phase separation.

*Figure 4.15* and *Figure 4.16* demonstrated that the resulting microstructure was unaffected by the solvent system used to manufacture the solvent-cast films in both Z3A1 and Z6A1. Alternatively, as outlined in *Section 4.3.2.1*, the resulting surface morphology was affected by the solvent system used. However, DSC micrographs show no change in the degree of phase mixing or separation when a different solvent system was used to manufacture these films. This indicated that the differences in surface morphology were not caused by a change in the micro-structure and in turn indicated that mechanical testing of these films would produce similar results. This also echoed results outlined in *Section 4.3.2.2* where no change in the nano-mechanical properties were observed when solvent-cast films produced from different solvents were investigated. The lack of a relationship between surface

topography and micro-domain structure indicates that the actual micro-domain size was much smaller than the features observed and refutes the hypothesis claimed by KoJoi *et al*. who hypothesise that each peak observed was a hard segment-rich area while all troughs are soft segment-rich areas [278].

Frick *et al.* reported that when no endothermal peaks are observed, the crystallisation in the material is very low and consequently, the material is relatively soft [166]. Similarly, Z1A1 was shown to behave as an amorphous thermoplastic in melt-processed, solvent-cast and electrospun form in *Figure 4.18* as no endothermal peaks could be observed at the melting temperature of polyurethane indicating no dissolution of HS crystallites.

When comparing different forms of Z6A1 in *Figure* 4.17, clear differences could be observed at the multiple melting temperatures of the polymers investigated. In melt-processed polymer samples provided by the manufacturer, two endothermal peaks of approximately equal size were seen for *Type I* and *Type II* HS crystallites indicating an equal distribution. Solvent-cast films demonstrated a larger *Type I* endotherm indicating increased HS phase mixing. On the other hand, electrospun samples demonstrated a larger *Type II* endotherm indicating that these samples comprised of a higher degree of phase separation. Even though the initial solutions used different polymer concentrations, it has been previously shown that a change in the solvent system does not result in a change in the degree of phase mixing signifying that this phenomenon can therefore only be attributed to the processing parameters. This could indicate that when the polymer was in solution, the two segments of the polyurethane are immiscible and the rapid evaporation of solvent from solution created by electrospinning does not allow enough time for phase mixing to occur. This would result in a decrease in modulus in electrospun fibres when compared to solvent-cast films if the same morphology was used.

A Z6A1 solvent-cast film was heated up to 250 $^{o}$C using the DSC, cooled down to 40 $^{o}$C and reheated in order to observe any changes in phase separation. The resulting thermographs were plotted in *Figure 4.19* and the endotherms observed on reheating

of the solvent-cast film were different to the initial heating. This highlighted once again that the microstructure was highly dependent on the thermal history. An increase in phase mixing would result in an increase in bulk mechanical properties of the final substrate and confirms that the substrate mechanical properties are dependent on the polymer chemistry as well as the manufacturing conditions. This observation was also made by Pompe *et al*. who investigated the effects on the resulting microstructure by varying the processing temperature [273]. They demonstrate that by varying the processing temperature, the resulting micro-phase separation was altered and consequently, a change in tensile strength of up to 18% was reported.

### 4.3.3.2. AFM phase imaging

Phase imaging was used in a number of publications to identify between hard and soft materials with the same sample. McLean *et al.* demonstrate the ability of identifying differences in hard and soft segments using AFM phase imaging. They demonstrate hard segment crystals of 5-10 nm in width with phase difference of $50^o$ between hard and soft segment areas [255]. Phase imaging was used to investigate whether the different micro-phases of hard and soft segment could be identified in the *Biomer b₉* polyurethane range. The size of these micro-domains could inform mechanical behaviour of these polymers.

Results from both Z1A1 and Z6A1 solvent-cast films did not demonstrate any clear indication of phase separation at any magnification and were open to interpretation. The phase difference in images presented in *Figure 4.21* and *Figure 4.22* was of about $5^o$ which is much less than what was reported by McLean *et al.* ($30^o$) [255]. The spindle-like patterns reported by these authors were also not observed in the results reported here. These differences might be attributed to the different chemical make-up of the polymers investigated. Polyurethanes can be fabricated from a wide range of chemical intermediates as outlined in *Table 3.1* and these will inevitably alter the resulting crystalline structure.

In Z6A1 solvent-cast films, while a superstructure with features of about 25 μm were observed in *Figure 4.23*, these structures themselves had a nano-structure with

features of about 100 nm in size revealed in *Figure 4.24*. In Z1A1, even though no superstructure was observed, a micro-structure with features of about 200 nm was observed in *Figure 4.22*. Albeit, these micro-structures still did not correspond to HS or SS rich phases. The final image presented in *Figure 4.25* was a 500 nm x 500 nm image with phase data overlaid on topographical data. Unlike observations made in Z1A1, phase differences of up to $60^o$ were observed on Z6A1 films in *Figure 4.25*. However, these large changes in phase were still linked to a change in topographical height. This therefore meant that it was difficult to conclude with certainty that the changes in AFM phase were caused by changes in the chemical micro-phases.

### 4.3.3.3. Phase imaging of electrospun fibres

AFM imaging in intermittent contact mode on electrospun Z6A1 fibres revealed topographically high ridges linked to a change in phase of up to $90^o$. It was difficult to explain with certainty why this change in phase occurred only on these topographically high areas of the fibres and not others. Repeating the scan under the same conditions and settings as shown in *Figure 4.31* confirmed the consistency of this observation and gives confidence that the observation was genuine and not momentary artefact. A possible argument could be that topographically high areas represented HS rich areas causing a shift in phase. It is however difficult to clarify why these segments would only show up on certain locations and not in others. Another argument is that high phase was only observed in suspended fibres that were free to vibrate during imaging and could be backed up by *Figure 4.27b* in which phase seems to be lowered when two fibres overlap. This would however ignore the observations made in which the change in phase was directly linked to change in topographical height. A further possible hypothesis was that in suspended fibres, these changes in topographical height are more pronounced making this change in phase more apparent. It was clear that two different phases are present on the surface of electrospun fibres. The presence of each different phase appears to be random and not homogenous throughout the electrospun surface. AFM phase imaging alone was however, not sufficient to accurately identify the source of the two different phases. Heterogeneities were observed in surface morphologies between different fibres on the same film and at different locations on the same fibre (*Figure 4.29c*). These

heterogeneities were caused by minute changes during the electrospinning process. Such changes caused by momentary fluctuations in the voltage field or whipping of fibres could not be accounted for during the electrospinning process. However, these changes contribute to the random nature of the process and attempting to control them would not be possible without completely altering the manufacturing technique.

## 4.4. Conclusions

The range of polymers made available by *Biomer Technology Limited* has been investigated on the macro – nano scale to investigate the influence of a number of processing parameters on the resulting specimens. Bulk, micro and nano-mechanical investigation of the various grades of polyurethane demonstrated that intrinsic differences in mechanical properties were maintained across all the scales. Since different modes of loading were investigated at different scales and using different equipment, absolute values of moduli could not be directly compared. Relative measurements of moduli, however, demonstrated that intrinsic mechanical properties were maintained down to the nano-scale.

Indentation size effects appeared to be predominant on the scale at which cells mechano-sense and effective moduli increased exponentially as indentation depths were decreased. The polymers investigated maintained a substantial difference in bulk and nano-mechanical properties when processed by electrospinning. Both bulk tensile testing and nano-indentation techniques demonstrated a difference in the mechanical properties of different polyurethane grades.

It was shown that processing parameters, such as the solvent system used, have a substantial influence on the resulting surface topography at the air-interface. Differences in topography were clear from AFM images and have been confirmed by surface roughness measurements. The changes on the glass-interface were however less substantial with near smooth surfaces being reported. Nano-mechanical properties and the chemical micro-phase structure appeared to be unaffected by the solvent system used.

The chemical micro-phase structure was then shown to be considerably different when comparing melt-processed, solvent-cast and electrospun form. This confirmed that surface properties of polyurethane films are not only dependent on the chemical make-up but also on the material processing technique as observed in previous publications [273]. DSC also demonstrated a difference between the two polymer grades with Z1A1 remaining amorphous even when electrospun. A major difference observed was in Z6A1 electrospun fibres that demonstrated an increase in phase mixing when compared to both solvent-cast films and melt-processed polymer. This increase in phase mixing has implications not only on the chemical structure of the resulting fibres but also on the resulting mechanical properties. Using AFM phase imaging alone, it was not possible to distinguish with confidence between HS rich and SS rich areas on either electrospun or solvent-cast form.

# Chapter 5

# Electrospun Mats with Heterogeneous Nano-mechanical Properties

## 5.1. Background

**Size-dependent mechanical properties of single nanofibers**

Nano-mechanical properties of electrospun fibres are dependent on a number of factors including fibre diameter and mode of loading as outlined in *Section.2.2.3*. Size effect theories indicate that a phenomenon is observed when three-point bending is performed on nano-meter sized rods. This theory indicates that an increase in modulus would be observed when fibres of lower fibre diameter are loaded in three-point bending [69].

In order to determine the nano-mechanical properties of individual fibres, three-point bending by atomic force microscopy is commonly used. Nanofibres are manufactured directly onto a stiff substrate that incorporates pores or trenches of a determined size as shown in *Figure 5.1*. An AFM is then used to image the substrate and determine fibre diameter, gap distance as well as locate the centre of the fibre. The same tip is then used to apply a force midway along the length of the suspended nanofiber. A graph showing the force applied over a set displacement is obtained from the AFM and Euler's theorem is used to derive the elastic modulus of each fibre. One of the assumptions made by this approach is that the fibre being loaded experiences no surface indentation meaning that, unlike nano-indentation, tip geometry has little importance on the resulting data obtained.
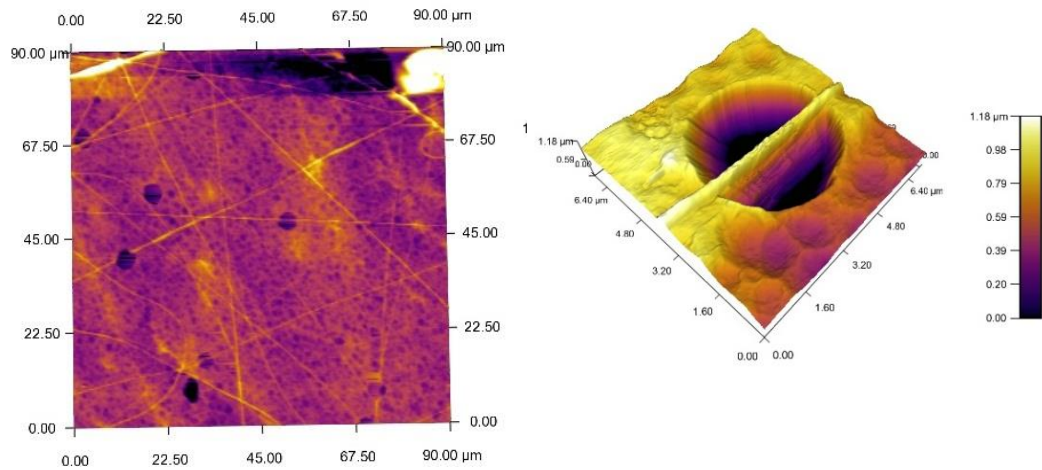
Figure 5.1 - AFM image of fibres over a substrate with pores of a specific diameter (left). Fibre suspended over a pore (right) [287]

A number of studies that characterise the mechanical properties of single nanofibres have been published. The majority of these studies originated from material science groups and have been carried out on ceramic and metallic materials such as Ag [281], $SiO_2$ [282] and $TiO_2$ [283] for use in high-strength, low-density composite materials and in various other applications. Studies have also been published that used the same technique to investigate polymeric materials such as polypyrol [284], poly-L-lactide (PLLA) [285], poly 2-acrylamido-2-methyl-1-propanesulfonic acid (PAMPS) [286] and poly(vinyl acetate) (PVA) [65]. The major observation presented in published research was that the calculated modulus varied significantly with fibre diameter. These studies have all indicated that size effects are present and moduli of single nanofibres increase exponentially with a decrease in fibre diameter. Fu *et al.* [65] investigated PVA nanofibres and reported an increase of fibre modulus from 50 GPa for fibre diameters of 160 nm to 500 GPa for diameters of 20 nm as shown in *Figure 5.2*. In their study on electroactive polymeric nanofibres, Min *et al.* describe an increase in fibre modulus from 0.2 GPa in fibres of 110 nm in diameter to 2.0 GPa when fibres had an mean of 55 nm as shown in [286]. Cuenot *et al*. report similar observations on polypyrrole nanotubes *Figure* 5.3 [284]. They further confirm the observed increase in modulus by plotting the calculated moduli against the geometric function of the individual measurements.
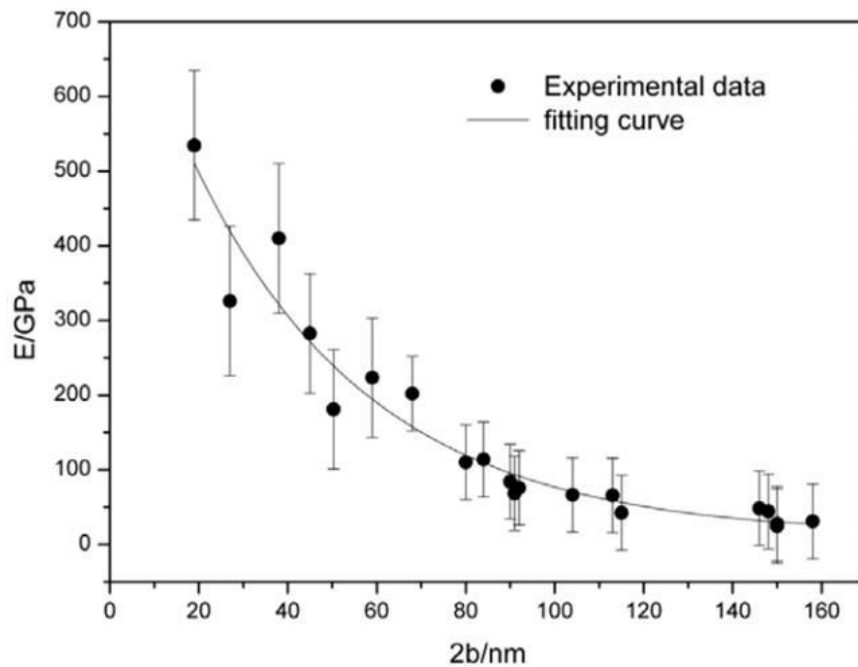
Figure 5.2 - Graph of Young's modulus as a function of diameter in PVA nanofibres from a paper by *Fu et. al.* [65]
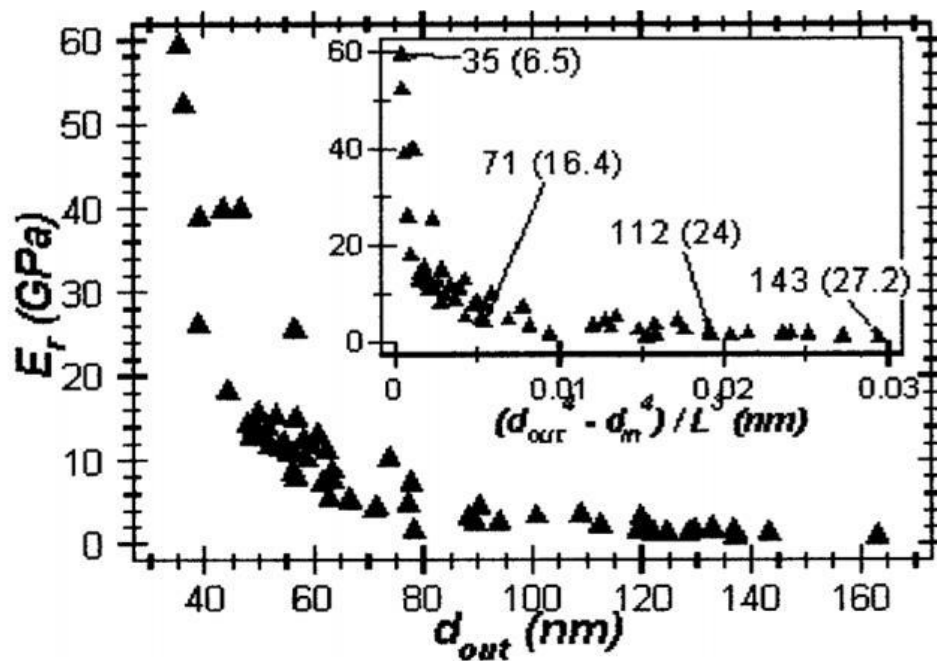


Figure 5.3 - Graph of reduced elastic modulus as a function of fibre diameter in polypyrrole nanotubes. The inset presents the modulus against a geometrical function of the nanotube and pore system with corresponding diameters and thicknesses between parentheses. [284]

**Size-dependent mechanical properties of single polyurethane nanofibers**

In a previous study performed as part of the author's MSc project, the size-dependent mechanical properties of single *Biomer Technology Limited b₉* polyurethane nanofibres when loaded in three-point-bending were investigated [287]. Electrospun fibres of Z1A1 and Z3A1 with a range of fibre diameters were suspended over pores of a fixed diameter and loaded in three-point-bending using atomic force microscopy. The mid-point of suspended fibres was located and a force of 4 nN was applied. This scale of loading was chosen as cells have been shown to apply forces on the same scale and would thus be a more effective representation of cell movement [138]. The findings of that study clearly indicated a steep increase in the calculated moduli with a decrease in fibre diameter. Results shown in *Figure 5.4* and *Figure 5.5* corroborated with observations made by various authors on different materials and were in-line with size effect theory. This meant that scaffolds manufactured from the same material with a different fibre diameter distribution would have similar bulk mechanical properties but different nano-mechanical properties. It was therefore important to take these nano-mechanical properties into consideration since cells interact with scaffolds on the nano - micro scale. The implications that these changes in nano-mechanical properties observed in fibrous scaffolds have on cell growth and differentiation had not been previously investigated.
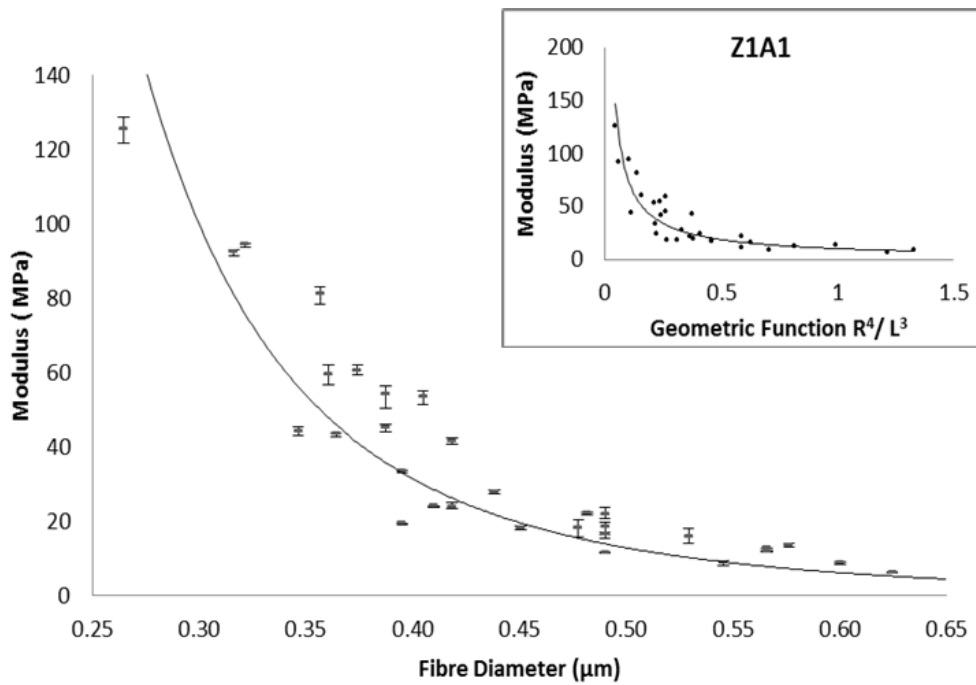
Figure 5.4 - Graph showing the moduli calculated for a given fibre diameter in Z1A1. Inset: Graph of moduli of Z1A1 plotted against the geometric function. [287]
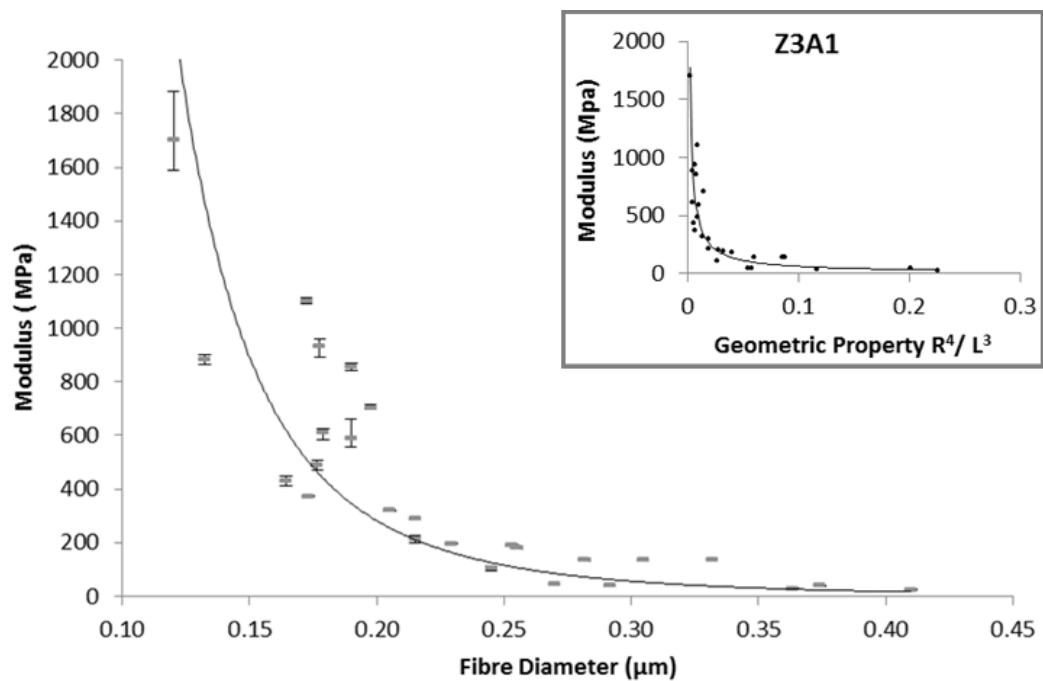


Figure 5.5 - Graph showing the moduli calculated for a given fibre diameter in Z3A1. Inset: Graph of moduli of Z3A1 plotted against the geometric function. [287]

Nano-mechanical cues sensed by cells on a fibrous scaffold depend on a number of parameters. A decrease in fibre diameter has been shown to result in an increase in the apparent modulus when the fibre is loaded in three-point bending [69]. In a randomly aligned fibrous mesh, fibres are connected randomly and tensile strain on one fibre might in turn cause three-point loading on another fibre. This means that altering fibre diameter distributions within the mesh will inevitably alter the nano-mechanical properties of the resulting scaffold.

The aim of work reported in this *Chapter* was to manufacture electrospun mats with diverse nano-mechanical properties from the range of polyurethanes available. The manufacture of such scaffolds could be used in the investigation of the influence of nano-mechanical properties on cell mechanotransduction. The grades of polyurethanes made available by *Biomer Technology Ltd.* were composed of the same chemical intermediates but comprised different intrinsic mechanical properties. Initially, electrospun mats composed of the same polymer but presenting a different fibre diameter distribution were manufactured. Such changes in fibre diameter distribution would cause a shift in the nano-mechanical properties of the resulting scaffolds while maintaining the same polymer makeup. Subsequently, two electrospun mats were fabricated from a different polyurethane grade but manufactured to a similar fibre diameter distribution. Once again, such fibrous mats would have different nano-mechanical properties while maintaining similar morphology and chemical cues. The final aim of the work reported in this *Chapter* was to fabricate an electrospun mat consisting of both Z1A1 and Z6A1 fibres with the same fibre diameter distribution. This would result in a single fibrous mat having a bi-modal range of nano-mechanical properties.

## 5.2. Results

### 5.2.1. Electrospinning of Z1A1

A number of electrospinning defects were initially observed as shown in *Figure 5.6*. Electrospinning parameters had to be optimised to the parameters stipulated in *Section 3.4.5* in an iterative process to obtain defect-free scaffolds.

a)

b)

c)

d)
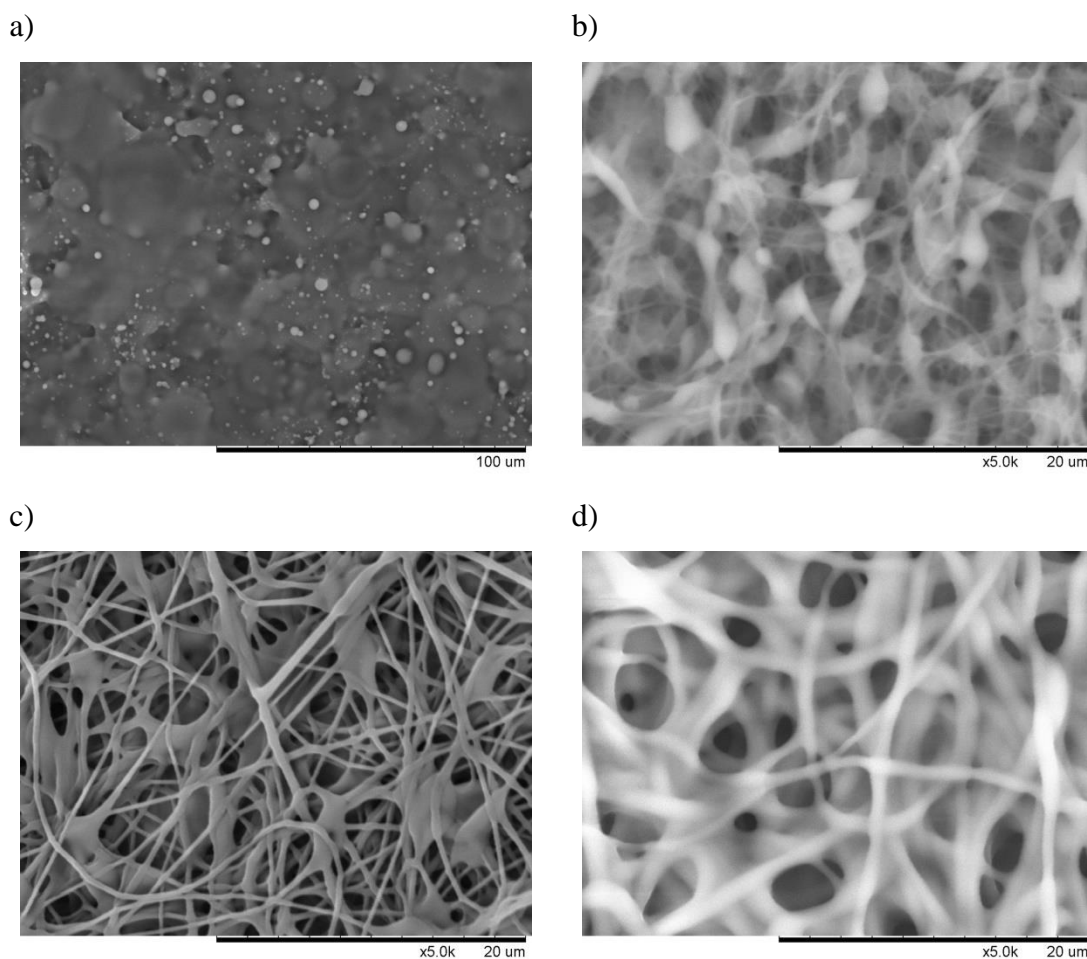


Figure 5.6 - SEM micrographs demonstrating various electrospinning defects. a) electro-spraying, b) bead defects, c) and d) wet fibres in which solvent was not completely evolved before reaching the collector

Five discrete samples were manufactured consecutively under similar conditions outlined in *Table 3.2 (b)* to investigate the reproducibility of the electrospinning setup. Images were then obtained using SEM at various magnifications as shown in *Figure 5.7* below. Images at x180 and x1,000 were used to evaluate the homogeneity of each sample while images at x5,000 and x10,000 were used to measure the fibre diameter distribution from the samples produced. Only a few defects were observed at the different magnifications.

a)

b)



c)

d)
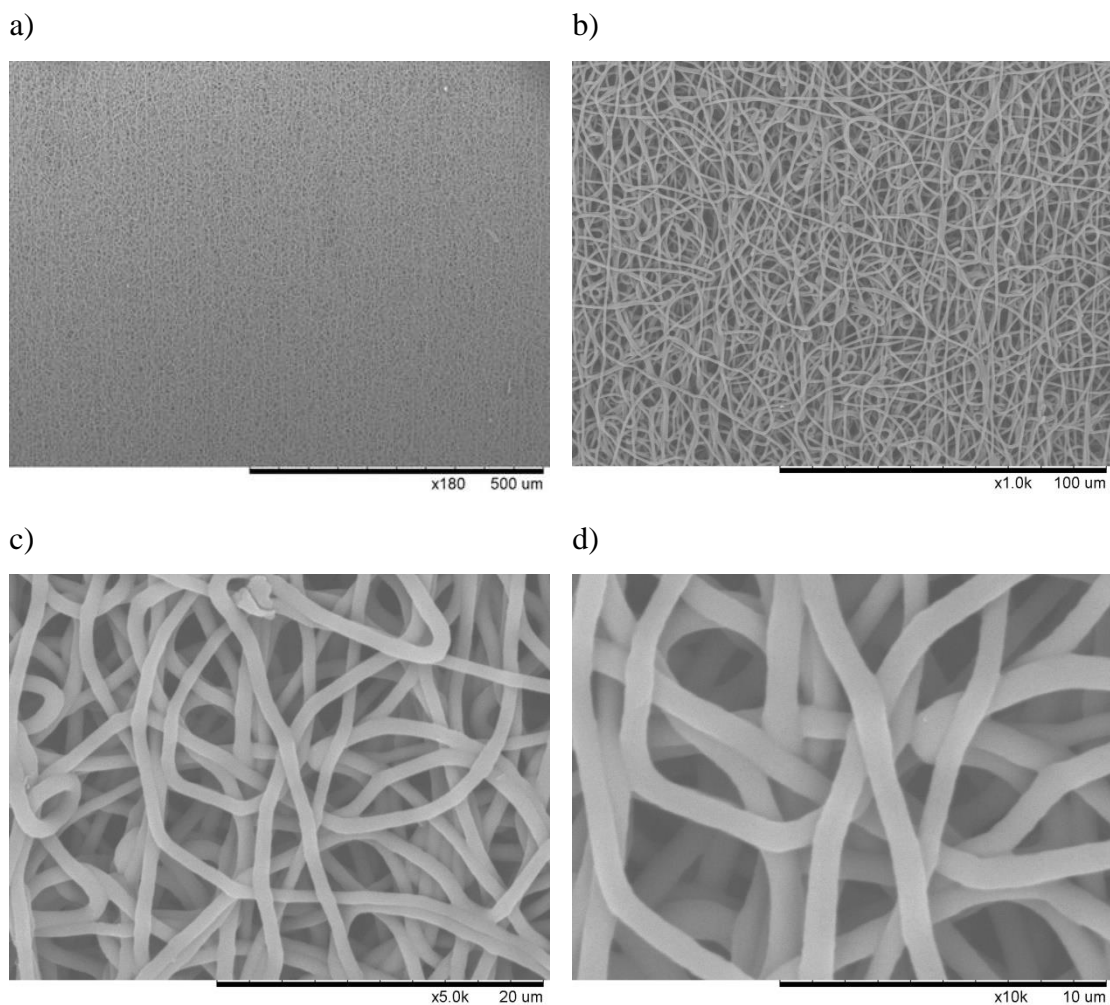


Figure 5.7 - Various SEM micrographs obtained at various magnifications on the same Z1A1 electrospun mat. x180 (a), x1,000 (b), x5,000 (c), x10,000 (d).

The fibre diameter distribution of each of the five discrete samples was calculated from three images from each sample following the methodology outlined in *Section 3.5.1.2.* In order to reduce discrepancies, the fibre diameter calculations were all obtained from the same side (right side) of each sample.
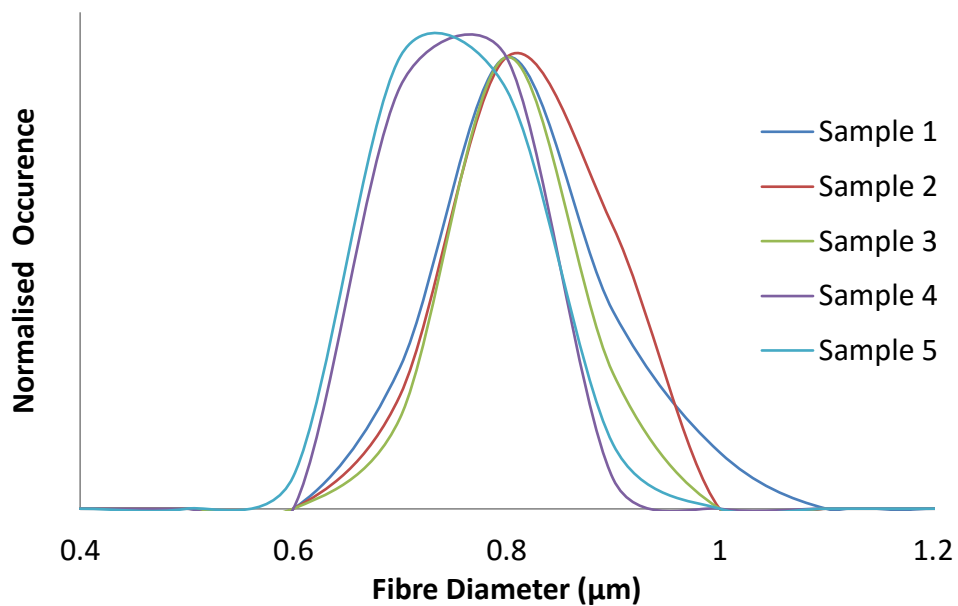


Figure 5.8 - Graph of fibre diameter distribution obtained from five discrete samples (n = 3) from the same extremity of the sample

Data obtained from all samples was then grouped together and plotted in *Figure 5.9.*
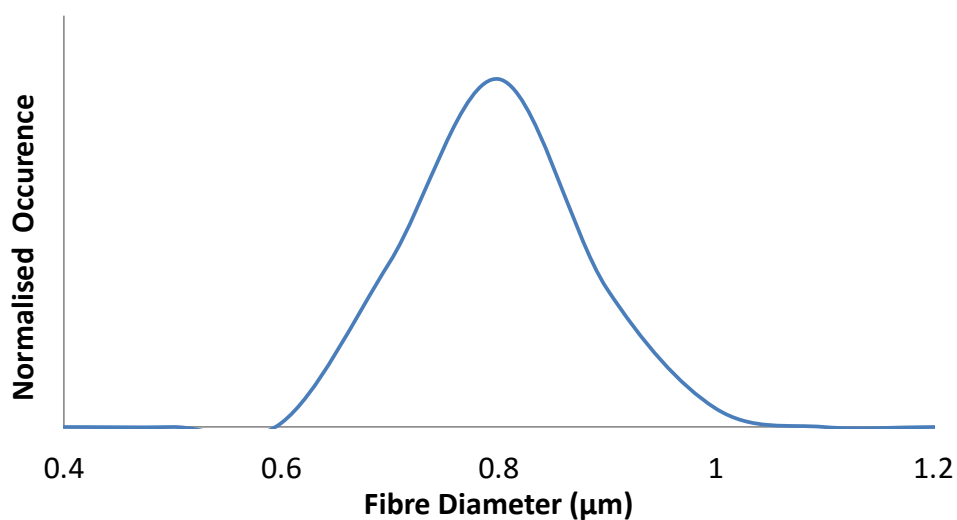


Figure 5.9 - Graph of grouped fibre diameter distribution from all five samples

The fibre diameters of one of the samples at different points across the whole length of a sample were measured to investigate any heterogeneity within the sample. Five positions along the same sample were investigated outlined in *Section 3.5.1.2* using a SEM and three images at x10,000 were analysed for each position.
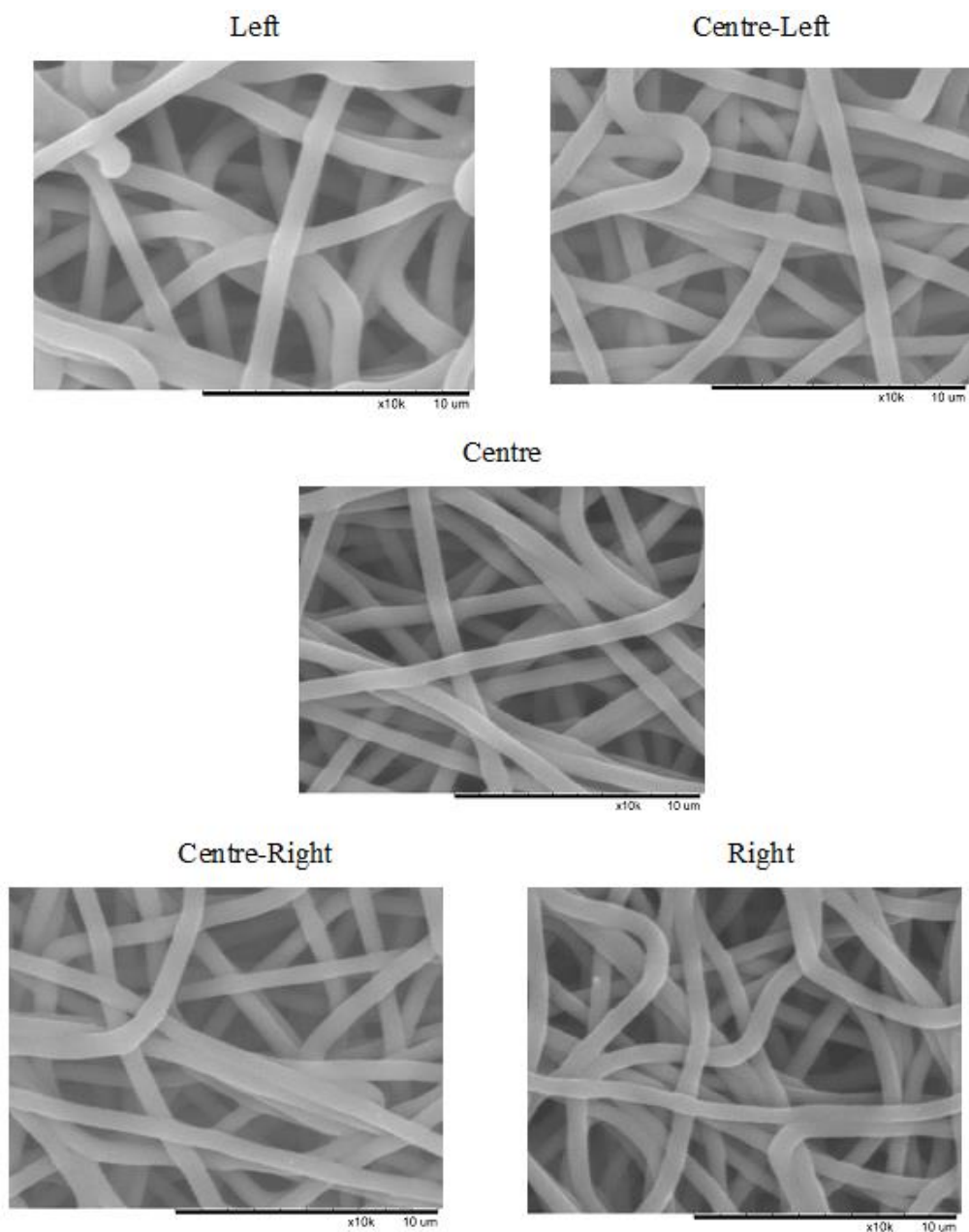


Figure 5.10 - Representative SEM micrographs from different locations on the same sample. All images were obtained at x10,000.

The fibre diameter distribution for each location was calculated from three images at x10,000 from each location. A standard box and whiskers plot was chosen to represent the data obtained in *Figure 5.11*.
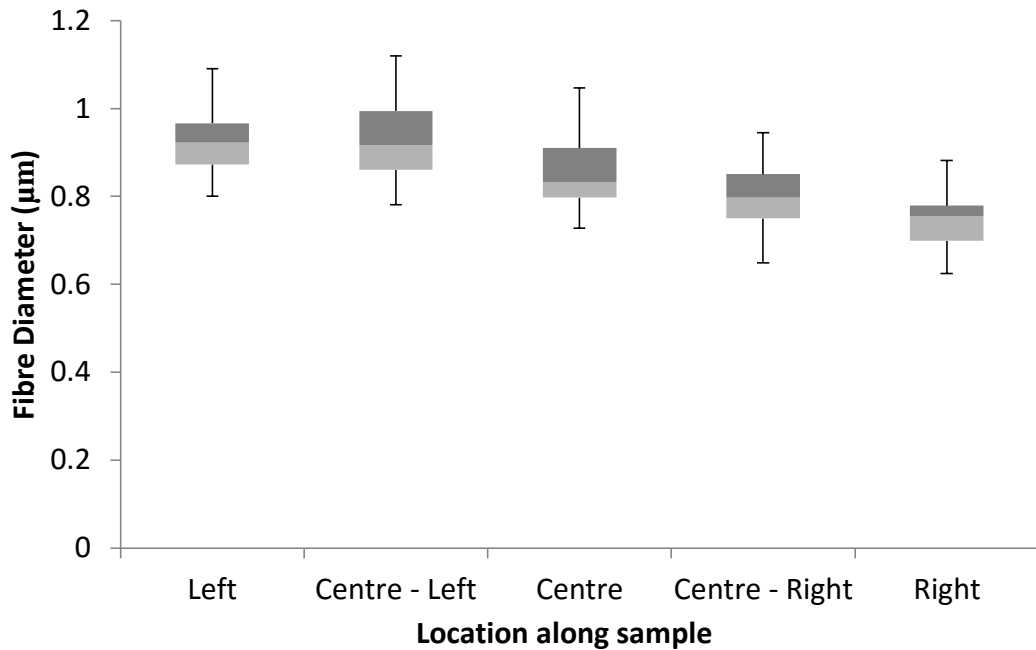


Figure 5.11 - Plot of fibre diameter distribution obtained from an electrospun Z1A1 sample at different locations across its length of 15 cm (n = 3).

It was noted that fibre diameter distributions varied depending on the location investigated. To further investigate this, the diameter distribution of the *Left side* and the *Right side* for each of the five samples was calculated and graphed as shown in *Figure 5.12* below. Three images were obtained for each location on every sample after the standard gold coating protocol was followed. *DiameterJ* was then used to calculate the fibre diameter distribution for each image obtained and data from each location was pooled together to obtain a mean fibre diameter distribution for each sample-location as outlined in *Section 3.5.1.2*. A standard box and whiskers plot was chosen to represent the data obtained in *Figure 5.12*.
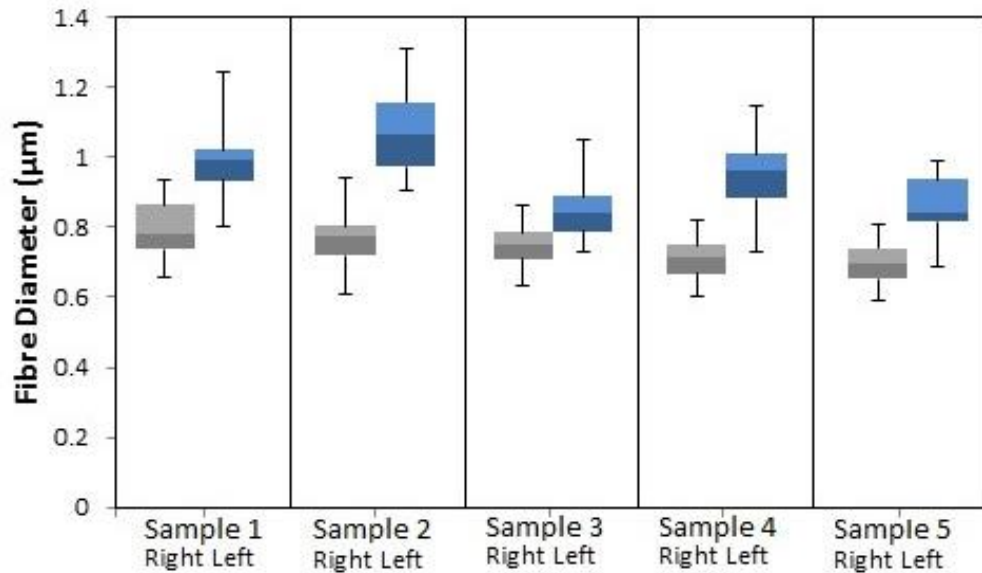
Figure 5.12 – Plot of fibre diameter distribution measured at both sides of each of the five samples (n = 3).

In order to demonstrate the ability of producing fibrous meshes with different nano-mechanical properties, a fibrous mesh with a lower fibre diameter distribution was manufactured using a different set of electrospinning parameters outlined in *Table 3.2 (c)*. Traverse movement was limited to 10 cm to avoid variations of fibre diameter within the sample. Three SEM micrographs were obtained for each of the five locations on the sample and the procedure outlined in *Section 3.5.1.2* was followed to obtain the fibre diameter distribution for each micrograph. All data was then pooled together, binned into 100 nm bins and plotted as shown in *Figure 5.15*. *Figure 5.13* illustrates representative SEM micrographs obtained from various locations across the sample. The resulting fibre diameter distribution was 0.45 μm ± 0.11 μm.
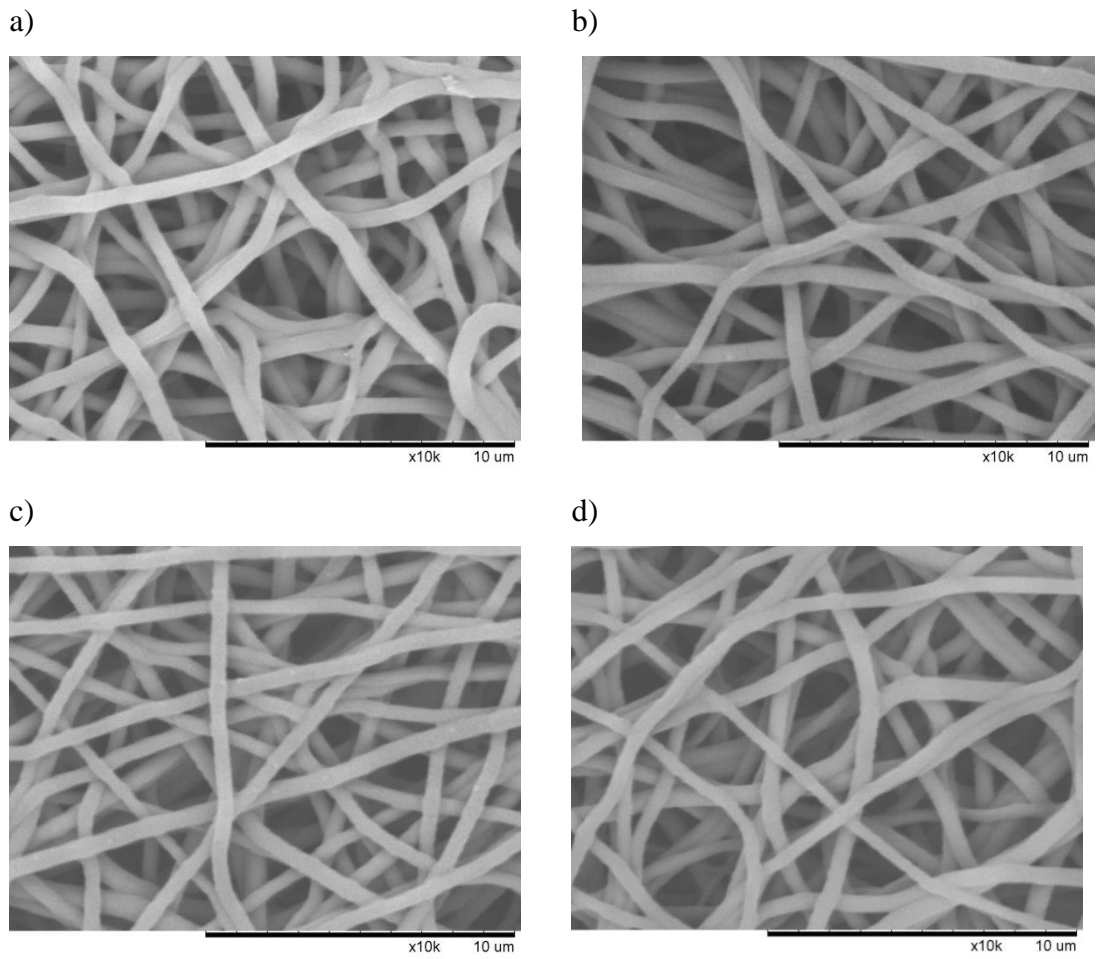
Figure 5.13 - Representative SEM micrographs of electrospun fibres with mean fibre diameter of 0.4 µm. All images were obtained at x10,000. a) left, b) centre-left, c) centre-right, d) right

A further set of samples with smaller fibre diameter distributions were manufactured from a 5 wt/wt% solution of Z1A1 in DMF using parameters outlined in *Table 3.2 (d)*. Three SEM micrographs were obtained for each of the five locations on the sample and the procedure outlined in *Section 3.5.1.2* was followed to obtain the fibre diameter distribution for each micrograph. All data was then pooled together, binned into 100 nm bins and plotted as shown in *Figure 5.15. Figure 5.14* illustrates representative SEM micrographs obtained from various locations across the sample. The resulting fibre diameter distribution was 0.31 µm ± 0.16 µm.

a)

b)

c)

d)
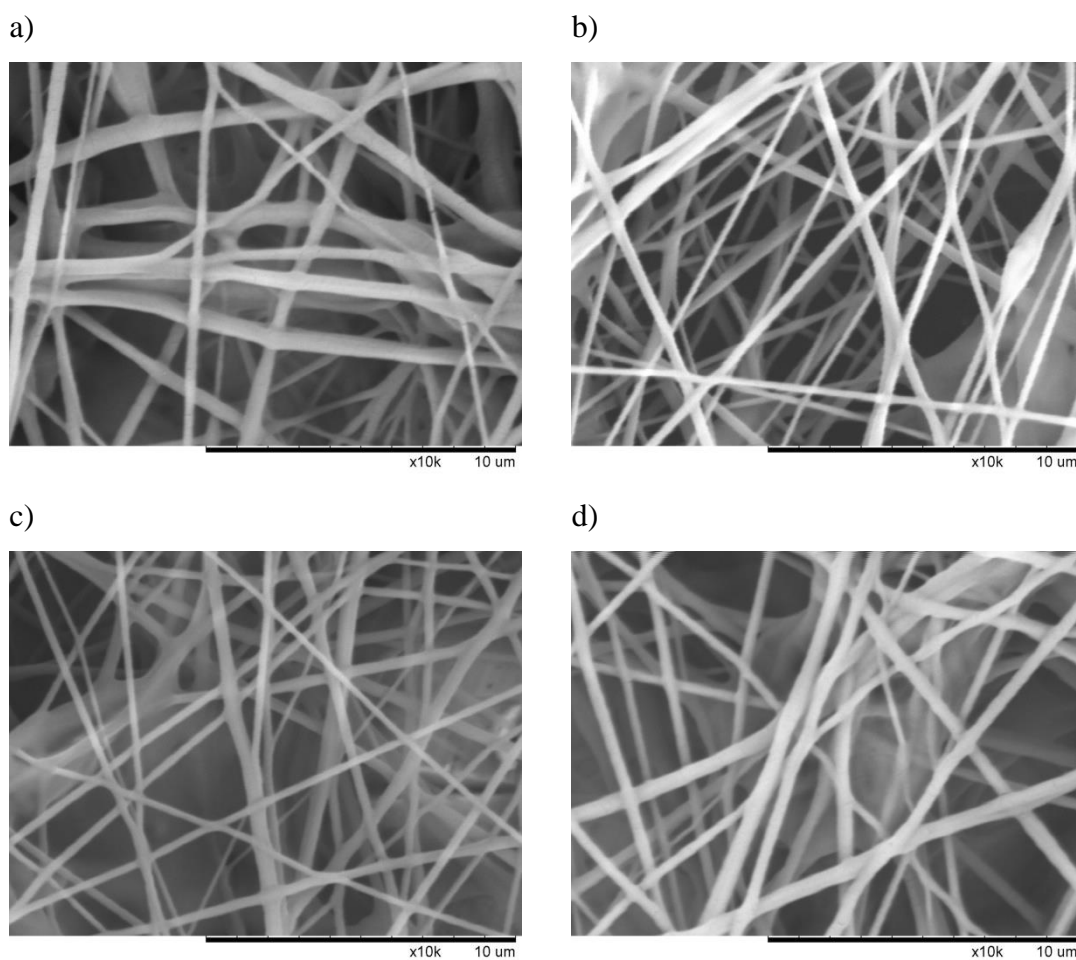
Figure 5.14 - Representative SEM micrographs of electrospun fibres with mean fibre diameter of 0.26 µm. All images were obtained at x10,000. a) left, b) centre-left, c) centre-right, d) right

The fibre diameter distributions from the various samples were plotted in *Figure 5.15* below.
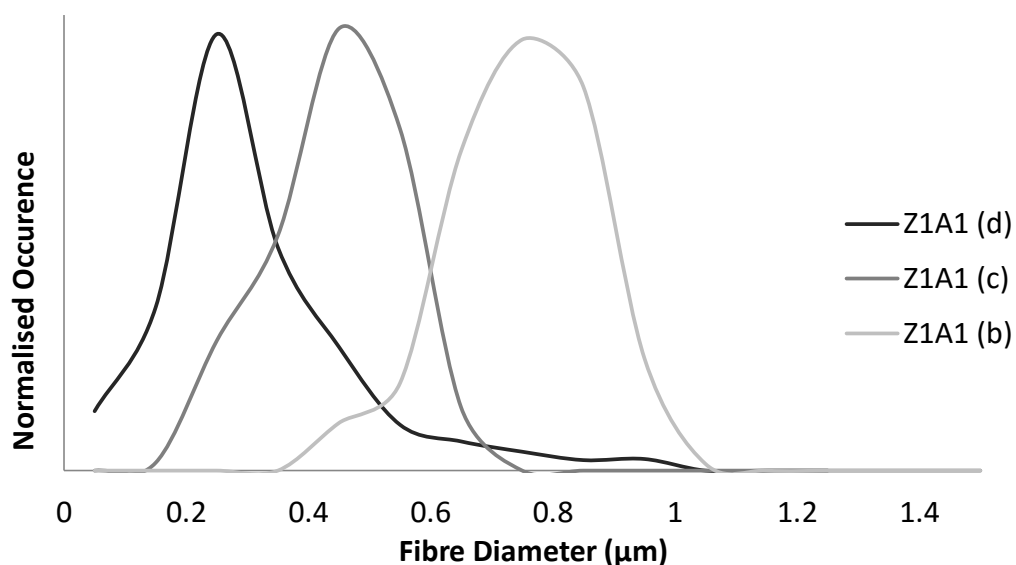


Figure 5.15 – Graph showing Z1A1 fibre diameter distribution obtained from three electrospun mats prepared using different electrospinning parameters outlined in *Table 3.2 (b), (c), (d).*

In summary, Z1A1 was electrospun into mats with three distinct fibre diameter distributions. A representative image from each fibre diameter distribution is shown in *Figure 5.16* below.

a)          b)          c)
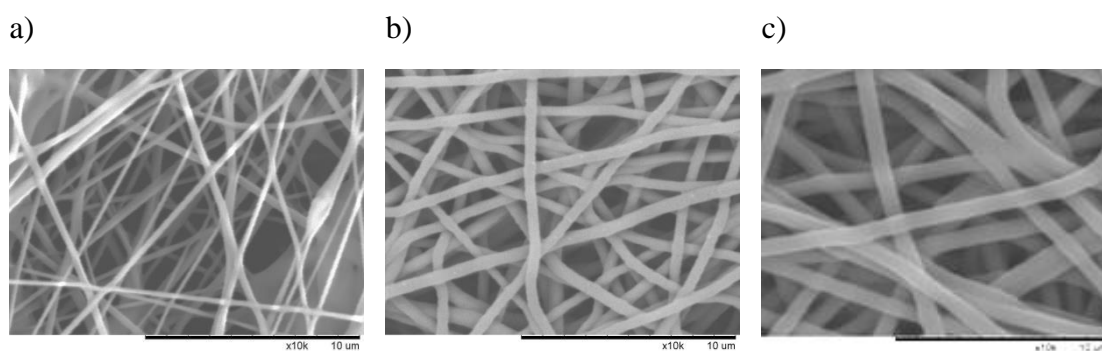


Figure 5.16 - SEM micrographs from Z1A1 electrospun samples with three different fibre diameter distributions. a) 0.31 µm ± 0.16 µm, b) 0.45 µm ± 0.11 µm, c) 0.75 µm ± 0.12 µm. All images were obtained at x10,000.

## 5.2.2. Electrospinning of Z6A1

Electrospun mats were then produced from solutions of Z6A1 in DMF. An iterative process was performed until defect free electrospun mats were obtained. This therefore resulted in electrospun mats with similar fibre morphology when compared to Z1A1, but different nano-mechanical properties even though the chemical intermediates were unaltered.

*Figure 5.18* demonstrates electrospun Z6A1 with a large variation in fibre diameter distribution caused by instability in the Taylor cone. After optimisation of the parameters, electrospinning of Z6A1 was successful and *Figure 5.17* illustrated a number of representative SEM micrographs collected at x10,000 after being gold-coated using a sputter coater following the methodology outlined in *Section 3.5.1.*

a)                                          b)



c)                                          d)
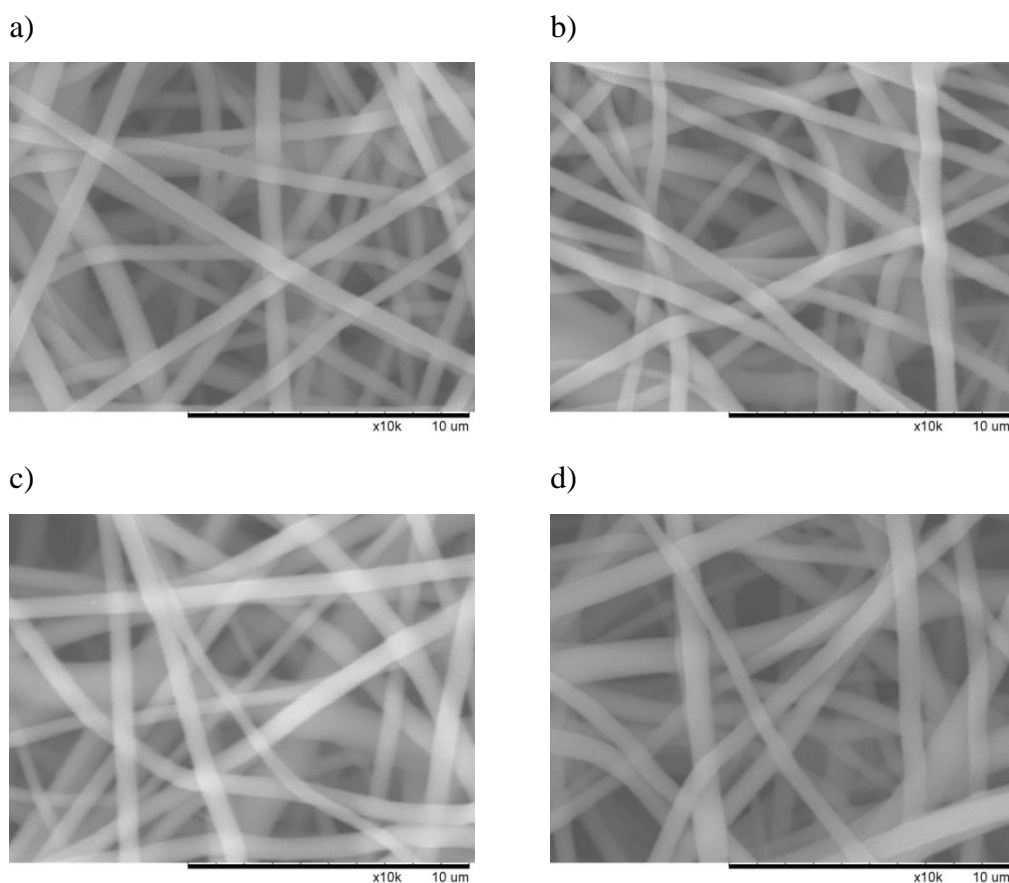


Figure 5.17 - Representative SEM micrographs from different locations on the same Z6A1 electrospun mat. All images were obtained at x10,000. a) left, b) centre-left, c) centre-right, d) right
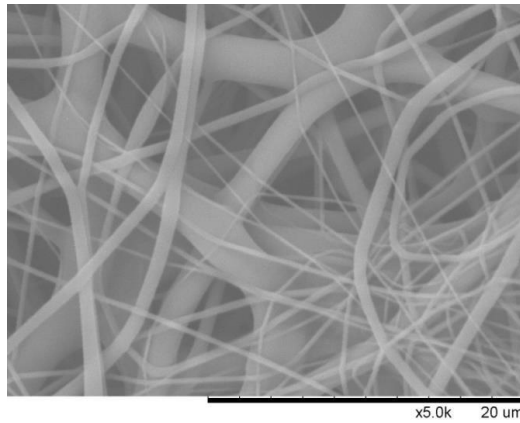
Figure 5.18 - SEM micrograph showing high variability in Z6A1 fibre diameter caused by instability in the Taylor cone. Image obtained at x5,000.

The fibre diameter distributions of three micrographs from each location were obtained using *DiameterJ* using the procedure outlined in *Section 3.5.1.2.* All the data was then pooled together, binned into 100 nm bins and plotted as shown in *Figure 5.19* below. The resulting fibre diameter distribution was 0.58 µm ± 0.27 µm.
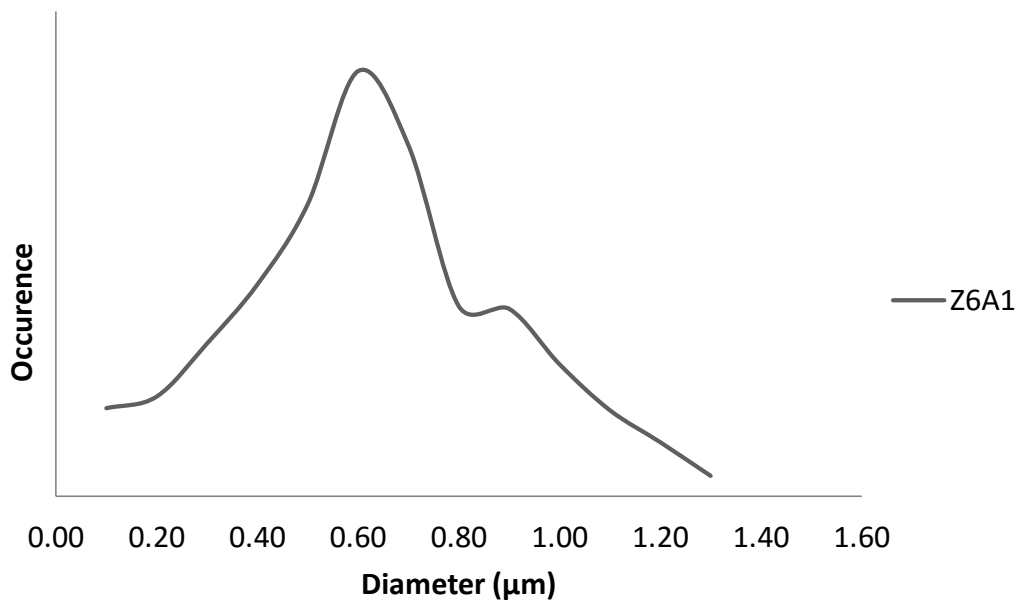


Figure 5.19 - Graph of fibre diameter distribution from a Z6A1 electrospun mat

## 5.2.3. Dual spinning of Z1A1 and Z6A1

Dual spinning was then used to investigate the capability of manufacturing electrospun mats with more than one nano-mechanical property using this family of polymers. Dual spinning allowed for two grades of polyurethane to be electrospun simultaneously and thus creating a mesh with mixed nano-mechanical properties. In order to achieve this, the resulting fibre diameter distributions from both polymers had to be similar to avoid size effects that have been previously discussed.

Following an iterative process detailed in *Section 3.4.5.5*, an electrospun mat with areas consisting of both Z1A1 and Z6A1 was manufactured. Fibre diameter distribution analysis was split into three areas: areas of only Z1A1, only Z6A1 and areas where Z1A1 and Z6A1 overlapped. This was performed to confirm the fibre diameter distribution of each constituent as well as the fibre diameter distribution in areas where both polymers overlap. Three samples were obtained from each area and gold coated using procedure described in *Section 3.5.1.2*. A representative image from each area is shown in *Figure 5.21*. Fibre diameter distribution was then calculated using *DiameterJ* for each image obtained. Data obtained from each area was then pooled together, binned in 100 nm bins and plotted as shown in *Figure 5.20*.
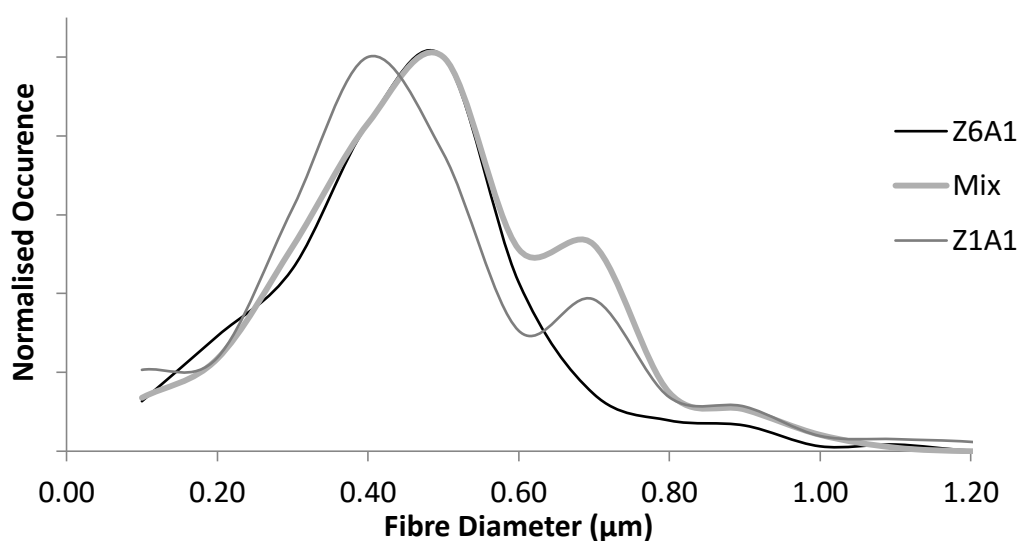


Figure 5.20 - Graph of fibre diameter distributions obtained from areas with electrospun fibres of Z6A1 only, Z1A1 only and a mix of Z1A1 and Z6A1

a)



b)



c)
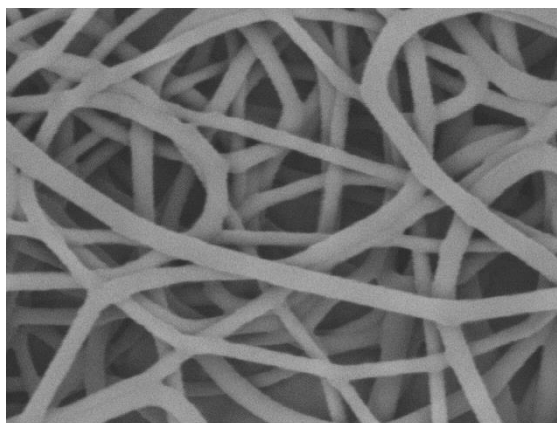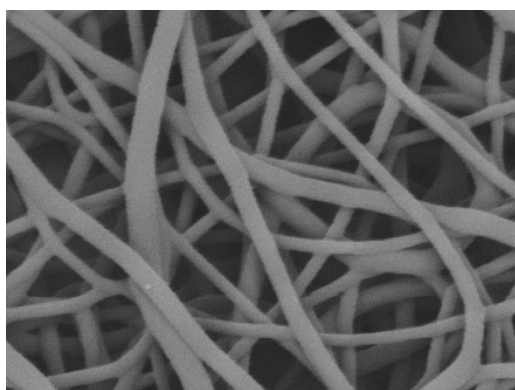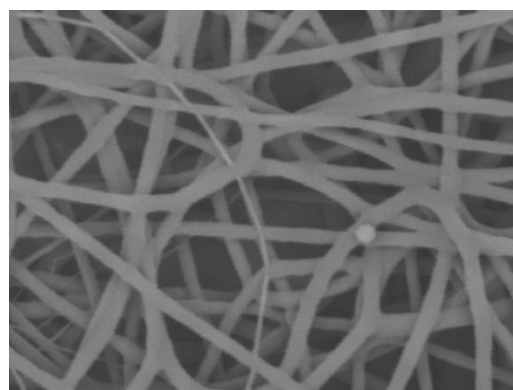


Figure 5.21 - SEM micrographs obtained from a single sample with areas where only Z1A1 was electrospun (b), a mix of Z1A1 and Z6A1 was electrospun (a) and only Z6A1 electrospun (c). All images were acquired at x10,000 magnification.

The resulting fibre diameter distribution were: 0.42 μm ± 0.21 μm for Z1A1, 0.40 μm ± 0.17 μm for Z6A1 and 0.44 μm ± 0.19 μm in areas were Z1A1 and Z6A1 overlapped.

### 5.2.3.1. Phase imaging on dual electrospun mats

Since SEM was not able to distinguish between the two polymer grades, AFM was used in intermittent contact mode in order to obtain a phase contrast image. This mode is able to detect between different surface properties as discussed in *Section 3.5.2.3* meaning that it was ideally suited to distinguish between the two polymer grades. *Figure 5.22* and *Figure 5.23* show representative images from areas where fibres from both polymer grades overlap. A distinct phase shift is apparent in these plots and was attributed to the different surface characteristics of each grade of polymer. Images that demonstrate topographical height were first presented as changes in topography (such as fibre diameter and roughness) are easier to observe. In these images, both image height and the change in colour represent a change in topographical height. This image is then accompanied by another image that demonstrates changes in phase. Since the phase image alone is not sufficient to provide a representative image of the electrospun mats, images are presented as a height image overlaid by the phase image. This means that image height represents actual topographical changes in height, while changes in colour represent changes in phase.
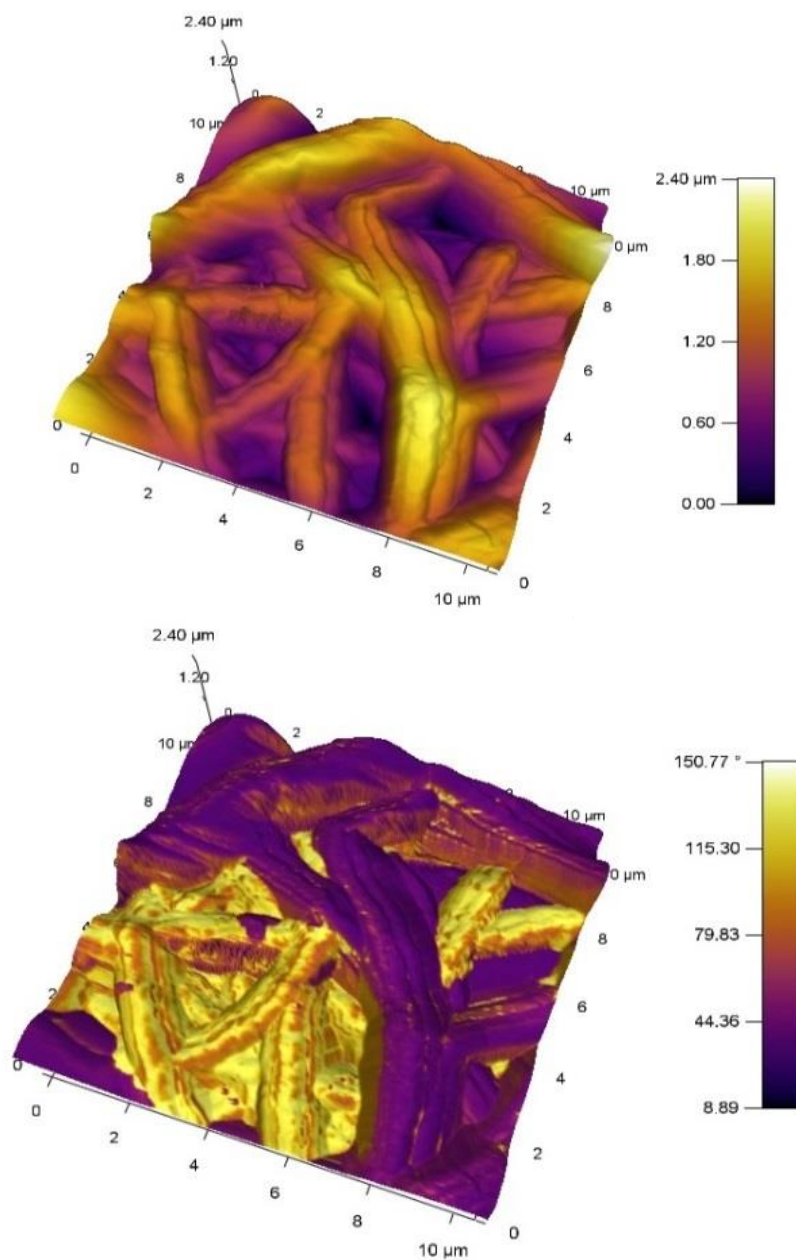
Figure 5.22 - AFM image for height (top) and height overlaid with phase (bottom) from an area showing fibres from both polymer grades.
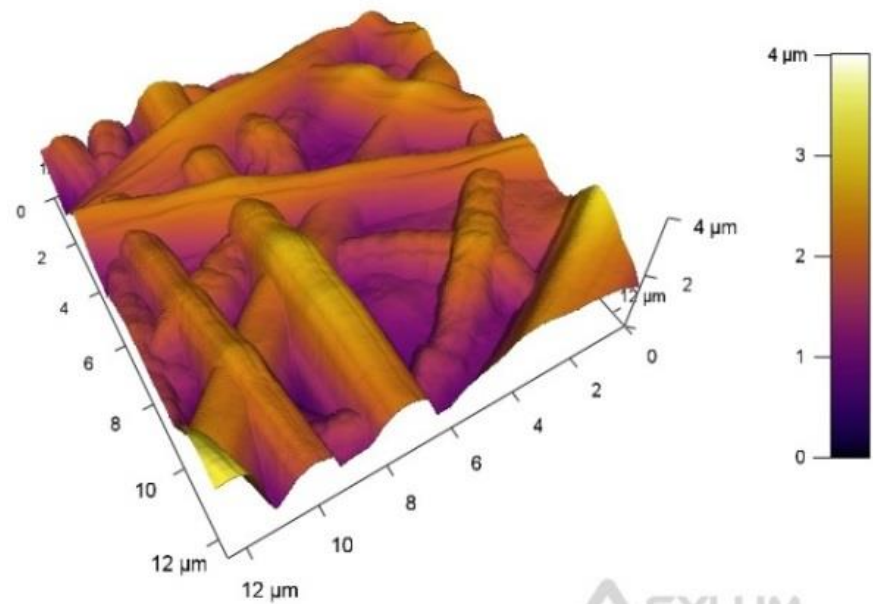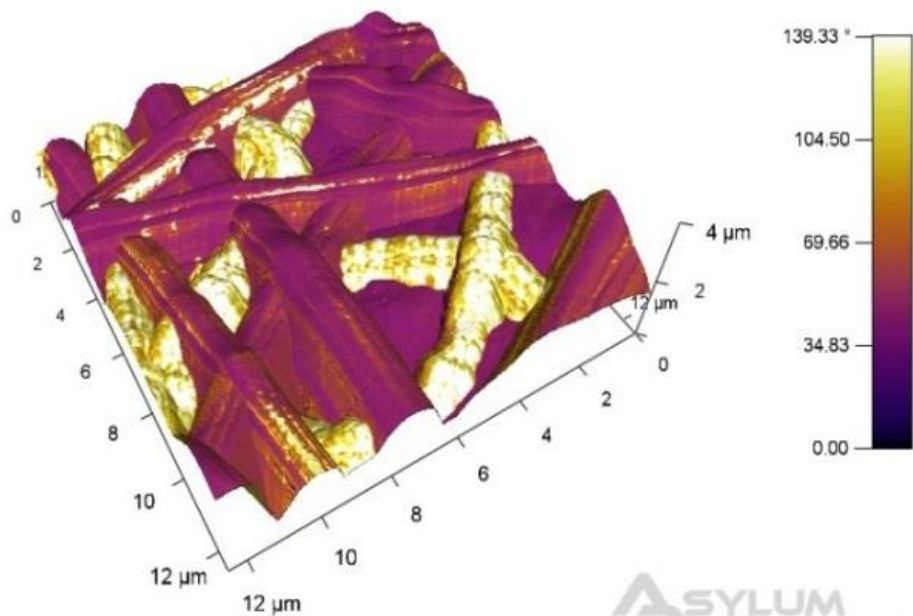
Figure 5.23 - AFM image for height (top) and height overlaid with phase (bottom) from an area showing fibres from both polymer grades.

AFM nano-indentation was carried out on fibres demonstrating both high and low phase reading to investigate whether the changes in phase were associated with a change in modulus. Discrete locations were indented to a specified cantilever displacement of 200 nm and Oliver-Pharr was used to obtain an indentation modulus from the first 40 % of the retraction curve.

Since fibres formed part of a mesh, the moduli reported in the table below are likely to be affected by the deformation of the fibre network as a whole. This meant that the data presented is qualitative rather than quantitative and should not be perceived as an absolute measurement of nano-indentation on electrospun fibres. The resulting moduli indicate that the changes in phase were in fact linked with a change in indentation modulus.

| Location 1 | | Location 2 | |
|---|---|---|---|
| High Phase (MPa) | Low Phase (MPa) | High Phase (MPa) | Low Phase (MPa) |
| 25 | 255 | 80 | 3190 |
| 68 | 277 | 65 | 3620 |
| 8 | 360 | 117 | 3420 |
| 15 | 994 | 87 | 3890 |

Table 5.1 - Table of moduli calculated from AFM nano-indentation on areas of high and low phase on two different images.

## 5.3. Discussion

### 5.3.1. Electrospinning of Z1A1 and Z6A1

The manufacture of polyurethane electrospun mats without defects from the *Biomer b9*™ polyurethane range was successful as shown in *Figure 5.7* but proved more demanding when compared to electrospinning of poly-caprolactone or acrylic based polymers (data not reported). The main challenge involved incidents where not enough polymer solution was being made available for a certain distance-voltage combination. This produced conditions more conducive to droplet formation and consequently electrospraying as opposed to electrospinning (*Figure 5.6 a*). The other extreme case was when too much solution was being presented for a set distance-voltage combination. This resulted in a substrate where solvent was not completely removed from the fibres by the time they reach the collector and formed a wet interlinked electrospun mesh (*Figure 5.6 d*). A less extreme form of this defect produced wet fibres that appeared to coalesce onto one another on contact producing an electrospun mat where fibres were attached to each other and not free to move (*Figure 5.6 c*). In contrast, bead defects were usually formed when the polymer concentration in the solution was too low and continuous fibres could not be produced successfully (*Figure 5.6 b*). These observations were in line with what is reported in literature when different polymers were electrospun into fibrous meshes [218, 288, 289]. Resolving such issues was not straightforward as altering one variable does not always produce a predictable change in the resulting film. The solution viscosity proved to be the main variable that determined the success rate of electrospun mats. This could only be altered by varying the percentage of polymer in the solution used which, if reduced too much, increases the amount of solvent present in the fibres and therefore increases the chance of producing wet fibres. To counteract this, the tip to collector distance could be increased to allow more time for the solvent to evaporate, however, this will in-turn decrease the electric field acting on the Taylor cone which has an exponential relationship with distance. Partially substituting DMF with THF made the process of electrospinning much easier in Z6A1 since this solvent had a lower boiling point making the resulting solution more volatile. Having a more volatile solvent solution meant that a wider range of

electrospinning variables were made available. These observations were also made in previous publications with Erdem *et al.* suggesting that a solution with 50/50 (V/V) of DMF/THF produced the best fibre formation [290]. Mondal *et al.* on the other hand suggest that a solution of 30/70 (V/V) of DMF/THF produced favourable results and demonstrate that varying solvent concentrations altered fibre morphology [206]. This highlights that different chemical compositions of polyurethane have to be treated individually and that it is difficult to extrapolate conclusions made from observations on polyurethanes with a different composition. Solvent mixtures were avoided whenever possible since this was shown in *Section 4.3.2.1* to affect the surface morphology in solvent-cast films.

Electrospinning of Z1A1 was successful after an iterative process resulting in films having low defects being produced from a relatively wide range of parameters. *Figure 5.8* and *Figure 5.9* presented the fibre diameter distributions on five different samples and demonstrate satisfactory repeatability between the samples. *Figure 5.10* and *Figure 5.11* however, demonstrated a change in fibre diameter distribution within the same sample over its length. *Figure 5.12* confirmed that a change in fibre diameter distribution was observed between the left and right side of all the samples. It was hypothesised that this was caused by the equipment's design in which the polymer reservoir (syringe) was stationary while only the needle moves across the traverse. This resulted in a change in polymer flow rate from one side of the traverse to the other with one of the sides (left side) having a stable and repeatable fibre diameter and the other side having a much higher variation. This phenomenon highlights the fact that very small changes in the parameters used for electrospinning have a substantial impact on the resulting fibrous films [291].

Electrospinning of Z1A1 polyurethane into meshes with different fibre diameter distribution was then demonstrated by altering the various electrospinning parameters. *Figure 5.13* and *Figure 5.14* presented SEM micrographs of electrospun Z1A1 with increasingly smaller fibre diameter distributions. SEM micrographs show little to no defects within the films and a visibly narrow fibre diameter distribution. *Figure 5.15* then illustrates the fibre diameter distributions obtained from the three

different sets of electrospinning variables. The distributions from Z1A1 were 0.31 μm ± 0.16 μm, 0.45 μm ± 0.11 μm, 0.75 μm ± 0.12 μm, These are relatively narrow distributions when compared to those reported by Tetteh *et al.* for Z3A1 (1.25 μm ± 1.56 μm) and Z9A1 (2.06 μm ± 3.09 μm) when only DMF was used [239]. The main aim of this section was to manufacture electrospun mats using the *Biomer Technology Limited b₉* polyurethane range with different nano-mechanical properties by altering fibre diameters and was achieved as shown in *Figure 5.15.* The effect that gold coating had on the resulting fibre diameter distributions was not taken into account as all samples were coated using the same coating protocol as outlined in *Section 3.5.1.2*, resulting in a uniform thickness increase on all the samples.

Electrospinning of Z1A1 into different diameter distribution was possible by altering the polymer concentration used and slightly tweaking the other parameters. This proved more demanding for Z6A1 as the instability of the Taylor cone was too high and obtaining a uniform mat from solutions of lower polymer concentrations was not possible. The same was observed by Tetteh *et al.* who reported that electrospun fibres were easier to fabricate from Z3A1 when compared to Z9A1 [239]. Even though these were not the same polymer grades discussed here, the only differences between all the grades discussed was the HS chain length as outlined in *Section 3.2.2.* In Z6A1, HS polymer chain lengths were longer than those in Z1A1. This resulted in a decrease in viscosity in Z6A1 when the same solvent concentration was used. In order to obtain viscosities similar to those used when Z1A1 was electrospun successfully, the polymer concentration had to be increased by approximately two-fold. Even though the resulting solution viscosity was similar, the percentage of solids in the solution was different, meaning that different electrospinning parameters still had to be used. A higher voltage for a set distance had to be used to initiate the electrospinning process. This resulted in unstable whipping of the Taylor cone and large variations in the fibre diameters as shown in *Figure 5.18* below. This was successfully counteracted to a certain extent by reducing the tip to collector distance and reducing the electrospinning voltage used. *Figure 5.19* illustrated the fibre diameter distribution data collected from Z6A1

electrospun mats. Even though this distribution is not multimodal, a larger variation in the Z6A1 fibre diameters (0.58 µm ± 0.27 µm) was still observed when compared to that observed in Z1A1 electrospun mats.

## 5.3.2. Electrospun mats with bi-modal nano-mechanical properties

In order to manufacture a scaffold that has a wide range of nano-mechanical properties, scaffolds were produced by simultaneously electrospinning nano-fibres from Z1A1 and Z6A1 by means of dual spinning. The main challenge in dual spinning was that one set of variables that produced fibres with low defects for both polymer solutions had to be established. The only variable that could be changed was the polymer solution concentration and solvent system used. Since it was previously shown that Z6A1 had a narrower range of variables that successfully produced nano-fibres, stable fibres were first produced for Z6A1. Electrospinning of Z1A1 solutions at different concentrations was then attempted using the parameter range that was established by the Z6A1 solution. As no two solutions were found to electrospin successfully when only DMF was used as a solvent, a solvent system of 70:30 (V/V) DMF:THF was used for Z6A1. This solution was not preferred as results from *Section 4.3.2* indicate that surface roughness was altered when different solvents were used.

Areas having exclusively Z1A1 or Z6A1 fibres showed no clear difference under SEM imaging in *Figure 5.21* with fibre diameter analysis showing similar distributions for both polymers in *Figure 5.20*. Since SEM was a non-contact imaging system, the technique was found to be useful for the assessment of fibre diameter. For further analysis of the scaffolds, AFM had to be used in nano-scale analysis of the fibres and to identify differences in nano-mechanical properties. After iteratively scanning various locations on the electrospun mat, phase imaging produced a very clear indication that fibres of different surface properties were being imaged with phase differences of up to $60^{o}$ between the two fibre types as shown in *Figure 5.22* and *Figure 5.23*. Bar *et al.* argue that it is difficult to assign phase image contrast to different components unless additional experiments are carried out [292]. Phase shift was reported to depend on both the amplitude of free oscillation of the

cantilever and the set-point amplitude during scanning. They demonstrate that phase can undergo a contrast reversal when these two variables are altered [292]. This has led to a number of authors making conflicting observations with some attributing high phase to relatively stiffer materials while others attribute high phase to softer materials [248, 293, 294]. In order to confirm that the change in phase was due to a change in mechanical properties, the different fibres were indented at both high and low phase difference. It could then be concluded from *Table 5.1* that fibres scanned using AFM showing a high phase reading were Z1A1 fibres while the darker fibres with lower phase readings were Z6A1.

The values for moduli obtained by nano-indenting fibres from a mesh of different materials shown in *Table 5.1* are a compound effect of a number of nanofibres stacked on top of each other and not an accurate measure on the individual fibre stiffness. However, a clear difference in mechanical properties was observed with moduli from Z6A1 indents being around six times stiffer when compared to moduli obtained from Z1A1 fibres. An observation that can be made from both *Figure 5.22* and *Figure 5.23* is that fibres demonstrating high phase (Z1A1 fibres) were underneath Z6A1 fibres in both instances. This was caused by the intrinsic properties of the manufacturing process of dual spinning in which two polymer solutions are electrospun simultaneously while the nozzles that deliver the polymer are moved transverse to the collector as outlined in *Section 3.4.5.5*. The stacking of polymers will therefore depend on which side the nozzles are when the electrospinning process is stopped.

The surface topography in regions where both fibres overlap also demonstrated a marked difference in surface morphology with Z1A1 fibres exhibiting a rougher surface when compared to Z6A1. This distinction was attributed to the difference in solvent solution used with the solution containing THF leaving a surface with lower roughness as observed on solvent-cast films in *Section 4.3.2.1*. The phase difference observed was not due to this change in surface morphology, however, due to a change in fibre material as demonstrated by nano-indentation on the individual fibres. AFM phase imaging therefore confirmed that the aim of the section was met

and an electrospun mat with a bi-modal distribution of nano-mechanical properties was fabricated.

## 5.4. Conclusions

The principal aim of this *Chapter* was to report on the manufacture of electrospun mats with diverse nano-mechanical properties from the *Biomer Technology Ltd. $b_9$* thermoplastic polyurethane range. This was achieved by altering fibre diameter distributions and by using polymer grades with intrinsically different mechanical properties while maintaining the same chemical intermediates.

Z1A1 was electrospun into a range of mats presenting fibre diameters from 0.31 μm ± 0.16 μm to 0.75 μm ± 0.12 μm. Such mats present considerably different nano-mechanical properties when loaded in three-point bending as shown in *Figure 5.4*. Z6A1, a different grade of polyurethane formulated from the same chemical intermediates as Z1A1 but demonstrating different intrinsic mechanical properties, was then successfully electrospun into fibrous mats. Defect-free Z6A1 electrospun mats having a fibre diameter distribution of 0.58 μm ± 0.27 μm were fabricated. This fibre diameter distribution lay within the range of possible Z1A1 fibre diameter distributions. This meant that two mats with similar fibre diameter distribution and chemical make-up, but with considerably different bulk and nano-mechanical properties could be compared.

In the final section, dual spinning was then used to successfully fabricate an electrospun mat consisting of both Z1A1 and Z6A1 fibres with the same fibre diameter distribution. This resulted in a fibrous mat that exhibited a bi-modal distribution of nano-mechanical properties which could be used in the investigation of the influence of nano-mechanical properties on cell mechanotransduction.

# Chapter 6

# In-vitro Degradation of

# Polyurethane

## 6.1. Introduction

Similar to metals, polymeric biomaterials are susceptible to chemical reactions that could lead to unintended deterioration of the mechanical or topographical characteristics of the original material. A book section by Lamba *et al.* provides a complete review of polyurethane degradation [295]. Polymer hydrolysis is the most common cause of degradation and involves the scission of susceptible molecular groups by reaction with water. Bond stability is the main factor influencing hydrolysis but other factors play an important role. Hydrophobicity and molecular weight are inversely proportional to the rate of hydrolysis while an increase in material porosity increases the rate of hydrolysis [296]. As previously described in *Table 3.1,* the range of possible polyurethane chemical compositions is considerably varied and the modes, rates and causes of degradation are different between the different polymer formulations. The soft segment in polyurethane has been shown to be more susceptible to hydrolysis, which has led to a decrease in the use of poly(ester) urethanes as these are very susceptible to hydrolysis [297]. The use of such materials as foams in the *Meme* breast implant had become the centre of considerable debate but poly(ester) urethane is still considered safe for use as temporary biomaterials in applications such as wound dressings and gastric bubbles [289 – 300]. On the other hand, poly(ether) urethanes have been shown to be the most resistant to hydrolysis when the effect of soft segment was investigated by Pavlova *et al.* [301].

The chemical intermediates used in the hard segment of polyurethanes will also influence the biodegradation of polyurethanes. Based on fundamental chemistry, aromatic isocyanates should be more stable than their aliphatic counterparts. However, research has shown that potentially carcinogenic compounds (2,4-toluene diamine (TDA) or 4,4' methylene dianiline (MDA)) can be released when cleavage occurs in polyurethanes containing aromatic isocyanates. A comprehensive body of work that investigates these observations on specific polyurethane formulations has been previously published [167, 170, 302, 303].

Part of the inflammatory response is the increase in an oxidative environment with various cells such as macrophages producing hypochlorite and peroxide [304]. This could then be further exacerbated if degradation products are released from an implant. Meijs *et al*. perform a series of experiments on a range of commercial biomedical grade poly(ether) urethanes to investigate their degradation in oxidative environments [164]. Samples were immersed in 25 % $H_2O_2$, water and dry atmosphere all at 100 $^o$C for 24, 96 and 336 hours. This caused an accelerated degradation of these polymers and resulted in a significant drop in ultimate tensile strength and sample mass even after 24 hours of immersion. From their study, they conclude that chain scission mainly occurred in the soft segments close to the interface with hard segments. Yang *et al*. investigate changes in the surface morphology of polyurethane coatings used in the aircraft industry after an accelerated weathering process [305]. AFM was used in conjunction with x-ray photoelectron spectroscopy (XPS) and Fourier transform infrared spectroscopy (FTIR) analysis to investigate any changes in the polymer surface and chemical make-up. AFM revealed a significant change in the surface morphology even after three weeks of exposure with blisters forming on exposed surfaces [305].

A change in surface roughness has been linked to changes in cellular behaviour in a number of publications [109, 306, 307]. Chung *et al.* have reported that an increase in nano-meter scale roughness in PU-PEG surfaces improved adhesion and growth of human umbilical vein endothelial cells (HUVEC) [308]. They conclude that even an increased roughness of 10 - 100 nm enhanced HUVEC adhesion and growth in both

GRGD-grafted and ungrafted surfaces. Keshel *et al.* used oxygen and argon microwave plasma to increase the surface roughness of polyurethane films and investigated the response of unrestricted somatic stem cells [309]. They conclude that increasing the surface roughness increased adhesion, growth and viability of these cells.

Changes in nano-scale surface roughness reported by Yang *et al.* caused by polymer degradation could therefore alter cell behaviour as reported by *Chung et al.* [305, 308]. In an investigation of the influence of nano-mechanical properties on cell behaviour, it has to be ensured that nano-mechanical cues are the only variables effecting cell behaviour. This *Chapter* investigated whether exposure to a physiological environment could alter the surface properties of the *Biomer Technology Limited* $b_9$ poly (ether) urethanes over an extended period of time. Samples were stored in a physiological solution and an oxidative solution mimicking inflammation. The effect of long term storage was investigated on both solvent-cast films and electrospun fibres to determine whether the large surface area to volume ratio in electrospun fibres contributes to an increased rate of degradation. Experiments were set-up according to general guidelines from *BS EN ISO 10993 - 13:2010.*

## 6.2. Materials and Methods

### 6.2.1. Materials

Two grades of polyurethane were investigated: Z1A1 and Z6A1. These grades were chosen for their substantial difference in bulk and nano-mechanical properties as demonstrated in *Section 4.3.1*. Polycaprolactone (PCL) is a bioresorbable biomaterial which degrades over a relatively long period of time (over 3 years) [310, 311]. It is also stable in ambient conditions, very cost effective and readily available [312, 313]. Polycaprolactone *($M_n$ 80,000, Sigma-Aldrich)* was therefore used as a positive control to determine whether the methods of measurement were sensitive to changes on the scale that was being investigated.

## 6.2.2. Storage of solvent-cast films in a physiological solution

Z1A1, Z6A1 and PCL were solvent-cast into films following the procedure described in *Section 3.3.3*. A fixed concentration of 15 wt/wt % of polymer in DMF was used to manufacture solvent-cast films of Z1A1, Z6A1 and PCL. Samples were then cut to a nominal size of 30 mm x 5 mm for storage and subsequent characterisation. Test specimens were stored individually at 37 $^{\circ}$C for 7, 14, 30, 60 and 90 days in a surplus of sterile phosphate buffered saline (PBS) (0.01 M phosphate buffer, 0.0027 M potassium chloride and 0.137 M sodium chloride, pH 7.4, at 25 °C) (approximately 20x the mass of the specimen). Glass bottles used for storage were scrubbed from any residue and cleaned using an ultrasonic cleaner in distilled water for 45 minutes in 15 minutes intervals. The bottles were then sterilised in an autoclave by heating up to 120 $^{\circ}$C for 30 minutes. Before storing the samples in their respective media, samples were cleaned in distilled water by sonication and allowed to air dry for four hours in a sterile laminar flow cupboard. Each sample was then rinsed in sterile distilled water and immersed in the relevant medium for storage. After the period of immersion, three samples for each polymer were removed from storage, rinsed in distilled water and sonicated for 45 minutes in 15 minute intervals.

## 6.2.3. Storage of solvent-cast films in an oxidative solution

Z1A1, Z6A1 and PCL solvent-cast films were manufactured from polymer solutions of 15 wt/wt % in DMF following the methodology outlined in *Section 3.3.3* and cut to a nominal size of 30 mm x 5 mm. Glass bottles and specimens were cleaned as outlined in *Section 6.2.2.* Hydrogen peroxide (*30 % w/w in H₂O, Sigma-Aldrich*) was diluted to 5% w/w by adding sterile distilled water as suggested in *BS EN ISO 10993 - 13:2010.* Specimens were then stored individually at 37 $^{\circ}$C for 2, 7, 14, 30 and 60 days in a surplus of 5 % $H_2O_2$ (about 20x the mass of the specimen). The solution was changed every 15 days in order to maintain the concentration of hydrogen peroxide. After the period of immersion, three samples for each polymer were removed from storage, rinsed in distilled water and sonicated for 45 minutes in 15 minute intervals.

## 6.2.4. Analysis of surface topography

Samples were mounted onto a glass slide for topographical characterisation using the *Asylum Research MFP-3D* AFM. Topographical images were obtained in contact mode using *AR-iDrive-N01 L* tips with low modulus for increased sensitivity. The glass interface of each solvent-cast film was imaged as this side has been demonstrated in *Section 4.3.2* to have less surface features resulting in a lower variability in surface roughness measurements. Multiple images were taken from two different locations. For each location, a "90 µm x 90 µm" image, three "20 µm x 20 µm" images and a "1 µm x 1 µm" image was obtained. This was repeated at two different locations on each sample resulting in 6 "20 µm x 20 µm" images for each sample and three samples for each polymer-time point as shown in *Figure 6.1*. Images were then flattened accordingly to avoid artefacts and a roughness measurement ($R_a$) was recorded. All scans were performed at 0.5 Hz with 256 points and lines which allowed for a good compromise between scan time and image quality.
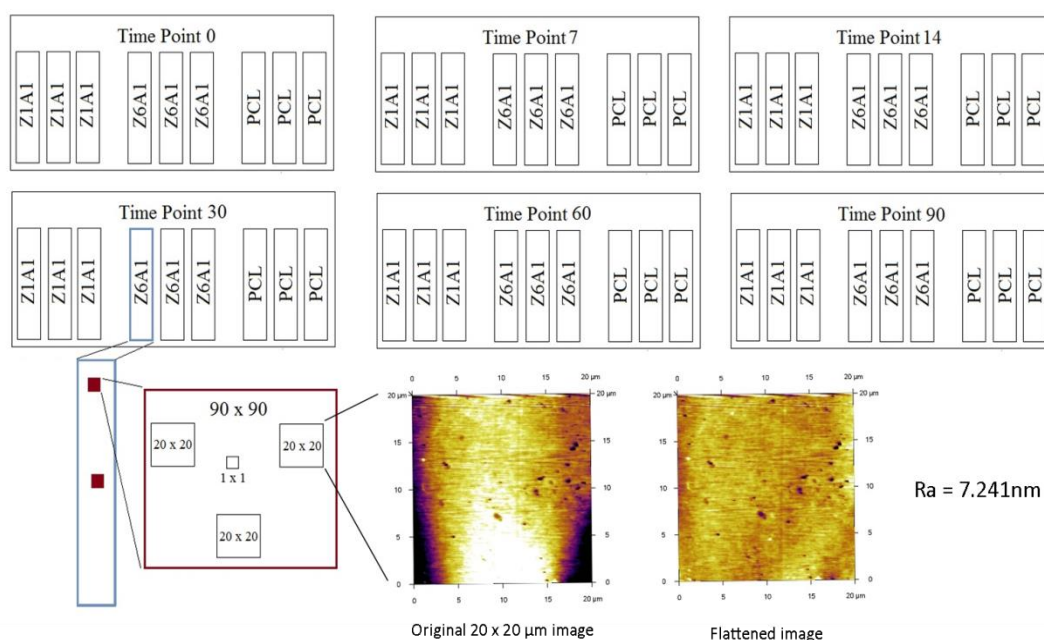


Figure 6.1 - Schematic representation of the data collection process. Three polymer grades were investigated and three samples for each polymer - time-point were characterised. Six images were obtained from each sample for a mean sample roughness calculation.

A one-way repeated measures ANOVA was conducted using SPSS version 23.0 to evaluate the null hypothesis that there is no change in sample roughness in each of the three different polymers after storage (n = 18).

## 6.2.5. Analysis of mechanical properties

The bulk and micro-mechanical properties of solvent-cast films were analysed. The bulk tensile moduli of solvent-cast films were investigated using the *Bose Electroforce 3200* using procedures outlined in *Section 3.6.2*. The moduli of three samples before and after storage were investigated. Statistical significance was determined following a two-tailed, un-paired student's t-test with significance set at $p \geq 0.05$.

The indentation moduli were then investigated using the dedicated nano-indenter following the methodology outlined in *Section 3.7.3*. Three samples from before and after storage in solution were indented 8 times, each in a different location to a set depth of 1.5 μm. Statistical significance was determined following a two-tailed, un-paired student's t-test with significance set at $p \geq 0.05$.

## 6.2.6. Storage of electrospun mats in an oxidative solution

In order to investigate whether the substantial increase in surface area has a change in the degradation of polyurethane, a study was carried out to investigate the degradation of electrospun polyurethane fibres in an oxidative solution. Electrospun fibres were produced from Z1A1, Z6A1 and PCL using the parameters outlined in *Table 3.2 (a), (f)* and *(g)* respectively. Test samples were cut out of a single sheet of electrospun fibres to reduce variability and stored individually at 37 $^{\circ}$C for 2, 7, 14, 30 and 60 days in a surplus of 5% $H_2O_2$ (about 20x the mass of the specimen). The solution was changed every 15 days in order to maintain the concentration of hydrogen peroxide. After the period of immersion, three samples for each polymer were removed from storage, rinsed in distilled water and sonicated for 45 minutes in 15 minute intervals. Samples were then prepared for SEM imaging using the methodology outlined in *Section 3.5.1.2*.

## 6.3. Results

### 6.3.1. Storage of solvent-cast films in a physiological solution

The effects of long term storage in a physiological solution on solvent-cast films produced from the *Biomer $b_9$* poly(ether) urethane materials was first investigated. The mean and standard deviation of the roughness from these 18 "20 µm x 20 µm" images was then plotted for each polymer time-point. The surface roughness obtained by AFM was plotted in *Figure 6.2* below. Each point therefore represents a mean and standard deviation of the roughness obtained from 18 images from three different samples per polymer. Results indicated a significant time effect on PCL ($p < 0.05$) while no significant effects were seen for Z1A1 ($p > 0.05$) and Z6A1 ($p > 0.05$).
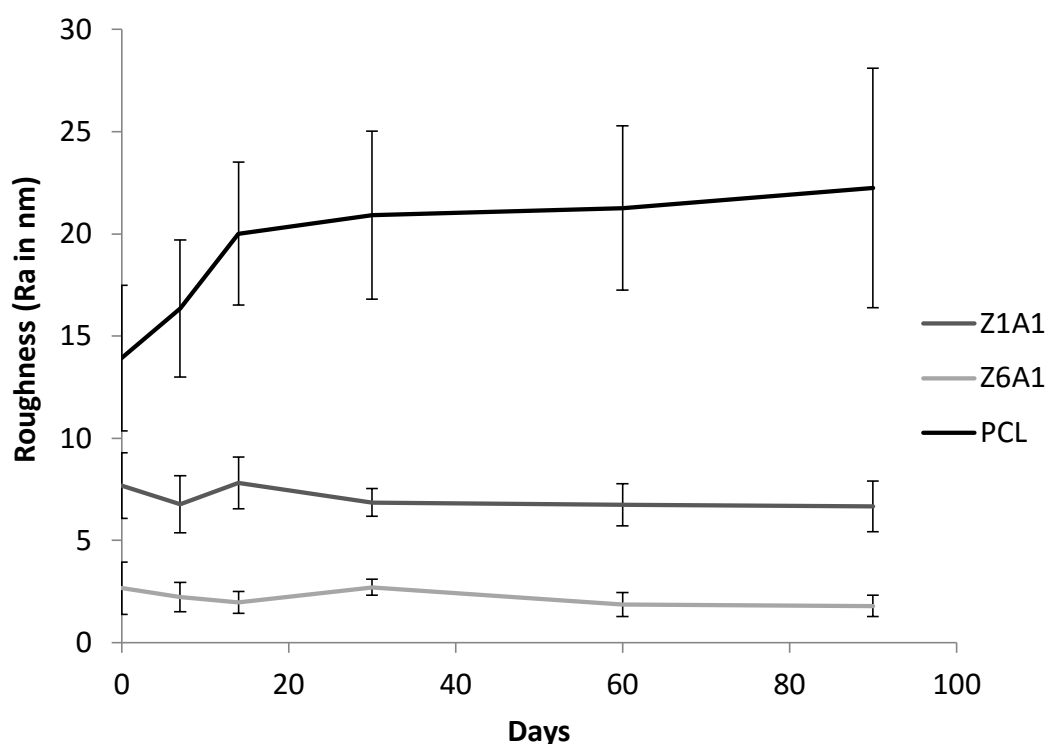


Figure 6.2 - Graph showing surface roughness mean and standard deviation measurements made from Z1A1, Z6A1 and PCL solvent-cast films after storage in PBS. (n = 18)

**Mechanical properties**

The bulk and micro-mechanical properties of solvent-cast films stored in PBS over a period of 90 days was analysed. The moduli of three samples before and after 90 days stored in PBS were investigated. The mean and standard deviation of three repeats obtained from three samples is shown in *Table 6.1* below. The resulting tensile moduli were statistically similar for both Z1A1 ($p > 0.05$) and Z6A1 ($p > 0.05$).

| | Tensile modulus (MPa) | |
|---|---|---|
| | Before | After |
| Z1A1 | $14.84 \pm 0.52$ | $14.04 \pm 1.25$ |
| Z6A1 | $379.80 \pm 36.41$ | $376.74 \pm 43.40$ |

Table 6.1 - Table showing bulk mechanical modulus of Z1A1 and Z6A1 both before and after 90 days storage in PBS ($n = 3$).

The indentation moduli were then investigated using the dedicated nano-indenter. Three samples from before and after 90 days stored in PBS were indented consecutively. The resulting means and standard deviations from three samples were shown in *Table 6.2* below. Indentation moduli were statistically similar for both Z1A1 ($p > 0.05$) and Z6A1 ($p > 0.05$).

| | Indentation modulus (MPa) | |
|---|---|---|
| | Before | After |
| Z1A1 | $4.14 \pm 0.52$ | $4.19 \pm 0.13$ |
| Z6A1 | $44.37 \pm 1.67$ | $45.17 \pm 1.36$ |

Table 6.2 - Table showing indentation modulus of Z1A1 and Z6A1 both before and after 90 days of storage in PBS ($n = 24$).

## 6.3.2. Storage of solvent-cast films in an oxidative solution

**Surface topography**

The effects of long term storage on the surface topography of solvent-cast films in an oxidative solution was investigated. The mean and standard deviation of the roughness from these 18 "20 μm x 20 μm" images was then plotted for each polymer time-point. Each point represents a mean and standard deviation of the roughness obtained from 18 "20 μm x 20 μm" images from three samples per polymer – time-point. Results indicated a significant time effect on PCL ($p < 0.05$), Z1A1 ($p < 0.05$) and Z6A1 ($p < 0.05$). Follow-up pairwise comparisons also indicated that statistical differences were observed after 15 days in storage and preceding roughness were all statistically similar ($p > 0.05$).
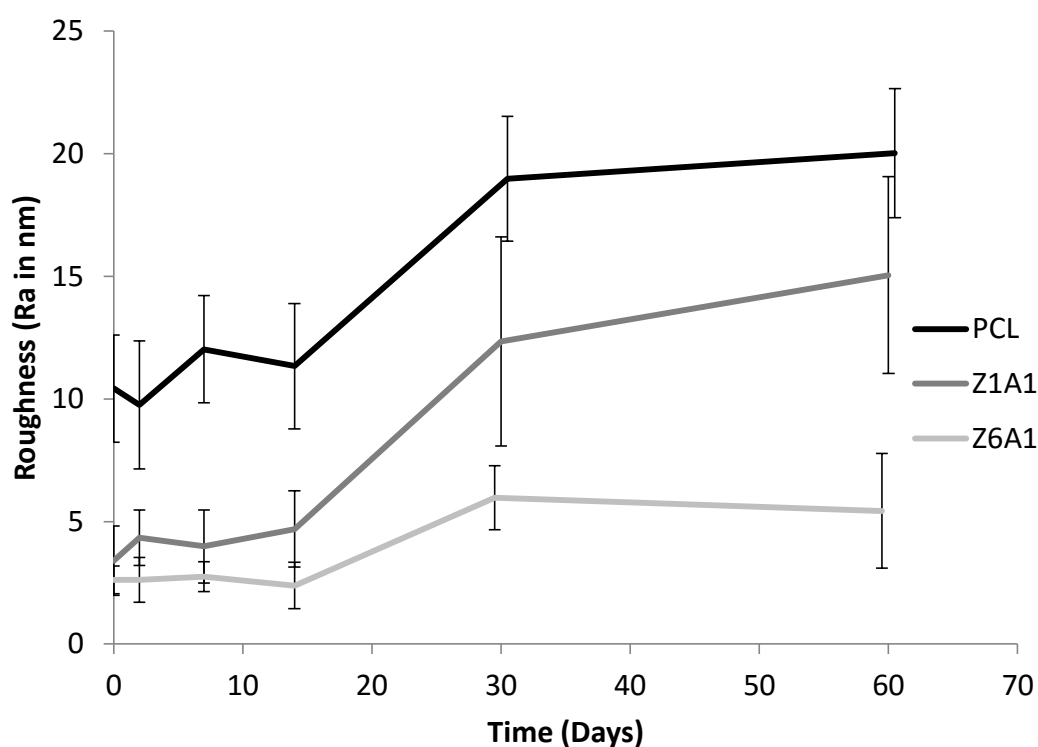


Figure 6.3 - Graph showing surface roughness measurements made from Z1A1, Z6A1 and PCL solvent-cast films after storage in 5 % $H_2O_2$ (n = 18).

Representative images obtained using AFM at time-point 0 and time-point 60 for both Z6A1 and Z1A1 were demonstrated in *Figure 6.4* and *Figure 6.5* respectively.

a)                                                                   b)
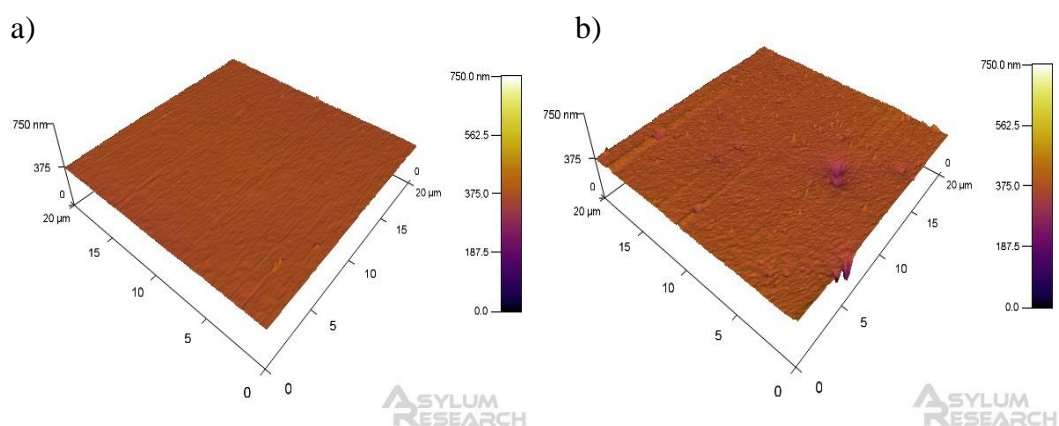


Figure 6.4 - 20 µm AFM images of Z6A1 cast films before degradation (a) and after 60 days of degradation in 5% $H_2O_2$ solution (b).

a)                                                                   b)
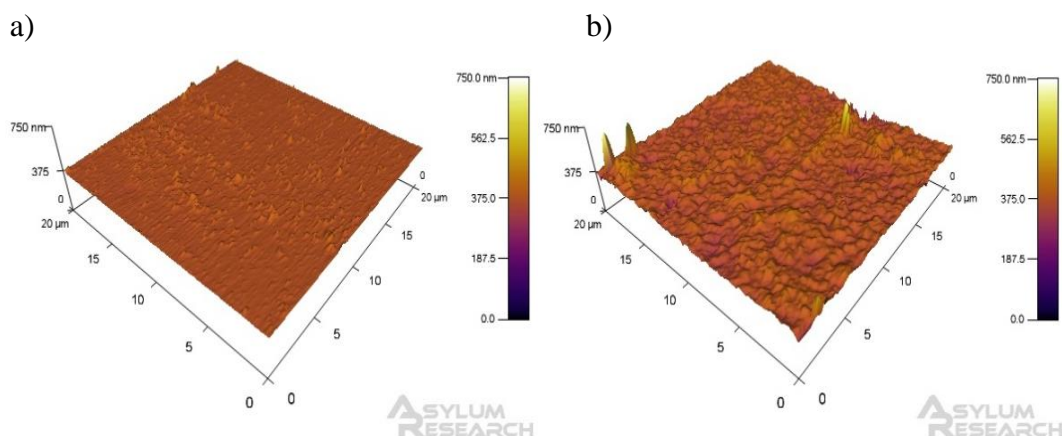


Figure 6.5 - 20 µm AFM images of Z1A1 cast films before degradation (a) and after 60 days of degradation in 5% $H_2O_2$ solution (b).

**Mechanical properties**

The bulk and micro-mechanical properties of solvent-cast films stored in an oxidative solution over a period of 90 days were analysed. The mean and standard deviation of three repeats obtained from three samples is shown in *Table 6.3* below. Tensile moduli were not statistically different for Z1A1 ($p > 0.05$) and Z6A1 ($p > 0.05$).

|  | Tensile modulus (MPa) | |
|---|---|---|
|  | Before | After |
| Z1A1 | 15.78 ± 0.81 | 15.17 ± 0.58 |
| Z6A1 | 399.79 ± 31.70 | 411.85 ± 29.06 |

Table 6.3 - Table showing bulk mechanical modulus of Z1A1 and Z6A1 both before and after 60 days storage in an oxidative solution (n = 3).

The indentation moduli were then investigated using the dedicated nano-indenter. Samples from before and after 60 days stored in an oxidative solution were indented consecutively. The resulting means and standard deviations from three samples were shown in *Table 6.4* below. Indentation moduli were statistically similar for both Z1A1 ($p > 0.05$) and Z6A1 ($p > 0.05$).

|  | Indentation modulus (MPa) | |
|---|---|---|
|  | Before | After |
| Z1A1 | 4.23 ± 0.14 | 4.13 ± 0.13 |
| Z6A1 | 44.10 ± 1.47 | 42.99 ± 2.23 |

Table 6.4 - Table showing indentation modulus of Z1A1 and Z6A1 both before and after 60 days of storage in an oxidative solution (n = 24).

## 6.3.3. Degradation of electrospun fibres in an oxidative solution

Electrospun samples were stored in a solution if 5 % $H_2O_2$ to observe whether the increased surface area to volume ratio had any substantial influence on the general surface properties of the individual fibres. Scanning electron microscopy carried out on the micro-metre scale revealed no obvious changes at either low or high magnification with the presented overall morphology remaining the same in samples after 90 days of storage in an oxidative solution. A representative image from before immersion and after 60 days of immersion was presented in *Figure 6.6* (Z1A1), *Figure 6.7* (Z6A1) and *Figure 6.8* (PCL) below.

a)                                      b)
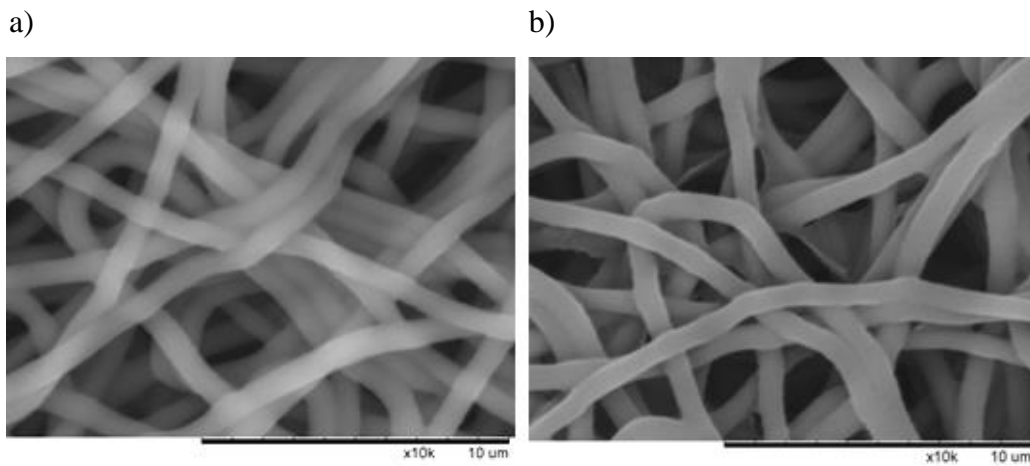


Figure 6.6 - SEM micrographs of electrospun Z1A1 before storage and after 60 days storage in a solution of 5 % H2O2 (x10,000).

a)                                      b)
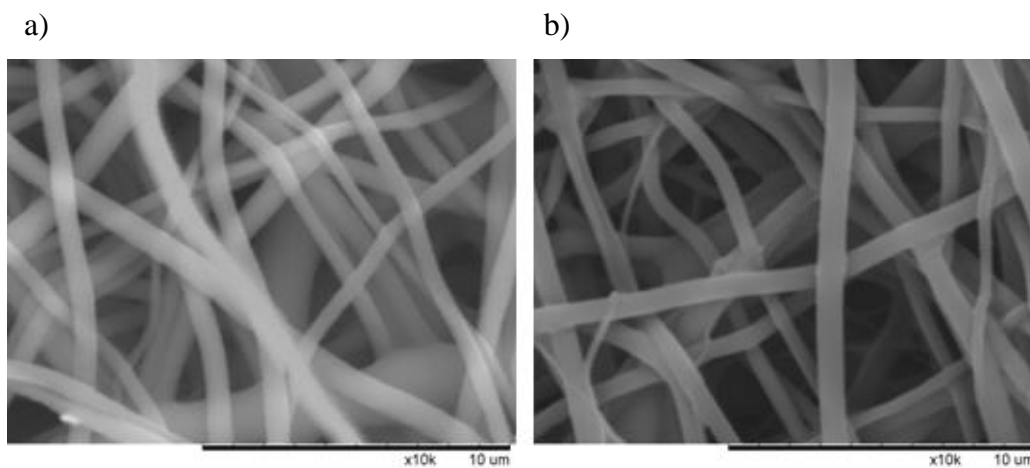


Figure 6.7 - SEM micrographs of electrospun Z6A1 before storage and after 60 days storage in a solution of 5 % $H_2O_2$ (x10,000).
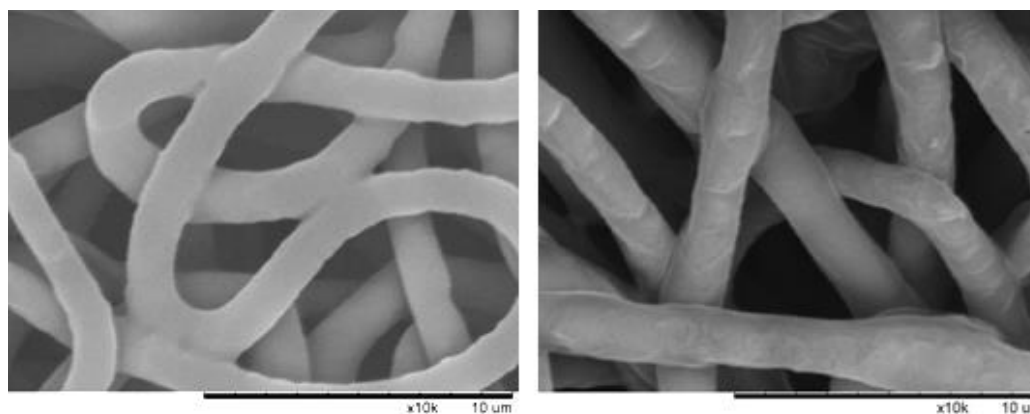


Figure 6.8 - SEM micrographs of electrospun PCL before storage and after 60 days storage in a solution of 5 % $H_2O_2$ (x10,000).

## 6.4. Discussion

Degradation testing of solvent-cast films carried out on Z1A1 and Z6A1 in a physiological solution and an oxidative solution resulted in no significant change in mechanical properties over the periods investigated. Overall structural integrity was maintained in all the samples tested with tensile testing and surface indentation demonstrating no significant difference over the periods of immersion. This meant that medical devices manufactured from *Biomer Technology Limited $b_9$* polyurethane grades would demonstrate no changes in their ability to bear loads over the periods investigated. Meijs *et al*. also performed mechanical testing on poly(ether) urethane after degradation [164]. Comparing results to what was observed by Meijs *et al.* was not possible as samples were stored in a considerably more aggressive environment (25 % $H_2O_2$ at 100 $^o$C). However, they demonstrate that different formulations of poly(ether) urethane exhibit different rates of degradation highlighting the need for characterisation of different formulations.

The surface topography of each solvent-cast film was investigated using AFM and an increase in roughness was observed in PCL solvent-cast films when stored in PBS. This was however not observed when polyurethane films of either grade were stored in similar conditions. The surface topography and the overall surface roughness observed were not statistically different over the 90 days of immersion in PBS. This indicated that even after 90 days stored in PBS, the grades of polyurethane investigated did not degrade topographically.

AFM also revealed a significant change in surface topography across all the sample materials tested when stored in an oxidative solution at 37 $^o$C. Similar to experiments carried out in PBS, PCL demonstrated an increase in surface roughness after 15 days of immersion. Both grades of polyurethane also demonstrated an increase in surface roughness after 15 days of immersion with the mean roughness increasing from 3.40 nm to 15.05 nm in Z1A1 and from 2.62 nm to 5.43 nm in Z6A1 over this period. The spread of data also increased significantly with the standard deviation increasing from 1.4 nm to 4.0 nm in Z1A1 and 0.57 nm to 2.34 nm in Z6A1. This increase in standard deviation of surface roughness was not only attributed to an

increase in variability across different samples but also to an increase in variability at different locations on the same sample. Since AFM scans were performed at 20μm x 20μm, the increase of surface roughness can only be ascribed to an overall increase in surface roughness and could not be attributed to specific phases within the micro-structure. Yang *et al*. have also investigated changes in surface morphology of polyurethane after a weathering process using AFM [305]. The accelerated weathering technique they used involved cyclic exposure to UV and condensation. Although the degradation protocol was completely different, roughening of surface topography on the nano-scale was reported even after 21 days of exposure.

As previously outlined, Chung *et al.* have reported that an increase in roughness of 10 nm had an increase in HUVEC adhesion and growth [308]. The nano-metre scale increase in roughness observed in polyurethane could have an influence on cell behaviour. With the mean surface roughness increasing from 3.40 nm to 15.05 nm in Z1A1 solvent-cast films, results discussed by Chung *et al.* would indicate a change in cell behaviour on such surfaces.

Detailed nano-scale analysis of electrospun fibres could not be carried out empirically. This was due to the large variation in nanoscale topography (*Section 4.3.3.2*) coupled with the fact that nano-indentation could only result in relative values (*Section 4.3.1.1*) within the same sample. Micro-metre scale analysis carried out using SEM was unable to detect any large differences in overall morphology across all three polymers after 90 days of storage in an oxidative solution. However, results obtained from solvent-cast films indicated a change on the scale of a few nanometres which could not be observed using the existing SEM setup. It could therefore only be assumed that similar changes occurred on electrospun mats.

## 6.5. Conclusions

The aim of this series of experiments was to investigate whether any nano-scale topographical changes occurred in two *Biomer Technology Limited b₉* polyurethane grades after long term storage in both a physiological solution and an oxidative solution. No changes were observed when these samples were stored in a physiological solution over a 90 day period while an increase in nano-scale roughness was observed when samples were stored in an oxidative solution after 15 days. These changes appear to plateau after 30 days and further investigation is warranted to confirm whether surface roughness continues to increase after 60 days of storage in an oxidative solution. It was suggested that the changes observed in surface roughness could influence cell behaviour as discussed in literature [109, 308, 309].

The changes observed after 60 days in an oxidative solution at 37 $^{\circ}$C were relatively small and would only influence the cellular scale. No significant changes were observed when mechanical properties were analysed. This meant that a tissue engineered product manufactured from these materials would have an unaltered ability to bear load.

Results obtained from this study were only representative of these polymer grades and would vary if a different chemical composition was used in the formulation of the polymers [164]. This range of polymers is formulated using a polyether diol which has previously been shown to be least susceptible to hydrolysis when compared to other soft segment compositions [301]. However, the mechanism that causes this change in surface roughness still needs to be investigated for a better understanding of the process involved. Different compositions of polyurethane could also be investigated in order to confirm that this change in nano-scale surface roughness is not an attribute of the current formulation.

# Chapter 7

# Initial Assessment of Cell Attachment

## 7.1. Introduction

Cell adhesion involves several processes and loss of cell anchorage is usually followed by anoikis [102, 165]. Cell viability has also been shown to largely depend on both the material as well as the form of the substrate [314]. Sangsanoh *et al.* investigated the ability of four different cell types to attach and proliferate on electrospun chitosan substrates when compared to solvent-cast films of the same material [315]. They highlight differences in cell behaviour between the two forms and demonstrate that growth on the electrospun substrates varied depending on the cell type investigated.

After having successfully fabricated and characterised solvent-cast films and electrospun mats from the *Biomer Technology Limited* $b_9$ polyurethane family, an initial assessment of cell attachment was performed. The aim of this *Chapter* was to investigate whether it was possible to culture cells on the *Biomer Technology Limited $b_9$* thermoplastic polyurethane range in both solvent-cast and electrospun forms. Two grades of polyurethane- Z1A1 and Z6A1, were selected for their wide difference in both bulk and nano-mechanical properties while maintaining similar polymer chemistry *(Section 3.2.2)*.

Experiments were carried out on three different adherent cell types, a fibroblast cell line, a neuroblastoma cell line and a primary endothelial cell line harvested directly from porcine pulmonary arteries. These different cell types were used in an attempt to encompass a range of cellular behaviour. Fibroblasts have been shown to prefer relatively stiff substrates while neuronal cells tend to thrive on softer substrates [153]. The use of immortalised cell lines facilitates the acquisition of such information due to their cost effectiveness, ruggedness and relative ease to maintain in culture. However, mutations in the genome necessary to produce such attributes meant that the biology of these cells might have been altered and must be taken into consideration when making any analysis [316]. Primary porcine pulmonary artery endothelial cells were also used in this experiment alongside the immortalised cell lines. Primary cells were harvested directly from living tissue and were only passaged a few times before being discarded to avoid changes in phenotype. This therefore meant that these cells were more representative of their main functional component within the tissue.

The experiments were also carried out on the different forms that were characterised in the previous *Chapter*, namely, solvent-cast films and electrospun mats. Solvent-cast and electrospun mats were manufactured from both Z1A1 and Z6A1, and the activity of each cell type when seeded on the different substrates was investigated. The experiment investigated three substrate variables: 1) solvent-cast films of Z1A1 and Z6A1, 2) electrospun Z1A1 and Z6A1 films of similar fibre diameter 3) electrospun Z1A1 films with two different fibre diameter distributions.

## 7.2. Materials and Methods

### 7.2.1. Scaffold preparation

Solvent-cast films were manufactured from solutions of 15 wt/wt % polymer in DMF using the procedure outlined in *Section 3.3.3*. The glass interface was used as this side was shown in *Section 4.3.2* to present similar surface morphology across the different materials. In order to further confirm that the solvent-cast films manufactured for use in this study had a similar surface roughness, 50 μm images were obtained using AFM from five different locations on the solvent-cast films and roughness was calculated from flattened images as outlined in *Section 3.5.2.6*. Disks of 13 mm diameter were then punched out of each solvent-cast film for use as substrates in these experiments.

Electrospun substrates were manufactured directly onto 13 mm diameter 316L stainless steel disks as shown in *Figure 7.2*. These were mounted onto a flat collector using conductive tape. Samples were then removed from the collector and dried at 70 °C for 3 hours to ensure complete removal of solvent. The electrospinning parameters used to produce large diameter Z1A1 fibres were outlined in *Table 3.2 (b)*, small diameter Z1A1 in *Table 3.2 (d)*, and Z6A1 electrospun mats in *Table 3.2 (e)*.

*Silastic® MDX4-4210* biomedical grade poly(dimethyl siloxane) (PDMS) was used as a negative control in these cell contact experiments. Previous publications have shown that this grade of PDMS was non-toxic to cells but discourages cell adhesion due to its elevated hydrophobicity [317, 318]. To reduce artefacts brought around by cells growing on a different surface to the one being tested, all substrate were mounted onto the bottom of a *ThinCert*[TM] using the same cell culture PDMS as shown in *Figure 7.1*. The PDMS used was a two-component product and was vulcanised by mixing the elastomer component with 10 wt/wt% of curing agent. This was then followed by thorough mechanical stirring and degassing. PDMS substrates were manufactured by injecting PDMS solution into the bottom of a well. PDMS was allowed to completely set at room temperature for twice the recommended

setting time (2 days). *Figure 7.3* shows the three resulting substrate types: solvent-cast, bare metal and electrospun.



Figure 7.1 - Schematic diagram of a *ThinCert* in a well (Left). Photograph of a *ThinCert* showing a metal substrate mounted using PDMS (Right).
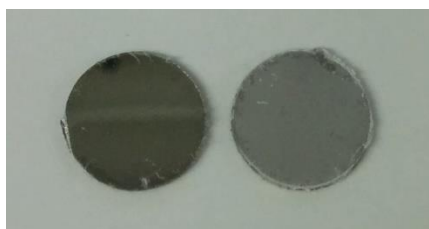


Figure 7.2 - Photograph showing fibres electrospun directly onto a 316L stainless steel disks. Bare metal disk (Left), coated disk (Right).



Figure 7.3 - Photograph of *ThinCert* with solvent-cast Z6A1 (Left), *ThinCert* with bare metal disk (Middle), *ThinCert* with electrospun mat (Right).

## 7.2.2. Experimental setup

Three separate experiments were set-up to investigate three substrate variables: 1) solvent-cast films of Z1A1 and Z6A1, 2) electrospun Z1A1 and Z6A1 mats of similar fibre diameter and 3) electrospun Z1A1 mats with two different fibre diameter distribution. 12-well plates were used and each plate was set up with three replicates for each variable. Tissue culture plastic (TCP) was used as the positive control in each experiment. The setup of each plate was shown in *Table 7.1* below.

Cast film experiment setup

|   | A | B | C | D |
|---|---|---|---|---|
| 1 | 1 | 2 | 3 | 4 |
| 2 | 1 | 2 | 3 | 4 |
| 3 | 1 | 2 | 3 | 4 |

1  Z1A1 Glass interface solvent-cast film
2  Z6A1 Glass interface solvent-cast film
3  PDMS (-ve control)
4  Tissue culture plastic (+ve control)

Electrospun polymer grade experiment

|   | A | B | C | D |
|---|---|---|---|---|
| 1 | 1 | 2 | 3 | 4 |
| 2 | 1 | 2 | 3 | 4 |
| 3 | 1 | 2 | 3 | 4 |

1  Z1A1 fibres
2  Z6A1 fibres
3  Bare metal disk
4  Tissue culture plastic (+ve control)

Electrospun fibre diameter experiment

|   | A | B | C | D |
|---|---|---|---|---|
| 1 | 1 | 2 | 3 | 4 |
| 2 | 1 | 2 | 3 | 4 |
| 3 | 1 | 2 | 3 | 4 |

1  Z1A1 Large diameter fibres
2  Z1A1 Small diameter fibres
3  Bare metal disk
4  Tissue culture plastic (+ve control)

Table 7.1 - Setup of 12-well plates in the 3 different experiments

A total of 27 12-well plates were set-up. Three cell types were investigated: 3T3 fibroblasts, SH-SY5Y neuroblastoma cells and primary porcine pulmonary artery endothelial cells (PPAEC). Three experiments were set-up for each cell type as outlined in *Table 7.1* with three replicates from the same passage in the same plate. Each experiment was also replicated three times from a different cell passage for each cell type. *Figure 7.4* demonstrates the overall experimental setup with three different cell types, three separate experiments for each cell type, three plates for each experiment of each cell type with a different passage number and three replicates for every variable in each plate with cells from the same passage number.
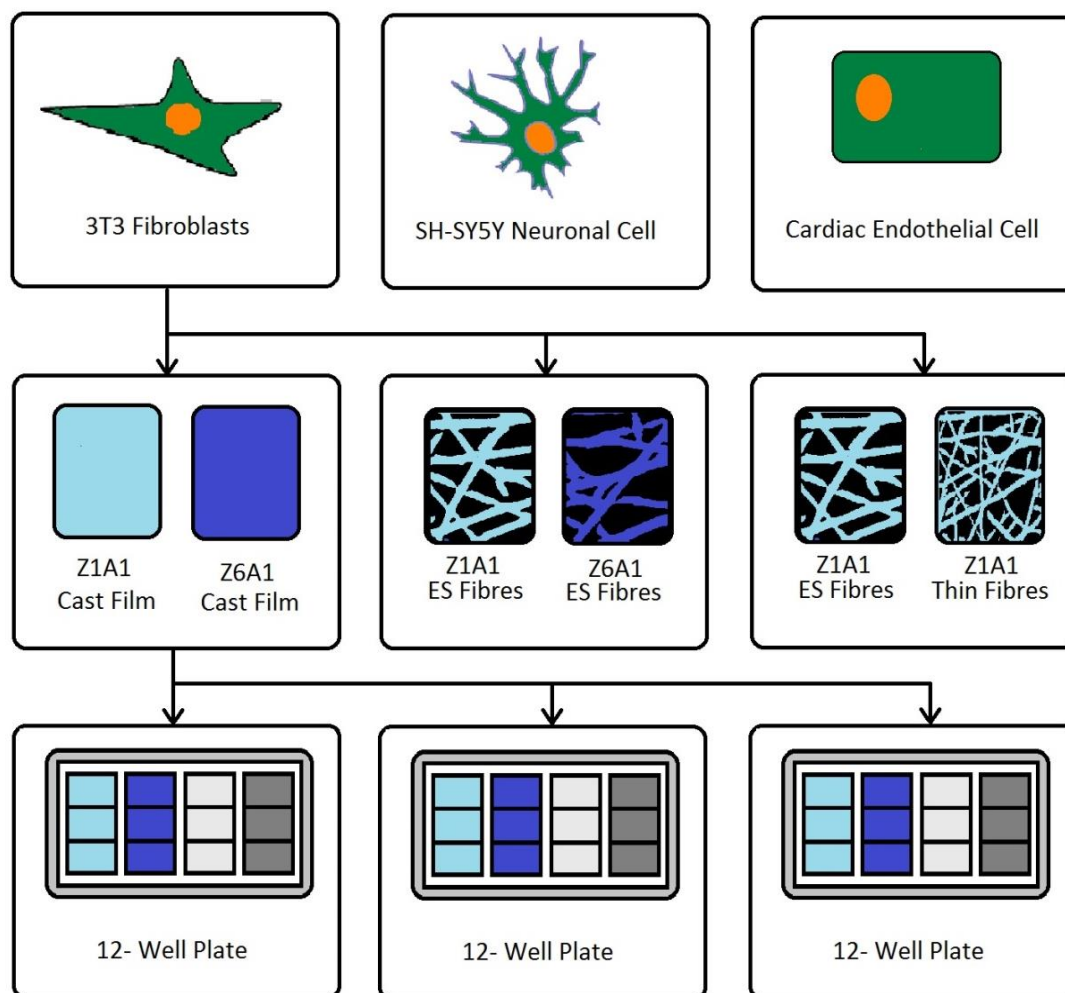


Figure 7.4 - Schematic diagram showing the cell contact experiment layout. Three cell types were investigated, three separate experiments were carried out for each experiment. Each experiment was carried out three times in a different 12-well plate with three replicates for each variable in each plate.

## 7.2.3. Cell Culture

Immortalised mouse fibroblast cell line 3T3 was cultured in Dulbecco's Modified Eagle's Medium (DMEM) (*Lonza, UK*) supplemented with 10 % fetal bovine serum (*Gibco, UK),* penicillin (100 units/ml) (*Gibco,UK*) and streptomycin (0.1 mg/ml) (*Gibco, UK*) in T-25 flasks at 37 °C in a humidified 5 % $CO_2$/air atmosphere. Cells were passaged when 90 % confluency was reached. Cells were washed with sterile Versene (*Lonza, UK*) twice and incubated with 1 ml of trypsin (*Gibco, UK*) for 2 minutes. The enzymatic reaction was then stopped with 5 ml of culture medium. Cells were split in a desired ratio and replaced into a new T-25 flask with fresh culture medium up to passage number 50.

SH-SY5Y human neuroblastoma cells were cultivated in a 1:1 mix of DMEM (*Lonza, UK*) and F-12 nutrient mix with *GlutaMAX* (*Gibco, UK*) and supplemented with 10 % fetal bovine serum (*Gibco, UK*), penicillin (100 units/ml) (*Gibco,UK*) and streptomycin (0.1 mg/ml) (*Gibco, UK*) in T-25 flasks at 37 °C in a humidified 5 % $CO_2$/air atmosphere. SH-SY5Y cells were passaged up to 20 times before being discarded. This cell line can be differentiated into mature neuronal cells possessing a neuron-like phenotype through the manipulation of the culture medium such as the addition of retinoic acid [319, 320]. Unlike differentiated cells, undifferentiated cells still express immature neuronal markers and can proliferate continuously. Since assays performed in this study aimed to investigate the ability culturing cells on polyurethane substrates, undifferentiated cells were used.

Primary endothelial cells were harvested from a porcine pulmonary artery by lightly scraping the tunica intima using a sterile scalpel. Cells were cultured in a 1:1 mix of Waymouth medium and F-12 nutrient mix (*Gibco,UK*) supplemented with 10 % fetal bovine serum (*Gibco, UK*), penicillin (100 units/ml) (*Gibco,UK*) and streptomycin (0.1 mg/ml) (Gibco, UK) in T-25 flasks at 37 °C in a humidified 5 % $CO_2$/air atmosphere. PPAEC were passaged up to 5 times before being discarded to avoid changes in the phenotype.

### 7.2.4. Cell seeding protocol

All the manufactured substrates were cleaned and sterilised prior to use in cell culture. Samples were cleaned by sonication for 15 minutes in a solution of 15 % ethanol to remove deposits. Each sample was then allowed to dry in a laminar flow cupboard for at least 8 hours followed by UV sterilisation for 15 minutes on each of the two sides of the *ThinCert* samples.

Cells were passaged using the standard procedure described previously and a solution of 30,000 cells/ml was produced. Cell seeding densities were kept constant at 112 cells/mm$^2$ across all substrates. This meant that 0.5 ml of the cell solution was placed in samples mounted on *ThinCert* as these had a surface area of 133 mm$^2$. 1.3 ml of the cell solution was added to substrates directly at the bottom of the well (PDMS and TCP) as these had a surface area of 346 mm$^2$.

The same cell seeding density per unit area was used since this resulted in confluency being kept constant across each substrate if cells grew at the same rate. The volume of media used was also proportional to the well size and meant that the same amount of nutrients were available per cell across both sizes of wells. In turn, when *AlamarBlue* was added, the volume of media within each well was proportional to the well surface area and thus the original cell seeding density. Cells where then incubated at 37 $^o$C and 5 % $CO_2$ for 72 hours providing sufficient time for attachment and proliferation.

## 7.2.5. AlamarBlue

*AlamarBlue* (*ThermoFisher Scientific UK)* is a reagent used to assess cellular health and proliferation. The assay is non-toxic and water soluble thus eliminating the need for washing, fixing and extraction steps required by other assays. *AlamarBlue* incorporates both a flurometric and colorimetric indicator based on an oxidation-reduction indicator in response to a chemical reduction of growth medium resulting from cell growth. As cells proliferate, innate metabolic activity results in a chemical reduction of *AlamarBlue*. This reduction causes the indicator to change from an oxidized form (non-fluorescent and blue) to a reduced form (fluorescent and red). This change can then be quantified by evaluating the absorbance at a wavelength of 570 nm and 600 nm or by measuring the fluorescence with excitation wavelength at 530 nm - 560 nm and emission wavelength at 590 nm.

A *Multiskan Ascent 96* Plate Reader was used to obtain these readings. This system provided accurate and reliable measurements within a few seconds and was completely automated. A range of filters were available including a 570 nm and a 600 nm filter, ideal for use with *AlamarBlue* in colorimetric analysis.

**Experimental methodology**

*AlamarBlue* was used to measure cell viability after 3 days of culture in each of the samples. Culture media was pipetted out of the substrates and fresh media with 10 % *AlamarBlue* was added slowly to reduce cell detachment. A separate 12 well plate was used to store controls needed for the *AlamarBlue* readout at the same conditions. Three wells were filled with the respective complete cell media without *AlamarBlue* and another three wells were filled with the respective complete media and 10 % *AlamarBlue* to control for 0 % and 100 % reduction during the *AlamarBlue* reduction calculation. Cells were then cultured for another six hours in the *AlamarBlue* solution which was shown to be sufficient to detect changes in cell densities for all cell types. Media from each well was then transferred into a 96 well plate along with control media and analysed using the *Multiskan Ascent 96* plate reader.

The following procedure was used to obtain the percentage reduction of *AlamarBlue*.

The correction factor $R_0$ was found using:

$$R_0 = \frac{AO_{LW}}{AO_{HW}} \qquad\qquad 4.1$$

Where: $AO_{LW}$ was the absorbance of AB in media at the lower wavelength

$\qquad$ $AO_{HW}$ was the absorbance of AB in media at the higher wavelength

The percentage reduction of *AlamarBlue* was calculated from:

$$Percentage\ reduction\ = [A_{Lw} - (A_{HW}\ x\ R_0)]\ x\ 100 \qquad 4.2$$

Where: $A_{LW}$ was the absorbance at the lower wavelength minus the media blank

$\qquad$ $A_{HW}$ was the absorbance at the higher wavelength minus the media blank

In order to represent the data in an unbiased format, a number of steps were performed as shown in *Figure 7.5* below. The mean from three wells for each variable with the same cell passage was first calculated from every culture plate. To eliminate issues arising from differences in cell seeding densities across the different plates as well as environmental issues affecting the rate of growth of cells, each variable was normalised against tissue culture plastic. The growth of cells on tissue culture plastic was assumed to be constant throughout each experiment and set as the maximum possible growth over the period of incubation. The resulting normalised means obtained from the three culture plates from different passages were then tabulated and the mean and standard deviation for each variable was calculated.
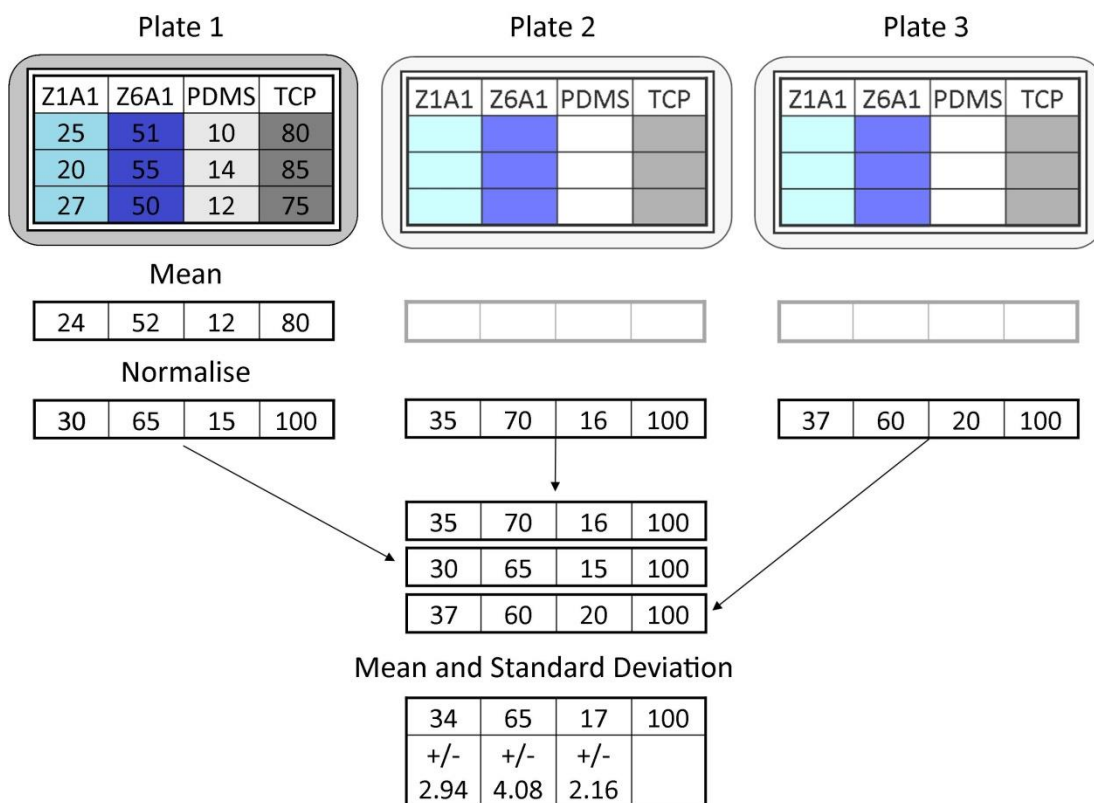
Figure 7.5 - Schematic diagram of data analysis regime showing the mean activity obtained from the *AlamarBlue* assay first being obtained from a single plate, normalised and then grouped with means obtained from another 2 plates.

## 7.2.6. Live/dead assay

A *Live/Dead* assay (*ThermoFisher, UK*) was used to visualise cells on substrate surfaces. This assay was used for its low toxicity, ease of use and sensitivity. *Calcein-AM* dyed live cells (visualised as green) while *Ethidium Homodimer-1* dyed dead cells (visualised as red). A *Zeiss Axiovision Imager Z1* was used to visualise stained cells using its range of objectives and dedicated filters.

**Experimental methodology**

After 72 hours in incubation, cells were stained using a live/dead assay and imaged using a fluorescence microscope to investigate whether cells were in fact attached to the surface being investigated. A solution of 2 mM *EthD-1* and 4 mM C*alcein AM* in tissue culture grade Dulbecco's Phosphate-Buffered Saline (D-PBS) was prepared. Culture media was pipetted out of the *ThinCert* and the substrate was rinsed in D-PBS. 150 µl of the staining solution was added slowly to avoid cells detaching from the surface. Cells were then incubated for 15 minutes. The stain was then pipetted out and D-PBS was used to rinse the substrate twice. This was then removed from the base of the *ThinCert* and placed in a petri dish. Enough D-PBS to cover the substrate was added into the petri dish and the sample imaged using the *Zeiss Axiovision Imager Z1* fluorescence microscope. All images presented were obtained using a 10x lens and were 900 µm x 900 µm in size.

## 7.2.7. Statistical analysis

Experiments were repeated in triplicate as outlined in *Section 7.2*. All data presented throughout this *Chapter* are expressed as mean values ± standard deviation. Statistical significance was determined following a student's t-test. Comparisons having 'p' values less than 0.05 were deemed to be statistically significant.

## 7.3. Results

### 7.3.1. Scaffold Preparation

The resulting surface roughness of solvent-cast films on the glass interface was investigated using AFM. Five images were obtained from various locations on the solvent-cast film. The resulting images were flattened in both X and Y-axis and the surface roughness measured. The resulting data shows a surface roughness on Z1A1 cast films was 6.985 nm ± 1.388 nm while that on Z6A1 was 5.126 nm ± 2.381 nm.

### 7.3.2. Cell activity on solvent-cast films

*AlamarBlue* was used as described in *Section 7.2.5* to investigate cell activity on solvent-cast polyurethane of two different grades: Z1A1 and Z6A1. The resulting data was normalised against tissue culture plastic and presented in form of a bar chart (*Figure 7.6*). Results demonstrated that cell activity was statistically different between Z1A1 and Z6A1 solvent-cast films in 3T3 ($p < 0.05$) and SH-SY5Y ($p < 0.05$) and statistically similar in PPAEC ($p > 0.05$). When cell types were cultured on PDMS, the resulting activity was lower than solvent-cast films for all cell types ($p < 0.05$).
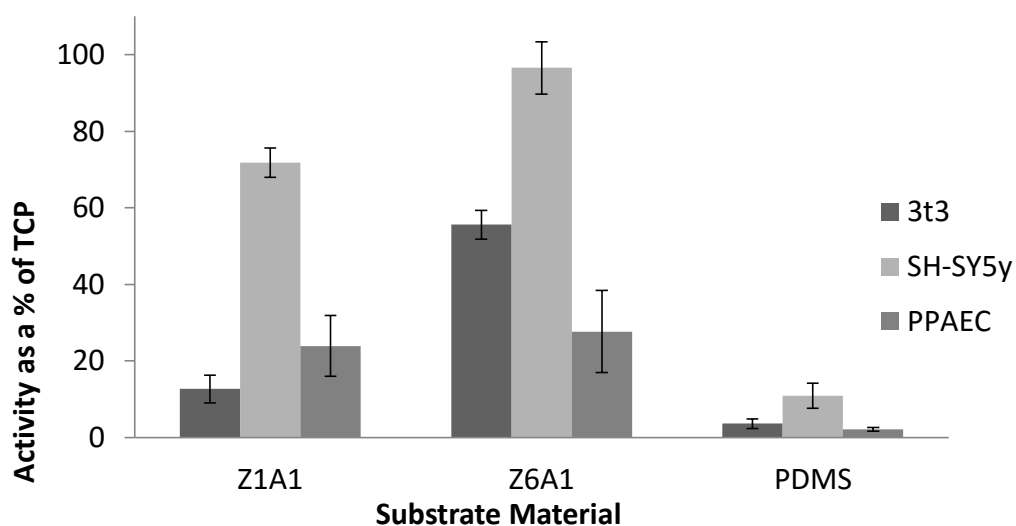


Figure 7.6 - Graph of mean and standard deviation of activity in three cell types when cultured on solvent-cast films calculated from reduction of *AlamarBlue* as a percentage of tissue culture plastic (n = 3).

## 7.3.3. Cell activity on electrospun fibres from different polymer grades

*AlamarBlue* was used as described in *Section 7.2.5* to investigate cell activity on electrospun polyurethane films of two different grades: Z1A1 and Z6A1. The resulting data was normalised against tissue culture plastic and presented in form of a bar chart (*Figure 7.7)*. Results demonstrated that cell activity was statistically similar between Z1A1 and Z6A1 electrospun mats in 3T3 ($p > 0.05$), SH-SY5Y ($p < 0.05$) and on PPAEC ($p > 0.05$). When cell types were cultured on bare metal discs, no statistical difference was observed with either Z1A1 or Z6A1 electrospun mats of either cell type ($p > 0.05$).
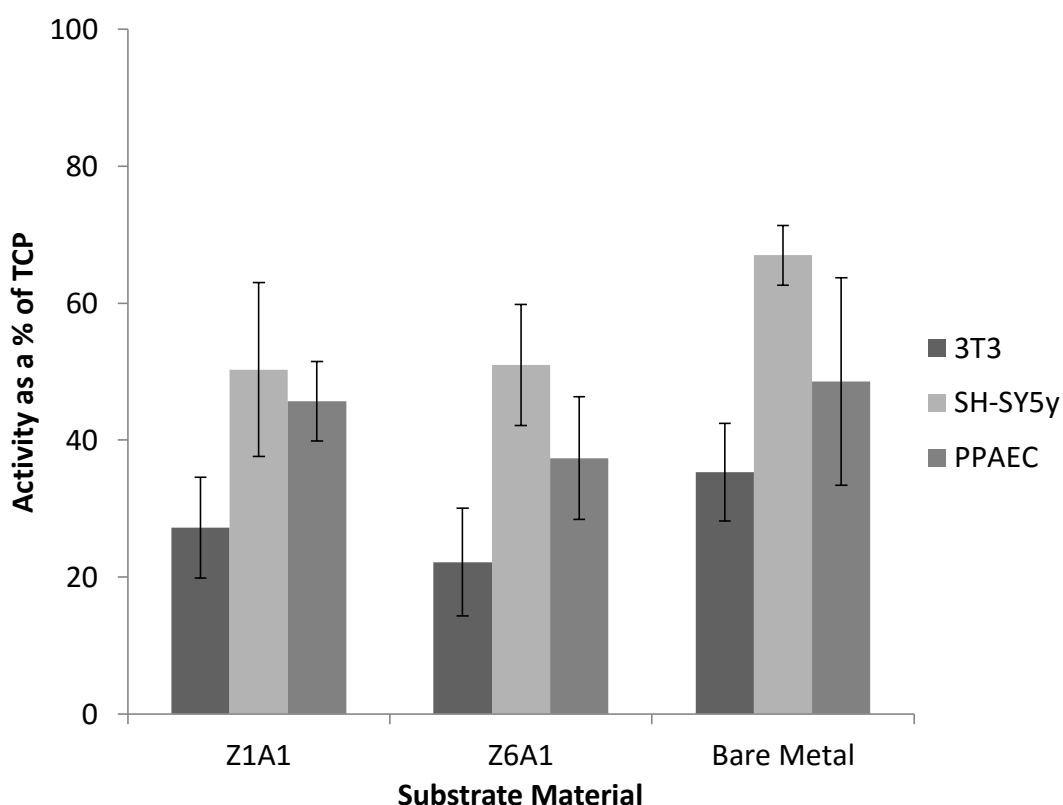


Figure 7.7 - Bar chart showing mean and standard deviation of cellular activity when cultured for 3 days on polyurethane electrospun mats of Z1A1 and Z6A1 calculated from the reduction of *AlamarBlue* as a percentage of tissue culture plastic ($n = 3$).

## 7.3.4. Cell activity on electrospun fibres from different fibre diameter distribution

Cell activity was investigated using *AlamarBlue* as described in *Section 7.2.5* on electrospun polyurethane films of two different fibre diameter distributions. The resulting data was normalised against tissue culture plastic and presented in form of a bar chart in *Figure 7.8*. Results demonstrated that cell activity is statistically similar between Z1A1 large and Z1A1 thin electrospun mats in 3T3 ($p > 0.05$), SH-SY5Y ($p < 0.05$) and in PPAEC ($p > 0.05$). When cell types were cultured on bare metal discs, no statistical difference was observed with either Z1A1 large or Z1A1 thin electrospun mats of either 3T3 ($p > 0.05$) or PPAEC ($p > 0.05$). A statistical difference was observed when SH-SY5Y cells were cultured on bare metal discs when compared to both Z1A1 large and Z1A1 thin electrospun fibres.
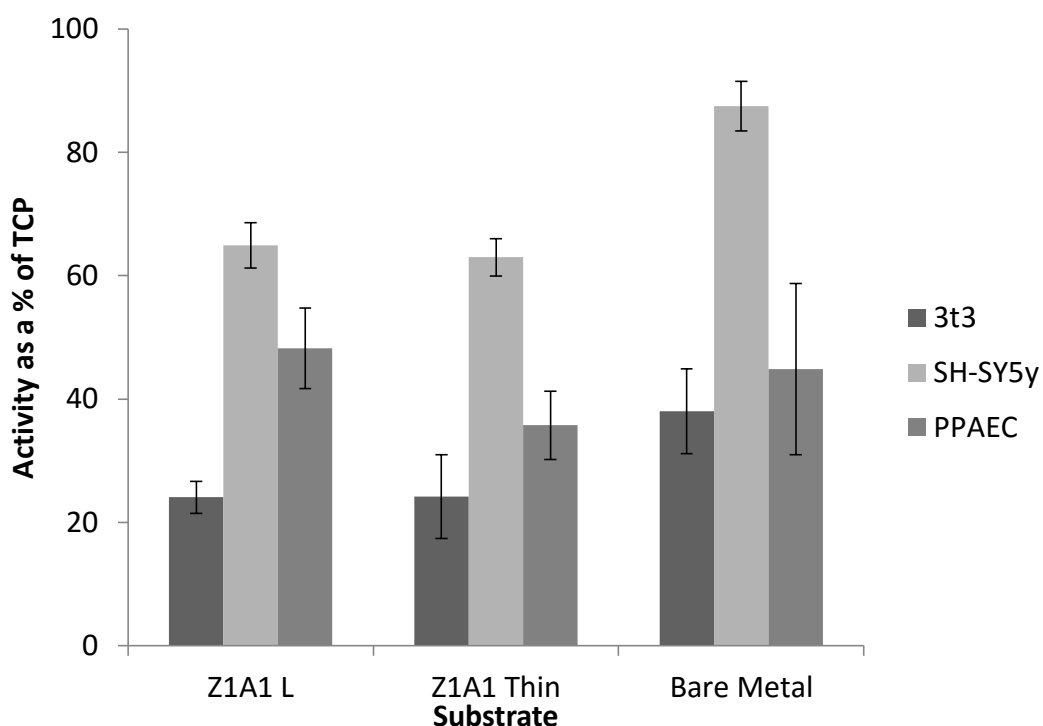


Figure 7.8 - Chart showing mean and standard deviation of cellular activity when cultured for 3 days on polyurethane electrospun mats of Z1A1 with different fibre diameter distribution calculated from the reduction of *AlamarBlue* as a percentage of tissue culture plastic (n = 3).

## 7.3.5. Live/dead assay

Imaging using the *Zeiss Axiovision Imager Z1* fluorescence microscope of the various cell types on the different substrates was carried out using a *Calcein AM* and *EthD-1* solution to investigate whether cells were attached to the substrate in question rather than the surrounding areas. Live cells, stained with *Calcein AM,* were represented in green while dead cell nuclei, stained with *EthD-1,* were represented in red. Imaging on tissue culture plastic and bare metal was relatively straightforward as cells were on a single focal plane. Imaging of cells on solvent-cast films in phase contrast revealed the topography that was previously observed by AFM in *Section 4.2.3* as shown in *Figure 7.9*. Even though cells were cultured on the glass interface of the solvent-cast film, light was diffracted when passing through the air interface making it difficult to focus on the correct plane.
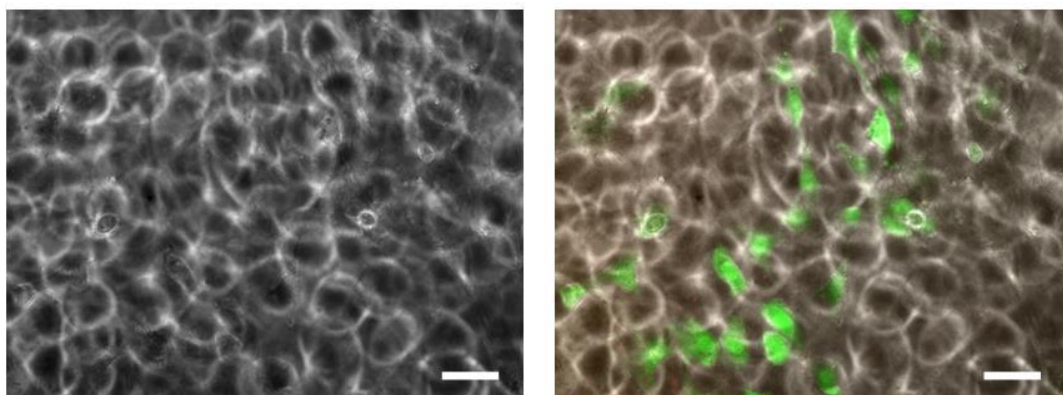


Figure 7.9 - Composite image of 3T3 Fibroblasts on Z6A1 solvent-cast film. Phase image (left) and fluorescent image overlaid on phase image (right). (Scale bar 100 μm)

When imaging of cells on electrospun fibres was attempted, similar to imaging on solvent-cast films, the depth of field was not limited to a single plane of focus as illustrated in *Figure 7.10*.
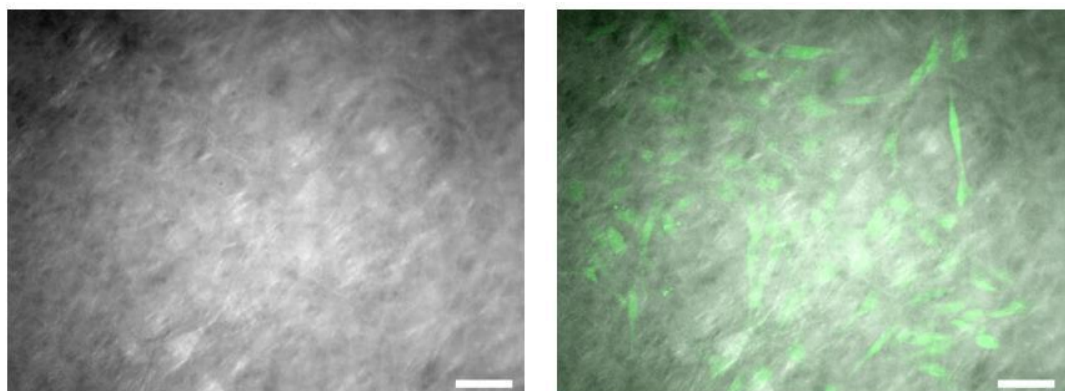
Figure 7.10 - Images of PPAEC on electrospun fibres. Optical phase image (left), optical phase image overlaid on fluorescent image (right). (Scale bar 100 µm)

### 3T3 Fibroblast cell line

Images of 3T3 fibroblast cell line obtained after three days in culture on respective substrates were shown in *Figure 7.11* below. 3T3 fibroblasts appeared to be attached to the substrates under investigation.
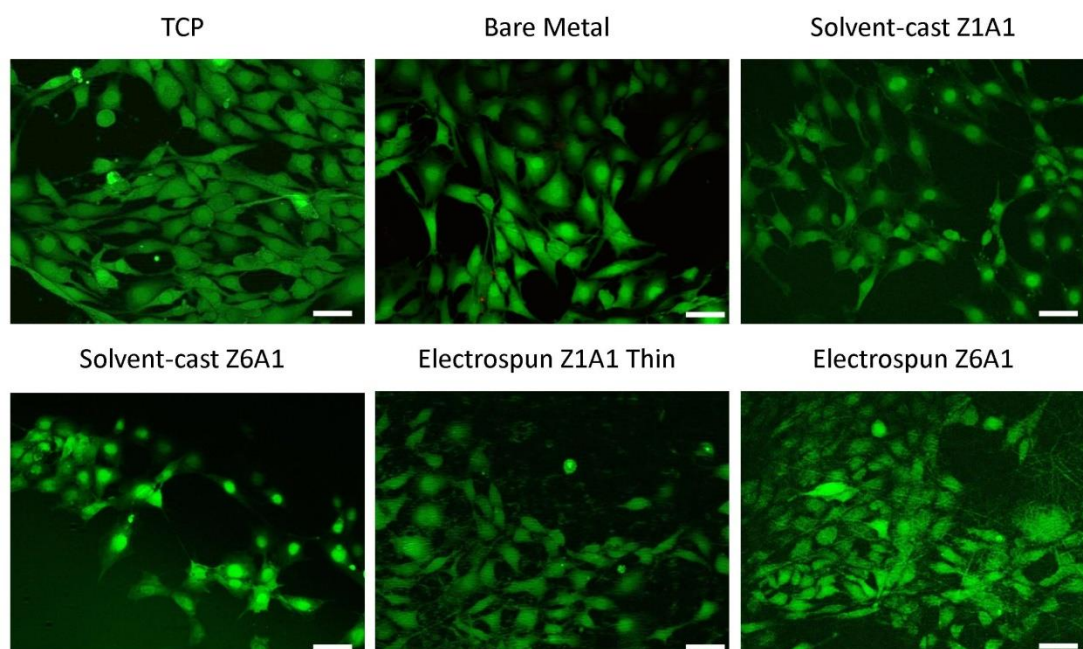


Figure 7.11 - Composite images of 3T3 fibroblasts cultured on various substrates. (Scale bar 100 µm)

## SH-SY5Y neuroblastoma cell line

Images of SH-SY5Y neuroblastoma cell line obtained after three days in culture on respective substrates were shown in *Figure 7.12* below. Cells appeared to be attached to the respective substrates.
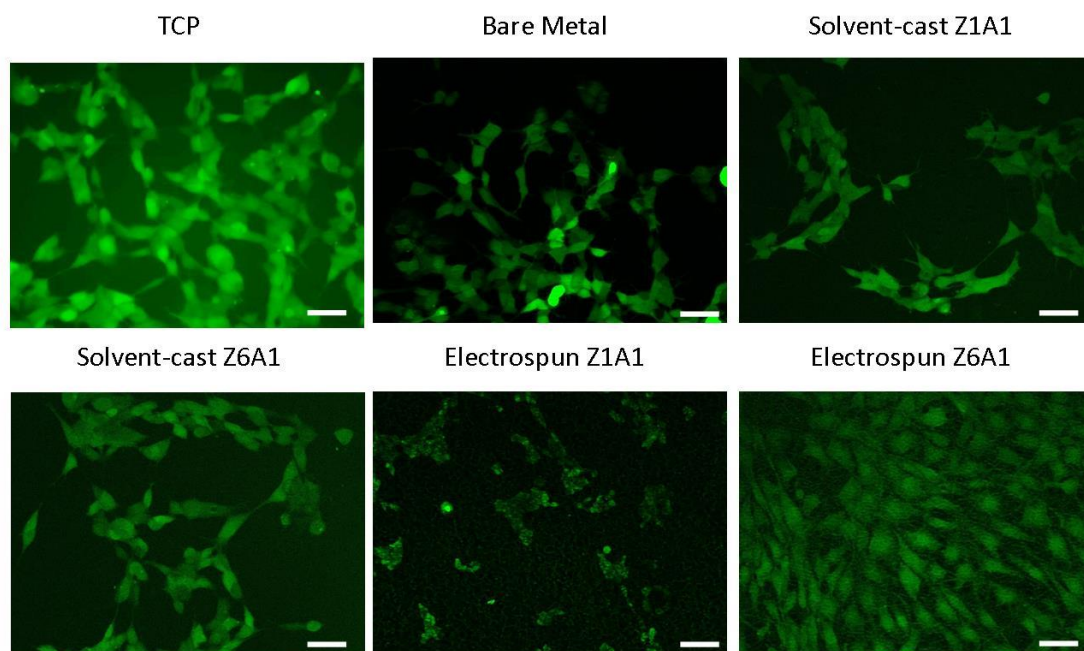


Figure 7.12 - Composite images of SH-SY5Y neuroblastoma cells cultured on various substrates. (Scale bar 100 µm)

## Primary porcine pulmonary artery endothelial cells

Images of PPAEC obtained after three days in culture on respective substrates were shown in *Figure 7.13*. Cells appeared to be attached to the respective substrates.
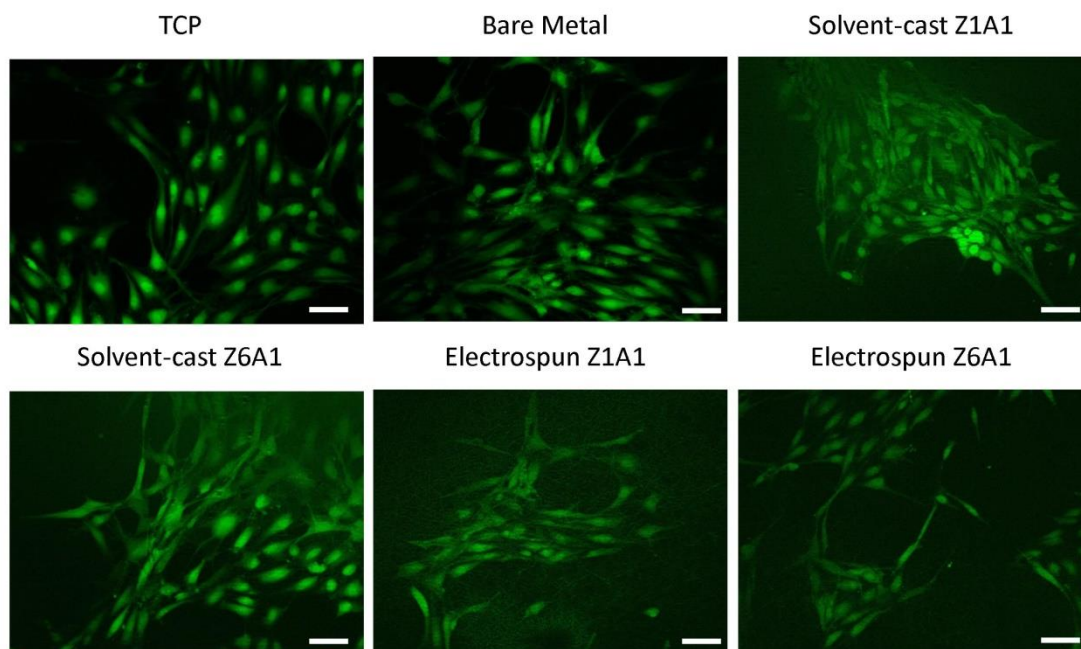
Figure 7.13 - Composite images of primary porcine pulmonary artery endothelial cells cultured on various substrates. (Scale bar 100 µm)

In all cases, the number of dead cells detected was much lower than the number of live cells. The concentration of *EthD-1* used was sufficient to stain dead cells as certain areas did reveal dead cells as shown in *Figure 7.14*
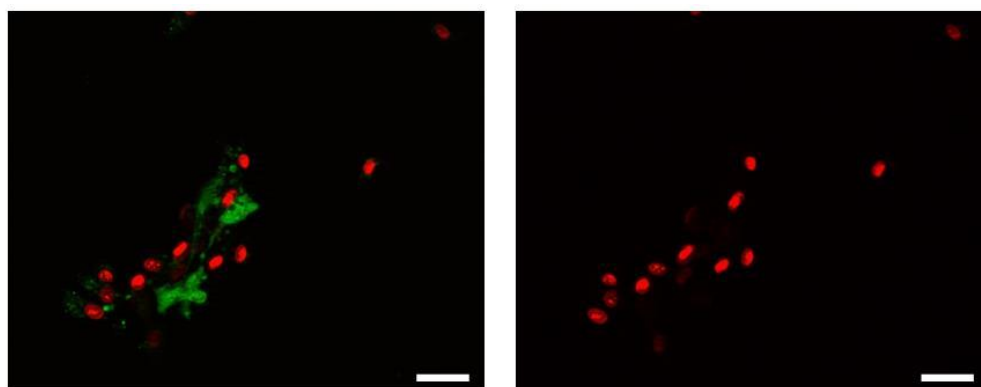


Figure 7.14 - Composite images of porcine pulmonary artery endothelial cells on a bare metal substrate coloured red (dead) and green (live). (Scale bar 100 µm)

## 7.4. Discussion

The 3T3 fibroblast cell line is a standard immortalised cell line that is widely used in experiments since these are very motile and multiply rapidly [321 – 323]. Lo *et al*. have shown that this cell line grows preferentially on stiffer substrates and also tends to migrate to stiffer areas when grown on substrates with a stiffness gradient [152]. This cell line appeared to attach and proliferate successfully when cultured on polyurethane solvent-cast films. Similar to observations made by Lo *et al*., a clear increase in activity was observed when these fibroblasts were cultured on the stiffer Z6A1 substrate ($p < 0.01$).

This observation was also made to a lesser degree when SH-SY5Y human neuroblastoma cells were cultured on solvent-cast films. Cells cultured on Z6A1 demonstrated no significant change when compared to those cultured on tissue culture plastic while only 71 % ± 3.8 % of this activity was seen when the same cell line was cultured on Z1A1. Unlike 3T3 fibroblasts, SH-SY5Y neuroblastoma cells were very slow growing and the absolute activity on tissue culture plastic was much lower when compared to the former (mean of 43 % ± 2.6 % reduction of *AlamarBlue* in 3T3 and 12 % ± 3 % in SH-SY5Y). This could have been counteracted by culturing SH-SY5Y cells for longer until the same degree of confluency observed in 3T3 fibroblasts was reached. In these experiments, this was not pursued in an attempt to keep all major variables the same across experiments with different cell types.

When primary porcine pulmonary artery endothelial cells were cultured on solvent-cast films, cells attached and proliferated successfully on both substrates. The activity of PPAEC was similar to that observed in 3T3 fibroblasts with absolute values on tissue culture plastic at 39 % ± 5 % reduction of *AlamarBlue*. Unlike the previous two cell lines, no significant difference was observed between the absorbance of *AlamarBlue* from cells grown on Z1A1 and Z6A1 solvent-cast films ($p = 0.408$). The use of a contractile cell type such as the smooth muscle cells found within the same porcine artery would have been preferred for such experiments.

Cells grown on PDMS substrates exhibited very low cellular activity across the range of cell types used. This was attributed to the fact that PDMS does not allow cells to adhere to its surfaces in the first place resulting in low motility and activity during the time period allowed [317, 318]. When media was changed to the *AlamarBlue* containing media for analysis, any live cells that were not adhered to the surface were washed away in the process.

All three cell lines were successfully cultured on electrospun fibres of both Z1A1 and Z6A1 with the same fibre diameter as well as on Z1A1 fibres with a smaller mean fibre diameter. All cell types demonstrated a decreased activity when compared with tissue culture plastic. This observation was attributed to the fact that unlike the polyurethane substrates, tissue culture plastic is routinely plasma treated in order to render the surface more conductive to cell attachment and proliferation. Amstein *et al.* reported favourable results when a number of cell types were cultured on such treated substrates [324]. When compared to tissue culture plastic, cell activity was supressed to different degrees depending on the cell type in question. The SH-SY5Y neuroblastoma cell line demonstrated the least reduction of activity (57.2 % of TCP) while 3T3 fibroblasts demonstrated the highest reduction in activity when cultured on electrospun polyurethane fibres (24.0 % of TCP)

Both 3T3 fibroblasts and SH-SY5Y neuroblastoma cells exhibited a significant difference in proliferation between cells cultured on Z1A1 and Z6A1 solvent-cast films. This difference was however not observed when electrospun mats of the same materials were investigated. The main differences between the two substrates were the mechanical properties. However, it was not possible to directly attribute differences in proliferation to the change in mechanical properties between the two substrates. The difference in protein absorption on the two materials was not investigated and could have a significant influence on the cell adhesion and proliferation. Further investigation into protein-binding behaviour on the different polymer grades would provide a better insight into cell adhesion. With polyurethane composed of two major chemical segments (soft segment and hard segment), it is unclear whether one segment has a higher affinity to cellular proteins over the other

[40]. With the ratios of the different chemical segments being different in the two polyurethane grades investigated, if this was shown to be true, it could have led to changes in protein absorption between the different polyurethane grades. George *et al.* demonstrated this using a poly(styrene-block-ethylene oxide) co-polymer surface coating which formed a micro-phase separated surface [325]. They conclude that the ratios of the two polymers in the final coating controlled protein adsorption and consequently cell attachment. The use of serum free media could help counteract this problem since the lack of growth and adhesion factors in the media reduces the bias brought around by differences in scaffold-protein interactions in the different grades of polyurethane [326]. Results obtained from cell culture in serum free media would therefore provide a more consistent and precise evaluation of cellular function on the various scaffold types.

When the growth of cells on electrospun polyurethane scaffolds was compared to that on bare metal substrates, only the SH-SY5Y neuroblastoma cell line demonstrated a significant difference (Z1A1 L: $p = 0.025$, Z6A1 : $p = 0.032$, Z1A1 T: $p = 0.003$). The activity observed when 3T3 fibroblast were cultured on bare metal substrates was statistically different when compared to large Z1A1 fibres ($p = 0.028$) and statistically similar when comparing to Z6A1 substrates ($p = 0.12$) and low fibre diameter Z1A1 fibres ($p = 0.143$). In the case of PPAEC, the cellular activity observed on electrospun substrates demonstrated no significant difference when compared to bare metal substrates (Z1A1 L: $p = 0.915$, Z6A1: $p = 0.516$, Z1A1 T: $p = 0.446$).

Live/dead staining of cells on the various substrates confirmed that the cells were attached to the substrates investigated and not the surrounding *ThinCert*, PDMS or underlying metal substrate. By using simple live/dead staining, the morphology of cells on the different substrates does not appear to be influenced by the substrate that they are on. However, a more detailed morphological analysis would have to be carried out to confirm this observation. Actin staining antibodies could be used for an in depth analysis of the difference in the morphology of cells on the different

substrate types. This could be coupled with live, time-lapse imaging of cells on the various substrates in order to obtain a more representative picture of cell motility.

## 7.5. Conclusions

Three distinctly different adherent cell types were successfully cultured on the *Biomer b₉* thermoplastic polyurethane range. 3T3 fibroblasts, SH-SY5Y neuroblastoma cells and primary endothelial cells were cultured on both solvent-cast and electrospun substrates. When compared to tissue culture plastic, the rate of growth of all cell types across the various substrates was significantly reduced. Tissue culture plastic is manufactured using a patented low-pressure gas plasma surface treatment that allows cells to adhere more efficiently by reducing the hydrophobicity of the surface [324]. TCP was therefore considered as a positive control that unlike the polyurethane surfaces, was actively treated to promote cell adhesion. Cell growth on polyurethane substrates was also compared to untreated, metal surfaces. This was a better comparison as similar to the polyurethane substrates, the 316L stainless steel substrates used in these experiments were not treated to promote cell adhesion. In this instance, cell growth was comparable and the differences observed were much smaller. It is still important to note that such experiments being performed *in vitro* have a very limited ability to replicate *in vivo* conditions. *In vitro* studies only provide a limited view of the complete picture and it should not be assumed that results produced from such experiments would be directly replicated *in vivo*.

The techniques used to investigate cell activity in these experiments were somewhat limited in scope and only provided an initial assessment of cell attachment on substrates manufactured using these materials. In order to investigate the influence of mechanical properties on cell mechanotransduction, a more detailed examination of cell activity will be required. The techniques used were however sufficient for the aim of this experiment which was to investigate whether it was possible to culture cells on the various *Biomer Technology Limited b₉* thermoplastic polyurethane range in both solvent-cast and electrospun forms.

# Chapter 8

# Discussion

## 8.1. Summary

Numerous publications have reported that cells interact with a scaffold mechanically and apply forces on the scale of a few nano-newtons [138 – 140]. Continuum mechanics approximates materials as a continuous phase, rather than comprising of discrete particles. Size effects indicate that this continuum breaks down on the length scales of interest in the context of cell mechanotransduction [81]. Consequently, this means that the effective modulus of the substrate is altered on the cellular scale. It was hypothesised that such changes in nano-mechanical properties influence cell behaviour through a number of mechanosensitive mechanisms as has been extensively reported elsewhere [151].

The mechanical properties of a family of medical grade, segmented polyurethanes at force and length scales of the same order as those exerted by individual cells during static culture were quantified. Size effects were clearly visible when indenting the different polymer grades to different depths using both a dedicated nano-indentation system (2 µm - 0.1 µm) and AFM nano-indentation (300 nm – 30 nm). Comparison of these two methods of indentation (AFM and nano-indenter) highlighted the challenge of obtaining absolute values on these scales despite systematic attempts to reduce artefacts arising from variables such as rate of indentation, surface roughness and sample preparation. Multiple authors demonstrate size effects in a number of polymers including: polycarbonate [327], polyamide/imide (PAI) [328], polymethylmethacrylate (PMMA) [86] and polystyrene [86]. Han *et al.* also explain that such effects are not visible on UHMWPE or PTFE as these have a homogeneous and highly flexible molecular structure and do not contain any rigid components

which are critical in the formation of size effects [81]. In the case of the polyurethanes on which the present study was based, size effects were clearly demonstrated and confirmed by means of AFM and nano-indentation. However, irrespective of the length scale investigated, an intrinsic difference between polymers of different bulk mechanical properties was still observed. In the case of Z6A1, indentations to 2 μm resulted in moduli of 37.6 μm ± 2.2 μm while indentations to 0.1 μm resulted in moduli of 390.8 μm ± 48.9 μm. Similarly, in Z1A1, indentations to 2 μm resulted in moduli of 5.1 μm ± 0.3 μm while indentations to 0.1 μm resulted in moduli of 74.7 μm ± 6.8 μm. While different polymers could be used to investigate the influence of nano-mechanical properties on cell behaviour, polyurethane is widely used in tissue engineering with numerous biomedical grades available. Intrinsic mechanical properties of polyurethanes can also be varied directly by altering the ratio of chemical constituents unlike other polymer substrates which indirectly vary mechanical properties by altering topographical features such as pore size [156]. This, therefore, meant that polyurethane was ideal for use in an investigation into the influence of nano-mechanical properties on cell behaviour.

Polymer process variables used in the fabrication of scaffolds were also investigated to determine changes that could influence cell behaviour. In solvent-cast films, a difference in surface topography was observed between the air interface and the glass interface. When a different solvent system was used in the solvent-casting process, differences in topographies of the air-interface were also observed. The glass interface was generally unaltered irrespective of solvent system or polymer grade used. Indentation on a scale of 2 μm to 0.1 μm revealed clear size effects but no differences were observed when comparing the air-interface to the glass-interface or when comparing solvent-cast films produced from different solvents. DSC results also indicated that the solvent system used did not alter the resulting microstructure. Further analysis by means of AFM phase imaging established that these changes in surface morphology could not be attributed to changes in chemical microstructure as had been previously hypothesised by KoJoi *et al* [278]. Topographical cues have been shown to influence cell behaviour as outlined in *Section 2.3.2*. This result implies that if cells were cultured on solvent-cast films fabricated from different

polyurethane grades, the glass interface should be used as changes in surface topography at the air interface would result in different topographical cues.

Fibrous scaffolds are widely used in tissue engineering as these mimic the extracellular matrix [32]. Size effect theories also indicate that in bending, beams display a size dependant effect with smaller diameter beams exhibiting an increased modulus [81]. Defect free electrospun mats presenting diverse nano-mechanical properties were fabricated. This was achieved by manufacturing electrospun mats from different polymer grades and with different fibre diameters. As with solvent-cast films, these fibrous mats maintained difference in both the bulk and nano-mechanical properties. Thermal analysis also revealed a distinct difference between the chemical microstructure of solvent-cast films and that of electrospun mats. Electrospun mats exhibited a greater degree of micro-phase separation suggesting that the intrinsic mechanical properties of the two forms may not be identical. Nano-mechanical properties were therefore considered as extrinsic properties of the substrate. Apart from varying depending on form and mode of loading, nano-mechanical properties were also altered in the different forms by a change in chemical microstructure. This finding highlights the difficulty of direct comparison of the nano-mechanical properties of these two forms. Scaffolds with one nominal mechanical modulus and mixed nano-mechanical properties were also fabricated by dual spinning of two polymer grades in *Section 5.3.2*. Cellular behaviour on such scaffolds could provide a better understanding of how cells interact with three-dimensional scaffolds and the importance of nano-mechanical properties for cell viability. The use of polyurethane facilitated direct comparison of cell viability on substrates having broadly similar chemistry but very different bulk and nano-mechanical properties.

A subsequent study was performed with a view to establish whether exposure to a physiological environment could alter the surface properties of the *Biomer Technology Limited* $b_9$ polyurethanes over an extended period of time. The surface properties investigated when polyurethanes were stored in physiological solution for periods of up to 90 days were unchanged ($p > 0.05$). When the same polymers were

stored in an oxidative solution replicating inflammatory response, changes in surface topography were detected after only 15 days immersion ($p < 0.05$). Surface analysis by AFM indicated an increase in surface roughness of both polymer grades tested, whereas no significant changes ($p > 0.05$) were observed in mechanical properties. Changes in topographical features have been shown by a number of authors to influence cell behaviour [329]. However, these results indicated that if these materials were used to investigate the influence of nano-mechanical properties on cell behaviour, surface topography will not be altered in the duration of the experiments.

The above investigations also served to highlight the need to characterise the mechanical properties of such substrates on a physiologically relevant length scale. Material selection, polymer processing and storage conditions all contributed to the surface and bulk mechanical properties of a given scaffold. Moreover, the nano-mechanical properties are highly dependent on the mode of loading and the morphology of substrate itself [81]. Fibre diameter alters nano-mechanical properties and the modulus increases as fibre diameter decreases when this is loaded in three-point bending [284]. In axial loading, no such change is observed and the elastic modulus is constant regardless of fibre diameter [87]. In flat, two-dimensional surfaces such as solvent-cast films, the elastic modulus was also seen to increase as a function of indentation depth [81]. These phenomena are not unique to the polymers on which the study is based, but rather an attribute of the mode of loading and would be apparent on any substrate material used. This has important implications for the design of scaffolds in the context of tissue engineering as cells interact with scaffolds and apply loads on the nano-scale where such size effects are predominant. Nevertheless the importance of this observation should be taken with caution. One has to keep in mind that cells residing in the niches of a scaffold are subject to a multitude of other factors, such as chemical stimuli or substrate strain, which may well dominate the effects on cell behaviour.

The findings of the initial assessment of cell adhesion demonstrated that all three cell types investigated were successfully cultured on both solvent-cast films and on

electrospun mats fabricated with fibres of different diameters. The results of this preliminary investigation have established the feasibility of experimental protocols in further studies into the influence of nano-mechanical properties on mechanotransduction.

Hench *et al.* suggest that the next generation of biomaterials should stimulate specific cellular responses in a defined manner at the molecular level [330]. The importance of this study therefore lies in a bottom-up philosophy and focuses on obtaining a better understanding of the factors that influence cell behaviour in order to inform the production of successful artificial tissues. To our knowledge, no studies have addressed the specific role of size effects on cell-substrate interactions. This work has applied advanced material analyses to undertake this investigation. To this end, scaffolds that demonstrated similar chemical properties and surface morphology while presenting different nano-mechanical properties were manufactured. Scaffolds were also characterised on the cellular scale to ensure that the nano-mechanical properties was the only variable influencing cell behaviour. Such scaffolds have therefore laid the foundation for further experiments into an investigation of the influence of nano-mechanical properties on cell behaviour.

## 8.2. Suggestions for Further Work

In order to accurately characterise the influence of nano-mechanical properties on cellular mechanotransduction using different polyurethane grades, all other intermediate variables have to be controlled. The literature confirms that interaction of proteins with scaffolds of different chemistry and topography has a significant influence on cell adhesion and proliferation [115]. In this study, surface topography has been controlled for and steps have been taken to ensure that when comparing different grades of polyurethane, the surface morphology presented was similar. Even though the chemical intermediates of the different grades of polyurethane are similar, the ratio of hard segment to soft segment is altered in order to create differences in mechanical properties [40]. This therefore means that stiffer grades such as Z6A1 have a significantly larger amount of diphenyl methane diisocyanate

when compared to less stiff grades such as Z1A1. Diverse protein affinity to such chemical components could alter protein concentration on the scaffold surface and eventually affect cell adhesion. Commercially assays, such as the *NanoOrange*® *Protein Quantification Kit* (ThermoFisher Scientific, UK) are available which can accurately provide a measure of protein absorption by binding to proteins and undergoing a large fluorescence enhancement [331]. Changes in the topography were observed in *Section 6.4* when scaffolds were stored in an oxidative solution for an extended period of time. These changes did not influence bulk mechanical properties but could have significant implications on protein and subsequently cell adhesion. Similar protein attachment studies previously outlined here can be carried out on these scaffolds to investigate any changes brought around by the increased surface roughness.

Studies of stiffness gradient studies commonly employ hydrogels or PDMS substrate with changes in cross-linker ratios that either change the porosity of hydrogels or alter the chemical characteristics in PDMS substrates [156]. If the suggested protein analysis indicates that the various grades of polyurethane do not alter protein adhesion, solvent-cast substrates with stiffness gradients can be fabricated by solvent-casting two different polymer grades in the same dish. The stiffness gradient of such substrates can then be confirmed using nano-indentation to specific indentation depths. Procedures similar to those followed in the literature could then be performed in order to investigate the influence of substrate stiffness on cell viability.

A more in-depth investigation of the macro-mechanical tensile properties of electrospun mats is also warranted. Viscoelastic characterisation of electrospun mats is routinely performed and the use of models allows for a better prediction of the material response to different loading conditions [332]. One such model is known as Fung's model of quasilinear viscoelasticity and has historically been used to describe a wide variety of biological materials such as tendons, collagen fibres and cardiac tissue, since these materials are naturally nonlinear and exhibit viscoelastic behaviour. The mechanical behaviour of electrospun mats produced from different

grades of polyurethane using dual spinning, such as those discussed in *Section 5.3.2,* are also warrented. Since such films incorporate more than one component, viscoelastic modelling would be necessary for a comprehensive understanding of the behaviour of such materials under diverse loading conditions.

Using the information and new knowledge gained from this body of work would undoubtedly improve our understanding of nano-mechanical properties on cell mechanotransduction. This goal could be achieved in a number of ways each using different aspects of the study. Dual spinning could be utilised to fabricate a scaffold with mixed nano-mechanical properties as previously shown. If one of the polymers is dyed using a fluorescent dye, fibre polymer grade could be identified using high enough magnification on the *Zeiss Axio Imager*. Live cell imaging of cells on such scaffolds could then be used to observe any preferential behaviour on either scaffold material.

During the electrospinning process it was noted that slight changes in polymer feed-rate altered resulting fibre diameters significantly across a traverse length of 15 cm. The infusion pump used (*Harvard Apparatus, PHD 2000, Kent, UK*) can be connected to a computer and programmed to alter polymer feed-rate over the span of the traverse movement. Such changes could potentially produce a larger change in fibre diameter over a shorter distance and thus producing a scaffold with a gradient of nano-mechanical properties. Cell migration towards specific fibre diameter distributions could then be monitored to extrapolate cell preference. The main drawback in such studies is that intrinsic fibre morphology has to be varied to alter nano-mechanical properties. This means that it would be difficult to deduce whether any changes observed would be caused by a change in nano-mechanical properties or by a change in scaffold topography due to the reduced fibre diameter.

Further in-depth cell attachment studies on scaffolds with the different nano-mechanical properties are also warranted. A common method used to measure cell adhesion is to seed Calcein-AM stained cells onto a surface, after enough time is allowed for attachment the remaining cells are rinsed off carefully using PBS. The

number of adherent cells on the surfaces can then be measured using a fluorescence plate reader. Understanding individual cell interaction with such surfaces is also important and could give a better insight into cell behaviour. High magnification individual cell tracking over a period of time on different scaffold materials would therefore provide more information about cell spreading and motility. This could be performed in conjunction with F-actin staining at various stages after cell fixation.

The hydrophilicity of the scaffolds and the individual electrospun fibres in various grades of polyurethane remains to be shown. Standard procedures for hydrophilicity on the macro-scale are readily available and usually involve the measurement of a contact angle made between a scaffold and a liquid solution. Nano-scale analysis of individual fibres is also well documented in material science applications and involves imaging of electrospun mats in a controlled environment scanning electron microscope [333]. In such microscopes, the atmospheric humidity can be increased until droplets form on the individual fibres. Contact angle measurements can then be made from images obtained by using the same equipment and can be used to further characterise electrospun scaffolds on the nano-scale. Such hydrophilicity measurements could also inform protein adhesion mechanisms which, as previously described, could potentially have an important role in cell adhesion.

# Bibliography

[1]     W. M. Saltzman, Tissue Engineering - Principles for the design of replacement organs and tissues, Oxford: Oxford University Press, 2004.

[2]     D. A.Soscia, "Antibiotic-Loaded PLGA Nanofibers for Wound Healing," *Advanced Biomaterials,* no. 12, pp. B83 - B88, 2010.

[3]     B. B. Association, "Standards," [Online]. Available: http://www.britishburnassociation.org/standards. [Accessed 15 4 2012].

[4]     V. Leung, "Biomedical applications of nanofibers," *Polymers advanced technologies,* no. 22, pp. 350-365, 2010.

[5]     V. E. Torres, "Hyperbranched polyglycerol electrospun nanofibers for wound," *Acta Biomaterialia,* no. 6, pp. 1069 - 1078, 2010.

[6]     M. Goldberg, . R. Lange and J. Xinqiao, "Nanostructured materials for applications in drug delivery and tissue engineering," *Journal of Biomaterial Science,* vol. 18, no. 3, pp. 241 - 268, 2007.

[7]     M. Prabaharan, R. Jayakumar and S. Nai, "Electrospun Nanofibrous Scaffolds-Current Status and Prospects in Drug Delivery," *Advances in polymer sceince,* vol. 246, pp. 241-262, 2012.

[8]     J. S. Temenoff and A. G. Mikos, "Review: tissue engineering for regeneration of articular cartilage," *Biomaterials,* vol. 21, pp. 431-440, 2000.

[9]     D. W. Hutmacher, "Scaffolds in tissue engineering bone and cartilage," *Biomaterials,* vol. 21, pp. 2529-2543, 2000.

[10]    X. Gu, F. Ding and D. F. Williams, "Neural tissue engineering options for peripheral nerve regeneration," *Biomaterials,* vol. 35, pp. 6143-6156, 2014.

[11]    B. Weber, P. Dijkman, J. Scherman, B. Sanders, M. Emmert, J. Grunenfelder, R. Verbeek, M. Bracher, M. Black, T. Franz, J. Kortsmit, P. Modregger, S. Peter, M. Stampanoni, J. Robert, D. Kehl, M. van Doeselaar, M. Schweiger, C. Brokopp, T. Walchli and Falk, "Off-the-shelf human decellularized tissue-engineered heart valves in a non-human primate model," *Biomaterials,* vol. 34,

no. 30, pp. 7269-7280, 2013.

[12] S. Badylak, "Xenogeneic extracellular matrix as a scaffold for tissue reconstruction," *Transplant Immunology,* vol. 12, no. 3-4, pp. 367-377, 2004.

[13] P. Crapo, T. Gilbert and S. Badylak, "An overview of tissue and whole organ decellularization processes," *Biomaterials,* vol. 32, no. 12, pp. 3233-3243, 2011.

[14] T. Gilbert, T. Sellaro and S. Badylak, "Decellularization of tissues and organs," *Biomaterials,* vol. 27, no. 19, pp. 3675 - 3683, 2006.

[15] R. Shyam, W. Colin, A. Kraus, K. Megerle, M. Choi, P. Brian, H. Pham and J. Chang, "Human Flexor Tendon Tissue Engineering: Decellularization of Human Flexor Tendons Reduces Immunogenicity In Vivo," *Tissue Engineering Part A,* vol. 18, no. 7-8, pp. 796 - 805, 2012.

[16] R. Grauss, M. Hazekamp, S. v. Vliet, A. G.-d. Groot and M. DeRuiter, "Decellularization of rat aortic valve allografts reduces leaflet destruction and extracellular matrix remodeling," *Journal of Thoracic and cardiovascular surgery,* vol. 126, no. 6, pp. 2003-2010, 2003.

[17] N. Martin, P. Schaner, T. Tulenko, I. Shapiro, C. DiMatteo, T. Williams, E. Hager and P. DiMuzio, "In vivo behavior of decellularized vein allograft," *Journal of surgical research,* vol. 129, no. 1, pp. 17-23, 2005.

[18] T. Hudson, S. Zawko, C. Deister, S. Lundy, C. Hu, L. K and C. Schmidt, "Optimized acellular nerve graft is immunologically tolerated and supports regeneration," *Tissue engineering,* vol. 10, no. 11-12, pp. 1641-1651, 2004.

[19] T. Keane, L. R, N. J. Turner and S. F. Badylak, "Consequences of ineffective decellularization of biologic scaffolds on the host response," *Biomaterials,* vol. 33, no. 6, pp. 1771-1781, 2012.

[20] T. Okano, N. Yamada, H. Sakai and Y. Sakurai, "A novel recovery system for cultured cells using plasma-treated polystyrene dishes grafted with poly(N-isopropylacrylamide)," *Journal of Biomedical Materials Research,* vol. 27, no. 10, pp. 1243-1251, 2004.

[21] T. Okano, N. Yamada, Okuhara, H. Sakai and Y. Sakurai, "Mechanism of cell

detachment from temperature-modulated, hydrophilic-hydrophobic polymer surfaces.," *Biomaterials,* vol. 16, no. 4, pp. 297-303, 1995.

[22] K. Nishida, M. Yamato, Y. Hayashida, K. Watanabe, K. Yamamoto, E. Adachi, S. Nagai, A. Kikuchi, N. Maeda, H. Watanabe, T. Okano and Y. Tano, "Corneal reconstruction with tissue-engineered cell sheets composed of autologous oral mucosal epithelium.," *The New England Journal of Medicine,* vol. 351, no. 12, pp. 1187-1196, 2004.

[23] T. Shimizu, M. Yamato, A. Kikuchi and T. Okano, "Cell sheet engineering for myocardial tissue reconstruction.," *Biomaterials,* vol. 24, no. 13, pp. 2309-2316, 2003.

[24] O. Gorka, R. M. Hernández, A. R. Gascón, R. Calafiore, T. M. Chang, P. D. Vos, G. Hortelano, D. Hunkeler, I. Lacík, A. J. Shapiro and J. L. Pedraz, "Cell encapsulation: Promise and progress," *Nature Medicine,* vol. 9, pp. 104-107, 2003.

[25] R. Lanza, J. Hayes and W. Chick, "Encapsulated cell technology," *Nature Biotechnology,* vol. 14, no. 9, pp. 1107-1111, 1996.

[26] D. Gray, "An overview of the immune system with specific reference to membrane encapsulation and islet transplantation.," *Annals of the New York Academy of Sciences,* vol. 944, pp. 226-239, 2001.

[27] Z. Ma, Z. Mao and C. Gao, "Surface modification and property analysis of biomedical polymers used for tissue engineering," *Colloids and Surfaces B-Biointerfaces,* vol. 60, no. 2, pp. 137 - 157, 2007.

[28] E. Chevalier, D. Chulia, P. C and M. Viana, "Fabrication of porous substrates: A review of processes using pore forming agents in the biomaterial field," *Journal of Pharmaceutical Sciences,* vol. 97, no. 3, pp. 1135-1154, 2008.

[29] V. Tran and X. Wen, "Rapid prototyping technologies for tissue regeneration," *Rapid Prototyping of Biomaterials: Principles and Applications,* no. 70, pp. 97-155, 2014.

[30] V. A. Liu and S. N. Bhatia, "Three-Dimensional Photopatterning of Hydrogels Containing Living Cells," *Biomedical Microdevices,* vol. 4, no. 4, pp. 257-266, 2002.

[31] T. Billiet, M. Vandenhaute, J. Schelfhout, S. V. Vlierberghe and P. Dubruel, "A review of trends and limitations in hydrogel-rapid prototyping for tissue engineering," *Biomaterials,* vol. 33, no. 26, pp. 6020-6041, 2012.

[32] K. Woo, J. Jun, V. Chen, J. Seo, J. Baek, H. Ryoo, K. GS, M. Somerman and P. Ma, "Nano-fibrous scaffolding promotes osteoblast differentiation and biomineralization," *Biomaterials,* vol. 28, no. 2, pp. 335 - 343, 2007.

[33] W. Li, J. Cooper, R. Mauck and R. Tuan, "Fabrication and characterization of six electrospun poly(alpha-hydroxy ester)-based fibrous scaffolds for tissue engineering applications," *ACTA Biomaterialia,* vol. 2, no. 4, pp. 377-385, 2006.

[34] F. R. Rose, L. A. Cyster, D. M. Grant, C. A. Scotchford, S. M. Howdle and K. M. Shakesheff, "In vitro assessment of cell penetration into porous hydroxyapatite scaffolds with a central aligned channel.," *Biomaterials,* vol. 25, no. 24, pp. 5507-5514, 2004.

[35] L. Nair and C. Laurencin, "Biodegradable polymers as biomaterials," *Progress in polymer science,* vol. 32, no. 8-9, pp. 762-798, 2007.

[36] A. S. Kulshrestha and A. Mahapatro, "Polymers for Biomedical Applications," *American Chemical Society,* 2008.

[37] M. Lutolf and J. Hubbell, "Synthetic biomaterials as instructive extracellular microenvironments for morphogenesis in tissue engineering," *Nature Biotechnology,* vol. 23, no. 1, pp. 47-55, 2005.

[38] J. Matthews, G. Wnek, D. Simpson and G. Bowlin, "Electrospinning of collagen nanofibers," *Biomacromolecules ,* vol. 3, no. 2, pp. 232-238, 2002.

[39] L. W. -. Ju and R. S. Tuan, "Polymeric Scaffolds for Cartilage Tissue Engineering," *International Union of Pure and Applied Chemistry,* vol. 227, pp. 65 - 75, 2005.

[40] R. J. Zdrahala and I. J. Zdrahala, "Biomedical Applications of Polyurethanes: A Review of Past Promises, Present Realities and a Vibrant Future," *Journal of Biomaterials Applications,* vol. 14, pp. 67 - 90, 1999.

[41] L. S. Naira and C. T. Laurencin, "Biodegradable polymers as biomaterials,"

*Progress in Polymer Science,* vol. 32, pp. 762 - 798, 2007.

[42]  B. Carlberg, M. Z. Axell, U. Nannmark, J. Liu and H. G. Kuhn, "Electrospun polyurethane scaffolds for proliferation and neuronal differentiation of human embryonic stem cells," *Biomedical Materials,* vol. 4, no. 4, 2009.

[43]  S. Grenier, M. Sandig, D. W. Holdsworth and K. Mequanin, "Interactions of coronary artery smooth muscle cells with 3D porous polyurethane scaffolds.," *Journal of Biomaterial Research ,* vol. 89, pp. 293 - 303, 2009.

[44]  S. Grenier, M. Sandig and K. Mequanint, "Polyurethane biomaterials for fabricating 3D porous scaffolds and supporting vascular cells," *Journal of biomedical materials research,* vol. 82A, no. 4, pp. 802 - 809, 2007.

[45]  A. S. Nain, J. C. Wong, C. Amon and M. Sitti, "Drawing suspended polymer micro-/nanofibers using glass micropipettes," *Applied Physics Letters,* vol. 89, 2006.

[46]  S. Ramakrishna, An Introduction to Electrospinning And Nanofibers, Singapore: World Scientific Publishing Co.Pte. Ltd, 2005.

[47]  W. Zhang, Z. Wu, H. Jiang and S. Yu, "anowire-Directed Templating Synthesis of Metal-Organic Framework Nanofibers and Their Derived Porous Doped Carbon Nanofibers for Enhanced Electrocatalysis," *Jounral of the american chemical society,* vol. 136, no. 41, pp. 14385-14388, 2014.

[48]  X. Lin, D. Tang and D. Haofei, "Self-assembly and controlled release behaviour of the water-insoluble drug nifedipine from electrospun PCL-based polyurethane nanofibres," *Journal of Pharmacy and Pharmacology,* vol. 65, no. 5, pp. 673-681, 2013.

[49]  M. Mazza, A. Patel, R. Pons, C. Bussy and K. Kostarelos, "Peptide nanofibres as molecular transporters: from self-assembly to in vivo degradation," *Faraday Discussions,* vol. 166, pp. 181-194, 2013.

[50]  A. L. Andrady, Science and Technology of Polymer Nanofibers, New Jersey: John Wiley & Sons, 2008.

[51]  V. Shabafrooz, M. Mozafari, D. Vashaee and L. Tayebi, "Electrospun Nanofibers: From Filtration Membranes to Highly Specialized Tissue

Engineering Scaffolds," *Journal of Nanoscience and Nanotechnology,* vol. 14, no. 1, pp. 522-534, 2014.

[52] L. A. Smith, X. Liu and P. X. Ma, "Tissue engineering with nano-fibrous scaffolds," *Soft Matter,* vol. 4, no. 11, pp. 2144 - 2149, 2008.

[53] K. Sisson, C. Zhang, M. C. Farach-Carson, D. B. Chase and J. F. Rabolt, "Fiber diameters control osteoblastic cell migration and differentiation in electrospun gelatin," *Journal of Biomedical Materials Research Part A,* vol. 94A, no. 4, pp. 1312 - 1320, 2010.

[54] S. Nikolov, C.-S. Han and D. Raabe, "On the origin of size effects in small-strain elasticity of solid polymers," *International Journal of Solids and Structures,* vol. 44, no. 5, pp. 1582 - 1592, 2007.

[55] A. E. Donius, M. A. Kiechel, C. L. Schauer and U. G. K. Wegst, "New crosslinkers for electrospun chitosan fibre mats. Part II: mechanical properties," *Journal of the Royal Society of Interface,* 2013.

[56] E. Vatankhaha, D. Semnania, M. P. Prabhakaranb, M. Tadayonc, S. Razavid and S. Ramakrishnab, "Artificial neural network for modeling the elastic modulus of electrospun polycaprolactone/gelatin scaffolds," *Acta Biomaterialia,* vol. 10, no. 2, pp. 709-721, 2014.

[57] P. Torricellia, M. Gioffrèc, A. Fioranic, S. Panzavoltac, C. Gualandic, M. Finia, M. L. Focaretec and A. Bigic, "Co-electrospun gelatin-poly(l-lactic acid) scaffolds: Modulation of mechanical properties and chondrocyte response as a function of composition," *Materials Science and Engineering: C,* vol. 36, pp. 130-138, 2014.

[58] J. Pu and K. Komvopoulos, "Mechanical properties of electrospun bilayer fibrous membranes as potential scaffolds for tissue engineering," *Acta Biomaterialia,* vol. 10, pp. 2718-2726, 2014.

[59] K. GH, "Electrospun PCL nanofibers with anisotropic mechanical properties as a biomedical scaffold," *Biomedical Materials,* vol. 3, no. 2, pp. 1-8, 2008.

[60] M. Rizvi, P. Kumar and A. P. D.S. Katti, "Mathematical model of mechanical behavior of micro/nanofibrous materials designed for extracellular matrix substitutes," *Acta Biomaterialia,* vol. 8, pp. 4111-4122, 2012.

[61] Y. Huang, F. Zhang, K. Hwang, W. Nix, G. Pharr and G. Feng, "A model of size effects in nano-indentation," *Journal of the Mechanics and Physics of Solids,* vol. 54, no. 8, pp. 1668-1686, 2006.

[62] Z.-M. Huang, "Electrospinning and mechanical characterization of gelatin nanofibers," *Polymer,* no. 45, pp. 5361 - 5368, 2004.

[63] Y. Zhang, "Nanomechanical Characterization of One-Dimensional Nanostructures," in *Micro and Nano Mechanical Testing of Materials and Devices*, Kentucky, Springer, 2008, pp. 105 - 120.

[64] G. Haugstad, Atomic Force Microscopy: Understanding Basic Modes and Advanced Applications, New Jersey: John Wiley & Sons, 2012.

[65] Q. Fu, Y. Jin, X. Song, J. Gao and X. Han, "Size-dependent mechanical properties of PVA nanofibers reduced via air plasma treatment," *Nanotechnology,* vol. 21, pp. 1 - 5, 2010.

[66] E. P. S. Tan, C. N. Goh, C. H. Sow and C. T. Lim, "Tensile test of a single nanofiber using an atomic force microscope tip," *Applied Physics Letters ,* vol. 86, 2005.

[67] B. Wu, A. Heidelberg and J. J. Boland, "Mechanical properties of ultrahigh-strength gold nanowires," *Nature Materials,* vol. 4, pp. 525 - 529, 2005 .

[68] H. Gao and Y. Huang, "Geometrically necessary dislocation and size-dependent plasticity," *Acta Materialia,* vol. 48, pp. 113-118, 2002.

[69] N. Fleck, G. Muller, M.F.Ashby and J.W.Hutchinson, "Strain Gradient plasticity: Theory and Experiment," *Acta metall. mater.,* vol. 42, no. 2, pp. 475-487, 1994.

[70] N. Fleck and J. Hutchinson, "Strain Gradient Plasticity," *Advances in Applied Mechanics,* vol. 33, pp. 259 - 362, 1997.

[71] M. Ashby, "The deformation of plastically non-homogeneous materials," *Philosophical Magazine,* vol. 21, no. 170, pp. 399-424, 1970.

[72] J. Nye, "Some geometrical relations in dislocated crystals," *Acta metallurgica,* vol. 1, no. 2, pp. 153-162, 1953.

[73] E. Kroner, "Dislocations and continuum mechanics," *Applied Mechanics,* vol.

15, no. 8, pp. 599-606, 1962.

[74] A. Arsenlis and D. Parks, "Crystallographic aspects of geometrically necessary and statistically-stored dislocation density," *Acta Metallurgica,* vol. 47, no. 5, pp. 1597 - 1611, 1999.

[75] A. Bray, "Theory of phase-ordering kinetics," *Advances in physics,* vol. 43, no. 3, pp. 357 - 459, 1994.

[76] P. G. d. Gennes and J. Prost, The Physics of Liquid Crystals, Oxford: Clarendon Press, 1995.

[77] A. J. Liu and G. H. Fredrickson, "Free energy functionals for semiflexible polymer solutions and blends," *Macromolecules,* vol. 26, no. 11, pp. 2817 - 2824, 1993.

[78] J. Fukuda, "Free energy of semiflexible polymers and structure of interfaces," *The European Physical Journal B - Condensed Matter and Complex Systems,* vol. 7, no. 4, pp. 573 - 583, 1999.

[79] J.-I. Fukuda and H. Yokoyama, "Frank elasticity revisited: contribution of rotational entropy," *Molecular Crystals and Liquid Crystals Science and Technology. Section A. Molecular Crystals and Liquid Crystals,* vol. 366, no. 1, pp. 151 - 156, 2001.

[80] C.-S. Han and S. Nikolov, "Indentation size effects in polymers and related rotation gradients," *Journal of Materials Research,* vol. 22, no. 6, pp. 1663 - 1672, 2007.

[81] C.-S. Han, "Influence of the molecular structure on indentation size effect in polymers," *Materials Science and Engineering A,* vol. 527, pp. 619 - 624, 2010.

[82] J. A. Tjernlund, E. K. Gamstedt and Z.-H. Xu, "Influence of molecular weight on strain-gradient yielding in polystyrene," *Polymer Engineering and Science,* vol. 44, no. 10, pp. 1987 - 1997, 2004.

[83] D. C. Lam and A. C. Chong, "Effect of cross-link density on strain gradient plasticity in epoxy," *Materials Science and Engineering: A,* vol. 281, no. 1-2, pp. 156 - 161, 2000.

[84]  Y. Y. Lim and M. M. Chaudhri, "Indentation of elastic solids with a rigid Vickers pyramidal indenter," *Mechanics of Materials,* vol. 38, no. 12, pp. 1213 - 1228, 2006.

[85]  C. A. Charitidis, "Nanoscale Deformation and Nanomechanical Properties of Polydimethylsiloxane (PDMS)," *American Chemical Society,* vol. 50, no. 2, pp. 565 - 570, 2011.

[86]  B. J. Briscoe, L. Fiori and E. Pelillo, "Nano-indentation of polymeric surfaces," *Journal of physics. D, Applied physics,* vol. 31, no. 19, pp. 2395-2405, 1998.

[87]  D. Lam, F. Yang, A. Chong, J. Wang and P. Tong, "Experiments and theory in strain gradient elasticity," *Journal of the Mechanics and Physics of Solids,* vol. 51, no. 8, pp. 1477 - 1508, 2003.

[88]  T.-Y. Zhang, W.-H. Xu and M.-H. Zhao, "The role of plastic deformation of rough surfaces in the size-dependent hardness," *Acta Materialia,* vol. 51, no. 1, pp. 57 - 68, 2004.

[89]  T.-Y. Zhang and W.-H. Xu, "Surface Effects on Nanoindentation," *Journal of Materials Research,* vol. 17, no. 7, pp. 1715 - 1720, 2002.

[90]  A. Campillo-Fernandez, R. Unger, K. Peters, S. Halstenberg, M. Santos, M. Sanchez and Duenas, "Analysis of the Biological Response of Endothelial and Fibroblast Cells Cultured on Synthetic Scaffolds with Various Hydrophilic/Hydrophobic Ratios: Influence of Fibronectin Adsorption and Conformation," *Tissue Engineering,* vol. 15, no. 6, pp. 1331 - 1341, 2009.

[91]  B. Lewin, Cells, Sudbury: Jones and Bartlett Publishers, 2007.

[92]  L. Wilson, "The Cytoskeleton, Part A, Cytoskeletal Proteins, Isolation and Characterization," in *Methods in Cell Biology*, London, Academic Press, Inc, 1982, pp. 1 - 429.

[93]  A. Pierres, A.-M. Benoliel, D. Touchard and P. Bongrand, "How Cells Tiptoe on Adhesive Surfaces before Sticking," *Biophysical Journal,* vol. 94, no. 10, pp. 4114 - 4122, 2008.

[94]  A. Mogilner and B. Rubinstein, "The Physics of Filopodial Protrusion,"

*Biophysical Journal,* vol. 89, pp. 782 - 795, 2005.

[95] I. D. Campbel and M. J. Humphries, "Integrin Structure, Activation, and Interactions," *Cold Spring Harbor Perspectives in Biology,* vol. 3, pp. 1 - 14, 2011.

[96] R. O. Hynes, "Integrins: A family of cell surface receptors," *Cell,* vol. 48, no. 4, pp. 549-554, 1987.

[97] R. O. Hynes, "Integrins: Versatility, modulation, and signaling in cell adhesion," *Cell,* vol. 69, no. 1, pp. 11-25, 1992.

[98] E. E. Marcantonio, "The structure and function of integrins," in *Advances in molecular and cell biology*, London, JAI Press Inc, 1996, pp. 1 - 30.

[99] J. W. Tamkun, D. W. DeSimone, D. Fonda, R. S. Patel, C. Buck, A. F. Horwitz and R. O. Hynes, "Structure of integrin, a glycoprotein involved in the transmembrane linkage between fibronectin and actin," *Cell,* vol. 46, no. 2, pp. 271-282, 1986.

[100] M. R. Koller and E. T. Papoutsakis, "Cell adhesions in animal cell culture: Physiological and fluid-mechanical implications," in *Cell Adhesion*, New York, Marcel Dekker, 1995, pp. 61 - 110.

[101] M. Biggs, R. Richards and M. Dalby, "Nanotopographical modification: a regulator of cellular function through focal adhesions," *Nanomedicine,* vol. 6, pp. 619 - 633, 2010.

[102] J. Grossmann, "Molecular mechanisms of "detachment-induced apoptosis—Anoikis," *Apoptosis,* vol. 7, pp. 247-260, 2002.

[103] A. Whitton, D. J. Flint and R. A. Black, "Differential effect of substrate stiffness and adsorbed fibronectin density on vascular smooth muscle migration rate," *European Cells and Materials,* vol. 18, no. 2, p. 29, 2009.

[104] T. Mitchison and L. Cramer, "Actin-Based Cell Motility and Cell Locomotion," *Cell,* vol. 84, no. 3, pp. 371-379, 1996.

[105] U. Hersel, C. Dahmen and H. Kessler, "RGD modified polymers: biomaterials for stimulated cell adhesion and beyond.," *Biomaterials,* vol. 24, no. 24, pp. 4385-4415, 2003.

[106] M. Arnold, E. A. Cavalcanti-Adam, R. Glass, J. Blummel, W. Eck, M. Kantlehner, H. Kessler and J. P. Spatz, "Activation of integrin function by nanopatterned adhesive interfaces.," *ChemPhysChem,* vol. 5, no. 3, pp. 383 - 388, 2004.

[107] H. Haga, C. Irahara, R. Kobayashi, T. Nakagaki and K. Kawabata, "Collective Movement of Epithelial Cells on a Collagen Gel Substrate," *Biophysics journal,* vol. 88, no. 3, pp. 2250-2256, 2005.

[108] M. Singh, C. Berkland and M. S. Detamore, "Strategies and Applications for Incorporating Physical and Chemical Signal Gradients in Tissue Engineering," *Tissue Engineering,* vol. 14, no. 4, pp. 341-366, 2008.

[109] Y. W. Chun, D. Khang, K. M. Haberstroh and T. J. Webster, "The role of polymer nanosurface roughness and submicron pores in improving bladder urothelial cell density and inhibiting calcium oxalate stone formation," *Nanotechnology,* vol. 20, no. 8, 2009.

[110] Y. Chen, J. Gong, M. Tanaka, K. Yasuda, S. Yamamoto, M. Shimomura and Y. Osada, "Tuning of cell proliferation on tough gels by critical charge effect," *Journal of biomedical material research,* vol. 88, no. 1, pp. 74-83, 2009.

[111] V. Bernardo, G. M. Luz, N. M. Alves and J. F. Mano, "Cell behaviour in new poly(l-lactic acid) films with crystallinity gradients," *Materials Letters,* vol. 87, pp. 105 - 108, 2012.

[112] M. Gail and C. Boone, "Cell-substrate adhesivity: A determinant of cell motility," *Experimental Cell Research,* vol. 70, no. 1, pp. 33-40, 1972.

[113] P. Clark, P. Connolly, A. Curtis, J. Dow and C. Wilkinson, "Topographical control of cell behaviour. I. Simple step cues.," *Development,* vol. 99, no. 3, pp. 439-448, 1987.

[114] B. Wójciak-Stothard, A. Curtis, M. W, K. MacDonald and C. Wilkinson, "Guidance and activation of murine macrophages by nanometric scale topography.," *Experimental Cell Research,* vol. 223, no. 2, pp. 426-435, 1996.

[115] M. J. P. Biggs, R. G. Richards and M. J. Dalby, "Nanotopographical modification: a regulator of cellular function through focal adhesions," *Nanomedicine,* vol. 6, pp. 619 - 633, 2010.

[116] S. Liliensiek, P. Nealey and C. Murphy, "Characterization of endothelial basement membrane nanotopography in rhesus macaque as a guide for vessel tissue engineering.," *Tissue Engineering Part A,* vol. 15, no. 9, pp. 2643- 2651, 2009.

[117] S. Brody, T. Anilkumar, S. Liliensiek, J. Last, C. Murphy and A. Pandit, "Characterizing nanoscale topography of the aortic heart valve basement membrane for tissue engineering heart valve scaffold design.," *Tissue Engineering,* vol. 12, no. 2, pp. 413 - 421, 2006.

[118] F. Bosman and I. Stamenkovic, "Functional structure and composition of the extracellular matrix.," *Journal of Pathology,* vol. 200, pp. 423 - 428, 2003.

[119] L. Bozec and M. A. Horton, "Skeletal tissues as nanomaterials," *Journal of Material Sceince,* vol. 17, pp. 1043 - 1048, 2006.

[120] Kshitiz, J. Afzal, S.-Y. Kim and D.-H. Kim, "A nanotopography approach for studying the structure-function relationships of cells and tissues," *Cell Adhesion & Migration,* vol. 9, no. 4, pp. 300 - 307, 2015.

[121] C. Selhuber-Unkel, M. López-García, H. Kessler and J. P. Spatz, "Cooperativity in Adhesion Cluster Formation during Initial Cell Adhesion," *Biophysical Journal,* vol. 95 , no. 11, pp. 5425 - 5431, 2008.

[122] J. Lim, J. Hansen, C. Siedlecki, R. Hengstebeck, J. Cheng, N. Winograd and H. Donahue, "Osteoblast adhesion on poly(L-lactic acid)/polystyrene demixed thin film blends: effect of nanotopography, surface chemistry, and wettability.," *Biomacromolecules,* vol. 6, no. 6, pp. 3319 - 3327, 2005.

[123] T. Sjöström, M. J. Dalby, A. Hart, R. Tare, R. O. Oreffo and B. Su, "Fabrication of pillar-like titania nanostructures on titanium and their interactions with human skeletal stem cells," *Acta Biomateriala,* vol. 5, no. 5, pp. 1433 - 1441, 2009.

[124] M. J. Dalby, S. J. Yarwood, M. O. Riehle, H. J. H. Johnstone, S. Affrossman and A. S. G. Curtis, "Increasing Fibroblast Response to Materials Using Nanotopography: Morphological and Genetic Measurements of Cell Response to 13-nm-High Polymer Demixed Islands," *Experimental Cell Research,* vol. 276, pp. 1 - 9, 2002.

[125] J. Y. Lim, J. C. Hansen, C. A. Siedlecki, J. Runt and H. J. Donahue, "Human foetal osteoblastic cell response to polymer-demixed nanotopographic interfaces," *Interface,* vol. 2, pp. 97 - 108, 2005.

[126] M. Dalby, S. Childs, M. Riehle, H. Johnstone, S. Affrossman and A. Curtis, "Fibroblast reaction to island topography: changes in cytoskeleton and morphology with time," *Biomaterials,* vol. 24, no. 6, pp. 927 - 935, 2003.

[127] M. Biggs, R. Richards, N. Gadegaard, C. Wilkinson and M. Dalby, "Regulation of implant surface cell adhesion: characterization and quantification of S-phase primary osteoblast adhesions on biomimetic nanoscale substrates.," *Journal of orthopedic research,* vol. 25, no. 2, pp. 273 - 282, 2007.

[128] J. Park, S. Bauer, K. v. d. Mark and P. Schmuki, "Nanosize and Vitality: TiO2 Nanotube Diameter Directs Cell Fate," *Nano Letters,* vol. 7, no. 6, pp. 1686 - 1691, 2007.

[129] B. Zhu, Q. Zhang, Q. Lu, Y. Xu, J. Yin, J. Hu and Z. Wang, "Nanotopographical guidance of C6 glioma cell alignment and oriented growth," *Biomaterials,* vol. 25, no. 18, pp. 4215 - 4223, 2004.

[130] L. Chou, J. Firth, V. Uitto and D. Brunette, "Substratum surface topography alters cell shape and regulates fibronectin mRNA level, mRNA stability, secretion and assembly in human fibroblasts," *Journal of cell science,* vol. 108, pp. 1563 - 1573, 1995.

[131] M. J. Dalby, A. Hart and S. J. Yarwood, "The effect of the RACK1 signalling protein on the regulation of cell adhesion and cell contact guidance on nanometric grooves," *Biomaterials,* vol. 29, no. 3, pp. 282 - 289, 2008.

[132] A. S. Crouch, D. Miller, K. J. Luebke and W. Hu, "Correlation of anisotropic cell behaviors with topographic aspect ratio," *Biomaterials,* vol. 30, pp. 1560 - 1567, 2009.

[133] G. Abrams, S. Goodman, P. Nealey, M. Franco and C. Murphy, "Nanoscale topography of the basement membrane underlying the corneal," *Cell Tissue Research,* vol. 299, no. 1, pp. 39-46, 2000.

[134] F. Alenghat and D. Ingber, "Mechanotransduction: all signals point to

cytoskeleton, matrix, and integrins.," *Science STKE,* vol. 119, 2002.

[135] T. A. Ulrich, E. M. d. J. Pardo and S. Kumar, "The Mechanical Rigidity of the Extracellular Matrix Regulates the Structure, Motility, and Proliferation of Glioma Cells," *Cancer Research,* vol. 69, no. 1, pp. 4167 -4174, 2009.

[136] U. Schwarz, "Soft matters in cell adhesion: rigidity sensing on soft elastic substrates," *Soft Matter,* vol. 3, pp. 263-266, 2006.

[137] D. Discher, P. Janmey and Y. Wang, "Tissue cells feel and respond to the stiffness of their substrate.," *Science,* vol. 310, pp. 1139-1143, 2005.

[138] A. Curtis, L. Sokolikova-Csaderova and G. Aitchison, "Measuring Cell Forces by a Photoelastic Method," *Biophysical Journal,* vol. 92, no. 6, pp. 2255-2261, 2007.

[139] J. L. Tan, J. Tien, D. M. Pirone, D. S. Gray, K. Bhadriraju and C. S. Chen, "Cells lying on a bed of microneedles: An approach to isolate mechanical force," *Proceedings of the National Academy of Science of the United States of America,* vol. 100, no. 4, pp. 1484 - 1489, 2003.

[140] Z. Yang, J.-S. Lin, J. Chen and J. H.-C. Wang, "Determining substrate displacement and cell traction fields - a new approach," *Journal of theoretical biology,* vol. 242, no. 3, pp. 604 - 616, 2006.

[141] J. H. Wen, L. G. Vincent, A. Fuhrmann, Y. S. Choi, K. C. Hribar, H. Taylor-Weiner, S. Chen and A. J. Engler, "Interplay of matrix stiffness and protein tethering in stem cell differentiation," *Nature Materials,* vol. 13, pp. 979 - 987, 2014.

[142] N. Wang, J. P. Butler and D. E. Ingber, "Mechanotransduction across the cell surface and through the cytoskeleton.," *Science,* vol. 260, no. 5111, pp. 1124 - 1127, 1993.

[143] S. Hughes, S. McBain, J. Dobson and A. J. E. Haj, "Selective activation of mechanosensitive ion channels using magnetic particles," *Journal of the Royal Society Interface,* vol. 5, no. 25, pp. 855 - 863, 2008.

[144] G. Jiang, A. H. Huang, Y. Cai, M. Tanase and M. P. Sheetz, "Rigidity Sensing at the Leading Edge through αvβ3 Integrins and RPTPα," *Biophysical Journal,*

vol. 90, no. 5, pp. 1804 - 1809, 2006.

[145] S. K. Mitra, D. A. Hanson and D. D. Schlaepfer, "Focal adhesion kinase: in command and control of cell motility," *Nature Reviews - Molecular Cell Biology,* vol. 6, pp. 56 - 68, 2005.

[146] J. Robert J. Pelham and Y.-l. Wang, "Cell locomotion and focal adhesions are regulated by substrate flexibility," *Proceedings of the National Academy of Science of the United States of America,* vol. 94, no. 25, pp. 13661 - 13665, 1997.

[147] K. Ghosh, Z. Pan, E. Guan, S. Ge, Y. Liu, T. Nakamura, X.-D. Rend, M. Rafailovich and R. A. Clark, "Cell adaptation to a physiologically relevant ECM mimic with different viscoelastic properties," *Biomaterials,* vol. 28, pp. 671 - 679, 2007.

[148] W.-h. Guo, M. T. Frey, N. A. Burnham and Y.-l. Wang, "Substrate Rigidity Regulates the Formation and Maintenance of Tissues," *Biophysical Journal,* vol. 90, no. 6, pp. 2213 - 2220, 2006.

[149] H.-B. Wang, M. Dembo and Y.-L. Wang, "Substrate flexibility regulates growth and apoptosis of normal but not transformed cells," *Cell Physiology,* vol. 279, no. 5, pp. 1345 - 1350, 2000.

[150] J. Solon, I. Levental, K. Sengupta, P. C. Georges and P. A. Janmey, "Fibroblast Adaptation and Stiffness Matching to Soft Elastic Substrates," *Biophysical Journal,* vol. 93, pp. 4453 - 4461, 2007.

[151] D. E. Ingber, "Cellular mechanotransduction: putting all the pieces together again," *The FASEB Journal,* vol. 20, no. 7, pp. 811 - 827, 2006.

[152] C.-M. Lo, H.-B. Wang, M. Dembo and Y.-l. Wang, "Cell Movement Is Guided by the Rigidity of the Substrate," *Biophysical Journal,* vol. 79, pp. 144-152, 2000.

[153] A. Engler, S. Shamik, L. Sweeney and D. Discher, "Matrix elasticity directs stem cell lineage specification," *Cell,* vol. 126, pp. 677-689, 2006.

[154] B. L. Bangasser, S. S. Rosenfeld and D. J. Odde, "Determinants of Maximal Force Transmission in a Motor-Clutch Model of Cell Traction in a Compliant

Microenvironment," *Biophysical Journal,* vol. 105, pp. 581 - 592, 2013.

[155] M. Paszek, N. Zahir, R. J. Kandice and L. Johnathon, "Tensional homeostasis and the malignant phenotype," *Cancer Cell,* vol. 8, no. 1, pp. 241 - 254, 2005.

[156] B. Trappmann, J. E. Gautrot, J. T. Connelly, D. G. T. Strange, M. L. O. Yuan Li, M. A. C. Stuart, H. Boehm, B. Li, V. Vogel, J. P. Spatz, F. M. Watt and W. T. S. Huck, "Extracellular-matrix tethering regulates stem-cell fate," *Nature Materials,* vol. 11, pp. 642-649, 2012.

[157] C. Selhuber-Unkel, T. Erdmann, M. López-García, H. Kessler, U. Schwarz and J. Spatz, "Cell adhesion strength is controlled by intermolecular spacing of adhesion receptors.," *Biophysics Journal,* vol. 98, no. 4, pp. 543-551, 2010.

[158] M. Chen, P. Patra, S. Warner and S. Bhowmick, "Role of Fiber Diameter in Adhesion and Proliferation of NIH 3T3 fibroblast on electrospun polycaprolactone scaffolds.," *Tissue Engineering,* vol. 13, no. 3, pp. 579 - 587, 2007.

[159] S. Noriega, G. Hasanova, M. Schneider, G. Larsen and A. Subramanian, "Effect of fiber diameter on the spreading, proliferation and differentiation of chondrocytes on electrospun chitosan matrices.," *Cells Tissues Organs,* vol. 195, no. 3, pp. 207 - 221, 2012.

[160] K. Park, B. Min, D. Han and K. Hasty, "Quantitative analysis of temporal and spatial variations of chondrocyte behavior in engineered cartilage during long-term culture.," *Annals of Biomedical Enginerring,* vol. 35, no. 3, pp. 419 - 428, 2007.

[161] W. Li, Y. Jiang and R. Tuan, "Chondrocyte phenotype in engineered fibrous matrix is regulated by fiber size.," *Tissue Engineering,* vol. 12, no. 7, pp. 1775 - 1785, 2006.

[162] B. Whited and M. Rylander, "The influence of electrospun scaffold topography on endothelial cell morphology, alignment, and adhesion in response to fluid flow.," *Biothechnology and Bioengineering,* vol. 111, no. 1, pp. 184 - 195, 2014.

[163] H. B. Wang, M. E. Mullins, J. M. Cregg, C. W. McCarthy and R. J. Gilbert, "Varying the diameter of aligned electrospun fibers alters neurite outgrowth

and Schwann cell migration," *Acta Biomateriala,* vol. 6, pp. 2970 - 2978, 2010.

[164] G. Meijs, S. McCarthy, E. Rizzardo, Y. Chen, R. Chatelier, A. Brandwood and K. Schindhelm, "Degradation of medical-grade polyurethane elastomers: the effect of hydrogen peroxide in vitro.," *Journal of Biomedical Material Research,* vol. 27, no. 3, pp. 345-356, 1993.

[165] E. Clark and J. Brugge, "Integrins and signal transduction pathways: the road taken," *Science,* vol. 268, no. 5208, pp. 233 - 239, 1995.

[166] A. Frick and A. Rochman, "Characterization of TPU-elastomers by thermal analysis (DSC)," *Polymer Testing,* vol. 23, pp. 413-417, 2004.

[167] N. M. Lamba, K. A. Woodhouse and S. L. Cooper, Polyurethanes in Biomedical Applications, CRC Press, 1998.

[168] R. Briber and E. Thomas, "Investigation of two crystal forms in MDI/BDO-based polyurethanes," *Journal of Applied Polymer Scence,* vol. B22, p. 509, 1983.

[169] G. Pathiraja and R. Adhikari, "Biodegradable synthetic polymers for tissue engineering," *European cells & materials,* vol. 5, pp. 1-16, 2003.

[170] H. Shintani and A. Nakamura, "Analysis of a carcinogen, 4,4'-methylenedianiline, from thermosetting polyurethane during sterilization.," *Journal of Analytical toxicology,* vol. 6, pp. 354-357, 1989.

[171] J. Guan, K. L. Fujimoto, M. S. Sacks and W. R. Wagner, "Preparation and characterization of highly porous, biodegradable polyurethane scaffolds for soft tissue applications," *Biomaterials,* vol. 26, no. 18, pp. 3961-3971, 2004.

[172] K. L. Fujimoto, K. Tobita, W. D. Merryman, J. Guan, N. Momoi, D. B. Stolz, M. S. Sacks, B. B. Keller and W. R. Wagner, "An elastic, biodegradable cardiac patch induces contractile smooth muscle and improves cardiac remodeling and function in subacute myocardial infarction," *Journal of the American College of Cardiology,* vol. 49, no. 23, pp. 2292-2300, 2007.

[173] S. Grad, L. Kupcsik, K. Gorna, S. Gogolewski and M. Alini, "The use of biodegradable polyurethane scaffolds for cartilage tissue engineering: potential

and limitations," *Biomaterials,* vol. 24, no. 28, pp. 5163-5171, 2003.

[174] J. J. Stankus, J. Guan, K. Fujimoto and W. R. Wagner, "Microintegrating smooth muscle cells into a biodegradable, elastomeric fiber matrix," *Biomaterials,* vol. 27, no. 5, pp. 735-744, 2006.

[175] J. J. Stankus, L. Soletti, K. Fujimoto, Y. Hong, D. A. Vorp and W. R. Wagner, "Fabrication of cell microintegrated blood vessel constructs through electrohydrodynamic atomization," *Biomaterials,* vol. 28, no. 17, pp. 2738-2746, 2007.

[176] C. J. Spaans, J. H. D. groot, V. W. Belgraver and A. J. Pennings, "A new biomedical polyurethane with a high modulus based on 1,4-butanediisocyanate and ε-caprolactone," *Materials in Medicine,* vol. 9, no. 12, pp. 675-678, 1998.

[177] Z. Dong, Y. Li and Q. Zou, "Degradation and biocompatibility of porous nano-hydroxyapatite/polyurethane composite scaffold for bone tissue engineering," *Applied Surface Science,* vol. 255, no. 12, pp. 6087-6091, 2009.

[178] E. David, G. Sibylle, G. Sylwester and A. Mauro, "Farsenol-modified biodegradable polyurethanes for cartilage tissue engineering," *Journal of biomedical materials research,* vol. 92, no. 1, pp. 393-408, 2010.

[179] M. Borkenhagen, R. Stoll, P. Neuenschwander, U. Suter and P. Aebischer, "In vivo performance of a new biodegradable polyester urethane system used as a nerve guidance channel," *Biomaterials,* vol. 19, no. 23, pp. 2155-2165, 1998.

[180] T. Hausner, R. Schmidhammer, Zandieh, R. Hopf, A. Schultz, S. Gogolewski, H. Hertz and H. Redl, "Nerve regeneration using tubular scaffolds from biodegradable polyurethane," *Acta Neurochirurgica Supplementum,* vol. 100, pp. 69-72, 2007.

[181] D. Wang, L. Feng, J. Ji, Y. Sun, X. Zheng and J. Elisseeff, "Novel human endothelial cell-engineered polyurethanebiomaterials for cardiovascular biomedical applications," *Journal of Biomedical Material Research. Part A,* vol. 65, no. 4, pp. 498-510, 2003.

[182] X. Kong, G. Liu and J. M. Curtis, "Novel polyurethane produced from canola oil based poly(ether ester) polyols: Synthesis, characterization and properties," *European Polymer Journal,* vol. 48, no. 12, pp. 2097-2106, 2012.

[183] E. Campos, R. Cordeiro, A. C. Santos, C. Matos and M. Gil, "Design and characterization of bi-soft segmented polyurethane microparticles for biomedical application," *Colloids and Surfaces B: Biointerfaces,* vol. 88, no. 1, pp. 477-482, 2011.

[184] D. Lee, S.-H. Lee, S. Kim, K. Char, J. H. Park and Y. H. Bae, "Micro-phase-separation behavior of amphiphilic polyurethanes involving poly(ethylene oxide) and poly(tetramethylene oxide)," *Polymer Physics ,* vol. 41, no. 20, pp. 2365-2374, 2003.

[185] K. Gorna and S. Gogolewski, "In vitro degradation of novel medical biodegradable aliphatic polyurethanes based on ϵ-caprolactone and Pluronics® with various hydrophilicities," *Polymer Degradation and Stability,* vol. 75, no. 1, pp. 113-122, 2002.

[186] S.-H. Chen, C.-T. Tsao, H.-C. Chou, C.-H. Chang, C.-T. Hsu, C.-N. Chuang, C.-K. Wang and K.-H. Hsieh, "Synthesis of poly(lactic acid)-based polyurethanes," *Polymer International,* vol. 62, no. 8, pp. 1159-1168, 2012.

[187] X. Jiang, J. Li, M. Ding, H. Tan, Q. Ling, Y. Zhong and Q. Fu, "Synthesis and degradation of nontoxic biodegradable waterborne polyurethanes elastomer with poly(epsilon-caprolactone) and poly(ethylene glycol) as soft segment," *European Polymer Journal,* vol. 43, no. 5, pp. 1838-1846, 2007.

[188] N. Teramoto, Y. Saitoh, A. Takahashi and M. Shibata, "Biodegradable Polyurethane Elastomers Prepared from Isocyanate-Terminated Poly(Ethylene Adipate), Castor Oil, and Glycerol," *Applied Polymer Science,* vol. 115, no. 6, pp. 3199-3204, 2010.

[189] F. Yu, P. Saha, P. W. Suh and J. K. Kim, "Green Polyurethane from Dimer Acid Based Polyether Polyols: Synthesis and Characterization," *Journal of applied polymer science,* vol. 132, no. 5, pp. 1-9, 2015.

[190] F. Wanga, Z. Lia, J. L. Lannuttia, W. R. Wagnerb and J. Guana, "Synthesis, characterization and surface modification of low moduli poly(ether carbonate urethane)ureas for soft tissue engineering," *Acta Biomaterialia,* vol. 5, no. 8, pp. 2901-2912, 2009.

[191] G. Erdodi, J. Kang, J. P. Kennedy, E. Yilgor and I. Yilgor, "Polyisobutylene-

based polyurethanes. III. Polyurethanes containing PIB/PTMO soft co-segments," *Journal of Polymer Science Part A: Polymer Chemistry,* vol. 47, no. 20, pp. 5278-5290, 2009.

[192] V. Thomas and M. Jayabalan, "A new generation of high flex life polyurethane urea for polymer heart valve—Studies on in vivo biocompatibility and biodurability," *Journal of Biomedical Materials Research Part A,* vol. 89A, no. 1, pp. 192-205, 2009.

[193] V. P. Marija, J. Nestorov, G. Tovilović-Kovačević, P. Jovančić, L. Pezo, D. Vasiljević-Radović and J. Đonlagić, "Surface characterization, hemo-and cytocompatibility of segmented poly(dimethylsiloxane)-based polyurethanes," *Hemijska industrija,* vol. 68, no. 6, pp. 731-741, 2014.

[194] H. Hoffmann, E. Leibold, C. Ehnes, E. Fabiana, R. Landsiedel, A.Gamer and A. Poole, "Dermal uptake and excretion of C-14-toluene diisocyante (TDI) and C-14-methylene diphenyl diisocyanate (MDI) in male rats. Clinical signs and histopathology following dermal exposure of male rats to TDI," *Toxicology Letters,* vol. 199, no. 3, pp. 364-371, 2010.

[195] M. Alishiri, A. Shojaei, M. Abdekhodaie and H. Yeganeh, "Synthesis and characterization of biodegradable acrylated polyurethane based on poly(epsilon-caprolactone) and 1,6-hexamethylene diisocyanate," *Materials Science and Engineering: C,* vol. 42, pp. 763-773, 2014.

[196] Z. Wang, L. Yu, M. Ding, H. Tan, J. Lia and Q. Fu, "Preparation and rapid degradation of nontoxic biodegradable polyurethanes based on poly(lactic acid)-poly(ethylene glycol)-poly(lactic acid) and L-lysine diisocyanate," *Polymer Chemistry,* vol. 2, no. 3, pp. 601-607, 2011.

[197] L. Tatai, T. G. Moore, R. Adhikari, F. Malherbe, R. Jayasekar and P. A. G. Ian Griffiths, "Thermoplastic biodegradable polyurethanes: The effect of chain extender structure on properties and in-vitro degradation," *Biomaterials,* vol. 28, no. 36, pp. 5407-5417, 2007.

[198] K. Bouchemal, S. Briançona, E. Perrier, H. Fessi, I. Bonnet and N. Zydowicz, "ynthesis and characterization of polyurethane and poly(ether urethane) nanocapsules using a new technique of interfacial polycondensation combined

to spontaneous emulsification," *International Journal of Pharmaceutics,* vol. 269, no. 1, pp. 89-100, 2004.

[199] A. Karchin, F. I. Simonovsky, B. D. Ratner and J. E. Sanders, "Melt electrospinning of biodegradable polyurethane scaffolds," *Acta Biomaterialia ,* vol. 7, no. 9, pp. 3277-3284, 2011.

[200] S. A. Guelcher, K. M. Gallagher, J. E. Didier, D. B. Klinedinst, J. S. Doctor, A. S. Goldstein, G. L. Wilkes, E. J. Beckman and J. O. Hollinger, "Synthesis of biocompatible segmented polyurethanes from aliphatic diisocyanates and diurea diol chain extenders," *Acta Biomaterilia,* vol. 1, no. 4, pp. 471-484, 2005.

[201] D. Chattopadhyay, B. Sreedhar and K. V. Raju, "Effect of Chain Extender on Phase Mixing and Coating Properties of Polyurethane Ureas," *Industrial & engineering chemistry research,* vol. 44, no. 6, pp. 1772-1779, 2005.

[202] G. A. Skarja and K. A. Woodhouse, "In vitro degradation and erosion of degradable, segmented polyurethanes containing an amino acid-based chain extender.," *Journal of biomaterials science, Polymer Edition,* vol. 12, no. 8, pp. 851-873, 2001.

[203] J. V. Cauich-Rodríguez, L. H. Chan-Chan, F. Hernandez-Sánchez and J. M. Cervantes-Uc, Advances in Biomaterials Science and Biomedical Applications, InTech, 2013.

[204] J. Kucinska-Lipka, I. Gubanska and H. J. M. Sienkiewicz, "Fabrication of polyurethane and polyurethane based composite fibres by the electrospinning technique for soft tissue engineering of cardiovascular system," *Materials Science and Engineering: C,* vol. 46, no. 1, pp. 166-176, 2015.

[205] H. Zhuo, J. Hu, S. Chen and L. Yeung, "Preparation of Polyurethane Nanofibers by Electrospinning," *Applied polymer science,* vol. 109, pp. 406-411, 2008.

[206] S. Mondal, "Influence of solvents properties on morphology of electrospun polyurethane nanofiber mats," *Polymer advanced technologies,* vol. 25, pp. 179-183, 2014.

[207] M. Demir, I. Yilgor and E. Yilgor, "Electrospinning of polyurethane fibers,"

*Polymer,* vol. 43, no. 11, pp. 3303-3309, 2002.

[208] D. Cozzens, X. Wei and R. Faust, "Electrospinning of biostable polyisobutylene-based thermoplastic polyurethanes," *Polymer Physics,* vol. 51, no. 6, pp. 452-459, 2012.

[209] U. Siemann, "Solvent cast technology – a versatile tool for thin film production," *Progress in Colloid and Polymer Science,* vol. 130, pp. 1-14, 2005.

[210] Z. Tang, R. A. Black, J. Curran, J. Hunt, N. Rhodes and D. Williams, "Surface properties and biocompatibility of solvent-cast poly[ε-caprolactone] films," *Biomaterials,* vol. 25, no. 19, pp. 4741-4748, 2004.

[211] N. Bhardwaj, "Electrospinning: A fascinating fiber fabrication technique," *Biotechnology Advances,* no. 28, pp. 325 - 347, 2010.

[212] J. H. Wendorff, S. Agarwal and A. Greiner, Electrospinning: Materials, Processing and Applications, Weinheim: Wiley, 2012.

[213] A. Yarin, S. Koombhongse and D. Reneker, "Taylor cone and jetting from liquid droplets in electrospinning of nanofibers," *Journal of Applied Physics,* vol. 90, no. 9, pp. 4839-4846, 2001.

[214] Z. Huang, Y. Zhang, M. Kotaki and S. Ramakrishna, "A review on polymer nanofibers by electrospinning and their applications in nanocomposites," *Composites science and technology,* vol. 63, no. 15, pp. 2223-2253, 2003.

[215] D. H. Reneker and I. Chun, "Nanometre diameter fibres of polymer, produced by electrospinning," *Nanotechnology,* vol. 7, pp. 216-223, 1996.

[216] Y. Shin, M. Hohman, M. Brenner and G. Rutledge, "Experimental characterization of electrospinning: the electrically forced jet and instabilities," *Polymer,* vol. 42, no. 25, p. 9955–9967, 2001.

[217] Y. Shin, M. Hohman, M. Brenner and G. Rutledge, "Electrospinning: A whipping fluid jet generates submicron polymer fibers," *Applied Physics Letters,* vol. 78, no. 8, pp. 1149-1151, 2001.

[218] J. Deitzel, J. Kleinmeyer, D. Harris and N. Tan, "The effect of processing variables on the morphology of electrospun nanofibers and textiles," *Polymer,*

vol. 42, no. 1, pp. 261-272, 2001.

[219] S. D. Vrieze, T. V. Camp, A. Nelvig, B. Hagstrom, P. Westbroek and K. D. Clerck, "The effect of temperature and humidity on electrospinning," *Journal of Material Science,* vol. 44, pp. 1357-1362, 2009.

[220] G. C. Rutledge and S. V. Fridrikh, "Formation of fibers by electrospinning," *Drug Delivery Reviews,* vol. 59, pp. 1384 - 1391, 2007.

[221] A. H. Hekmati, A. Rashidi, R. Ghazisaeidi and J.-Y. Drean, "Effect of needle length, electrospinning distance, and solution concentration on morphological properties of polyamide-6 electrospun nanowebs," *Textile Research Journal ,* vol. 83, no. 14, pp. 1452-1466, 2013.

[222] T. Uyar and F. Besenbacher, "Electrospinning of uniform polystyrene fibers: The effect of solvent conductivity," *Polymer,* vol. 49, no. 24, pp. 5336-5343, 2008.

[223] F. Wang, W. Zhang, Z. Shao, Y. Sun and C. Ru, "Electrospinning system with tunable collector for fabricating three- dimensional nanofibrous structures," *Micro & Nano Letters,* vol. 9, no. 1, pp. 24-27, 2014.

[224] V. Beachley and X. Wen, "Effect of electrospinning parameters on the nanofiber diameter and length," *Materials Science and Engineering C,* vol. 29, pp. 663-668, 2009.

[225] D. Li, Y. Wang and Y. Xia, "Electrospinning of Polymeric and Ceramic Nanofibers as Uniaxially Aligned Arrays," *Nano Letters,* vol. 3, no. 8, pp. 1167-1171, 2003.

[226] R. Samatham and K. Kim, "Electric current as a control variable in the electrospinning process," *Polymer Engineering and Science,* vol. 46, no. 7, pp. 954-959, 2006.

[227] D. Fallahi, M. Rafizadeh, N. Mohammadi and B. Vahidi, "Effect of applied voltage on jet electric current and flow rate in electrospinning of polyacrylonitrile solutions," *Polymer International,* vol. 57, no. 12, pp. 1363-1368, 2006.

[228] G. Viswanadam and G. Chase, "Modified electric fields to control the direction

of electrospinning jets," *Polymer,* vol. 54, no. 4, pp. 1397-1404, 2013.

[229] U. Ali, X. Wang and T. Lin, "Effect of nozzle polarity and connection on electrospinning of polyacrylonitrile nanofibers," *The Journal of The Textile Institute,* vol. 130, no. 11, pp. 1160-1168, 2012.

[230] A. K. F. Oruc and A. Demir, "Effects of Polarity on Electrospinning Process," *Textile Research Journal,* vol. 78, no. 6, pp. 532-539, 2008.

[231] H.-W. Tong, M. Wang and W. W. Lu, "Enhancing the biological performance of osteoconductive nanocomposite scaffolds through negative voltage electrospinning," *Nanomedicine,* vol. 8, no. 4, pp. 577-589, 2013.

[232] J. A. Hunt, B. F. Flanagan, P. J. McLaughlin, I. Strickland and D. F. Williams, "Effect of biomaterial surface charge on the inflammatory response: Evaluation of cellular infiltration and TNF alpha production," *Journal of biomedical materials research,* vol. 31, no. 1, pp. 139-144, 1996.

[233] S. Basu, M. Jassal and A. Agrawal, "Concept of minimum electrospinning voltage (MEV) in electrospinning of PAN-DMF system: effect of distance," *Journal of the Textile Institute,* vol. 104, no. 2, pp. 158-163, 2013.

[234] A. G.Whitton, Development and investigation of polymeric vascular graft materials, Glasgow: University of Strathclyde, 2012.

[235] J. J. Stankus, J. Guan, K. Fujimoto and W. R. Wagner, "Microintegrating smooth muscle cells into a biodegradable elastomeric fiber matrix," *Biomaterials,* vol. 27, pp. 735-744, 2006.

[236] M. Khil, D. Cha, H. Kim, I. Kim and N. Bhattarai, "Electrospun Nanofibrous Polyurethane Membraneas Wound Dressing," *Journal of Biomedical Research B,* vol. 67, no. 2, pp. 675-679, 2003.

[237] E.-R. Kenawy, F. I. Abdel-Hay, M. H. El-Newehy and G. E. Wnek, "Processing of polymer nanofibers through electrospinning as drug delivery systems," *Materials Chemistry and Physics,* vol. 113, pp. 296-302, 2009.

[238] H. Karakas, A. Saraç, T. Polat, E. Budak, S. Bayram, N. Dağ and S. Jahangiri, "Polyurethane Nanofibers Obtained By Electrospinning Process," *International Journal of Biological, Biomolecular, Agricultural, Food and*

*Biotechnological Engineering,* vol. 7, no. 3, pp. 177-180, 2013.

[239] G. Tetteh, A. Khan, R. Delaine-Smith, G. Reilly and I. Rehman, "Electrospun polyurethane/hydroxyapatite bioactive scaffolds for bone tissue engineering: the role of solvent and hydroxyapatite particles.," *Mechanical Behaviour of Biomedical Materials,* vol. 39, pp. 95-110, 2014.

[240] N. A. Hotaling, K. Bharti, H. Kriel and C. G. S. Jr., "DiameterJ: A validated open source nanofiber diameter measurement tool," *Biomaterials,* vol. 61, pp. 327 - 338, 2015.

[241] G. Binnig and C. Quate, "Atomic Force Microscope," *Physical Review Letters,* vol. 56, no. 9, pp. 930 - 933, 1986.

[242] B. Kainz, E. Oprzeska-Zingrebe and J. Toca-Herrera, "Biomaterial and cellular properties as examined through atomic force microscopy, fluorescence optical microscopies and spectroscopic techniques," *Biotechnology Journal,* vol. 9, no. 1, pp. 51-60, 2014.

[243] P. C. Braga, Atomic Force Microscopy - Biomedical Methods and Applications, New Jersey: Humana Press Inc., 2004.

[244] W. Bowen, Atomic Force Microscopes in Process Engineering, Oxford: Elsevier Ltd., 2009.

[245] P. Eaton and P. West, Atomic Force Microscopy, Oxford, 2010.

[246] "Atomic Force Microscopy," nanoScience instruments, [Online]. Available: http://www.nanoscience.com/. [Accessed 29 3 2012].

[247] Bhushan, Handbook of Nano-technology, Berlin: Springer, 2004.

[248] S. Magonov, V. Elings and M.-H. Whangbo, "Phase imaging and stiffness in tapping-mode atomic force microscopy," *Surface Science,* vol. 375, no. 2-3, pp. L385 -L391, 1997.

[249] D. F. Ogletree, R. W. Carpick and M. Salmeron, "Calibration of frictional forces in atomic force microscopy," *Review of Scientific Instruments,* vol. 67, no. 9, pp. 3298 - 3306, 1996.

[250] M. Marcus, R. Carpick, D. Sasaki and M. Eriksson, "Material anisotropy revealed by phase contrast in intermittent contact atomic force microscopy.,"

*Physical review letters,* vol. 88, no. 22, 2002.

[251] A. Noy, C. H. Sanders, D. V. Vezenov, S. S. Wong and C. M. Lieber, "Chemically-Sensitive Imaging in Tapping Mode by Chemical Force Microscopy: Relationship between Phase Lag and Adhesion," *Langmuir,* vol. 14, no. 7, pp. 1508 - 1511, 1998.

[252] J. Tamayo and R. García, "Effects of elastic and inelastic interactions on phase contrast images in tapping-mode scanning force microscopy," *Applied Physics Letters,* vol. 71, no. 16, pp. 2394 - 2396, 1997.

[253] D. M. Czajkowsky, M. J. Allen, V. Elings and Z. Shao, "Direct visualization of surface charge in aqueous solution," *Ultramicroscopy Letter,* vol. 74, pp. 1 - 5, 1998.

[254] Y. Wang, R. Song, Y. Li and J. Shen, "Understanding tapping-mode atomic force microscopy data on the surface of soft block copolymers," *Surface Science,* vol. 532, pp. 136-148, 2003.

[255] R. S. McLean and B. B. Sauer, "Tapping-Mode AFM Studies Using Phase Detection for Resolution of Nanophases in Segmented Polyurethanes and Other Block Copolymers," *Macromolecules ,* vol. 30, pp. 8314-8317, 1997.

[256] P. West, "A Guide to AFM Image Artifacts," Pacific Nanotechnology.

[257] C. Canale, B. Torre, D. Ricci and P. C. Braga, "Recognizing and avoiding artifacts in atomic force microscopy imaging.," *Methods in Molecular Biology ,* vol. 736, pp. 31-43, 2011.

[258] G. Haugstad, Atomic Force Microscopy: Understanding Basic Modes and Advanced Applications, Hoboken, New Jersey: John Wiley & Sons, Inc., 2012.

[259] S. Pathak, D. Stojakovic, R. Doherty and S. R. Kalidindi, "Importance of surface preparation on the nano-indentation stress-strain curves measured in metals," *Journal of materials research ,* vol. 24, no. 3, pp. 1142-1155, 2009.

[260] M. Li, W. Chen, Y.-T. Cheng and C.-M. Cheng, "Influence of contact geometry on hardness behavior in nano-indentation," *Mechanics of advanced materials and structures,* vol. 84, no. 2, pp. 315-320, 2009.

[261] S. Mukherjee, T. Khraishi and Y. Shen, "Modeling the effects of particles,

interstitials, vacancies and tip geometry on indentation-induced plasticity," *Molecular simulation,* vol. 32, no. 8, pp. 651-656, 2006.

[262] M. R. Vanlandingham, S. H. McKnight, G. R. Palmese, J. Elings, X. Huang, T. A. Bogetti, R. F. Eduljee and J. W. Jr., "Nanoscale indentation of polymer systems using the atomic force microscope," *The journal of adhesion ,* vol. 64, pp. 31-59, 1997.

[263] Lim and C. Tan, "Mechanical characterization of a single nanofiber," *Nanomechanics of Materials and Structures,* pp. 121 - 136, 2006.

[264] M. Doernera and W. Nixa, "A method for interpreting the data from depth-sensing indentation instruments," *Journal of Materials Research,* vol. 1, no. 4, pp. 601-609, 1986.

[265] W. Oliver and G. Pharr, "An improved technique for determining hardness and elastic modulus using load and displacement sensing indentation experiments," *Journal of Materials,* vol. 7, no. 6, pp. 1564 - 1583, 1992.

[266] H. Hertz, "Über die berührung fester elastischer Körper (On the contact of rigid elastic solids)," *Miscellaneous Papers,* p. 156, 1896.

[267] I. N. Sneddon, "The relation between load and penetration in the axisymmetric boussinesq problem for a punch of arbitrary pro," *International Journal of Engineering Science,* vol. 3, pp. 47-57, 1964.

[268] W. Oliver and G. Pharr, "Measurement of hardness and elastic modulus by instrumented indentation: Advances in understanding and refinements to methodology," *Journal of Materials Research,* vol. 19, no. 1, pp. 3 - 20, 2003.

[269] T. Y. Tsui and G. M. Pharr, "Substrate effects on nanoindentation mechanical property measurement of soft films on hard substrates," *Journal of materials research,* vol. 14, no. 1, pp. 292-301, 1998.

[270] C. Schick, "Differential scanning calorimetry (DSC) of semicrystalline polymers," *Analytical and Bioanalytical Chemistry,* vol. 295, no. 6, pp. 1589-1611, 2009.

[271] V. Chemie, Calorimetry - fundamentals and practice, Weinheim: VCH, 1984.

[272] S. Simon, "Temperature-modulated differential scanning calorimetry: theory

and application," *Thermochimica Acta,* vol. 374, no. 1, pp. 55-71, 2001.

[273] G. Pompe, A. Pohlers, P. Potschke and J.Pionteck, "Influence of processing conditions on the multiphase structure of segmented polyurethane," *Polymer,* vol. 39, no. 21, pp. 5147 - 5153, 1998.

[274] M. Iijima, T. Muguruma, W. A. Brantley and I. Mizoguchi, "Comparisons of nanoindentation, 3-point bending, and tension tests for orthodontic wires," *American Journal of Orthodontics and Dentofacial Orthopedics,* vol. 140, no. 1, pp. 65-71, 2011.

[275] J. Han, N. Pugno and S. Ryu, "Nanoindentation cannot accurately predict the tensile strength of graphene or other 2D materials.," *Nanoscale,* vol. 7, no. 38, pp. 15672-15679, 2015.

[276] R. Rodriıguez and I. Gutierrez, "Correlation between nanoindentation and tensile properties: Influence of the indentation size effect," *Materials Science and Engineering,* pp. 377-384, 2003.

[277] Y. Xu, Z. Petrovic, S. Das and G. L. Wilkes, "Morphology and properties of thermoplastic polyurethanes with dangling chains in ricinoleate-based soft segments," *Polymer,* vol. 49, pp. 4248-4258, 2008.

[278] K. Kojio, S. Kugumiya, Y. Uchiba, Y. Nishino and M. Furukawa, "The Microphase-separated Structure of Polyurethane Bulk and Thin Film," *Polymer Journal,* vol. 41, no. 2, pp. 118-124, 2009.

[279] D. J. Martin, G. F. Meijs, P. A. Gunatillake, S. J. McCarthy and G. M. Renwick, "The Effect of Average Soft Segment Length on Morphology and Properties of a Series of Polyurethane Elastomers. II. SAXS-DSC Annealing Study," *Journal of Applied Polymer Science,* vol. 64, no. 4, pp. 803-817, 1997.

[280] R. W. Seymour and S. L. Cooper, "Thermal Analysis of Polyurethane Block Polymers," *Macromolecules,* vol. 6, no. 1, pp. 48-52, 1972.

[281] B. Wu, A. Heidelberg, J. Boland, J. Sader, X. Sun and Y. Li, "Microstructure-hardened silver nanowires," *Nano Letters,* vol. 6, no. 3, pp. 468 - 472, 2006.

[282] N. Hai, X. Li and G. Hongsheng, "Elastic modulus of amorphous SiO2 nanowires," *Nanoscale Science and Design,* vol. 88, no. 4, 2005.

[283] S. Lee, C. Tekmen and W. Sigmund, "Three-point bending of electrospun TiO2 nanofibers," *Material science and engineering,* vol. 398, no. 1-2, pp. 77 - 81, 2005.

[284] S. Cuenot, S. Demoustier-Champagne and B. Nysten, "Elastic Modulus of Polypyrrole Nanotubes," *Physical Review Letters,* vol. 85, no. 8, pp. 1690 - 1693, 2000.

[285] E. Tan and C. T. Lim, "Effects of annealing on the structural and mechanical properties of electrospun polymeric nanofibres," *Nanotechnology,* vol. 17, pp. 2649 - 2654, 2006.

[286] S. K. Min, S. I. Kim and S. J. Kim, "Size-dependent elastic modulus of single electroactive polymer nanofibers," *Applied Physics Letters,* vol. 89, 2006.

[287] M. J. Cardona, Size-dependent mechanical properties of single polyurethane nanofibres, Glasgow: University of Strathclyde, 2012.

[288] H. Chen and Y. A. Elabd, "Polymerized Ionic Liquids: Solution Properties and Electrospinning," *Macromolecules,* vol. 42, pp. 3368-3373, 2009.

[289] X. Zong, K. Kim, D. Fang, S. Ran, B. S. Hsiao and B. Chu, "Structure and process relationship of electrospun," *Polymer,* vol. 43, pp. 4403-4412, 2002.

[290] R. Erdem, İ. Usta, M. Akalin, O. Atak, M. Yuksek and A. Pars, "The impact of solvent type and mixing ratios of solvents on the properties of polyurethane based electrospun nanofibers," *Applied Surface Science,* vol. 334, pp. 227-230, 2015.

[291] S. Theron, E. Zussman and A. Yarin, "Experimental investigation of the governing parameters in the electrospinning of polymer solutions," *Polymer,* vol. 45, no. 6, pp. 2017-2030, 2004.

[292] G. Bar, Y. Thomann, R. Brandsch, H.-J. Cantow and M.-H. Whangbo, "Factors Affecting the Height and Phase Images in Tapping Mode Atomic Force Microscopy. Study of Phase-Separated Polymer Blends of Poly(ethene-co-styrene) and Poly(2,6-dimethyl-1,4-phenylene oxide)," *Langmuir,* vol. 13, pp. 3807 -3812, 1997.

[293] B. B. Sauer, R. S. McLean and R. R. Thomas, "Tapping Mode AFM Studies of

Nano-Phases on Fluorine-Containing Polyester Coatings and Octadecyltrichlorosilane Monolayers," *Langmuir,* vol. 14, pp. 3045-3051, 1998.

[294] S. Magonov, V. Elings and V. Papkov, "AFM study of thermotropic structural transitions in poly(diethylsiloxane)," *Polymer,* vol. 38, no. 2, pp. 297 -307, 1997.

[295] N. M. Lamba, K. A. Woodhouse and S. L. Cooper, "Degradation of Polyurethanes," in *Polyurethanes in Biomedical Applications*, New york, CRC press, 1997.

[296] L. Fambri, A. Pegoretti, J.Kolarik, C. Gavazza and A. Penati, "Thermal stabilities of different polyurethanes after hydrolitic treatment," *Journal of thermal analysis,* vol. 52, pp. 789-79, 1998.

[297] A. Takahara, A. J. Coury, R. W. Hergenrother and S. L. Cooper, "Effect of soft segment chemistry on the biostability of segmented polyurethanes. I. In vitro oxidation.," *Journal of biomedical materials research,* vol. 25, no. 3, pp. 341-356, 1991.

[298] C. Nikki, S.-S. Taylor, D. Peter, F. Anna and P. F. Don, "Polyurethane-Coated Breast Implants Revisited:A 30-Year Follow-Up," *Archives of Plastic Surgery,* pp. 186-193, 2014.

[299] F. Benoit, "Degradation of polyurethane foams used in the Même breast implant.," *Journal of Biomedical Material Research,* vol. 10, pp. 1341-1348, 1993.

[300] M.-S. Khil, D.-I. Cha, H.-Y. Kim, I.-S. Kim and N. Bhattarai, "Electrospun nanofibrous polyurethane membrane as wound dressing," *Journal of Biomedical Materials Research Part B: Applied Biomaterials,* vol. 67B, no. 2, pp. 675-679, 2003.

[301] M. Pavlova and M. Draganova, "Hydrolytic stability of polyurethane medical adhesive dressings," *Biomaterials,* vol. 12, no. 1, pp. 59-62, 1994.

[302] H. Shintani and A. Nakamura, "Formation of 4,4'-methylenedianiline in polyurethane potting materials by either gamma-ray or autoclave sterilization.," *Journal of Biomedical Material Research,* vol. 10, pp. 1275-

1286, 1991.

[303] C. Batich, "TDA release from polyurethane covered breast implants may be a problem.," *Journal of Biomedical Material Research,* vol. 9, p. 1209, 1993.

[304] J. M. Anderson and K. M. Miller, "Biomaterial biocompatibility and the macrophage," *Biomaterials,* vol. 5, no. 1, pp. 5-10, 1984.

[305] X. Yang, C. Vang, D. Tallman, G. Bierwagen, S. Croll and S. Rohlik, "Weathering degradation of a polyurethane coating," *Polymer Degradation and Stability,* vol. 75, pp. 341-351, 2001.

[306] D. D. Deligianni, N. D. Katsala, P. G. Koutsoukos and Y. F. Missirlis, "Effect of surface roughness of hydroxyapatite on human bone marrow cell adhesion," *Biomaterials,* vol. 22, pp. 87-96, 2001.

[307] E. Biazar, M. Heidari, A. Asefnezhad and N. Montazeri, "The relationship between cellular adhesion and surface roughness in polystyrene modified by microwave plasma radiation," *International Journal of Nanomedicine,* vol. 6, pp. 631-639, 2011.

[308] T.-W. Chung, D.-Z. Liu, S.-Y. Wang and S.-S. Wang, "Enhancement of the growth of human endothelial cells by surface roughness at nanometer scale," *Biomaterials,* vol. 24, no. 25, pp. 4655-4661, 2003.

[309] S. Keshel, S. Azhdadi, A. Asefnejad, M. Sadraeian, M. Montazeri and E. Biazar, "The relationship between cellular adhesion and surface roughness for polyurethane modified by microwave plasma radiation," *International Journal of Nanomedicine,* vol. 6, pp. 641 - 647, 2011.

[310] D. Chen, J. Bei and S. Wang, "Polycaprolactone microparticles and their biodegradation," *Polymer Degradation and Stability ,* vol. 67, pp. 455-459, 2000.

[311] C. L. Salgado, E. M. S. Sanchez, C. A. C. Zavaglia and P. L. Granja, "Biocompatibility and biodegradation of polycaprolactone-sebacicacid blended gels," *Journal of Biomedical Materials Research Part A,* vol. 100A, pp. 243 - 251, 2012.

[312] J. M. Williams, A. Adewunmi, R. M. Schek, C. L. Flanagana, P. H. Krebsbach,

S. E. Feinberg, S. J. Hollister and S. Das, "Bone tissue engineering using polycaprolactone scaffolds fabricated via selective laser sintering," *Biomaterials,* vol. 26, pp. 4817 - 4827, 2005.

[313] H.-W. Kim, J. C. Knowles and H.-E. Kim, "Hydroxyapatite/poly(e-caprolactone) composite coatings on hydroxyapatite porous bone scaffold for drug delivery," *Biomaterials,* vol. 25, pp. 1279 - 1287, 2004.

[314] S. Suresh and R. A. Black, "Electrospun polyurethane as an alternative ventricular catheter and in vitro model of shunt obstruction," *Journal of Biomaterials Applications,* vol. 29, no. 7, pp. 1028 - 1038, 2014.

[315] P. Sangsanoh, O. Suwantong, A. Neamnark, P. Cheepsunthorn, P. Pavasant and P. Supaphol, "In vitro biocompatibility of electrospun and solvent-cast chitosan substrata towards Schwann, osteoblast, keratinocyte and fibroblast cells," *European polymer journal,* vol. 46, no. 3, pp. 428-440, 2009.

[316] L. Donnelly, "Airway epithelial cells (primaries vs cell lines)," in *Human Airway inflammation*, vol. 56, London, Humana Press Inc, 2001, pp. 127-136.

[317] S. M. Rezaei and Z. A. M. Ishak, "Grafting of collagen onto interpenetrating polymer networks of poly(2-hydroxyethyl methacrylate) and poly(dimethyl siloxane) polymer films for biomedical applications," *eXPRESS Polymer Letters,* pp. 39-49, 2014.

[318] I. Cifcová, P. Lopour, P. Vondráek and F. Jelínek, "Silicone rubber-hydrogel composites as polymeric biomaterials: I. Biogical properties of the silicone rubberp(HEMA) composite," *Biomaterials,* vol. 11, pp. 393 - 396, 1990.

[319] J. Kovalevich and D. Langford, "Considerations for the Use of SH-SY5Y Neuroblastoma Cells in Neurobiology," in *Neuronal cell culture: methods and protocols*, Totowa, Humana Press Inc, 2013, pp. 9-21.

[320] S. Påhlman, A. Ruusala, L. Abrahamsson, M. Mattsson and T. Esscher, "Retinoic acid-induced differentiation of cultured human neuroblastoma cells: a comparison with phorbolester-induced differentiation.," *Cell Differentiation,* vol. 14, no. 2, pp. 135-44, 1984.

[321] R. Pelham and Y. Wang, "Cell locomotion and focal adhesions are regulated by substrate flexibility," *Proceedings of the national academy of sciences of*

*the USA,* vol. 94, no. 25, pp. 13661-13665, 1997.

[322] K. Parker, A. Brock, C. Brangwynne, R. Mannix, N. Wang, E. Ostuni, N. Geisse, J. Adams, G. Whitesides and D. Ingber, "Directional control of lamellipodia extension by constraining cell shape and orienting cell tractional forces," *Faseb Journal,* vol. 16, no. 10, pp. 1195-1204, 2002.

[323] L. Smilenov, A. Mikhailov, R. Pelham, E. Marcantonio and G. Gundersen, "Focal Adhesion Motility Revealed in Stationary Fibroblasts," *Science,* vol. 286, no. 5442, pp. 1172-1174, 1999.

[324] C. F. Amstein and P. A. Hartman, "Adaptation of plastic surfaces for tissue culture by glow discharge.," *Journal of Clinical Microbiology,* vol. 2, no. 1, pp. 46-54, 1975.

[325] P. A. George, B. C. Donose and J. J. Cooper-White, "Self-assembling polystyrene-block-poly(ethylene oxide) copolymer surface coatings: Resistance to protein and cell adhesion," *Biomaterials,* vol. 30, pp. 2449-2456, 2009.

[326] H. Romijn, "Development and advantages of serum-free, chemically defined nutrient media for culturing of nerve tissue.," *Biology of the cell,* vol. 63, no. 3, pp. 263-268, 1988.

[327] A. Chong and D. Lam, "Strain gradient plasticity effect in indentation hardness of polymers," *Journal of Materials Research,* vol. 14, pp. 4103 - 4110, 1999.

[328] R. Tatiraju and C. Han, "Rate dependence of indentation size effects in filled silicone rubber," *ournal of mechanics of materials and structures ,* vol. 5, no. 2, pp. 477 - 288, 2010.

[329] A. Curtis and C. Wilkinson, "Topographical control of cells," *Biomaterials,* vol. 18, no. 24, pp. 1573-1583, 1997.

[330] L. L. Hench and J. M. Polak, "Third-Generation Biomedical Materials," *Science,* vol. 295, no. 5557, pp. 1014 - 1017, 2002.

[331] L. Jones, R. Haugland and V. Singer, "Development and characterization of the NanoOrange (R) protein quantitation assay: A fluorescence-based assay of proteins in solution," *BioTechniques,* vol. 34, no. 4, pp. 850-858, 2003.

[332] R. R. Duling, R. B. Dupaix, N. Katsube and J. Lannutti, "Mechanical characterization of electrospun polycaprolactone (PCL): a potential scaffold for tissue engineering.," *Journal of biomechanical engineering,* vol. 130, no. 1, p. 011006, 2008.

[333] Q. Wei, W. Gao, D. Hou and X. Wang, "Surface modification of polymer nanofibres by plasma treatment," *Applied surface science,* vol. 245, no. 1 - 4, pp. 16 - 20, 2005.